Advances in Materials Science and Engineering

Durability of Reinforced Concrete under the Influence of Combined Mechanical and Environmental Load

Lead Guest Editor: Peng Zhang
Guest Editors: Michael Vogel and Zhendi Wang

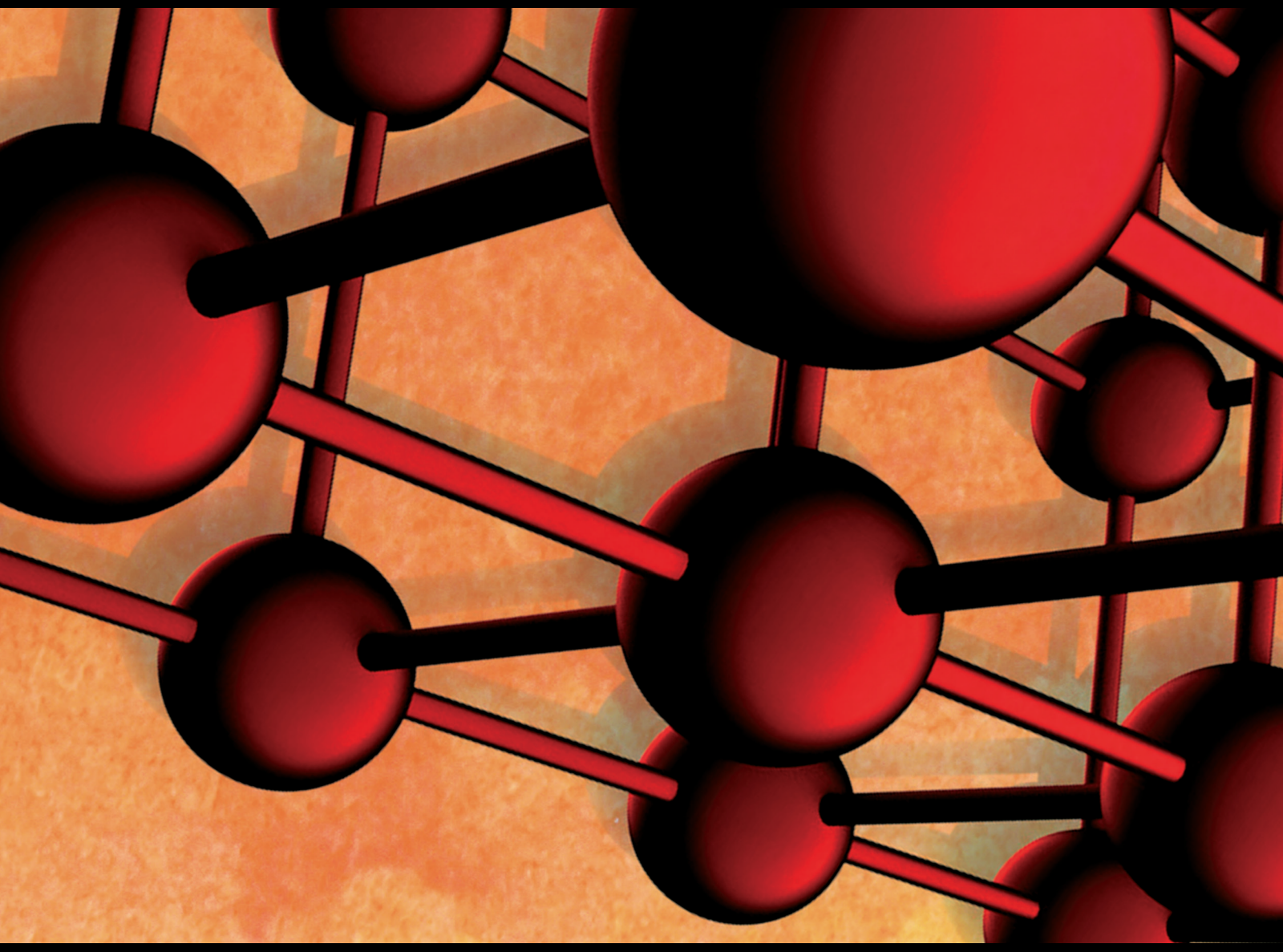

Durability of Reinforced Concrete under the Influence of Combined Mechanical and Environmental Load

Advances in Materials Science and Engineering

Durability of Reinforced Concrete under the Influence of Combined Mechanical and Environmental Load

Lead Guest Editor: Peng Zhang
Guest Editors: Michael Vogel and Zhendi Wang

Contents

Axial Compression Behaviors of the Steel Tube Confined Reinforced Concrete Columns with Binding Bars

Hao Hu, Zhengliang Li, Xi Tu, and Junfeng Tang

Research Article (12 pages), Article ID 6683429, Volume 2020 (2020)

Hindawi
Advances in Materials Science and Engineering
Volume 2021, Article ID 9920945, 14 pages
https://doi.org/10.1155/2021/9920945

Research Article

Early Cracking Risk Prediction Model of Concrete under the Action of Multifield Coupling

Caiyun Jin,[1] **Jianglin Liu**,[2] **Zigeng Wang**,[2] **and Yue Li**[2]

[1]*College of Applied Sciences, Beijing University of Technology, No. 100 Pingleyuan Chaoyang District, Beijing 100124, China*
[2]*The Key Laboratory of Urban Security and Disaster Engineering, MOE, Beijing University of Technology, Beijing 100124, China*

Correspondence should be addressed to Jianglin Liu; liujl@emails.bjut.edu.cn

Received 31 March 2021; Accepted 5 July 2021; Published 15 July 2021

Academic Editor: Peng Zhang

Through the adiabatic temperature rise experiment, the adiabatic temperature rise of concrete with hydration time was recorded. Based on the maturity degree theory, the relationship between the hydration degree of the concrete and the equivalent age was determined. Then, the hydration degree prediction model of the concrete's early elastic modulus and tensile strength was established. The local temperature and humidity of the concrete were measured by the shrinkage experiment, and based on the capillary water tension theory, a temperature-humidity prediction model for the early shrinkage of the concrete was designed. According to the ratio of the creep deformation and elastic deformation of concrete which were obtained through the restraint ring experiment, a model for predicting the early creep coefficient of concrete was proposed. Based on the coupling effect of "hydration-temperature-humidity," a prediction model of early cracking risk coefficient of concrete under multifield coupling was proposed. Finally, several groups of slab cracking frame experiments were carried out, and the cracking risk prediction results of concrete were consistent with the actual situation, which indicated the correctness of the early cracking risk prediction model of concrete.

1. Introduction

The large use of superplasticizers and mineral admixtures, the higher fineness of cement, and the lower water-binder ratio are the typical characteristics of modern concrete. Therefore, the strength of concrete can be significantly improved. However, there are some problems of modern concrete, such as the rapid hydration, the large shrinkage, the rapid internal temperature rises, and the rapid internal humidity decrease, which led to early cracking of concrete. If the early cracks of concrete cannot be strictly controlled, especially the cracks caused by nonload factors in the early stage of concrete structure, the durability and safety of concrete would be reduced [1–5]. Meanwhile, fiber [6] would be used to improve the anticracking property of concrete.

A large number of studies have shown that [7–12] the anticracking property of concrete would be directly or indirectly affected by the change of internal factors such as hydration, temperature, humidity, shrinkage, and creep. Shen et al.'s [10] research found that the curing condition of concrete at 20°C had better anticracking properties than that of 45°C. Zhang et al. [8] established a relationship between the internal humidity of concrete and the free shrinkage strain of concrete at the macro level. The results show that the faster the internal humidity of concrete decreased, the greater the shrinkage at the macro level. Bentz [9] defined the ratio of creep strain to effective shrinkage strain as the creep coefficient of concrete, and the shrinkage of concrete was one of the main factors affecting the cracking, so the early anticracking property of concrete would also be affected by the early creep of concrete. The above research showed that the early anticracking property of concrete had a complex relationship with cement hydration, temperature, humidity, shrinkage, and creep. Many scholars have studied the early anticracking property of concrete with mineral admixtures such as fly ash and slag but have not yet reached a consistent conclusion [2, 13–15]. Therefore, it is necessary to

propose an accurate method to predict the early cracking risk of modern concrete.

Liu et al. [16] used the dumbbell method to evaluate the early anticracking performance of concrete materials under constraint conditions. Although this method can quickly evaluate the anticracking property of different concrete materials, it was only aimed at the rapid qualitative detection and analysis of the construction site and cannot quantitatively evaluate the cracking of concrete. Meagher [6] used HIPERPAV software to simulate the influence of admixtures on the early cracking risk of concrete repair plate; Zhang [6] used the ring restraint experiment to evaluate the anticracking property of low shrinkage cement-based materials. Although the above method can evaluate the early anticracking property of concrete, the root cause of the early cracking of concrete cannot be obtained.

Based on (1), Bendimerad et al., [17] neglected the early creep of concrete and considered that the deformation tensile stress $\sigma_t(t)$ was only a function of the elastic modulus $E_{(t)}$ and the plastic shrinkage strain $\varepsilon_{sh}(t)$, that is, $\sigma_t(t) = E_{(t)} \times \varepsilon_{sh}(t)$, and the plastic shrinkage and cracking risk of recycled aggregate concrete within 24 hours was explored. Which method can predict the risk factor η of concrete cracking within 24 hours and the mathematical model of early cracking prediction of concrete has also been defined. However, as the age of concrete increased, the creep of concrete would become larger [18, 19], and it also led to the limitation of Ahmed's method to predict the early cracking of concrete due to neglecting creep, which was only applicable to the evaluation of concrete cracking resistance within 24 hours.

$$\eta = \frac{\sigma_t(t)}{f_t(t)}. \tag{1}$$

Therefore, based on the adiabatic temperature rise experiment, shrinkage experiment, and creep experiment of concrete, a prediction model that described the cracking of concrete due to early multifield coupling effects such as "hydration-temperature-humidity" was proposed in this study. The basic cause of concrete early cracking from the mechanism was explained, and the early cracking prediction model of concrete proposed by Bendimerad et al., [17] has been further improved by this prediction model. At the same time, the slab cracking frame experiment method was used to test the cracking resistance of several groups of concrete. Finally, the test results of Khan et al. [20] and Zhang et al. [6] were selected, and the cracking risk prediction model proposed in this study was used to verify the test results of the literature [6, 20].

2. Experiment

2.1. Materials and Experiment Design

2.1.1. Material Properties. The raw materials used for concrete were cement, fly ash, slag, sand, coarse aggregate, superplasticizer, and tap water. The physical and chemical properties of these raw materials were as follows: P·O42.5 ordinary Portland cement conformed with the current Chinese national standard GB 175-2007 "Common Portland Cement." The 3 d and 28 d compressive strength of P·O42.5 ordinary Portland cement was 27 MPa and 49 MPa, respectively, and the specific gravity and specific surface area were 3.16 g/cm^3 and 354 m^2/kg respectively. Grade I fly ash conformed with the current Chinese national standard GB/T 1596-2017 "Fly ash used for cement and concrete." The ignition loss, water demand ratio, and moisture content of fly ash were 3.7%, 88%, and 0.4%, respectively; The specific surface area, 7-day activity index, and ignition loss of slag were 425 m^2/kg, 78%, and 0.26%, respectively. And the main chemical composition is shown in Table 1. The fineness modulus of the river sand was 2.56. The particle size of calcareous coarse aggregate was a continuous gradation of 5–20 mm. The polycarboxylate superplasticizer had a water reduction rate of 31%.

2.1.2. Mix Proportion Design of Concrete. According to the concrete mix proportion shown in Table 2, the elastic modulus experiment, axial tensile experiment, adiabatic temperature rise experiment, shrinkage experiment, and creep experiment of concrete were carried out in this study. The above experiments were mainly used to determine the parameters in the prediction model of concrete cracking risk coefficient. Finally, in order to verify the applicability of the early cracking prediction model of concrete, 3 groups of slab cracking frame experiments were carried out according to the concrete mix proportion shown in Table 2. The dosage of aggregate and cementitious material was determined by the trial mix proportion of the control target based on the strength (when the design strength of concrete was C40, W/B = 0.45; when the design strength of concrete was C60, W/B = 0.35; when the design strength of concrete was C80, W/B = 0.25). The slump of TS-1, TS-2, and TS-3 concrete was 85 mm, 88 mm, and 93 mm, respectively. The compressive strength of TS-1, TS-2, and TS-3 concrete was 42.3 MPa, 63.5 MPa, and 81.7 MPa, respectively.

2.2. Experiment Method

2.2.1. Tensile Strength and Elastic Modulus Experiment of Concrete. According to the current Chinese national standard for "Standard for test method of mechanical properties on ordinary concrete" (GB/T50081-2016), based on the mix proportion shown in Table 2, the elastic modulus and tensile strength of concrete in 1 d, 3 d, 5 d, 7 d, 14 d, 21 d, and 28 d were tested.

2.2.2. Adiabatic Temperature Rise Experiment of Concrete. According to the current Chinese national standard for "Test code for hydraulic concrete" (SL 352-2006), based on the 3 types of concrete mix proportions shown in Table 2, 50 L concrete samples were selected for the adiabatic temperature rise experiment. At the early stage of the experiment, the adiabatic temperature rise was recorded every 0.5 h, and every 5 h after 24 h, until the end of the adiabatic temperature rise experiment, which lasted a total of 7 days. The

Table 1: Main chemical composition of cementitious material (mass fraction%).

Materials	CaO	SiO_2	Al_2O_3	Fe_2O_3	SO_3	MgO
Cement	59.98	23.6	7.21	3.07	2.14	2.07
Fly ash	2.93	55.10	20.5	7.7	0.28	2.25
Slag	42.49	38.61	7.27	0.4	0.9	6.71
Silica fume	0.40	95.00	0.40	0.80	0.50	0.30

Table 2: Mix proportion of concrete (kg/m^3).

No.	W/B	Cement	Fly ash	Slag	Silica fume	Sand	Coarse aggregate	Superplasticizer
TS-1	0.45	250	65	65	0	920	930	6
TS-2	0.35	270	85	95	0	830	930	8
TS-3	0.25	360	90	100	50	770	920	12

Note. TS-1, TS-2, and TS-3 represented 3 experiment mix proportions of concrete, respectively.

adiabatic temperature rise experiment device is shown in Figure 1(a). The temperature sensor in the figure was used to record the adiabatic temperature rise value of the concrete. The temperature compensation circuit and the heat insulation layer were mainly used to avoid the loss of hydration heat of concrete.

2.2.3. Shrinkage Experiment of Concrete. The coupling effect of the early "temperature-humidity" field of concrete was considered in this study, according to the current Chinese national standard for "Test code for hydraulic concrete" (SL 352-2006), based on the 3 types of concrete mix proportions shown in Table 2, the concrete shrinkage deformer as shown in Figure 1(b) [8] was used, the size of the concrete specimen was 100 mm × 100 mm × 515 mm, and a temperature and humidity senor was installed in the center of the specimen, which can automatically collect the deformation, temperature, and humidity at the inner center of the concrete. The room temperature was about 22°C, and the relative humidity was about 60%. The shrinkage of concrete in 1 d, 3 d, 5 d, 7 d, 14 d, 21 d, and 28 d was recorded.

2.2.4. Creep Experiment of Concrete. Gawin et al. [21] proposed a mathematical calculation method for creep of concrete, which decomposed the total creep strain rate tensor into two parts: viscoelastic strain rate and viscous flow strain rate. Li et al. [11] analyzed the early creep performance of concrete by using the ring restraint experiment, which showed that this method can not only ensure the accuracy of the early creep of concrete measured by the experiment but also be simpler than the calculation method of concrete early creep proposed by Gawin et al. [21]. Therefore, the ring restraint experiment was also adopted in this study, and the early creep experiment of concrete was carried out according to the concrete mix proportion shown in Table 2.

2.2.5. Early Cracking Experiment of Concrete. According to the current Chinese national standard for "Standard for test method for long-term performance and durability of ordinary concrete" (GB/T 50082-2009) in this study, a slab cracking frame as shown in Figure 1(c) was selected. The size of the cracking frame was 900 mm × 700 mm × 100 mm. The side plates, bolts, and stiffening rib were mainly used to fix the steel formwork of the cracking frame, and the crack inducer was mainly used to induce the early cracking of concrete due to shrinkage. This experiment was mainly to observe the cracking conditions after the initial setting of concrete and was used to verify the correctness of the cracking risk prediction model proposed in this paper. The room temperature was about 22°C, and the relative humidity was about 60%. When the concrete cracked, the test observation stopped.

3. Establishment of Cracking Risk Coefficient Prediction Model

3.1. The Establishment of Early Cracking Risk Prediction Model of Concrete. According to the criterion of concrete cracking [17], the cracking risk coefficient η was used to evaluate the early cracking resistance of modern concrete, as shown in the following equation:

$$\eta = \frac{\sigma_t(t)}{f_t(t)} = \frac{E_{(t)} \times \varepsilon_{\text{sh-e}}(t)}{f_t(t)}, \tag{2}$$

where $\sigma_t(t)$ is the deformation tensile stress (cracking driving force) of concrete at the early age t, MPa; $f_t(t)$ is the tensile strength of concrete at the early age t, MPa; $E_{(t)}$ is the elastic modulus of the concrete at the early age t, MPa; $\varepsilon_{\text{sh-e}}(t)$ is the effective shrinkage strain of the concrete at the early age t. Among them, when $\eta < 0.7$, the concrete does not crack; when $0.7 \le \eta \le 1.0$, the concrete may crack; when $\eta > 1.0$, the concrete cracks.

Gao et al.'s [22, 23] research showed that the effective shrinkage strain $\varepsilon_{\text{sh-e}}(t)$ was the result of the interaction of the shrinkage strain and the creep strain (strain of concrete due to creep) of the concrete, as shown in

$$\varepsilon_{sh-e}(t) = \varepsilon_{sh}(t) - \varepsilon_{\text{creep}}(t, t_0), \tag{3}$$

where t and t_0 are the age of concrete and the age of concrete under loading, respectively, d; $\varepsilon_{sh}(t)$ is the shrinkage strain of the concrete at the age t; $\varepsilon_{\text{creep}}(t, t_0)$ is the shrinkage strain of the concrete due to creep in the early age (t, t_0).

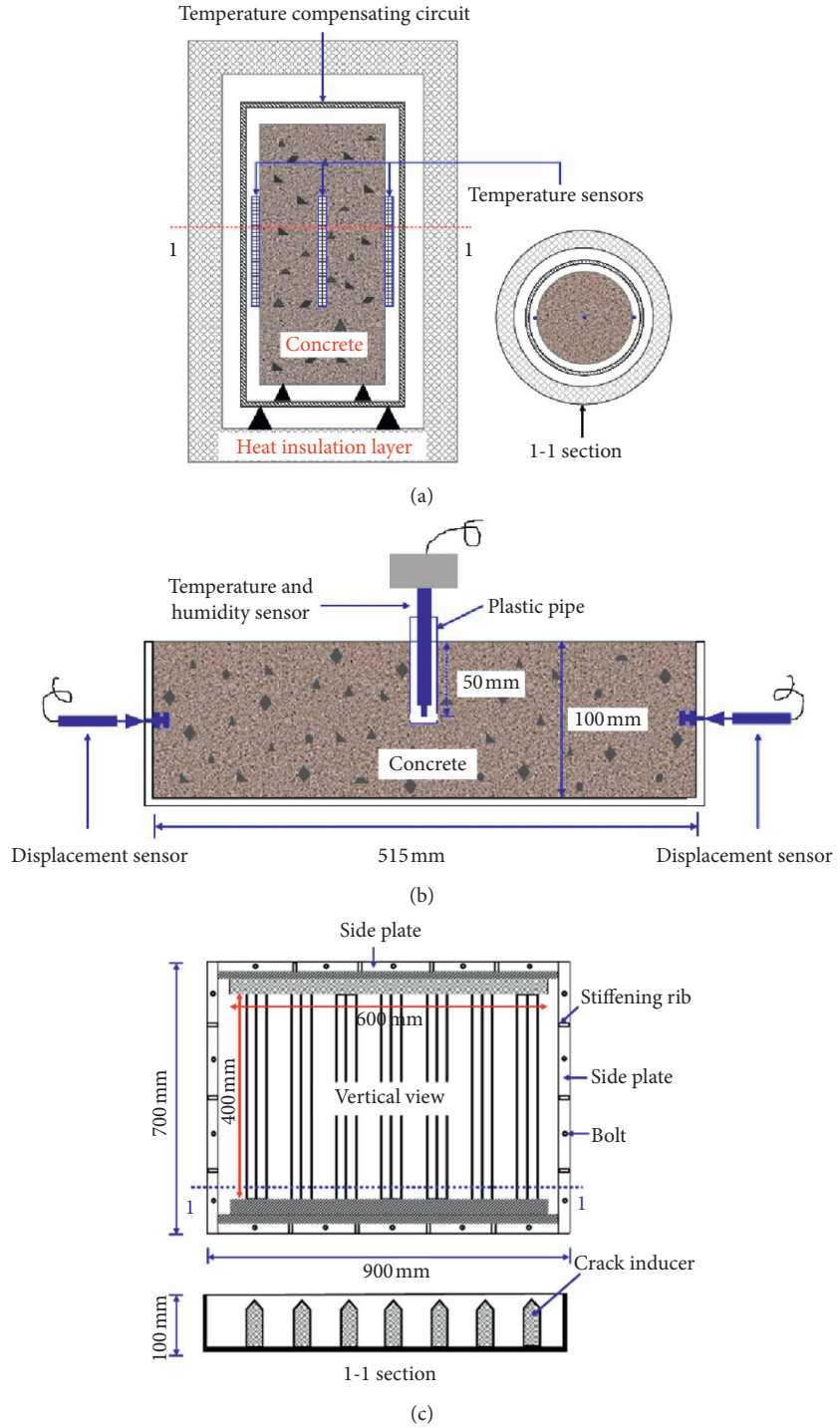

Figure 1: Schematic diagram of the test device. (a) Adiabatic temperature rise experiment for concrete. (b) Shrinkage experiment of concrete. (c) Slab cracking frame experiment of concrete.

Bentz et al.'s [9, 23] study showed that the relationship between creep strain and effective shrinkage strain can be expressed by creep coefficient φ, as shown in

$$\phi_{(t,t_0)} = \frac{\varepsilon_{\text{creep}}(t,t_0)}{\varepsilon_{\text{sh-e}}(t,t_0)}, \tag{4}$$

where $\phi_{(t,t_0)}$ is the creep coefficient of concrete at an early age (t,t_0).

It can be known from equations (3) and (4) that the expression of the relationship between the effective shrinkage strain $\varepsilon_{\text{sh-e}}$ of concrete at an early age (t,t_0) is shown as follows:

$$\varepsilon_{sh-e}(t,t_0) = \frac{\varepsilon_{sh}(t)}{1+\phi_{(t,t_0)}}. \quad (5)$$

Equation (5) was substituted into equation (2), and the risk prediction model of early cracking of modern concrete was obtained as follows:

$$\eta = \frac{E_{(t)} \cdot \varepsilon_{sh}(t)}{f_t(t) \cdot \left(1+\phi_{(t,t_0)}\right)}. \quad (6)$$

Therefore, based on the prediction model of concrete cracking proposed by Ahmed [17], the effect of creep on the early cracking of concrete was further considered, and the prediction model of modern concrete cracking risk with creep coefficient was put forward innovatively. In Section 3.2, based on the coupling effect of multifields such as "hydration-temperature-humidity-force" in the early stage of concrete, the elastic modulus $E_{(t)}$, tensile strength $f_t(t)$, shrinkage strain $\varepsilon_{sh}(t)$, and creep coefficient $\phi_{(t,t_0)}$ of concrete at age t would be determined.

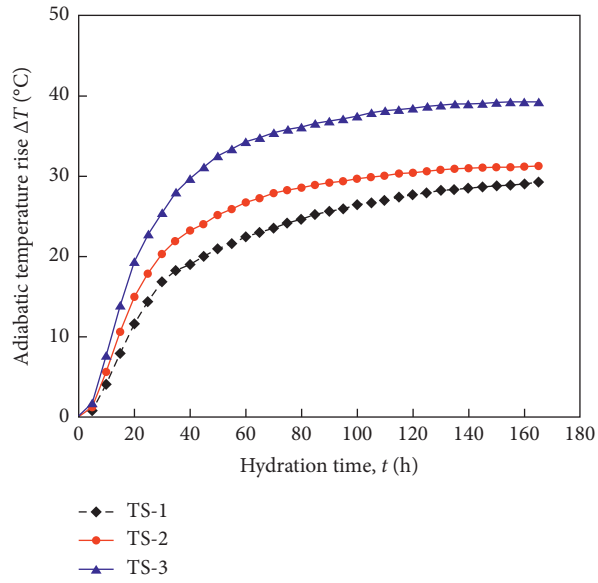

Figure 2: Adiabatic temperature rise curve of concrete.

3.2. Multifield Coupling Control Mechanism and Determination of Mechanical Parameters

3.2.1. Experiment Results of Adiabatic Temperature Rise and Determination of Cement Hydration Degree. The adiabatic temperature rise experiment results of TS-1, TS-2, and TS-3 concrete are shown in Figure 2. Based on the adiabatic temperature rise experiment of concrete, the hydration degree α of cement can be expressed as [7]

$$\alpha = \frac{\Delta T_{(t)}}{\Delta T_{\infty}}, \quad (7)$$

where $\Delta T_{(t)}$ is the adiabatic temperature rise value of the concrete temperature rise sample at the age t, ˚C; ΔT_{∞} is the adiabatic temperature rise value reached when the concrete is fully hydrated, ˚C.

However, the cement in the concrete cannot be completely hydrated [7, 24]. It was assumed that when the adiabatic temperature rise of the concrete reached $\Delta T_{\max}$, the cement hydration was completed, and the final hydration degree α_u of the cement can be expressed as

$$\alpha_u = \frac{\Delta T_{\max}}{\Delta T_{\infty}}. \quad (8)$$

An important typical characteristic of modern concrete was used of mineral admixtures. Schindler and Folliard [25] had studied a lot of research on the final hydration degree of cement in modern concrete mixed with slag and fly ash, and the final hydration degree model of cement containing slag and fly ash was proposed as follows:

$$\alpha_u = \frac{1.031 \cdot (W/C)}{0.194 + (W/C)} + 0.50 \cdot P_F + 0.30 \cdot P_S \le 1.0, \quad (9)$$

where W/C represents the mass ratio of water and cement in concrete; P_F represents the mass percentage of fly ash in cement in total cementitious materials; P_S represents the percentage of slag in cement in total cementitious materials.

Luzio and Cusatis [26] concluded that the final hydration degree of cement in concrete mixed with silica fume was expressed as follows:

$$\alpha_\alpha = \frac{1.032 \cdot W/C - 0.279\,(s/c)\alpha_s^{\infty}}{0.194 + W/C}, \quad (10)$$

where α_s^{∞} is the final reaction degree of silica fume, which was expressed as follows [27]:

$$\alpha_s^{\infty} = SF^{\text{eff}} \min\left[1, \frac{(S/C)_{\text{req}}}{(S/C)}\right], \quad (11)$$

where SF^{eff} is the "effective coefficient" of silica fume, that is, the mass fraction of SiO2 in silica fume; $(S/C)_{\text{req}} = \min(0.16, 0.4\,(W/C))$.

According to equations (7) and (8), the relationship between the hydration degree $\alpha(t)$ of cement at age t and the final hydration degree α_u of the cement can be expressed as

$$\alpha(t) = \alpha_u \frac{\Delta T_{(t)}}{\Delta T_{\max}}, \quad (12)$$

where $\Delta T_{(t)}$ and $\Delta T_{\max}$ can be obtained from the adiabatic temperature rise curve. Theoretically, the longer the adiabatic temperature rise experiment duration, the more accurate the measured value of $\Delta T_{\max}$ was.

However, under different temperature histories of the same mix ratio, the internal cement hydration degree was different at the same age. Therefore, based on the maturity theory, the concept of equivalent age was introduced to eliminate the influence of the temperature history of concrete on its concrete internal hydration. The age t required for cement hydration in concrete under different temperature histories was equivalent to the age t_{eq} required for concrete under reference temperature (usually 20˚C), and its calculation expression was as follows [7]:

$$t_{\mathrm{eq}} = \int_0^t e^{\frac{1}{R}\left(\frac{U_{\mathrm{ar}}}{293} - \frac{U_{\mathrm{aT}}}{273+T}\right)} \mathrm{d}t, \tag{13}$$

where t_{eq} is the equivalent age, d; R is the ideal gas constant, 8.314 J/(mol · K); U_{ar} is the activation energy of the internal cement hydration reaction at the reference temperature of the concrete; T is the temperature of the concrete, ˚C; U_{aT} is the activation energy of the internal cement hydration reaction at temperature T of the concrete.

Kim [28] found that the apparent activation energy can be regarded as a constant in the early stage of cement hydration. However, with the hydration reaction proceeds of the cement, the effects of temperature T and curing time on the apparent activation energy of the cement need to be considered. At this time, U_{aT} can be expressed as

$$U_{aT} = (42830 - 43T)e^{(-0.00017T)t}, \tag{14}$$

where t is the curing age, d. The continuous curve of (13) was divided into n segments, the interval of each segment is $(t_i - t_{i-1})$, and the expression as shown in (15) was obtained:

$$t_{eq} = \sum_{i=1}^{n} e^{\frac{1}{R}\left(\frac{U_{ar}}{293} - \frac{U_{aT}}{273+T}\right)} \cdot (t_i - t_{i-1}). \tag{15}$$

Pane and Hansen [29] explored the relationship between the hydration degree α of cement and the equivalent age t_{eq}, a model of the equivalent age and adiabatic temperature rise experiment of the cement hydration degree was established, and the relationship expression as shown in equation (16) was proposed:

$$\alpha(t) = \alpha_u e^{\left(\frac{A}{t_{\mathrm{eq}}}\right)^B}, \tag{16}$$

where the constants of A and B were obtained by fitting the model according to the above equation.

Therefore, the research ideas were as follows in this section, the fresh concrete was placed in the adiabatic temperature rise experiment chamber, and then the temperature inside the adiabatic temperature rise experiment chamber was recorded by the temperature sensor, and the relationship curve between adiabatic temperature rise values and hydration time was drawn. The final hydration degree α_u of concrete was calculated according to equation (10), and then the hydration degree $\alpha(t)$ corresponding to each hydration time was determined according to equation (12). At the same time, based on the maturity theory, the concept of equivalent age was introduced to eliminate the influence of the temperature history of concrete on its internal cement hydration degree. According to equation (15), the equivalent age t_{eq} corresponding to the actual hydration time was determined. Finally, based on (16), the parameters A and B were determined; that is, the mathematical model of concrete hydration degree and equivalent age was determined.

To sum up, according to the adiabatic temperature rise curve shown in Figure 2 and equations (7)–(16) in Section 3.1, the test value and fitting curve of cement hydration degree and equivalent age are obtained as shown in Figure 3,

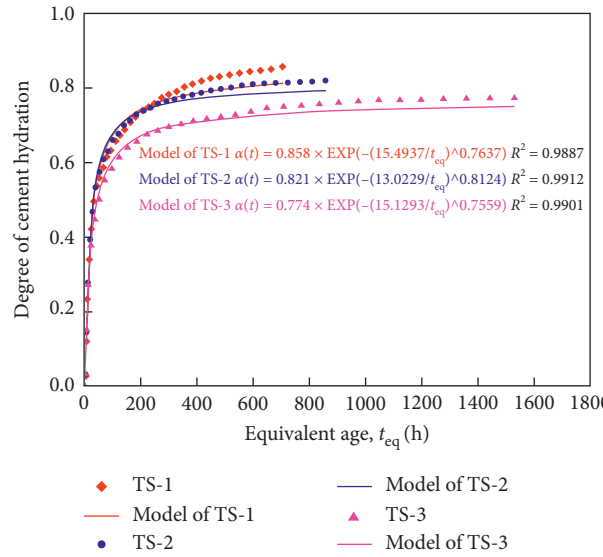

Figure 3: Test value and fitting value of cement hydration degree and equivalent age in the concrete of TS-1 concrete, TS-2 concrete, and TS-3 concrete.

and the relevant parameters and model fitting parameters are listed in Table 3.

The R^2 values of the model result and the test result in Figure 3 were not less than 0.98, indicating that the correlation was very high. It can be seen that the model of cement hydration degree and equivalent age proposed by Pane [29] can be well described the development law of cement hydration degree and equivalent age in different concrete mix proportions, and the effect of temperature history on cement internal hydration degree of the concrete can be eliminated.

3.2.2. Determination of Early Elastic Modulus Prediction Model of Concrete. Zhang and Schutter [7, 30] have explored the relationship between the mechanical properties (elastic modulus, tensile strength, etc.) of concrete and the hydration degree of cement. Therefore, according to the test results of the elastic modulus of concrete, the hydration degree method was used to describe the early elastic modulus of concrete. The prediction model of the hydration degree of the elastic modulus was as follows:

$$E(\alpha) = \beta_E \cdot E_{28} \cdot \left(\frac{\alpha - \alpha_0}{\alpha_u - \alpha_0}\right)^b, \tag{17}$$

where $E(\alpha)$ is the elastic modulus of concrete when the degree of cement hydration is α, MPa; β_E is the subsequent increase coefficient of the elastic modulus of concrete after 28 days, 1.05; E_{28} is the elastic modulus of concrete after 28 days of curing, GPa; α_0 is the hydration degree at the initial setting of the concrete; α_u is the final hydration degree of the concrete; b is a constant obtained by fitting the hydration degree model of the concrete's elastic modulus to the test values. The measured value and fitting curve of elastic modulus of concrete are shown in Figure 4, and the relevant

Table 3: Test parameters and fitting parameters of concrete.

No.	α_0	α_u	A	B	b	d
TS-1	0.152	0.858	14.49	0.76	1.575	1.144
TS-2	0.125	0.821	13.02	0.81	1.910	1.434
TS-3	0.106	0.529	15.13	0.76	1.350	1.175

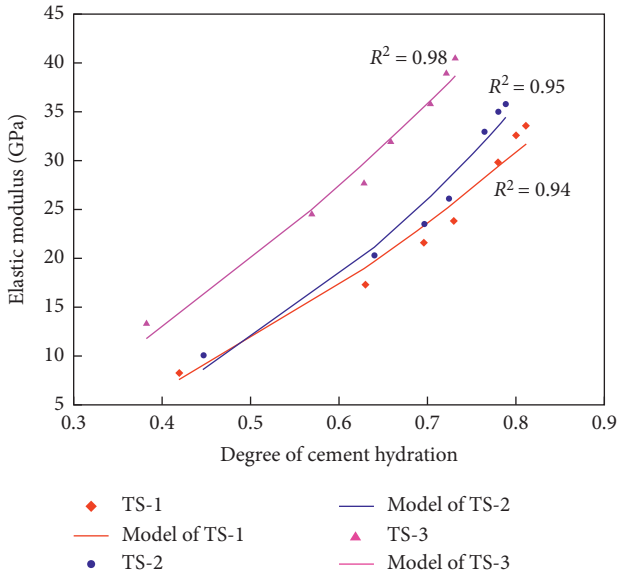

Figure 4: Test and fitting values of concrete elastic modulus and hydration degree of TS-1 concrete, TS-2 concrete, and TS-3 concrete.

parameters and model fitting parameters are listed in Table 3.

In Figure 4, R2 of TS-1, TS-2, and TS-3 model results and test values were 0.94, 0.95, and 0.98, respectively, with high correlation. It can be seen that the early elastic modulus prediction model of concrete proposed by Zhang and Schutter [7, 30] can be well described the relationship between the elastic modulus and hydration degree of concrete.

3.2.3. Determination of Early Tensile Strength Prediction Model of Concrete. According to the test results of the tensile strength of concrete, the hydration degree of concrete was used to describe the early tensile strength. The prediction model of the tensile strength was [17,31]

$$f(\alpha) = \beta_f \cdot f_{28} \cdot \left(\frac{\alpha - \alpha_0}{\alpha_u - \alpha_0}^{d}\right), \quad (18)$$

where $f(\alpha)$ is the tensile strength of concrete when the degree of cement hydration is α, MPa; β_f is the subsequent increase coefficient of the tensile strength of concrete after 28 days, 1.05; f_{28} is the tensile strength of concrete after 28 days of curing, GPa; the meaning of α_0 and α_u was shown in equation (17); d is a constant obtained by fitting the hydration degree model of the concrete's tensile strength to the test values. The measured tensile strength and fitting curve of concrete are shown in Figure 5, and the relevant parameters and model fitting parameters are listed in Table 3.

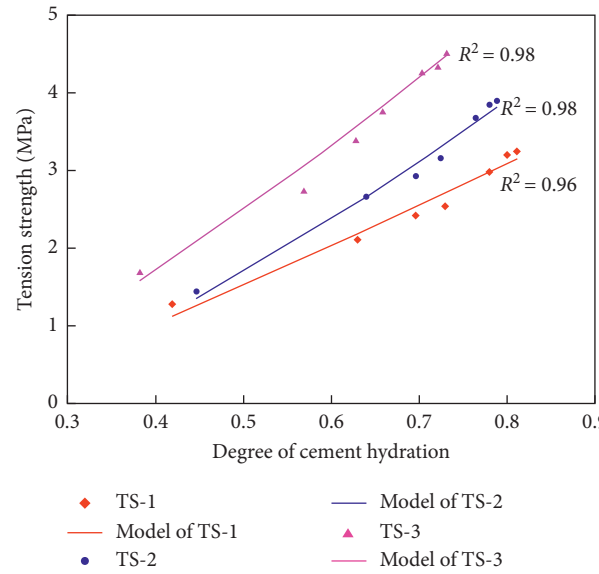

Figure 5: Test and fitting values of concrete tensile strength and hydration degree of TS-1 concrete, TS-2 concrete, and TS-3 concrete.

The R2 values of model results and test values in Figure 5 were not less than 0.95, and the correlation between the predicted results and test results was very high. It can be seen that the early tensile strength prediction model of concrete proposed by Zhang and Schutter [7, 30] can be well described the relationship between concrete tensile strength and hydration degree.

3.2.4. Early Shrinkage Prediction Model of Concrete. Zhang [8] considered that the change of the internal humidity of concrete was the root cause of the early autogenous shrinkage and dry shrinkage of concrete, and the relationship between early shrinkage of concrete and internal humidity was explored by using a normal experiment environment without temperature control. The results showed that although the internal humidity of the concrete changed gradually along the thickness direction of the specimen, the local humidity can be used to estimate the shrinkage strain of the concrete specimen at the macro level, and then the shrinkage stress of the structure can be calculated. Bentz et al., [32] used capillary water tension theory to predict the shrinkage deformation of concrete. The results showed that the concrete shrinkage value can be calculated by knowing the internal relative humidity of the concrete. Therefore, based on the coupling effect of the "temperature-humidity" field in the early stage of the concrete, the capillary water tension theory was used to establish the early shrinkage strain prediction model of the concrete according to the local temperature and humidity of the concrete.

(1) Shrinkage Prediction Model of Concrete Based on Humidity Field. The change of internal relative humidity of concrete would lead to the change of capillary water tension. The relationship between the internal humidity of concrete and the age measured by the shrinkage experiment in this study is

shown in Figure 6. The mechanical model of the concrete element under the tension of capillary water is shown in Figure 7. The calculation process of concrete element shrinkage caused by capillary water tension was as follows: where d_x, d_y, and d_z are the side lengths of the concrete element.

$$V_0 = d_x \cdot d_y \cdot d_z, \tag{19}$$

When the volume of a concrete element changes due to internal humidity, the shrinkage strains of the concrete element along the X-axis, Y-axis, Z-axis directions were assumed as ε_x, ε_y, and ε_z, respectively, and the volume V of the concrete element at this time was

$$V = d_x(1+\varepsilon_x)\cdot d_y\left(1+\varepsilon_y\right)\cdot d_z(1+\varepsilon_z). \tag{20}$$

Therefore, the volume strain ε_V (change of unit volume) of the concrete was

$$\begin{aligned}\varepsilon_V &= \frac{V-V_0}{V_0}\\ &= \varepsilon_x+\varepsilon_y+\varepsilon_z+\varepsilon_x\cdot\varepsilon_y+\varepsilon_y\cdot\varepsilon_z+\varepsilon_x\cdot\varepsilon_z.\end{aligned} \tag{21}$$

After the concrete element was loaded, the shrinkage strain of the concrete element along the X-axis, Y-axis, and Z-axis directions was

$$\varepsilon_x = \frac{1}{E}\left(\sigma_x-\mu\left(\sigma_y+\sigma_z\right)\right), \tag{22}$$

$$\varepsilon_y = \frac{1}{E}\left(\sigma_y-\mu\left(\sigma_x+\sigma_z\right)\right), \tag{23}$$

$$\varepsilon_z = \frac{1}{E}\left(\sigma_z-\mu\left(\sigma_x+\sigma_y\right)\right), \tag{24}$$

where E is the static elastic modulus of the concrete, GPa; μ is Poisson's ratio of the concrete, taking 0.2 [33]; σ_x, σ_y, and σ_z represent the capillary water tension of the concrete element in the X-axis, Y-axis, and Z-axis directions.

The higher-order terms of equation (21) were ignored, equations (22)–(24) were substituted into (21), and the volume strain of concrete was obtained as follows:

$$\begin{aligned}\varepsilon_V &= \varepsilon_x+\varepsilon_y+\varepsilon_z\\ &= \frac{1-2\mu}{E}\left(\sigma_x+\sigma_y+\sigma_z\right)\\ &= \frac{\left(\sigma_x+\sigma_y+\sigma_z\right)}{3K},\end{aligned} \tag{25}$$

where the bulk modulus $K = E/3(1-2\mu)$, GPa.

Assuming that the strains in each direction of concrete shrinkage were equal. Under the action of capillary water tension σ, the shrinkage strain ε_w in the X-axis, Y-axis, and Z-axis directions was

$$\varepsilon_w = \frac{\sigma}{3K}. \tag{26}$$

Lura et al. [33] considered that the capillary pores caused by chemical shrinkage of the cementitious material internal the concrete were completely wetted, and the contact angle between water and solids was 0. At this time, the capillary water tension of the concrete was

$$\sigma = -\frac{\rho R(273+T)\ln RH}{M}, \tag{27}$$

where σ is the capillary water tension of concrete; ρ is the density of water, kg/m^3; R is the ideal gas constant, 8.314 J/(molK); T is the internal temperature of the concrete as shown in Figure 6, ˚C; RH is the internal relative humidity of the concrete as shown in Figure 6; M is the molar mass of water, g/mol.

However, concrete was a heterogeneous material and contains pores in it, so the bulk modulus K of the concrete in equations (25)–(26) needed to be modified [34]. Meanwhile, because the water in the pores was consumed at the hydration of cement in the early stage, making the pores tend to be unsaturated [31], it was necessary to introduce saturation S to further modify the shrinkage strain of concrete in (26). Therefore, the equation after modify of concrete was (shrinkage prediction model of concrete based on humidity field)

$$\varepsilon_w = S\cdot\frac{\sigma}{3K}, \tag{28}$$

where σ is the capillary water tension of the concrete, which was calculated according to equation (27); the specific calculation process of the modified bulk modulus K and the saturation S was shown in equations (29)-(30).

The reciprocal of the modified bulk modulus K [4, 34] was

$$\frac{1}{K} = \frac{1}{K_C}-\frac{1}{K_s}, \tag{29}$$

where K is the bulk modulus used for calculating the shrinkage strain of concrete in equation (28); the bulk modulus $K_C = E_C/3(1-2\mu)$, where E_C is the elastic modulus of concrete (calculated according to (17)); μ is Poisson's ratio of concrete, taking 0.2 [33], the units of K_C and E_C are GPa; K_S is the bulk modulus of the solid material, taking 44 GPa [33].

The saturation S [35] was

$$S = \frac{p-0.7(1-p)\alpha}{p-0.5(1-p)\alpha}, \tag{30}$$

where $p = (W/C)/(W/C)+(\rho_W/\rho_C)$, W/C is the mass ratio of water and cement, ρ_W/ρ_C is the density ratio of water and cement, and α is the hydration degree of concrete.

(2) Shrinkage Prediction Model of Concrete Based on Temperature Field. Based on the shrinkage experiment of concrete, the relationship between the internal temperature of concrete and its age was measured in this study as shown in Figure 6. The finite element method was used by Liu et al. [36, 37] to predict the anticracking property of concrete. The thermal expansion coefficient of concrete was regarded as a constant, and the values were 9.94 $\mu\varepsilon$/˚C and 10 $\mu\varepsilon$/˚C. Li [11] determined that the thermal expansion coefficient of C30 and C80

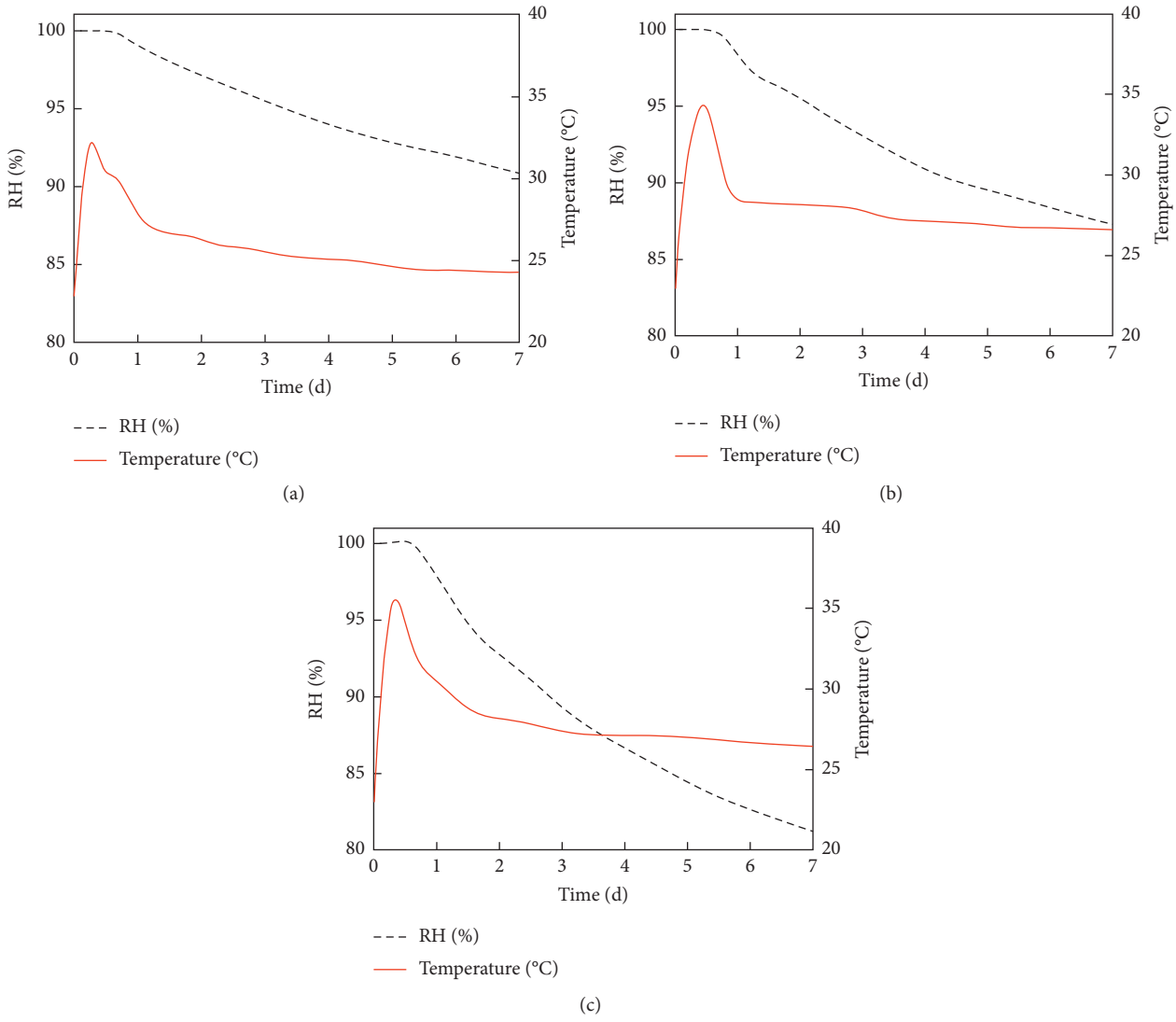

Figure 6: The relation curve of concrete internal humidity-temperature and age. (a) TS-1 concrete. (b) TS-2 concrete. (c) TS-3 concrete.

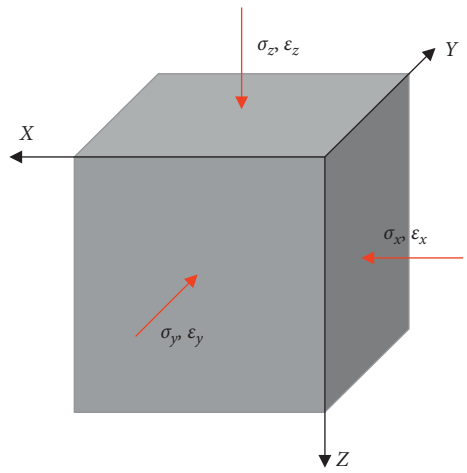

Figure 7: Schematic diagram of capillary water tension of concrete element.

concrete was between $10\,\mu\varepsilon/^{\circ}\mathrm{C}$ and $12\,\mu\varepsilon/^{\circ}\mathrm{C}$ through the variable temperature experiment of concrete. Therefore, the thermal expansion coefficient was taken as $10\,\mu\varepsilon/^{\circ}\mathrm{C}$ in this study, and it was applied to the prediction model of concrete shrinkage. At this time, the temperature deformation ε_T of concrete with temperature history between (T_0, T) was (shrinkage prediction model of concrete based on temperature field)

$$\begin{aligned}\varepsilon_T &= \int_{T_0}^{T} \beta_T \mathrm{d}T \\ &= \int_{T_0}^{T} 10 \mathrm{d}T \\ &= 10 \cdot (T - T_0) \\ &= 10 \cdot \Delta T,\end{aligned} \tag{31}$$

where β_T is the thermal expansion coefficient of concrete, $\mu\varepsilon/^{\circ}\mathrm{C}$; T_0 is the internal temperature of the concrete at the initial setting, $^{\circ}\mathrm{C}$; T is the internal temperature of the

concrete at time t, °C; and ΔT is the difference between T and T_0, °C.

(3) Determination and Verification of Early Shrinkage Prediction Model of Concrete. In this study, the shrinkage prediction model of concrete was determined based on the humidity field (based on the capillary water tension theory) and the temperature field in Section 3.2.4 (2), and the shrinkage prediction model of concrete in the early stage under the coupling effect of "temperature-humidity" field was obtained as follows:

$$\varepsilon = \varepsilon_w + \varepsilon_T = S \cdot \frac{\sigma}{3K} + 10 \cdot \Delta T. \tag{32}$$

Therefore, based on equation (32), according to the relationship curve of temperature-humidity and age shown in Figure 6, combined with the hydration degree prediction model of concrete elastic modulus, the prediction value of concrete shrinkage strain shown in Figure 8 was obtained, which showed that the test results almost coincided with the prediction results, indicating that the method of using the local temperature and humidity inside the concrete to predict the macro shrinkage of the component was feasible and also verified the accuracy of the early shrinkage prediction model of concrete, which was consistent with the conclusion of Zhang [8].

3.2.5. Determination of Early Creep Prediction Model of Concrete. In this study, based on the ring restraint test results in Section 2.2.4, the creep coefficient of concrete was defined as the ratio of creep deformation to elastic deformation under circumferential constraint [9]. The early creep coefficient of concrete obtained by the test is shown in Figure 9. According to the early creep results of concrete explored by Jiang et al. [38], the concrete creep coefficient was fitted with an exponential model, and the specific fitting equation was as follows:

$$\varphi_t = D_1 \cdot e^{\left(-t/D_2\right)} + \varphi_0, \tag{33}$$

where φ_t represents the creep coefficient of concrete at time t; D_1, D_2, and φ_0 are parameters obtained by fitting the test values based on the exponential model (equation (33)), and the fitting results are shown in Table 4.

The R^2 values of the predicted results and test values in Figure 9 were not less than 95%, and the correlation between the predicted results and test results was very high. It can be seen that the early creep prediction model of concrete proposed by Schutter [7, 30] can well describe the relationship between concrete early creep and age.

3.3. Determination of Cracking Risk Prediction Model of Concrete under the Action of Multifield Coupling. According to the coupling effect of multiple-fields such as "hydration-temperature-humidity-force" in the early stage of concrete, and based on equation (6), from the perspective of the change mechanism of the internal hydration degree, temperature, and humidity of the concrete, the cracking risk prediction model of modern concrete was proposed as follows:

$$\eta = \frac{E_{(t)} \cdot \varepsilon_{sh}(t)}{f_t(t) \cdot \left(1 + \phi_{(t,t_0)}\right)} = \frac{\left(\beta_E \cdot E_{28} \cdot \left((\alpha - \alpha_0)/(\alpha_u - \alpha_0)\right)^b\right) \times (S \cdot (\sigma/3K) + 10 \cdot \Delta T)}{\left(\beta_f \cdot f_{28} \cdot \left((\alpha - \alpha_0)/(\alpha_u - \alpha_0)\right)^d\right) \times \left(1 + \left(D_1 \cdot e^{\left(-t/D_2\right)} + \phi_0\right)\right)}. \tag{34}$$

4. Verification of the Cracking Risk Prediction Model of Modern Concrete

In this study, a slab cracking frame was used for the early cracking experiment of concrete, and the cracking of TS-1, TS-2, and TS-3 concrete after the initial setting was recorded. Based on equation (6), according to the elastic modulus, tensile strength, macro shrinkage strain, and creep coefficient of concrete, the experimental value of the concrete cracking risk coefficient was calculated. Meanwhile, based on equation (34), according to the hydration degree, temperature, humidity, and creep of concrete in the early stage, the predicted value of the concrete cracking risk coefficient was calculated. Finally, according to the cracking risk coefficients calculated by equations (6) and (34), they were compared with the cracking state measured by the slab cracking frame experiment to verify the accuracy of the early cracking risk prediction model of concrete. In addition, the experiment results of Khan [20] and Zhang [6] were selected in this paper, and the cracking risk prediction model proposed in this study was used to verify the test results of the literature [6, 20].

4.1. Cracking the State of Concrete in the Slab Cracking Frame Experiment. The cracking state of the concrete in the slab cracking frame experiment is shown in Figure 10. The TS-1 mix proportion was used for the slab cracking frame experiment, and the concrete began to crack on the third day. The TS-2 mix proportion was used for the slab cracking frame experiment, and the concrete cracks appeared on the first day. The TS-3 mix proportion was used for the slab cracking frame experiment, and the concrete had cracks on the first day.

4.2. Verification of the Cracking Risk Prediction Model of Concrete. Based on the test results of the elastic modulus, tensile strength, shrinkage strain, creep coefficient, and adiabatic temperature rise values of the concrete, the cracking risk coefficients calculated according to equations (6) and (34) are shown in Table 5. Khan et al. [20] believed that the early cracking of concrete was caused by creep and shrinkage. Finally, the correctness of his opinion was verified by the finite element method. Based on the restraint ring experiment, the concept of equivalent shrinkage strain (equivalent shrinkage strain was $K \times \varepsilon$, where K is the creep coefficient of concrete) was proposed by Zhang et al. [6], and

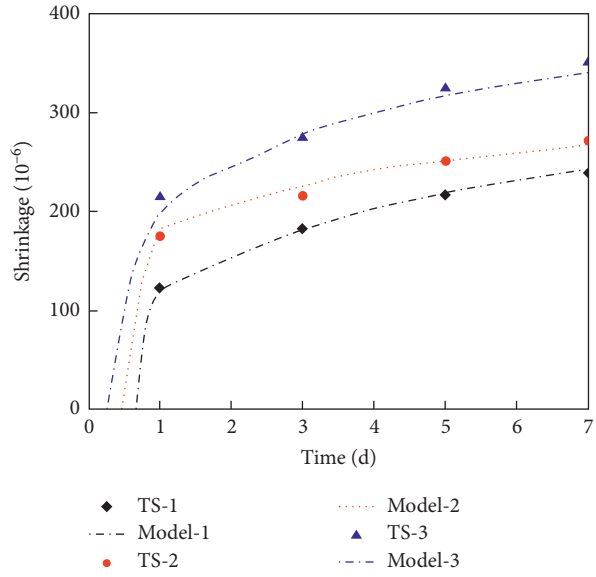

Figure 8: Experimental and predicted values of concrete shrinkage and age.

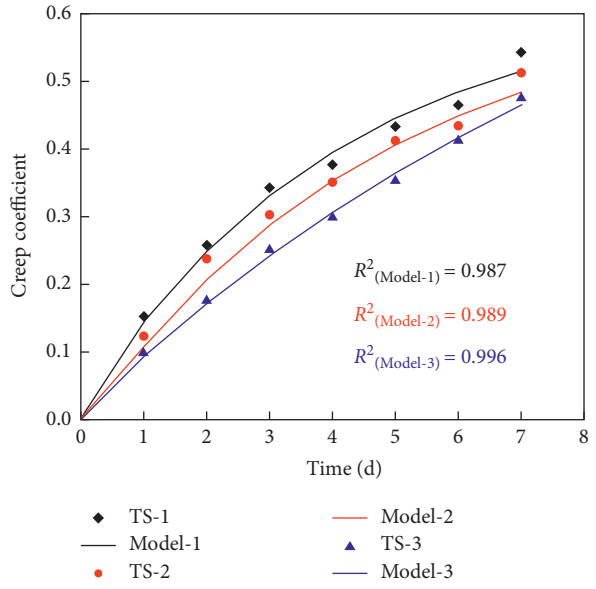

Figure 9: Experimental and fitting values of the relationship between early creep and age of concrete.

Table 4: Test parameters and fitting parameters of concrete.

No.	D_1	D_2	φ_0
TS-1	−0.6176	4.0831	0.6270
TS-2	−0.6250	4.7436	0.6333
TS-3	−0.9237	10.1974	0.9302

the anticracking property of ECC (traditional engineered cementitious composite) and LSECC (low shrinkage engineered cementitious composite) concrete was evaluated by mathematical calculation model. Therefore, the test results of Khan et al. [20] and Zhang et al. [6] were selected in this study, the cracking risk prediction model proposed in this paper was adopted, and the test results of literature [6, 20] were further verified. The calculation data and results of cracking risk are listed in Table 5.

It can be seen from Table 5 that the early cracking risk coefficient of concrete calculated based on equations (6) and (34) was basically consistent with the actual cracking time

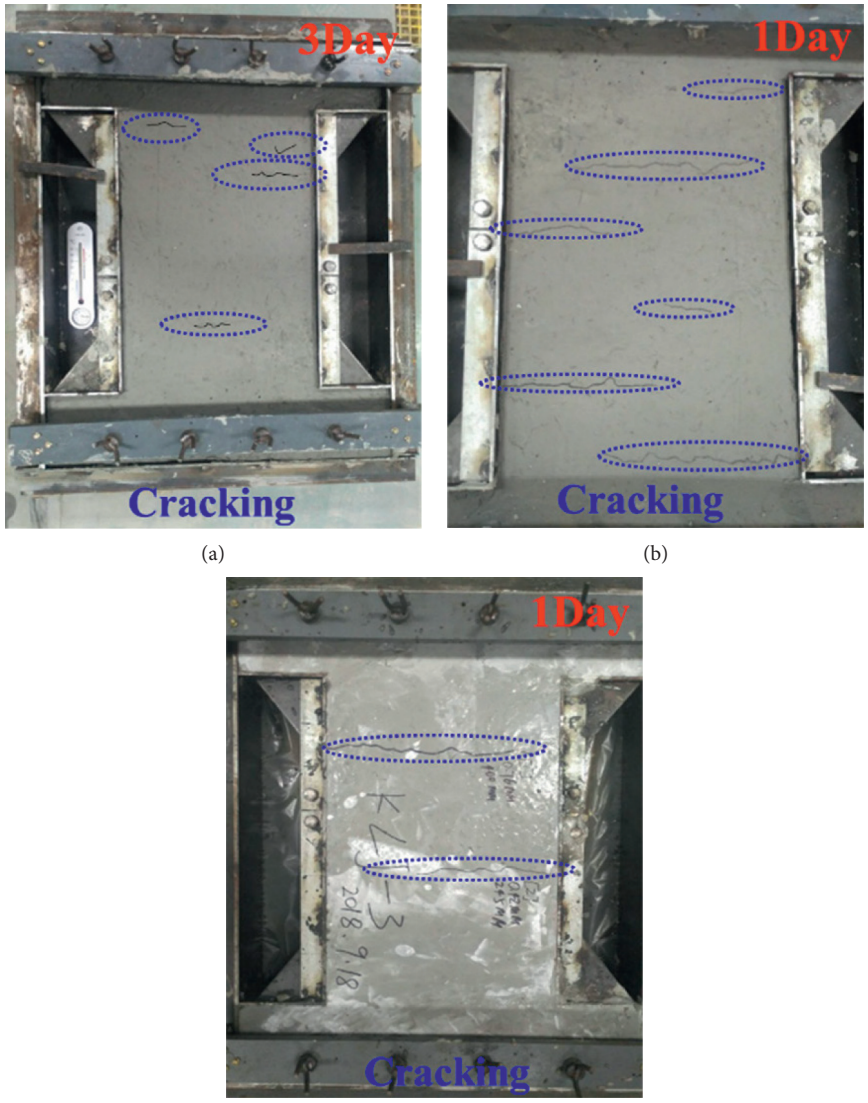

Figure 10: The cracking state of the concrete in the slab cracking frame. (a) TS-1 concrete; (b) TS-2 concrete; (c) TS-3 concrete.

and cracking state of concrete, which showed that the early cracking risk prediction model of the modern concrete can be well predicted the cracking resistance of concrete.

Khan et al. [20] used the restraint ring experiment to test the creep of concrete and found that the concrete just cracked on the 15.5 days. According to the relevant data of literature [20] (as shown in Table 5), and based on the prediction model of cracking risk coefficient proposed in this paper, the cracking risk coefficient of concrete on the 15.5 days was calculated to be 1.0033. According to the cracking criteria of concrete, it can be seen that the concrete just cracks at this time, which was consistent with the results of the literature [20].

Based on the restraint ring experiment, Zhang et al. [6] proposed a mathematical model for predicting the cracking of ECC and LSECC concrete, which predicted that the ECC concrete would crack on the 5th day, while the cracking time of the experiment was on the 7th day; LSECC concrete mixed with fiber had not been cracked. According to the relevant data of literature [6] (as shown in Table 5), and based on the prediction model of cracking risk coefficient proposed in this paper, the cracking risk coefficient of ECC concrete on the 5th day was 0.798, and the cracking risk coefficient on the 7th day was 2.135; the cracking risk coefficient of LSECC concrete on the 28th day was 0.697. Therefore, the prediction results showed that ECC concrete could crack on the 5th day, and it was certain that the cracking would occur on the 7th day, while the cracking of LSECC concrete had not been cracked within 28 d, and the prediction results were consistent with the literature [6], which further showed that the concrete cracking risk prediction model proposed in this paper was correct and reasonable.

Table 5: Test value and verification of early cracking risk coefficient of concrete.

No.	Age (d)	Et (GPa)	ft (MPa)	ε ($\times 10^{-6}$)	φt	Predicted value, η	Predicted status	Actual status
TS-1 (equation (6))	3	17.3	2.11	183	0.343	1.117	C	C
TS-1 (equation (34))	3	19.02	2.36	181	0.331	1.096	C	C
TS-2 (equation (6))	1	10.1	1.44	175	0.123	1.093	C	C
TS-2 (equation (34))	1	8.61	1.35	182	0.107	1.049	C	C
TS-3 (equation (6))	1	13.3	1.68	215	0.098	1.550	C	C
TS-3 (equation (34))	1	12.3	1.58	197	0.092	1.404	C	C
Khan et al. [20]	15.5	28	3.2	305	1.16	1.003	C	C
	Age (d)	Et (GPa)	ft (MPa)	$K \times \varepsilon$ ($\times 10^{-6}$)	Type of concrete	Predicted value, η	Predicted status	Actual status
Zhang et al. [6]	5	17	2.45	115	ECC	0.798	PC	NC
Zhang et al. [6]	7	19	2.67	300	ECC	2.135	C	C
Zhang et al. [6]	28	18.9	4.45	164	LSECC	0.697	NC	NC

Note. "TS-1 (equation (6))" denotes the cracking risk coefficient of concrete calculated according to equation (6); "TS-1 (equation (34))" denotes the cracking risk coefficient of concrete calculated according to equation (34); "C" denotes cracking of concrete; "PC" denotes possible cracking of concrete; "NC" denotes not cracking of concrete.

5. Conclusion

According to the adiabatic temperature rise experiment, shrinkage experiment, creep experiment, and theoretical analysis of concrete, the early cracking risk prediction model of modern concrete was established. The early cracking risk coefficient of concrete calculated by the model was consistent with the actual cracking state based on the slab cracking frame experiment of concrete. The following conclusions were drawn:

(1) Based on the capillary water tension theory, the shrinkage strain of the specimen at the macro level can be estimated by using the local temperature and humidity inside the concrete, and then the shrinkage stress of the structure can be calculated

(2) The concrete cracking risk prediction model with creep coefficient can well predict the early cracking of the concrete

(3) When the concrete mix proportion, adiabatic temperature rise curve, 28 d elastic modulus, 28 d tensile strength, internal temperature and humidity curve, and early creep coefficient are known, the cracking risk coefficient of concrete can be well predicted, and then the early cracking resistance of concrete can be evaluated

Data Availability

The data used to support the findings of this study are included within the article.

Conflicts of Interest

The authors declare that they have no conflicts of interest.

Acknowledgments

The authors would like to acknowledge the financial support provided by the National Natural Science Foundation of China (51808015 and 52078015), the general project of science and technology plan of Beijing Municipal Commission of Education (KM202110005018), and Beijing Natural Science Foundation (8202005).

References

[1] J. P. Liu, Q. Tian, and C. W. Miao, "Investigation on the plastic shrinkage of cementitious materials under drying conditions: mechanism and theoretical model," *Magazine of Concrete Research*, vol. 64, no. 6, pp. 550–561, 2012.

[2] G. Li and Z. Wang, "A mesoscopic simulation for the early-age shrinkage cracking process of high performance concrete in bridge engineering," *Advances in Materials Science and Engineering*, vol. 2017, Article ID 9504945, 12 pages, 2017.

[3] B. Menu, M. Jolin, and B. Bissonnette, "Assessing the shrinkage cracking potential of concrete using ring specimens with different boundary conditions," *Advances in Materials Science and Engineering*, vol. 2020, Article ID 4842369, 13 pages, 2020.

[4] Z. M. Li, T. S. Lu, X. H. Liang, H. Dong, and G. Ye, "Mechanisms of autogenous shrinkage of alkali-activated slag and fly ash pastes," *Cement and Concrete Research*, vol. 135, 2020.

[5] G. Ji, T. Kanstad, and O. Bjontegaard, "Numerical modelling of field test for crack risk assessment of early age concrete containing fly ash," *Advances in Materials Science and Engineering*, vol. 2018, Article ID 1058170, 16 pages, 2018.

[6] T. Meagher, N. Shanahan, D. Buidens, K. A. Riding, and A. Zayed, "Effects of chloride and chloride-free accelerators combined with typical admixtures on the early-age cracking risk of concrete repair slabs," *Construction and Building Materials*, vol. 94, pp. 270–279, 2015.

[7] J. Zhang, Y. Han, J. Han, and Z. Wang, "Cement hydration based model to predict the mechanical properties of precast concrete," *Magazine of Concrete Research*, vol. 66, no. 12, pp. 603–617, 2014.

[8] J. Zhang, H. Dongwei, and S. Wei, "Experimental study on the relationship between shrinkage and interior humidity of concrete at early age," *Magazine of Concrete Research*, vol. 62, no. 3, pp. 191–199, 2010.

[9] D. P. Bentz, "A review of early-age properties of cement-based materials," *Cement and Concrete Research*, vol. 38, no. 2, pp. 196–204, 2008.

[10] D. Shen, J. Jiang, J. Shen, P. Yao, and G. Jiang, "Influence of curing temperature on autogenous shrinkage and cracking

resistance of high-performance concrete at an early age," *Construction and Building Materials*, vol. 103, pp. 67–76, 2016.

[11] H. Li, J. Liu, Y. Wang, T. Yao, Q. Tian, and S. Li, "Deformation and cracking modeling for early-age sidewall concrete based on the multi-field coupling mechanism," *Construction and Building Materials*, vol. 88, pp. 84–93, 2015.

[12] K. Olivier, A. Darquennes, F. Benboudjema, and R. Gagné, "Early-age self-healing of cementitious materials containing ground granulated blast-furnace slag under water curing," *Journal of Advanced Concrete Technology*, vol. 14, no. 11, pp. 717–727, 2016.

[13] R. W. Burrows, *The Visible and Invisible Cracking of concrete*, ACI International, Farmington Hills, MI, USA, 1998.

[14] N. N. Shi, J. S. Ouyang, R. X. Zhang, and D. H. Huang, "Experimental study on early-age crack of mass concrete under the controlled temperature history," *Advances in Materials Science and Engineering*, vol. 2014, Article ID 671795, 10 pages, 2014.

[15] L. Wu, N. Farzadnia, C. Shi, Z. Zhang, and H. Wang, "Autogenous shrinkage of high performance concrete: a review," *Construction and Building Materials*, vol. 149, pp. 62–75, 2017.

[16] Y. Liu, Z. G. Luo, and J. Cao, "Dumbbell test method for evaluation of the early age cracking property of concrete material by stress risers," in *Frontiers of Manufacturing Science and Measuring Technology II, Pts 1 and 2*, W. P. Sung, J. C. M. Kao, and R. Chen, Eds., vol. 503-504, pp. 473–476, Trans Tech Publications Ltd, Stafa-Zurich, Switzerland, 2012.

[17] A. Z. Bendimerad, E. Rozière, and A. Loukili, "Plastic shrinkage and cracking risk of recycled aggregates concrete," *Construction and Building Materials*, vol. 121, pp. 733–745, 2016.

[18] P. Rossi, J. L. Tailhan, F.L. Maou, L. Gaillet, and E. Martin, "Basic creep behavior of concretes investigation of the physical mechanisms by using acoustic emission," *Cement and Concrete Research*, vol. 42, no. 1, pp. 61–73, 2012.

[19] D. Shen, J. Jiang, M. Zhang, P. Yao, and G. Jiang, "Tensile creep and cracking potential of high performance concrete internally cured with super absorbent polymers at early age," *Construction and Building Materials*, vol. 165, pp. 451–461, 2018.

[20] I. Khan, A. Castel, and R. I. Gilbert, "Tensile creep and early-age concrete cracking due to restrained shrinkage," *Construction and Building Materials*, vol. 149, pp. 705–715, 2017.

[21] D. Gawin, F. Pesavento, and B. A. Schrefler, "Hygro-thermo-chemo-mechanical modelling of concrete at early ages and beyond. Part II: shrinkage and creep of concrete," *International Journal for Numerical Methods in Engineering*, vol. 67, no. 3, pp. 332–363, 2006.

[22] Y. Gao, J. Zhang, and P. Han, "Determination of stress relaxation parameters of concrete in tension at early-age by ring test," *Construction and Building Materials*, vol. 41, pp. 152–164, 2013.

[23] L. Yue, H. W. Li, Y. N. Li, and C. Y. Jin, "Optimum design of high-strength concrete mix proportion for crack resistance using artificial neural networks and genetic algorithm," *Frontiers in Materials*, vol. 7, 2020.

[24] S. Subasi, H. Ozturk, and M. Emiroglu, "Utilizing of waste ceramic powders as filler material in self-consolidating concrete," *Constr Build Mater*, vol. 149, pp. 567–574, 2017.

[25] A. K. Schindler and K. J. Folliard, "Heat of hydration models for cementitious materials," *ACI Material Journal*, vol. 102, no. 1, pp. 24–33, 2005.

[26] G.D. Luzio and G. Cusatis, "Hygro-thermo-chemical modeling of high performance concrete. I: Theory," *Cement and Concrete Composites*, vol. 31, no. 5, pp. 301–308, 2009.

[27] M. Sule and K. V. Breugel, "Cracking behaviour of reinforced concrete subjected to early-age shrinkage," *Materials and Structures*, vol. 34, no. 239, pp. 284–292, 2001.

[28] J. Zhang, Y. Gao, Y. Han, and J. Wang, "Evaluation of shrinkage induced cracking in early age concrete: from ring test to circular column," *International Journal of Damage Mechanics*, vol. 26, no. 5, pp. 771–797, 2017.

[29] I. Pane and W. Hansen, "Concrete hydration and mechanical properties under nonisothermal conditions," *ACI Material Journal*, vol. 99, no. 6, pp. 534–542, 2002.

[30] G.D. Schutter and L. Taerwe, "Degree of hydration-based description of mechanical properties of early age concrete," *Materials and Structures*, vol. 29, no. 190, pp. 335–344, 1996.

[31] D. Shen, J. Jiang, W. Wang, J. Shen, and G. Jiang, "Tensile creep and cracking resistance of concrete with different water-to-cement ratios at early age," *Construction and Building Materials*, vol. 146, pp. 410–418, 2017.

[32] D. P. Bentz, E. J. Garboczi, and D. A. Quenard, "Modelling drying shrinkage in reconstructed porous materials: application to porous Vycor glass," *Modelling and Simulation in Materials Science and Engineering*, vol. 6, no. 3, pp. 211–236, 1999.

[33] P. Lura, O. M. Jensen, and K.V. Breugel, "Autogenous shrinkage in high-performance cement paste: an evaluation of basic mechanisms," *Cement and Concrete Research*, vol. 33, no. 2, pp. 223–232, 2003.

[34] X. Zhai, "Surface of concrete," *Concrete Surface Engineering*, vol. 5, no. 6, pp. 11–33, 2015.

[35] E. A. B. Koenders and K.V. Breugel, "Numerical modelling of autogenous shrinkage of hardening cement paste," *Cement and Concrete Research*, vol. 27, no. 10, pp. 1489–1499, 1997.

[36] Y. Liu, A. K. Schindler, and J. S. Davidson, "Finite-element modeling and analysis of early-age cracking risk of cast-in-place concrete culverts," *Transportation Research Record: Journal of the Transportation Research Board*, vol. 2672, no. 27, pp. 24–36, 2018.

[37] S. Wu, D. Huang, F. B. Lin, H. Zhao, and P. Wang, "Estimation of cracking risk of concrete at early age based on thermal stress analysis," *Journal of Thermal Analysis and Calorimetry*, vol. 105, no. 1, pp. 171–186, 2011.

[38] W. Jiang, G.D. Schutter, and Y. Yuan, "Degree of hydration based prediction of early age basic creep and creep recovery of blended concrete," *Cement and Concrete Composites*, vol. 48, pp. 83–90, 2014.

Hindawi
Advances in Materials Science and Engineering
Volume 2021, Article ID 7656613, 14 pages
https://doi.org/10.1155/2021/7656613

Research Article

Field Monitoring and Numerical Analysis of the Reinforced Concrete Foundation of a Large-Scale Wind Turbine

Yanming Zhou,[1] Xinxi Liu,[1] Zongwei Deng,[2] and Qian-Feng Gao[3]

[1]*School of Civil Engineering, Changsha University of Science and Technology, Changsha 410114, China*
[2]*College of Civil Engineering, Hunan City University, Yiyang 413000, China*
[3]*School of Traffic and Transportation Engineering, Changsha University of Science and Technology, Changsha 410114, China*

Correspondence should be addressed to Zongwei Deng; dengzongwei@hncu.edu.cn

Received 4 May 2021; Revised 21 June 2021; Accepted 25 June 2021; Published 5 July 2021

Academic Editor: Peng Zhang

The objective of this study is to examine the performance of the shallow reinforced concrete foundation of a large-scale wind turbine under the influence of environmental loads. A 2 MW horizontal-axis onshore wind turbine supported by a shallow concrete foundation was considered. The foundation stresses, foundation settlements, and static and dynamic contact pressures at various positions of the shallow foundation were monitored from the construction phase to the operation phase in the field. Numerical simulations were also performed to further analyze the behavior of the wind turbine foundation in different cases. The results demonstrate that the responses of the reinforced concrete foundation, i.e., foundation stresses, contact pressures, and foundation settlements, were variables closely related to the wind direction and wind speed. The distribution of foundation stresses suggested that a reasonable design of steel reinforcement cages around the foundation steel ring is important. The dynamic contact pressure of the foundation could reach 5 kPa, so the influence of dynamic wind loads on the foundation response could not be always neglected, particularly for the foundations seated on weak soils. The foundation settlement during the operation phase could be characterized by the logistic model, but its distribution was uneven due to the presence of eccentric upper weight and wind load. The findings would provide guidance for the foundation design of onshore wind turbines in hilly areas.

1. Introduction

As a clean, safe, and sustainable natural source, wind energy becomes increasingly important in power supply [1–3]. Plenty of new wind farms have been installed in mountainous and hilly regions in many countries as a strategy for narrowing the regional energy disparity [4, 5]. For instance, from 2016 to 2020, China has built 42,000 MW wind turbines in its central eastern and southern regions [6, 7], where there are mainly hilly, plateau, and mountainous terrains. Wind turbines therein are usually supported by large-scale shallow foundations lied on the strongly weathered rock, karst, or residual soils. Unlike building structures, dynamic wind loads are the main forces for a wind turbine, which could produce considerable vibrations and increased stresses, strains, and deformations in the structure, foundation, and subsoil [8–10]. Therefore, the shallow foundation of a wind turbine in mountainous and hilly regions must show satisfactory performances in resisting large wind loads.

To date, various methods have been applied to analyze the responses of shallow foundations [11–13]. Al-Homoud and Al-Maaitah [14] carried out forced vertical vibration tests on shallow foundations resting on sand. The authors reported that the natural frequency increases while the vibration amplitude declines as the embedment depth, degree of saturation, and foundation base area increase. EI Sawwaf and Nazir [15] performed model tests on strip foundations supported on a loose sandy slope under both monotonic and cyclic loads. Their results indicated that the inclusion of soil reinforcement in the replaced sand not only significantly increases the stability of the sandy slope itself but also decreases much both the monotonic and cumulative cyclic settlements. Pasten et al. [16] developed a numerical method

to analyze dynamic responses under repetitive vertical loads. It was found that the vertical settlement, horizontal displacement, foundation rotation, and stress redistribution within the soil mass change with increasing number of load cycles. Moreover, the displacement and rotation become more pronounced as the cyclic load amplitude increases. Chen et al. [17] conducted dimensionless parametric analyses to evaluate the dynamic responses of soil-foundation systems subjected to harmonic horizontal forces and rocking moments. Panique Lazcano et al. [18] proposed a pore-water pressure generation equation and evaluated the influence of pore pressure in the calculation of bearing capacity of shallow foundation on cohesive soil. The formulation is able to calculate the maximum cyclic load that a cohesive soil can resist before failure. Fattah et al. [19] examined the distribution of contact pressures under a circular shallow foundation subjected to vertical and rocking vibrations. It was found that the shallow foundation tends to have escalated stress distribution in the direction of rocking vibration to reach a peak at the center followed by a gentle drop.

Nevertheless, only a few related works have been reported in the field of wind turbines [3, 4]. The work of Harte et al. [20] and Taddei et al. [21] stated that the soil-structure interaction plays an important role in the performance of wind turbine shallow foundations. Madaschi et al. [22] examined the dynamic behavior of the shallow foundation of a small full-scale wind turbine. It was noted that the vibration of the wind turbine tower induces a sort of forced, damped harmonic excitation in the foundation. More recently, Gao et al. [9] and Deng et al. [23] conducted numerical simulations and physical model tests on a 2 MW wind turbine subjected to random wind loads. The authors demonstrated that the surrounding environment of the wind turbine foundation is affected by dynamic wind loads, and the dynamic amplification factors strongly depend on the wind speed and spatial position. However, the previous work did not concern the behavior of wind turbine foundation itself in the construction phase. Using numerical methods, Pham et al. [24] analyzed the responses of the shallow foundation of an onshore wind turbine resting on natural or improved ground. They stated that the soil settlement and the foundation rotation decrease when the area improvement ratio increases; meanwhile, the presence of the overturning moment on the raft increases the total and differential soil settlements. Wang and Ishihara [25] developed a dynamic Winkler model for the dynamic response analysis of shallow foundation supported wind turbines. It was found that without considering the foundation uplift, the moment on the wind turbine tower is slightly overestimated, while that on the shallow foundation is significantly underestimated for the large soil stiffness. He et al. [10] conducted structural health monitoring of a 1.5 MW onshore wind turbine foundation with embedded ring. The authors reported that the long-term monitoring of the local concrete deformation is necessary to ensure the safety of the foundation, but their work mainly focused on the performance of embedded rings.

The purpose of the current study is to investigate the performance of wind turbine foundations under environmental loads. A common 2 MW horizontal-axis wind turbine supported by a shallow concrete foundation was considered. The foundation stresses, foundation settlements, static contact pressures, and dynamic contact pressures at various positions of the shallow foundation of this type of wind turbine were collected from a wind farm in China. Numerical simulations were also conducted to further examine the performance of the wind turbine foundation. The monitored data and calculated results were analyzed and compared. The findings obtained from this study would provide guidance for the design of wind turbine foundations in hilly and mountainous areas.

2. Engineering Background

The Qiaoshi wind farm (25°29′06.4″ N, 112°40′16.7″ E) is located in Guiyang County, Chenzhou City, China (Figure 1). This region is a subtropical monsoon climate, with abundant rainfall and distinctive seasons. Over the past 40 years, the average annual temperature is 17.2°C, the average annual wind speed is 2.04 m/s, and the maximum average annual wind speed is 2.65 m/s. The prevailing wind direction is from the north-northeast (NNE) and south (S), among which the NNE direction has the largest frequency of about 15%. The elevation of the Qiaoshi wind farm is 400–600 m, and the landscape is characterized by low hills with mean slopes of 15°–30°. The natural surface of the ground is covered by low shrubs. The ground is extensively covered with quaternary residual soils, and the bedrocks mainly include granite porphyry, limestone, sandstone, and dolomite. Dozens of 2 MW horizontal-axis wind turbines (XEMC Windpower Company, China) have been installed on this wind farm. The specification of the wind turbine is shown in Table 1. All wind turbines were installed on hill tops or ridges and supported by circular spread foundations made of reinforced concrete. The external diameters and the embedment depths of the foundations were 18.4 m and 3.1 m, respectively.

A representative wind turbine on the Qiaoshi wind farm was investigated. The wind turbine was supported by a circular spread concrete foundation that was situated on a hillside. The physical and mechanical properties of the subsoil and bedrock are shown in Table 2.

3. Study Methods

3.1. Field Monitoring. The monitored items included the foundation stress, the foundation settlement, and the static and dynamic contact pressures between the foundation and the subsoil, which are important indicators to evaluate the performance of a shallow foundation.

The axial stresses of many steel bars in different positions and directions of the shallow foundation were monitored by stress gauges (see Figure 2). On the one hand, 32 stress gauges labeled SG-V1-0°~335°, SG-V2-0°~335°, SG-V3-0°~335° and SG-V4-0°~335° were set to measure the axial stresses of the vertical steel bars in the foundation. On the other hand, another 32 stress gauges (i.e., SG-B1-0°~335°, SG-B2-0°~335°, SG-T1-0°~335°, and SG-T2-0°~335°) were

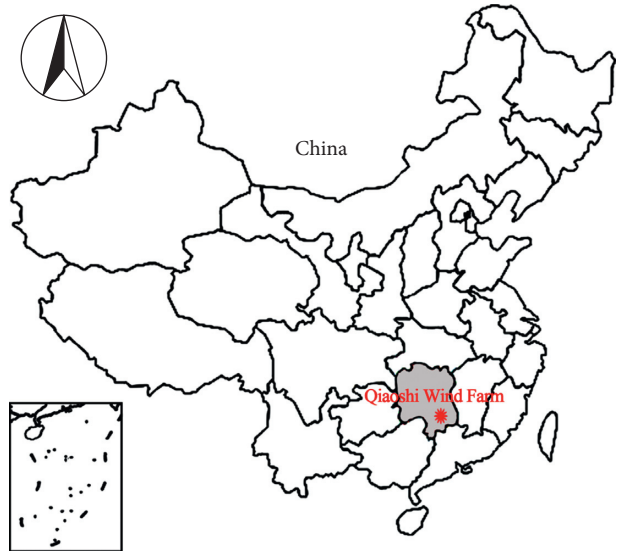

Figure 1: Geographical location of Qiaoshi wind farm (25°29′06.4″ N 112°40′16.7″ E).

Table 1: Specification of the 2 MW horizontal-axis wind turbine.

Rated output power (MW)	Rotor diameter (m)	Hub height (m)	Rated wind speed (m/s)	Rated rotor speed (r/min)	Nacelle and rotor mass (t)	Tower mass (t)
2.0	93.4	80.0	11.0	12.3	128.5	155.0

Table 2: Physical and mechanical properties of the soil and rock.

Soil/rock	Thickness (m)	Natural density (g/cm^3)	Specific gravity	Internal friction angle (°)	Cohesion (kPa)	Modulus (MPa)	Bearing capacity (kPa)
Residual soil	3–6	1.7–2.1	2.70	15–20	12–22	5–8	150–220
Strongly weathered sandy shale	4–12	2.4–2.5	2.6–2.7	—	—	8000–10000	200–400
Moderately weathered sandy shale	>20	2.5–2.6	2.65–2.75	—	—	11000–12000	>500

Note: The data in the "modulus" column represent the compressive modulus for residual soil and the deformation modulus for rocks.

used to acquire the axial stresses of the radial steel bars near the foundation bottom and top surfaces in eight directions. The axis direction of each cylinder marking in Figure 2 represents the test direction of a stress gauge. Note that the 0° direction represents the prevailing wind direction in this study. The stress gauges had a measurement range of −200 MPa–350 MPa, a sensitivity of 0.1 MPa, and a precision of 0.2% FS.

The geometric leveling method was used to observe the settlements of the wind turbine foundation. Four observation marks (i.e., SM-0°~270°) were fixed on the foundation edge in different directions, as shown in Figure 3. The benchmark was positioned on the exposed bedrock near the foundation. During the observation, closed leveling lines were established from the benchmarks and passing each observation mark. The closing error of the leveling line must be less than $\pm 5\sqrt{L}$ (L is the distance).

Static Earth pressure cells were employed to monitor the static contact pressures between the foundation and the subsoil [26]. The Earth pressure cells were circular with 118 mm in diameter and 30 mm in thickness. The Earth pressure cells had a measurement range of 0.6 MPa, a sensitivity of 0.1 kPa, and a precision of 0.1% FS. Their locations are illustrated in Figure 4. One Earth pressure cell (i.e., PC0-0°) was installed in the center of the foundation bottom, eight Earth pressure cells (i.e., PC1-0°~315°) were placed in eight directions at a radius of 3 m, and another eight Earth pressure cells (i.e., PC2-0°~315°) were installed in eight directions at a radius of 6 m. Static Earth pressure cells were also used to measure the static contact pressures between the lateral surface of the foundation and the backfill. Four Earth pressure cells (i.e., PC-S-0°~270°) were fixed in four directions at a shallow depth, and another four Earth pressure cells (i.e., PC-D-0°~270°) were installed in four

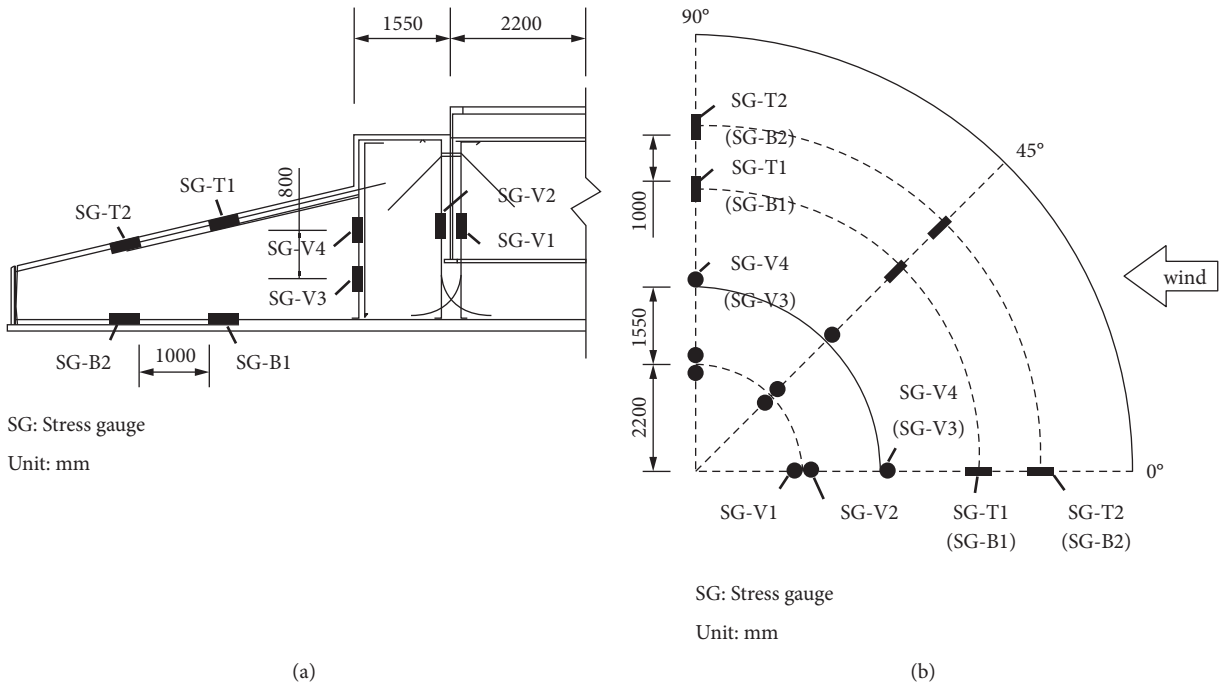

Figure 2: Layout drawing of stress gauges in the foundation.

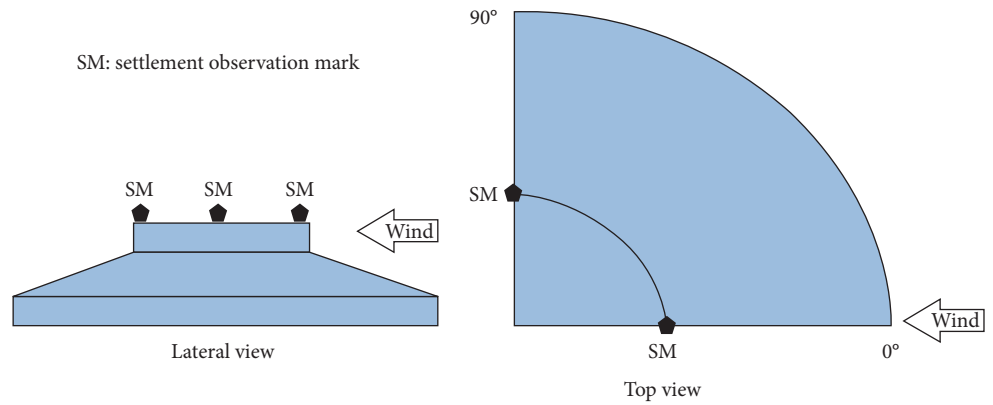

Figure 3: Layout drawing of settlement observation marks on the foundation.

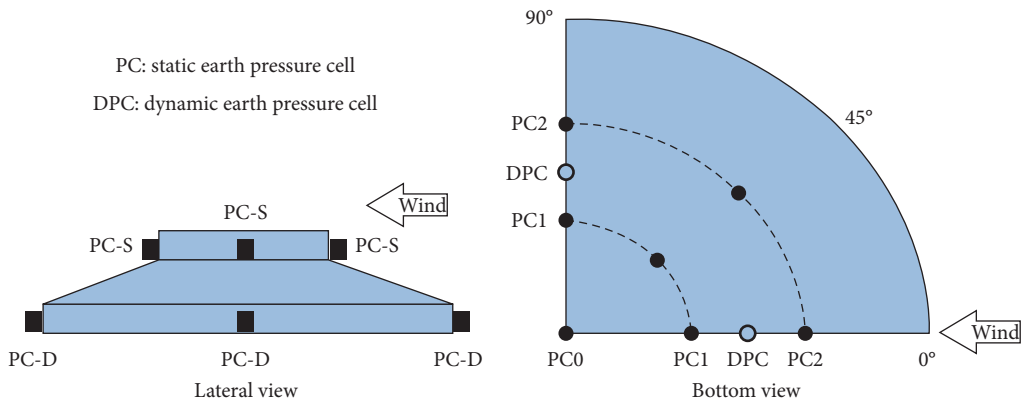

Figure 4: Layout drawing of Earth pressure cells on the bottom and lateral surface of the foundation.

directions at a deeper position. In addition, the dynamic contact pressures of the wind turbine foundation were monitored using four dynamic Earth pressure cells (i.e., DPC-0°~270°) with a range of 0.8 MPa and a precision of 0.1 kPa.

The field monitoring started at the beginning of the construction phase of the foundation and lasted to the operation phase of the wind turbine. Some important time points of the construction and operation phases are listed in Table 3.

Table 3: Important time points of the construction and operation phases.

Day	Phase	Description
0	Construction	Construct the foundation
35		Backfill the foundation pit
68		Install the tower
74		Install the nacelle and rotor
86		Complete the installation
103	Operation	Start the operation
117		Operation case 1# (hub wind speed = 12 m/s)
200		Operation case 2# (hub wind speed = 14 m/s)
...		Continue the operation

4. Numerical Simulation

A three-dimensional numerical model of the wind turbine foundation is created using the finite element software ABAQUS, as shown in Figure 5. The model basically consists of the foundation (the steel ring, the steel reinforcement cage, and concrete) and the subsoil (diameter = 80 m, height = 30 m). The dimension of the foundation model is the same as that of the foundation of the monitored wind turbine on the Qiaoshi wind farm. For simplicity, the subsoil is regarded to be a single layer of residual soils. This simplification will not greatly affect the numerical results since this study mainly focuses on the response of the foundation rather than the behavior of the subsoil. The concrete and steel are modeled as isotropic elastic materials, and the subsoil is modeled using the Mohr-Coulomb model. The material properties used in the simulation are given in Table 4. The used soil properties are failing into the ranges of measured data shown in Table 2. The properties of the steel and concrete are determined referring to relevant Chinese specifications [27, 28]. The steel reinforcement cage is simulated by beam elements (B31), while the remaining parts (i.e., concrete, subsoil, and steel ring) are simulated by solid elements (C3D10). [29] The element size is determined after convergence analysis considering the calculation accuracy and computation cost. The whole finite element model contains 63895 elements and 56941 nodes in total.

The steel reinforcement cage is linked to the concrete using the embedded technique [30]. Coulomb's friction law with a friction coefficient of 0.35 is applied to simulate the tangential behavior between the foundation and the subsoil [4, 9]. The contact in the normal direction at the interface between the foundation and the subsoil is considered to be a hard contact. The mesh tie constraint provided in ABAQUS is adopted to connect the concrete to the steel ring. The bottom boundary of the model is fully fixed in both the vertical and horizontal directions, and the lateral boundary of the finite element model is fixed in the horizontal direction. Two cases (i.e., #1 and #2) with wind speeds of 12 m/s and 14 m/s at the hub height are considered in simulations to compare with the monitored results. The loads transmitted from the superstructure to the foundation top are simplified into a horizontal load, a vertical load, and a moment rotating around a horizontal axis [3]. The loads shown in Table 5 are calculated using the GH Bladed software, which is a commercial software widely used in wind turbine design and analysis.

5. Results and Discussion

5.1. Foundation Stress. Figure 6 illustrates the simulated axial stress contours of the entire steel reinforcement cage of the foundation in difference cases. It is observed that in both cases (i.e., #1 and #2) the axial stresses of the steel reinforcement cage were in the range of −10 MPa–5 MPa, which were far less than the strengths of the steel. Moreover, the part on the downwind side likely undergone compressive stress while that on the upwind side generally withstood tensile stress. Compared with the circumferential steel bars, the radial steel bars and vertical steel bars suffer higher stresses. Both the maximum compressive stress and tensile stress appeared in the vertical steel bars near the foundation steel ring. It suggests that a reasonable design of the steel reinforcement cage around the foundation steel ring is critical for the safety of the shallow foundation of a wind turbine [10].

Figures 7 and 8 compare the axial stresses of steel bars in the foundation obtained by field monitoring and numerical simulations. It is noted that some of the vertical steel bars (e.g., SG-V2-90°, 135°, 180°, 225° in Case #1) were in tension while the others (e.g., SG-V2-270°, 315°, 0°, 45° in Case #1) were in compression. Furthermore, the axial stresses of the vertical steel bars were obviously affected by the wind speed. Generally, the larger the wind speed was, the larger the horizontal wind load and moment applied to the wind turbine were, and thus the larger the tensile stresses or compressive stresses of the vertical steel bars were. The vertical steel bars at SG-V3 and SG-V4 mainly suffered compressive stresses. The radial steel bars near the foundation top surface (i.e., at SG-T1 and SG-T2) were mainly in compression while the radial steel bars on the foundation bottom (i.e., at SG-B1 and SG-B2) were mainly in tension. Overall, both the simulated and monitored results showed similar variations and distributions although the values were not exactly the same. This is reasonable because some simplifications or assumptions are made to the materials and loads in numerical simulations. Hence, the numerical model is considered to be capable of characterizing the behavior of the wind turbine foundation for engineering purposes.

5.2. Static Contact Pressure. Figure 9 presents the time histories of the monitored static contact pressures on the foundation bottom. It is observed that the static contact

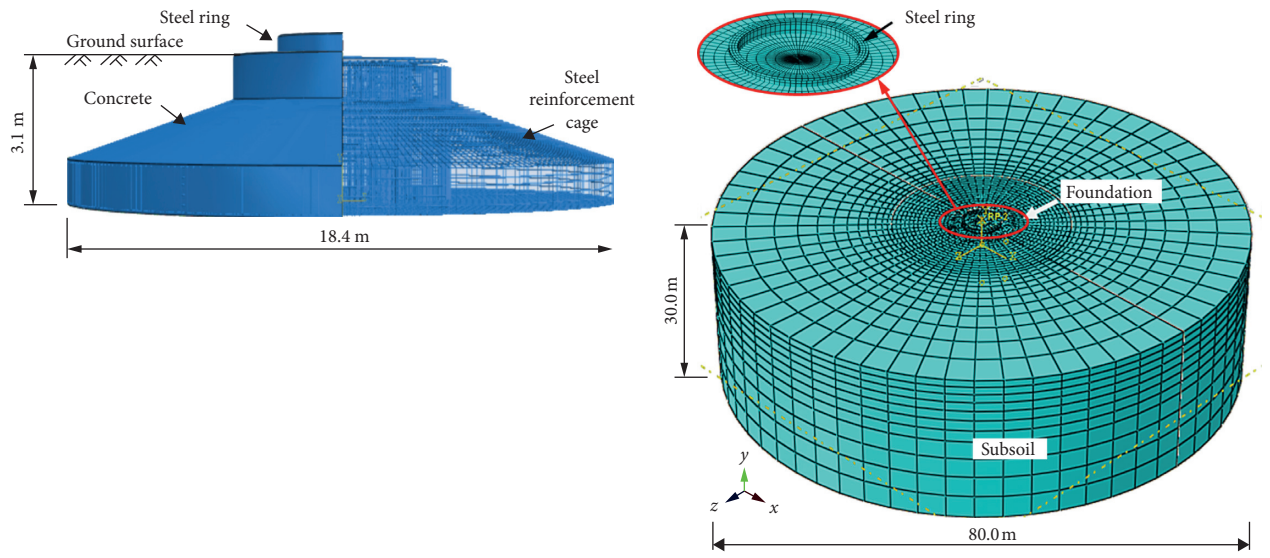

Figure 5: Numerical model of the wind turbine foundation and subsoil: (a) foundation model; (b) element generation.

Table 4: Material properties used in numerical simulations.

Material	Mass density ρ (kg/m^3)	Elastic modulus E (MPa)	Poisson's ratio μ	Internal friction angle ψ (°)	Cohesion c (kPa)	Bearing capacity (kPa)
Subsoil	2000	20	0.4	18	20	200
Steel ring	7850	206000	0.3	—	—	—
Steel reinforcement cage	7850	200000	0.3	—	—	—
Concrete	2500	31500	0.2	—	—	—

Table 5: Loading cases.

Case	Hub wind speed v (m/s)	Vertical load F_v (kN)	Horizontal load F_h (kN)	Horizontal moment M_h (kN·m)
#1	12.0	2649.5	184.0	11115.0
#2	14.0	2653.2	243.0	15492.0

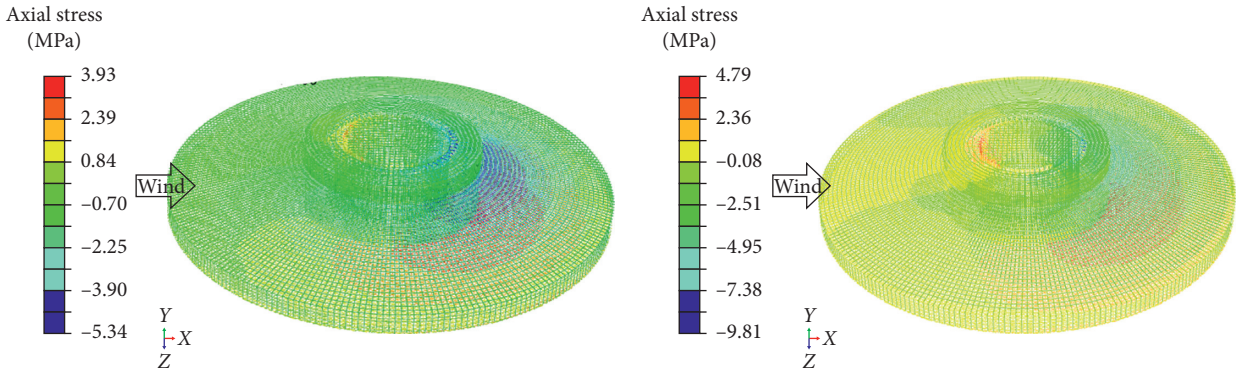

Figure 6: Simulated axial stress contours of the steel reinforcement cage: (a) in Case #1; (b) in Case #2.

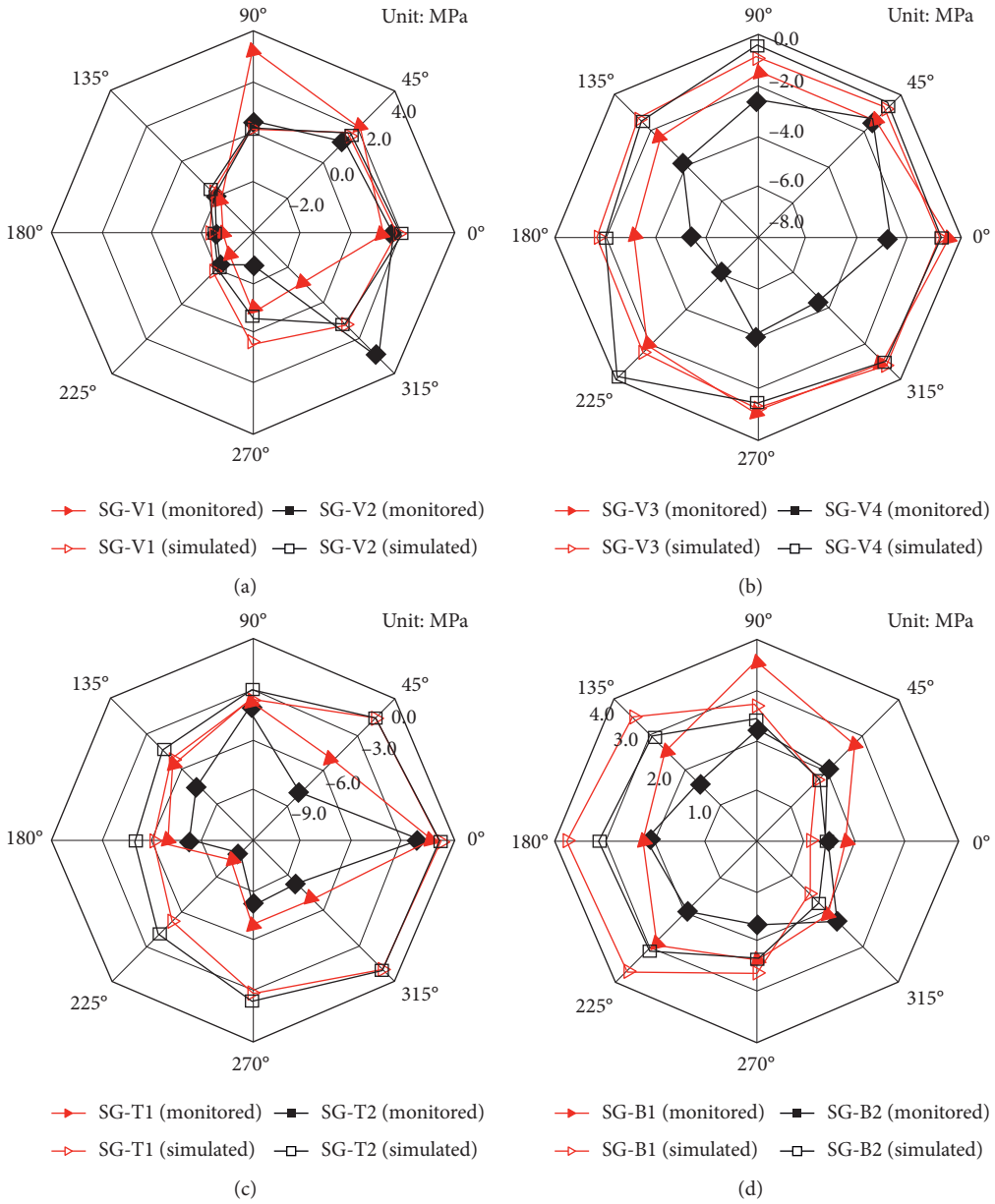

Figure 7: Axial stresses of steel bars in the foundation in Case #1: (a) at SG-V1 and SG-V2; (b) at SG-V3 and SG-V4; (c) at SG-T1 and SG-T2; (d) at SG-B1 and SG-B2.

pressures at various monitoring points considerably went up during the foundation construction and backfilling process (i.e., $t = 0$–35 d). As the superstructure (i.e., tower, nacelle, and rotor) was gradually installed on the foundation (i.e., $t = 68$–86 d), the distribution of static contact pressures gradually slightly varied from homogeneous to uneven due to the eccentricity of the weight of wind turbine superstructure. During the operation of the wind turbine (i.e., $t > 103$ d), large wind loads were applied to the superstructure of the wind turbine; this led to an obvious variation of the static contact pressure. In this process, the direction of the monitoring point where the static contact pressure was the maximum changed with the change in wind direction. Furthermore, one can note that the static contact pressures at PC2 were generally smaller than those at PC1. The static contact pressures on the upwind side were smaller than those monitored on the downwind side, which is in line with the axial stresses of steel bars on the foundation bottom.

Figure 10 illustrates the simulated contours of static contact pressures on the foundation bottom in two different cases (i.e., #1 and #2). It is observed that the static contact pressure was not homogeneously distributed but exhibited large values on the downwind side and relatively small values on the upwind side. This finding is broadly in agreement with the monitored results and those reported in the literature [9]. The abnormal contact pressures at individual points in Case #1 appear due to stress concentrations when the eccentricity of the foundation is relatively small.

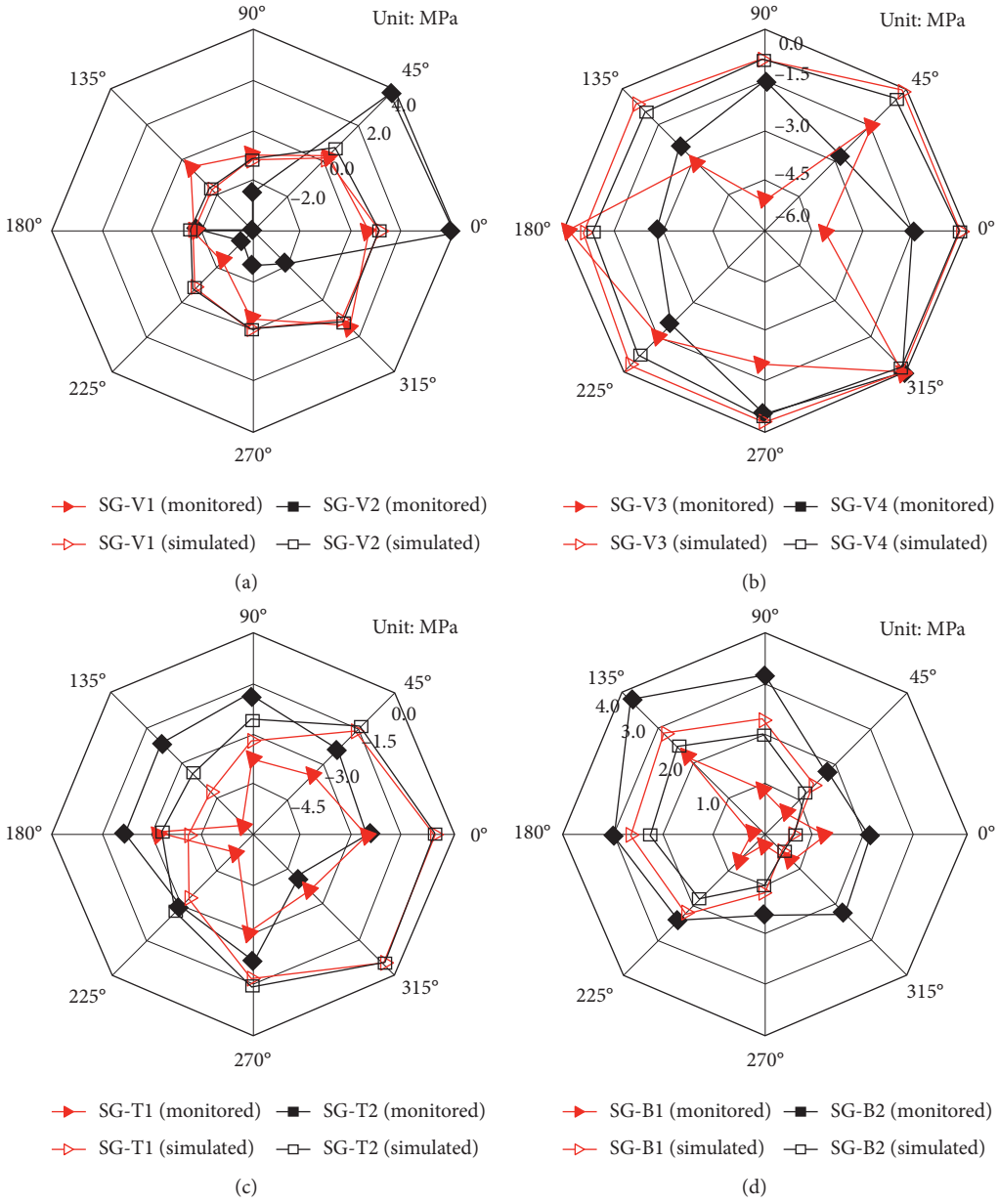

FIGURE 8: Axial stresses of steel bars in the foundation in Case #2: (a) at SG-V1 and SG-V2; (b) at SG-V3 and SG-V4; (c) at SG-T1 and SG-T2; (d) at SG-B1 and SG-B2.

Figure 11 compares the simulated static contact pressures with those monitored in the field. Obviously, the simulated data and the monitored values were not precisely consistent. But, as expected, the simulated and monitored static contact pressures showed similar distributions. Additionally, one can note that the distribution of static contact pressures on the foundation bottom was affected by the wind speed. For example, the static contact pressures monitored on $t = 117$ d with a hub wind speed of 12 m/s were quite different from those monitored on $t = 200$ d with a hub wind speed of about 14 m/s.

Figure 12 presents the time histories of the monitored static contact pressures on the lateral side of the foundation. As expected, the static lateral contact pressures at a smaller depth (i.e., PC-S) were smaller than those at a larger depth (i.e., PC-D). Generally, the static lateral contact pressures of the foundation showed a similar variation trend as the static contact pressures on the foundation bottom during the process of foundation construction and backfilling (see Figure 9). In this process, the static lateral contact pressures considerably increased from zero up to around 13 kPa at PC-S and 34 kPa at PC-D, respectively. Afterward, the static lateral contact pressures exhibited great fluctuations during the installation of the superstructure of the wind turbine and relatively small fluctuations during the operation phase. As a whole, the static contact pressures on the lateral side of the foundation are several times smaller than those on the bottom.

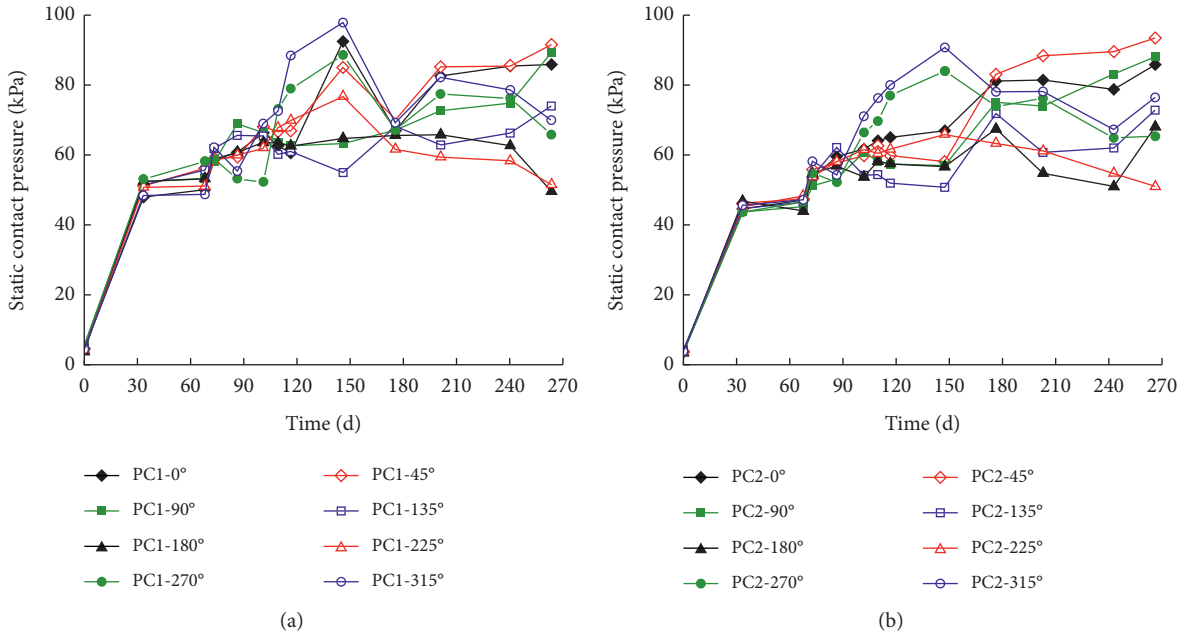

Figure 9: Time histories of monitored static contact pressures on the foundation bottom: (a) at PC1; (b) at PC2.

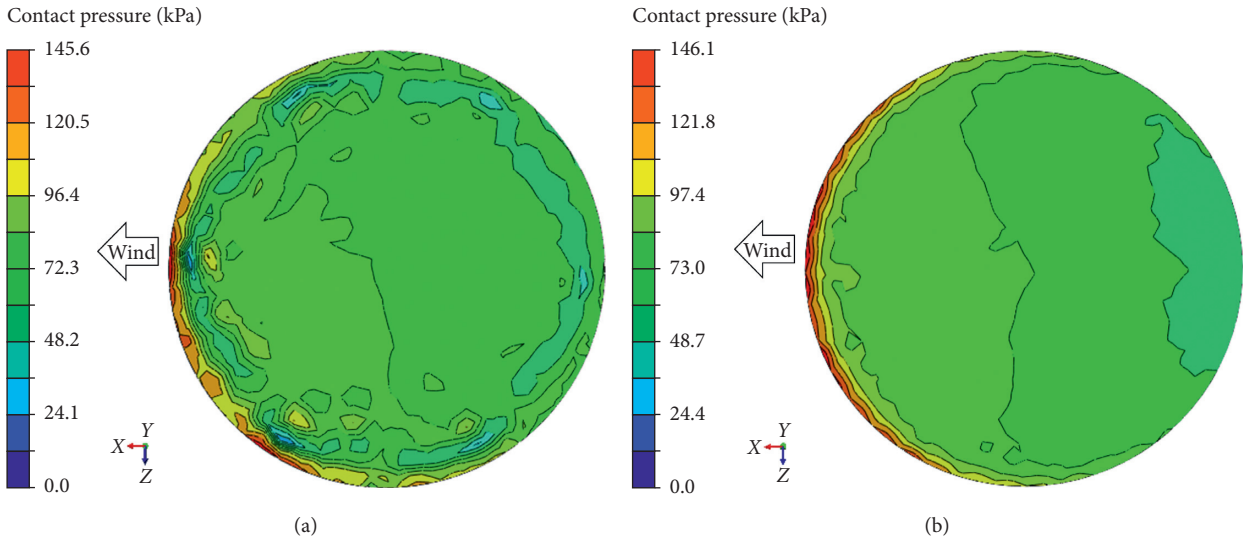

Figure 10: Simulated contours of static contact pressures on the foundation bottom: (a) in Case #1; (b) in Case #2.

6. Foundation Settlement

Figure 13 shows the time histories of the foundation settlements from the backfilling phase to the operation phase. It is noted that the foundation settlements slightly increased when the foundation pit was backfilled (i.e., $t = 35$–68 d). During the installation of the superstructure of the wind turbine (i.e., $t = 68$–86 d), the foundation settlement showed a significant increase in a step-like manner. This is because the tower sections, nacelle, and wind rotor were installed successively. One can also note a slight wave of the curve in this process; this is likely due to the movement of wheel cranes and transport vehicles. Moreover, because of the eccentricity of the upper weights and the existence of wind loads, the foundation settlements at different positions were different. The foundation settlements were then stabilized during the period between $t = 86$ d and $t = 103$ d. As the operation of the wind turbine was started (i.e., $t > 103$ d), the foundation settlements increased with a decreasing rate. Three months later, the foundation settlements reached the equilibrium. After the equilibrium, the maximum foundation settlement was about 15.0 mm at SM-180°, and the minimum foundation settlement was 8.6 mm at SM-0°. The differential settlement was (15.0–8.6) mm/7.5 m = 0.85 mm/

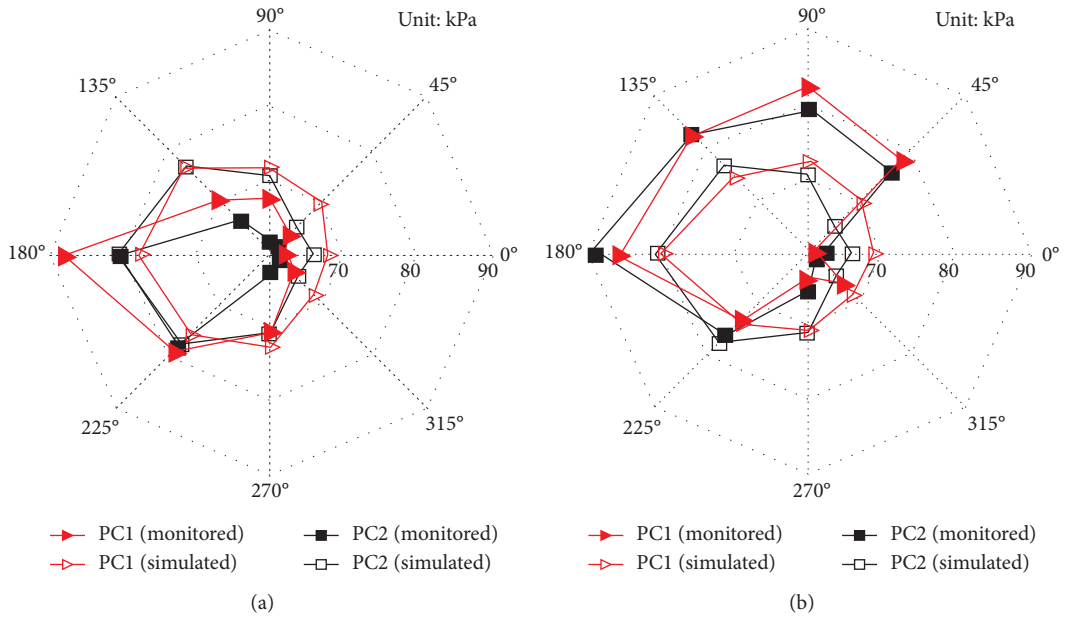

Figure 11: Comparison between monitored and simulated static contact pressures: (a) in Case #1; (b) in Case #2.

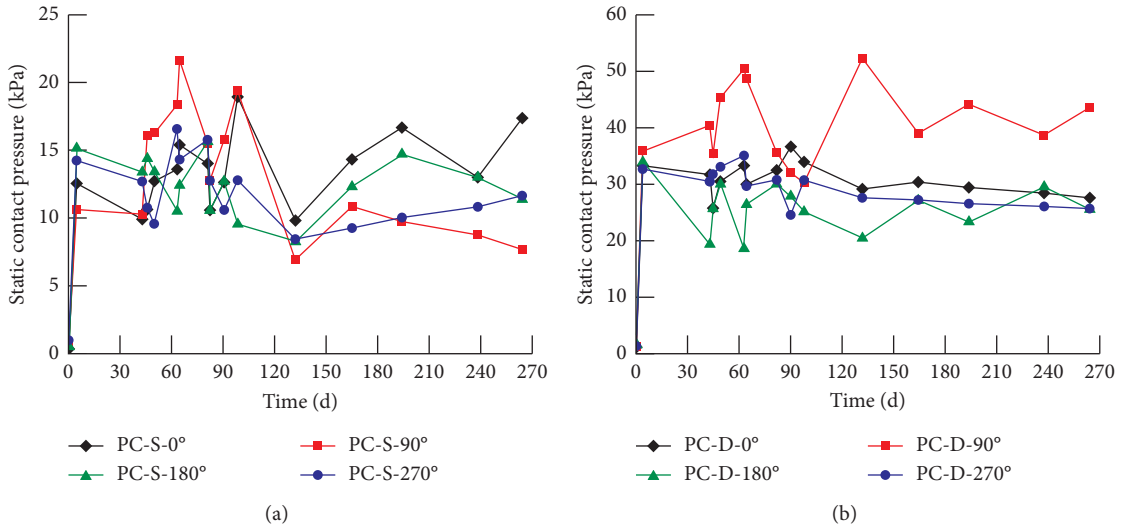

Figure 12: Time histories of static lateral contact pressures of the foundation: (a) at PC-S; (b) at PC-D.

m, which is in the range of allowable value [31]. This indicates that the wind turbine foundation was stable.

The variation of foundation settlements during the operation can be described by the logistic model, which has the following form:

$$s = \frac{K}{1 + ce^{-at}}, \tag{1}$$

where s is the settlement of the wind turbine foundation; t is the time; a is the instant settlement rate; K is the final settlement; c is a constant.

The fitting parameters of two example curves are summarized in Table 6. It shows that the logistic model can well characterize the settlement evolution of the wind turbine foundation.

Figure 14 depicts the simulated contour of the foundation settlement. One can note that the foundation settlement showed an uneven distribution. The simulated settlements of the foundation baseplate varied from 20.0 mm to 25.6 mm in Case #1 and from 19.0 mm to 26.9 mm in Case #2. The simulated foundation settlements were nearly twice the monitored results, but they had the same order of magnitude. The numerical work of Gao et al. [9] showed that the maximum settlement at a hub wind speed of 11 m/s is about 3.5 mm, occurring near the downwind edge of the foundation. Obviously, the previous results are close to those of the current study.

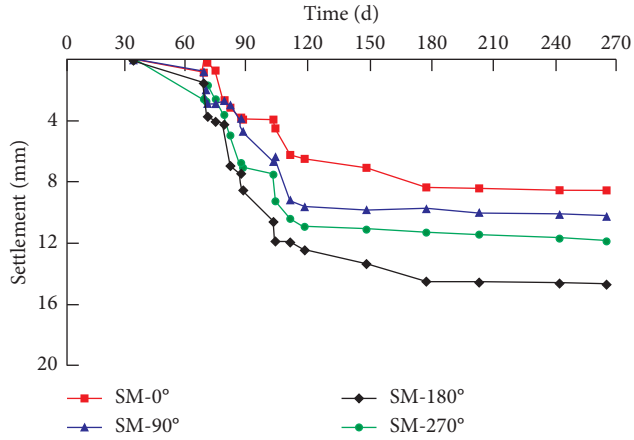

Figure 13: Time histories of the settlements of wind turbine foundation.

Table 6: Parameters of the logistic model.

Monitoring point	K	a	c	R^2
SM-0°	8.58	0.0386	4.09	0.985
SM-180°	15.09	0.0296	3.96	0.943

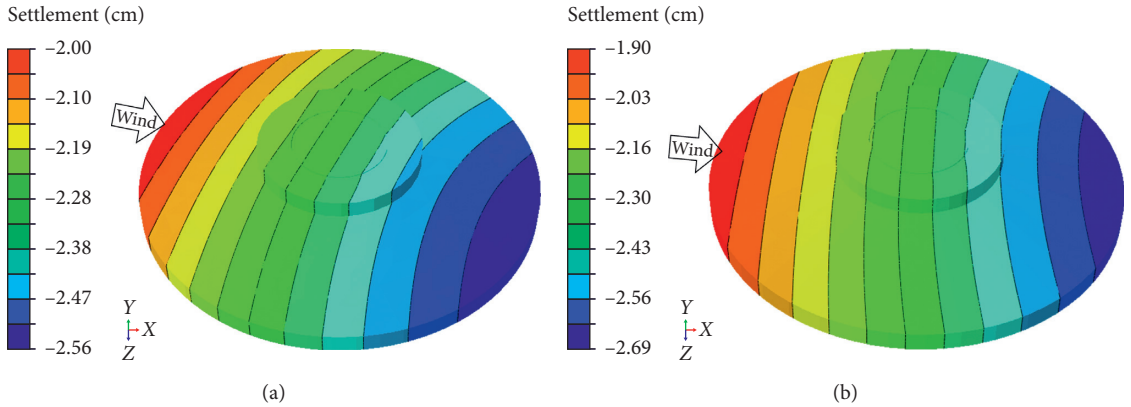

Figure 14: Simulated settlement contours of the shallow foundation: (a) in Case #1; (b) in Case #2.

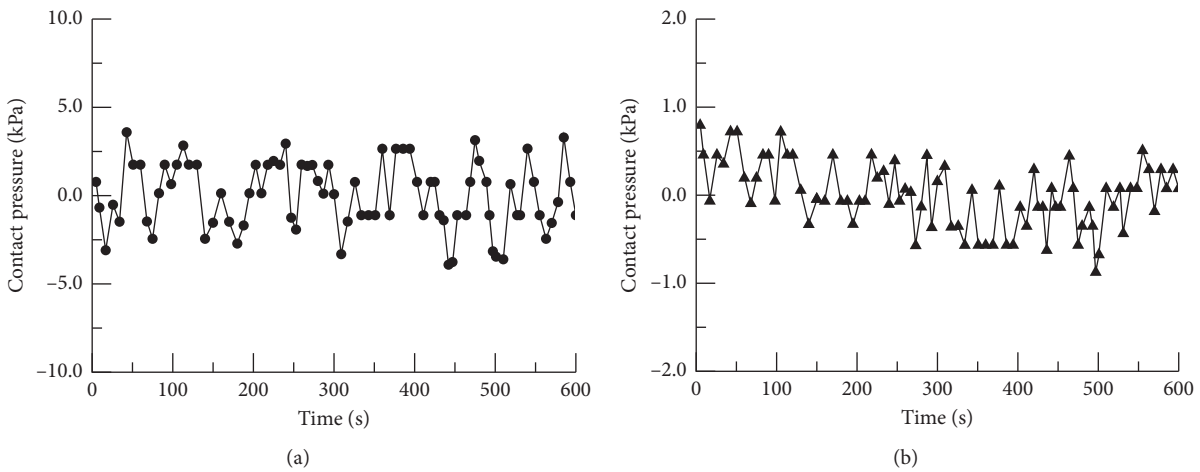

Figure 15: Continued.

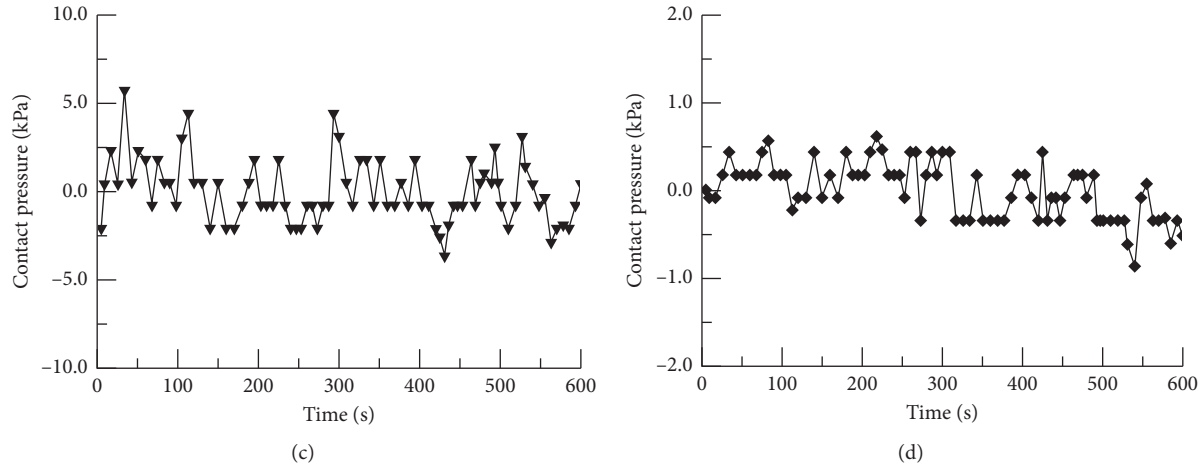

Figure 15: Time histories of monitored dynamic contact pressures on the foundation bottom: (a) at DPC-0°; (b) at DPC-90°; (c) at DPC-180°; (d) at DPC-270°.

6.1. Dynamic Contact Pressure. Figure 15 presents the time histories of the dynamic (i.e., fluctuating) contact pressures in Case #1. It is noted that the maximum dynamic contact pressure was 3.59 kPa at DPC-0°. Since DPC-0° was located between PC1-0° and PC2-0° (Figure 11), the static contact pressure at DPC-0° is assumed to be the average value of the static contact pressures at PC1-0° and PC2-0°. The estimated static contact pressure at DPC-0° was about 61.75 kPa, so the dynamic amplification factor at DPC-0° was 3.59/61.75 = 5.8%. Since the maximum dynamic contact pressure at DPC-180° was 5.73 kPa and the static contact pressure at DPC-180° was about 84.75 kPa, the dynamic amplification factor at DPC-180° was 5.73/84.75 = 6.8%. Similarly, it is derived that maximum dynamic contact pressure was 0.79 kPa and the dynamic amplification factor was 1.2% at DPC-90°; the maximum dynamic contact pressure was 0.62 kPa and the dynamic amplification factor was 1.0% at DPC-270°. These findings were roughly in agreement with those reported by Deng et al. [23], indicating that the wind load had a dynamic effect on the contact pressures of the wind turbine foundation.

7. Conclusions

This paper presented a case study of the reinforced concrete foundation of a large-scale wind turbine on the Qiaoshi wind farm in China. The foundation stresses, foundation settlements, static contact pressures, and dynamic contact pressures of the foundation at various positions were monitored and simulated. The following conclusions can be drawn:

(1) Radial steel bars in the foundation baseplate mainly underwent tensile stress while those near the top surface of the foundation mainly suffered from compressive stress. The stresses of the vertical steel bars were either compressive or tensile depending on the position. However, the stresses of all steel bars were far less than the tensile or compressive strength of the steel.

(2) The contact pressures on the bottom of the reinforced concrete foundation were variables that are highly dependent on the wind direction and wind speed. The dynamic contact pressure of the foundation could reach 5 kPa, indicating that the influence of dynamic wind loads on the performance of the reinforced concrete foundation should not be always neglected, particularly for the foundations seated on weak soils.

(3) The settlement of the wind turbine foundation was uneven due to the presence of eccentric upper weight and wind load. The monitored settlement values were usually in the range of 0–20 mm from the foundation backfilling phase to the operation phase. The evolution of foundation settlement during the operation phase could be characterized by the logistic model.

(4) A reasonable design of the steel reinforcement cage around the foundation steel ring is critical for the safety of the reinforced concrete foundation of wind turbines. Meanwhile, the wind-induced dynamic effect also needs to be taken into consideration in the design of wind turbine foundations although the effect may be not obvious in regular cases.

Data Availability

Because the data in the paper are still a project of the National Natural Science Foundation of China, the data need to be used in the follow-up study of the project. So, all the figures and tables data used to support the findings of this study were supplied by the corresponding author under license and so cannot be made freely available. Requests for access to these data should be made to Zongwei Deng, Hunan City University, No. 518, Yingbin East Road, 413000, YiYang, Hunan, China (tel:086–13973760738; e-mail: dengzongwei@hncu.edu.cn).

Conflicts of Interest

The authors declare that they have no conflicts of interest.

Acknowledgments

This work was supported by the Postgraduate Research and Innovation Project of Hunan Province (CX20190657), the National Natural Science Foundation of China (51674041 and 51474103), the Natural Science Foundation of Hunan Province, China (2020JJ4156), and the Changsha Municipal Natural Science Foundation (kq2014110).

References

[1] J. R. F. Diógenes, J. Claro, J. C. Rodrigues, and M. V. Loureiro, "Barriers to onshore wind energy implementation: a systematic review," *Energy Research & Social Science*, vol. 60, Article ID 101337, 2020.

[2] C. H. Chiang, K. T. Hsu, C. P. Yu, C. C. Cheng, and J. Z. Pan, "Remote measurements and vibration analysis of existing wind turbines," *Journal of Testing and Evaluation*, vol. 47, no. 3, pp. 2193–2206, 2019.

[3] G. Xing, C. Liu, S. Li, and W. Xuan, "HM bearing capacity of cone-shaped foundation for onshore wind turbine under monotonic horizontal loading," *Advances in Materials Science and Engineering*, vol. 2019, Article ID 3409561, 14 pages, 2019.

[4] S. Li, Y. Zhang, and D. Li, "Capacity of cone-shaped hollow flexible reinforced concrete foundation (CHFRF) in sand under horizontal loading," *Advances in Materials Science and Engineering*, vol. 2020, Article ID 6346590, 14 pages, 2020.

[5] U. E. Hansen, I. Nygaard, M. Morris, and G. Robbins, "The effects of local content requirements in auction schemes for renewable energy in developing countries: a literature review," *Renewable and Sustainable Energy Reviews*, vol. 127, Article ID 109843, 2020.

[6] X. C. Fan and W. Q. Wang, "Spatial patterns and influencing factors of China′ s wind turbine manufacturing industry: a review," *Renewable and Sustainable Energy Reviews*, vol. 54, pp. 482–496, 2016.

[7] L. Li, X. Ren, Y. Yang, P. Zhang, and X. Chen, "Analysis and recommendations for onshore wind power policies in China," *Renewable and Sustainable Energy Reviews*, vol. 82, pp. 156–167, 2018.

[8] M. Lee, M. Yoo, K. Bae, Y. Kim, B. Nam, and H. Youn, "Centrifuge tests on the lateral behavior of offshore monopile in saturated dense sand under cyclic loading," *Journal of Testing and Evaluation*, vol. 47, no. 3, pp. 1809–1828, 2019.

[9] Q. F. Gao, H. Dong, Z. W. Deng, and Y. Y. Ma, "Wind-induced dynamic amplification effects on the shallow foundation of a horizontal-axis wind turbine," *Computers and Geotechnics*, vol. 88, pp. 9–17, 2017.

[10] M. He, X. Bai, R. Ma, and D. Huang, "Structural monitoring of an onshore wind turbine foundation using strain sensors," *Structure and Infrastructure Engineering*, vol. 15, no. 3, pp. 1–20, 2019.

[11] M. Shariati, S. M. Azar, M. A. Arjomand, H. S. Tehrani, M. Daei, and M. Safa, "Comparison of dynamic behavior of shallow foundations based on pile and geosynthetic materials in fine-grained clayey soils," *Geomechanics and Engineering*, vol. 19, no. 6, pp. 473–484, 2019.

[12] A. Kumar and S. Kumari, "Numerical modeling of shallow foundation on liquefiable soil under sinusoidal loading," *Geotechnical & Geological Engineering*, vol. 37, no. 2, pp. 517–532, 2019.

[13] J. Qin, X. Zeng, F. H. Neff, and H. Ming, "Influence of fabric anisotropy on seismic response of circular foundation," *Soil Dynamics and Earthquake Engineering*, vol. 124, pp. 151–161, 2019.

[14] A. S. Al-Homoud and O. N. Al-Maaitah, "An experimental investigation of vertical vibration of model footings on sand," *Soil Dynamics and Earthquake Engineering*, vol. 15, no. 7, pp. 431–445, 1996.

[15] M. A. El Sawwaf and A. K. Nazir, "Cyclic settlement behavior of strip footings resting on reinforced layered sand slope," *Journal of Advanced Research*, vol. 3, no. 4, pp. 315–324, 2012.

[16] C. Pasten, H. Shin, and J. C. Santamarina, "Long-term foundation response to repetitive loading," *Journal of Geotechnical and Geoenvironmental Engineering*, vol. 140, no. 4, 2014.

[17] S.-S. Chen, K.-H. Liao, and J. Y. Shi, "A dimensionless parametric study for forced vibrations of foundation-soil systems," *Computers and Geotechnics*, vol. 76, pp. 184–193, 2016.

[18] D. R. Panique Lazcano, R. Galindo Aires, and H. Patiño Nieto, "Bearing capacity of shallow foundation under cyclic load on cohesive soil," *Computers and Geotechnics*, vol. 123, Article ID 103556, 2020.

[19] M. Y. Fattah, N. M. Salim, and K. K. Alwan, "Contact pressure distribution under circular shallow foundation subjected to vertical and rocking vibration modes," *Journal of Building Engineering*, vol. 26, Article ID 100908, 2019.

[20] M. Harte, B. Basu, and S. R. K. Nielsen, "Dynamic analysis of wind turbines including soil-structure interaction," *Engineering Structures*, vol. 45, pp. 509–518, 2012.

[21] F. Taddei, C. Butenweg, and S. Klinkel, "Parametric investigation of the soil-structure interaction effects on the dynamic behaviour of a shallow foundation supported wind turbine considering a layered soil," *Wind Energy*, vol. 18, no. 3, pp. 399–417, 2015.

[22] A. Madaschi, A. Gajo, M. Molinari, and D. Zonta, "Characterization of the dynamic behavior of shallow foundations with full-scale dynamic tests," *Journal of Geotechnical and Geoenvironmental Engineering*, vol. 142, no. 7, Article ID 04016026, 2016.

[23] Z.-W. Deng, Q.-F. Gao, H. Dong, and L.-X. Li, "Dynamic responses of the shallow foundation of an onshore wind turbine," *International Journal of Physical Modelling in Geotechnics*, vol. 19, no. 5, pp. 247–260, 2019.

[24] H. V. Pham, D. Dias, T. Miranda, N. Cristelo, and N. Araújo, "3D numerical modeling of foundation solutions for wind turbines," *International Journal of Geomechanics*, vol. 18, no. 12, 12 pages, Article ID 04018164, 2018.

[25] L. Wang and T. Ishihara, "A study of the effects of foundation uplift on the seismic loading of wind turbine tower and shallow foundation using a new dynamic Winkler model," *Engineering Structures*, vol. 219, Article ID 110745, 2020.

[26] J. Xiao, Y. Wang, D. Zhang, X. Zhang, and J. Guo, "Testing of contact stress at ballast bed-soil subgrade interface under cyclic loading using the thin-film pressure sensor," *Journal of Testing and Evaluation*, vol. 48. , 2020 In press.

[27] G. B. 50017, *Standard for Design of Steel Structures*, China Architecture& Building Press, Beijing, China, 2017, in Chinese.

[28] G. B. 50010, *Code for Design of Concrete Structures*, China Architecture& Building Press, Beijing, China, 2014, in Chinese.

[29] A. A. El Ezz and K. Galal, "Compression behavior of confined concrete masonry boundary elements," *Engineering Structures*, vol. 132, pp. 562–575, 2017.

[30] W. Zhao, C. Du, L. Sun, and X. Chen, "Field measurements and numerical studies of the behaviour of anchored sheet pile walls constructed with excavating and backfilling procedures," *Engineering Geology*, vol. 259, Article ID 105165, 2019.

[31] E. Ntambakwa, H. Yu, C. Guzman, and M. Rogers, "Geotechnical design considerations for onshore wind turbine shallow foundations," *Geotechnical and Structural Engineering Congress*, vol. 2016, pp. 1153–1165, 2016.

Hindawi
Advances in Materials Science and Engineering
Volume 2021, Article ID 5534917, 13 pages
https://doi.org/10.1155/2021/5534917

Research Article

Experimental Study on the Effect of Boric Acid Corrosion on the Performance of Reinforced Concrete

Qianying Wang,[1] Jigang Zhang ,[2,3] Mingchao Shan,[4] Bingying Yu,[4] Yang Zhao,[5] and Ran Yang[2]

[1]*College of Civil Engineering & Architecture, Qingdao Agricultural University, Qingdao, Shandong, China*
[2]*College of Civil Engineering, Qingdao University of Technology, Qingdao, Shandong, China*
[3]*Cooperative Innovation Center of Engineering Construction and Safety in Shandong Blue Economic Zone, Qingdao, China*
[4]*Shandong Nuclear Power Co. Ltd., Haiyang, Shandong, China*
[5]*Qingdao Gong High-Tech Material Co. Ltd., Qingdao, Shandong, China*

Correspondence should be addressed to Jigang Zhang; jigangzhang@126.com

Received 25 February 2021; Accepted 4 June 2021; Published 19 June 2021

Academic Editor: Shengwen Tang

In this study, the effect of boric acid in the cooling water system of nuclear power plants on the durability of reinforced concrete was experimentally studied. The mechanical properties of reinforced concrete under boric acid solution environments were studied by accelerated test methods. In addition, the effect of boric acid on the electrochemical behavior of steel bar and microstructure of concrete was studied. The results showed that boric acid corrosion does not affect reinforced concrete to a large extent, as corrosion only occurs on the surface of reinforced concrete, and thus, the internal reinforced concrete still maintains a high alkaline environment. At a boric acid concentration of 3%, corrosion products are crystallized on the surface of the specimen, which inhibits further corrosion.

1. Introduction

Boric acid, as a nuclear reactor moderator, is widely used in the cooling water system of nuclear power plants. With the increasing service time of nuclear power plants, the leakage of boric acid solution from the cooling water systems has gradually become an apparent problem. Besides, the impact of boric acid corrosion on the safety of nuclear power plant structures has become an issue of great concern.

Nuclear power plant structures have high importance and should have a long service life. In general, they are constructed of reinforced concrete. In recent years, some nuclear power plant structures have also been constructed using steel plate concrete structures [1]. Boric acid plays an important role in the cooling water system for nuclear fuel reactivity control and is present in the primary loop cooling water, which is in direct contact with the core and nuclear fuel. In addition, it is also present in the in-containment refueling water storage tank (IRWST) and spent fuel pool, which are constructed with reinforced concrete with stainless steel coating. The operating characteristics of the nuclear power plant do not allow IRWST and spent fuel pool to be emptied frequently for inspection, and thus, liquid leakage from them will have the long-term effect of boric acid corrosion on concrete. Therefore, the effect of boric acid corrosion on reinforced concrete needs to be studied in a systematic way.

In recent years, many studies have been carried out on the durability of concrete materials and structures [2–6]. There have been no cases of overall structure destruction of the IRWST due to boric acid corrosion [7]; therefore, the effects of reinforced concrete properties in boric acid corrosion environments have been less investigated [8, 9]. Based on the main functional characteristics of the wet surface area of IRWST, Wu et al. indicated that the facing steel plate should have good mechanical properties, corrosion

resistance, and processing and welding properties [10]. Huang et al. conducted an experimental study on the basic mechanical properties of concrete under different concentrations of boric acid immersion environment, and the results showed a relatively weak effect of boric acid on mechanical properties such as compressive strength and elastic modulus of concrete [11]. Rong et al. drilled core samples on the site for nuclear power plants where boric acid solution leakage occurred and found that the corrosion of concrete by boric acid only occurred on the surface of the specimen. The corrosion products inside the concrete were not monitored, and the compressive strength of concrete in the corroded area was slightly reduced [12].

In this study, the effect of boric acid leakage on the performance of reinforced concrete was investigated in the actual environment of nuclear power station primary loop water, and the properties of reinforced concrete under the corrosion of boric acid were studied by laboratory simulation methods to investigate the corrosion effects of boric acid solutions on reinforced concrete.

2. Test Materials and Concrete Mixture Ratio

2.1. Test Materials. Portland cement (P.O42.5) was used as the cementitious material in this test. Natural fine aggregate was river sand with a fineness modulus of 2.98. The coarse aggregate was crushed stone with continuous gradation with particle sizes ranging from 4.75 to 19 mm and 19 to 37.5 mm. Class I fly ash, high-efficiency water reducing agent, and air-entraining agent were used in the test. Normal tap water was used for concrete mixing.

The test was conducted using ordinary hot-rolled ribbed seismic steel bars with diameters of 10, 16, and 20 mm for flexural test, mechanical properties of steel bars, and reinforced concrete bond strength test, respectively. A35 standard tensile specimens with a thickness of 5 mm were used for determining the basic mechanical properties of steel plates. The testing steel bar and steel plates used are shown in Figure 1.

2.2. Concrete Mix. The durability of concrete materials and structures is influenced by many factors, including the environment, aggregates, and additives [13, 14]. The concrete proportions used for the tests were in accordance with the Code Requirements for Nuclear Safety-Related Concrete Structure (ACI 349-01), with a water-cement ratio (W/C) of 0.59, a sand ratio of 41%, and a design slump of 150 ± 25 mm. The proportions used for the tests are the same as those used for nuclear island concrete in a nuclear power plant, with the aim of facilitating the use of the test results to guide operation and maintenance. The composition of the concrete mix is listed in Table 1.

3. Test Method

3.1. Test Environments. The mode of action and concentration of corrosion solution determine the degree of corrosion of reinforced concrete. For the purpose of the comparative study of the boric acid corrosion effect, a blank control group (distilled water environment) was set up. Considering the actual environment in the primary loop of the nuclear power plant, the concentration of the boric acid solution was chosen to be 0.27%. At the same time, in order to accelerate the corrosion rate of reinforced concrete, the test was also carried out with boric acid concentrations of 0.8% and 3%. In order to simulate the real environmental conditions, two test environments including immersion and alternating wet and dry conditions were established. The alternating wet and dry process cycle using corrosion solution involved soaking for four days and natural drying for three days. The IRWST operates at a temperature of approximately 55°C; therefore, the test was carried out at room temperature.

Figure 1: Testing rebar and steel plates.

3.2. Mechanical Property Test. The mechanical properties of steel plates and reinforced concrete including compressive strength, splitting tensile strength, and static elastic modulus of concrete, flexural strength, and bond strength were investigated. A total of 8 different test environments including 2 test conditions of immersion and alternating wet and dry and 4 different boric acid concentrations were set for each test condition. The reinforced concrete specimens were maintained under the standard conditions for 28 days and then placed in the corrosion solution with the descaled steel and steel plate specimens, and these tests were conducted every 2 months at 60 days, 120 days, 180 days, 240 days, and 300 days.

The compressive strength, splitting tensile strength, static elastic modulus, and flexural strength tests were conducted according to the standard test method for mechanical properties of ordinary concrete (GB/T 50081-2002). Cube specimens of $100\,\text{mm} \times 100\,\text{mm} \times 100\,\text{mm}$ were used to test the compressive and splitting tensile strengths. The static elastic modulus was determined using $100\,\text{mm} \times 100\,\text{mm} \times 300\,\text{mm}$ size specimens. Two ordinary hot-rolled ribbed seismic steel bars of 10 mm diameter were placed inside the reinforced concrete flexural test specimen with the specimen size of $100\,\text{mm} \times 100\,\text{mm} \times 400\,\text{mm}$. Transverse cracks of 0.2 mm were preset in the middle of the specimen by steel pieces.

The basic mechanical properties of the steel bars and steel plates were tested according to the tensile test of metal materials (GB/T 228.1-2010). The ordinary hot-rolled ribbed seismic steel bars with a diameter of 16 mm and A35 carbon steel plate with a thickness of 5 mm were used in this study [15].

Table 1: Concrete mixture ratio (kg/m^3).

Medium sand (0–4.75 mm)	Small-medium stone (4.75–19 mm)	Big stone (19–37.5 mm)	Cement	Fly ash	Water reducer (0.8%)	Air-entraining agent (0.003%)	Mixing water
734	581	475	273	91	2.912	0.0109	160

The reinforced concrete bond strength test was carried out according to the test specification for hydraulic concrete (SL 352-2006). A cube specimen of 150 mm × 150 mm × 150 mm was used, and an ordinary hot-rolled ribbed seismic steel bar of 20 mm diameter was placed at the center.

3.3. Microstructural Analysis of Concrete and Reinforcement. The corrosion products and microstructure of concrete were analyzed by the concrete powder at 0 and 2 cm below the concrete surface by X-ray scanning using a D8 ADVANCE series X-ray diffractometer (Bruker). The crushed concrete specimens were analyzed by scanning electron microscopy using a HITACHI S-3500N series scanning electron microscope.

The corrosion of reinforcing steel was analyzed through electrochemical impedance spectroscopy tests on the reinforcing bars in the flexural specimens using a PARSTAT 4000A series electrochemical workstation. The bars were derusted before pouring to avoid the original oxide film affecting the generation of passivation film of steel bars [16].

4. Test Results and Analysis

4.1. Effect on Mechanical Property of Concrete. The compressive strength, splitting strength, and elastic modulus of concrete under each environment are shown in Table 2. A group of three specimens was set up for each test environment and each age, and the average values of the mechanical properties of each group are listed in Table 2. The compressive strength, splitting strength, and elastic modulus loss rates were calculated based on the mechanical properties of distilled water (boric acid concentration 0%) immersion and dry-wet alternating groups, and the results are shown in Figure 2.

The maximum compressive strength loss rate of concrete was 5.04% at a boric acid concentration of 3% for 240 days in alternating wet and dry conditions. At a boric acid concentration of 3%, the compressive strength loss rate fluctuates at the late stage of corrosion, mainly because the corrosion products attached to the surface of the specimen are gradually uniform, and the stress concentration caused by the corrosion products gradually disappears.

The maximum loss rate of splitting tensile strength of concrete (3.94%) was observed at a boric acid concentration of 3% at 180 days of wet and dry alternation. No significant relationship was observed between the loss rate of splitting tensile strength and the concentration of boric acid at 60 days of corrosion in different concentrations.

The loss rate of concrete elastic modulus was less affected by the boric acid concentration. The maximum loss rate of concrete elastic modulus was 1.57% at a boric acid concentration of 3% at 240 days of alternating wet and dry conditions. The loss rate of elastic modulus in the alternating wet and dry environment at 0.27% boric acid concentration was the smallest and at 0.8% boric acid concentration was the same as that in the immersion environment at 0.27% boric acid concentration. The corrosion effect of boric acid on the concrete elastic modulus indicated a relatively weak corrosion effect of low concentration boric acid solution.

Figure 2 shows that the concrete compressive strength loss rate in the dry and wet alternating corrosion environment is greater than that in the immersion environment. The main reason is that the crystallization of boric acid during the drying process of the specimen increases the porosity of the concrete surface. At a boric acid concentration of 3% of 120 days, corrosion crystals began to appear on the surface of concrete specimens in both corrosive environments. The corrosion time of 120 and 180 days compared with the alternating wet and dry environment shows that the growth rate of compressive strength loss rate is relatively low under the immersion environment, mainly because more corrosion products adhere to the concrete surface in the immersion environment.

Figure 3 shows the surface of the test block after 300 days of corrosion in the presence of boric acid. At a corrosion age of 300 days, corrosion crystals appeared on the surface of concrete specimens under the immersion environment with a concentration of 0.8%, while the surface of specimens under alternating wet and dry environments remained bright and clean.

4.2. Effect on Mechanical Property of Reinforcement. The mechanical properties of steel bars and steel plates under each environment are shown in Tables 3 and 4. The yield and the ultimate strength loss rates of the steel bar and steel plate specimens with different corrosion times under immersion and alternating wet and dry environments only showed irregular fluctuations and no significant decrease in the test cycle, mainly because the corrosion rate of the steel bar and steel plate specimens is low, and the stress concentration caused by the cross-sectional dimensioning of the corrosion area does not occur during the test. The boric acid corrosive environment set up in the test has a low effect on the steel bar and steel plate. The yield and ultimate strengths of the steel bar and A36 steel plate specimens still meet the strength requirements during service.

The corrosion rate is the rate of mass loss of the specimens after corrosion. Tables 3 and 4 show that the overall corrosion rate of specimens is small and increases with time. The corrosion rate of the specimens in the alternating wet and dry environment was slightly higher than that in the soaking environment.

Table 2: Mechanical properties of concrete.

Test environment		Immersion			Dry-wet cycles		
Age (d)	Concentration (%)	Compressive strength (MPa)	Splitting tensile strength (MPa)	Elastic modules (10^4 MPa)	Compressive strength (MPa)	Splitting tensile strength (MPa)	Elastic modules (10^4 MPa)
60	0	60.0	3.90	3.54	58.3	3.78	3.52
	0.27	59.6	3.88	3.54	57.7	3.78	3.52
	0.8	59.3	3.89	3.54	57.2	3.76	3.51
	3	58.7	3.87	3.53	56.8	3.77	3.51
120	0	63.7	4.39	3.61	62.2	4.28	3.59
	0.27	63.0	4.36	3.60	61.1	4.24	3.58
	0.8	62.3	4.32	3.60	60.5	4.21	3.58
	3	61.5	4.29	3.59	59.7	4.17	3.56
180	0	66.9	4.66	3.67	64.7	4.57	3.65
	0.27	65.9	4.61	3.65	63.2	4.50	3.64
	0.8	64.9	4.58	3.65	62.5	4.46	3.64
	3	64.1	4.51	3.63	61.5	4.39	3.61
240	0	68.8	4.78	3.85	67.5	4.72	3.83
	0.27	67.7	4.72	3.82	66.0	4.65	3.81
	0.8	66.7	4.69	3.81	65.2	4.60	3.80
	3	66.0	4.63	3.80	64.1	4.55	3.77
300	0	69.6	4.85	3.92	69.0	4.83	3.91
	0.27	68.4	4.79	3.89	67.4	4.75	3.89
	0.8	67.5	4.76	3.88	66.7	4.71	3.88
	3	66.7	4.69	3.87	65.8	4.65	3.86

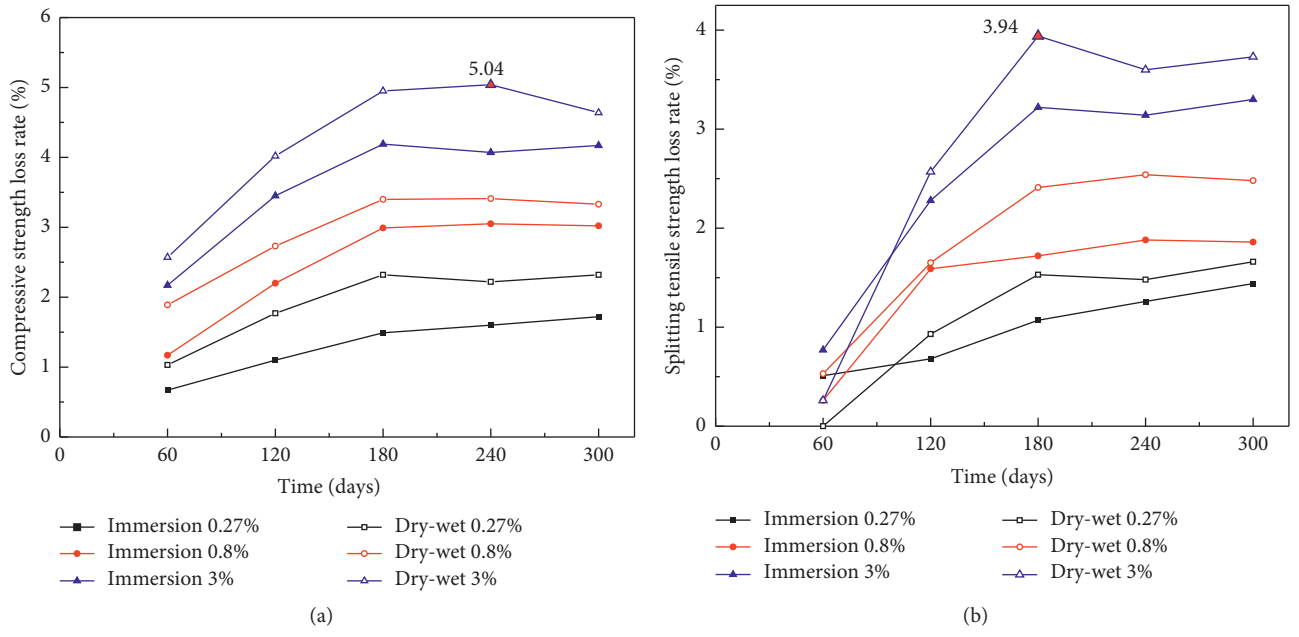

Figure 2: Continued.

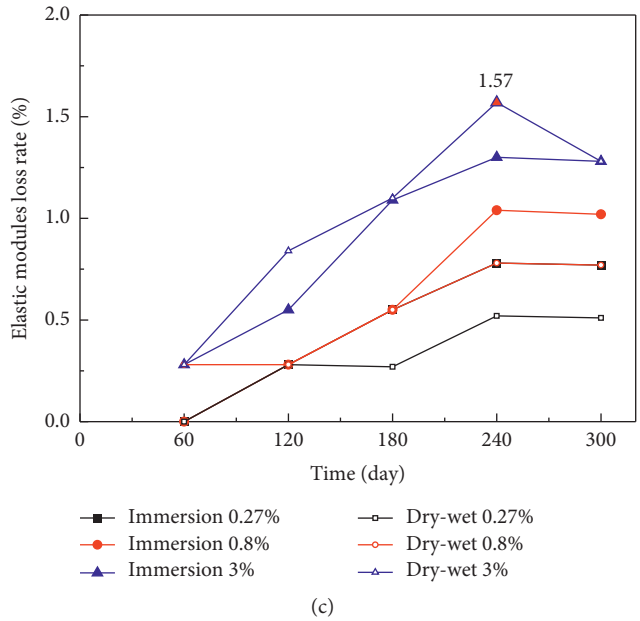

Figure 2: Loss rate of mechanical properties of concrete.

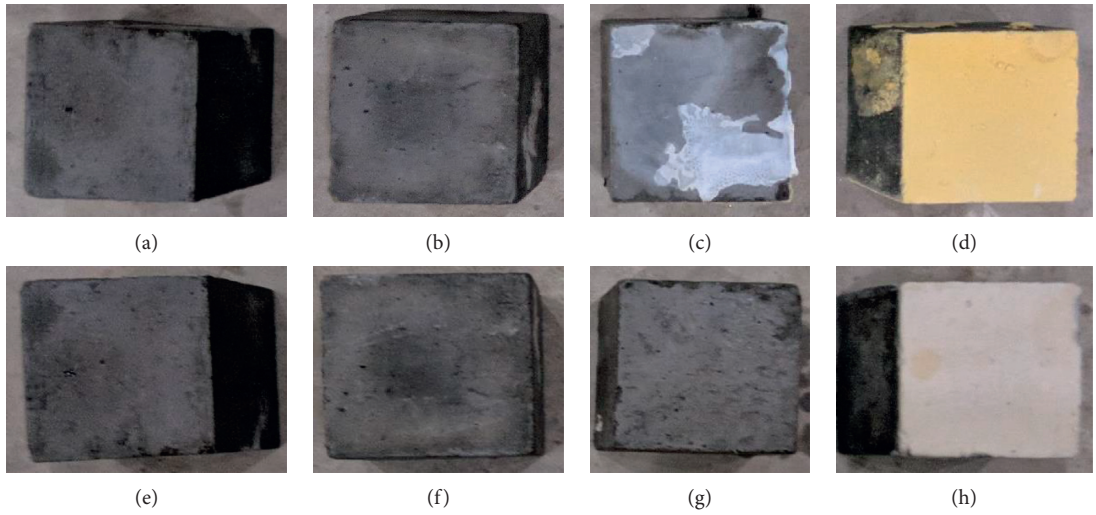

Figure 3: Concrete specimens after 300 days of corrosion: (a) immersion 0%, (b) immersion 0.27%, (c) immersion 0.8%, (d) immersion 3%, (e) dry-wet 0%, (f) dry-wet 0.27%, (g) dry-wet 0.8%, and (h) dry-wet 3%.

The steel bar and steel plate specimens at a corrosion test age of 300 days are shown in Figure 4. In the boric acid solution with a concentration of 3% after 120 days of corrosion, the surface of the steel specimen started being covered by corrosion products. When the corrosion age reached 300 days, after removing the corrosion products on the surface of the specimen, the internal steel bar and steel plates are only partially covered with black rust on the surface, while most areas remain bright. Combining the observed phenomenon with the mass loss of the steel bars and steel plates leads to the following observation:

(a) The effect of boric acid on steel is weak

(b) Corrosion products have a certain degree of denseness, inhibiting further corrosion of steel

4.3. Effect on Mechanical Property of Reinforcement Concrete. The flexural and bond strengths of reinforced concrete under each test environment are listed in Table 5. The mechanical properties of distilled water (boric acid concentration 0%) immersion and dry-wet alternating groups were used as the benchmark to calculate the loss rate of flexural strength and bond strength, and the results are shown in Figure 5.

The maximum flexural strength loss rate of the specimen was 3.57% at a boric acid concentration of 3% for 180 days in

Table 3: Mechanical properties of steel bar and steel plate in an immersion environment.

Test environment		Steel bar			Steel plate		
Age (d)	Concentration (%)	Yield strength (MPa)	Ultimate strength (MPa)	Corrosion rate (%)	Yield strength (MPa)	Ultimate strength (MPa)	Corrosion rate (%)
60	0	461.2	619.8	0.086	312.0	471.5	0.047
	0.27	460.7	619.6	0.086	312.3	471.2	0.063
	0.8	461.0	619.8	0.090	312.5	471.3	0.068
	3	461.2	620.0	0.092	312.5	471.2	0.078
120	0	461.2	619.8	0.113	312.5	471.5	0.063
	0.27	461.0	619.6	0.129	312.3	471.4	0.073
	0.8	461.0	619.6	0.132	312.2	471.4	0.078
	3	460.8	619.6	0.139	312.3	471.2	0.089
180	0	461.1	620.0	0.135	312.4	471.6	0.094
	0.27	461.0	619.7	0.140	312.6	471.3	0.100
	0.8	461.0	619.7	0.148	312.0	471.5	0.109
	3	461.0	619.7	0.146	312.4	471.2	0.099
240	0	462.0	620.3	0.160	312.3	471.4	0.120
	0.27	461.5	619.3	0.166	312.8	471.5	0.131
	0.8	460.8	620.0	0.174	312.1	471.1	0.146
	3	461.2	620.5	0.180	312.5	471.3	0.125
300	0	460.5	618.9	0.176	312.0	470.0	0.156
	0.27	460.0	618.5	0.170	312.2	470.5	0.172
	0.8	461.8	619.3	0.180	311.0	470.8	0.199
	3	459.7	619.6	0.158	311.6	471.0	0.121

Table 4: Mechanical properties of steel bar and steel plate under dry-wet cycles.

Test environment		Steel bar			Steel plate		
Age (d)	Concentration (%)	Yield strength (MPa)	Ultimate strength (MPa)	Corrosion rate (%)	Yield strength (MPa)	Ultimate strength (MPa)	Corrosion rate (%)
60	0	460.9	620.0	0.099	312.3	471.5	0.073
	0.27	461.0	619.7	0.101	312.0	471.0	0.079
	0.8	461.3	619.6	0.105	312.5	471.3	0.099
	3	461.0	620.1	0.107	312.5	471.3	0.120
120	0	461.2	619.8	0.137	312.1	471.2	0.121
	0.27	461.0	619.8	0.144	312.4	471.2	0.131
	0.8	460.9	619.8	0.148	312.0	471.0	0.142
	3	461.0	619.6	0.153	312.3	470.8	0.151
180	0	460.8	619.3	0.164	312.4	471.6	0.157
	0.27	461.2	619.5	0.171	312.4	471.7	0.162
	0.8	461.0	619.0	0.185	312.2	471.0	0.173
	3	460.8	619.6	0.167	312.3	471.4	0.167
240	0	461.3	619.0	0.190	312.5	471.7	0.183
	0.27	461.0	619.3	0.188	312.0	471.5	0.194
	0.8	461.5	618.8	0.191	311.8	471.2	0.197
	3	460.9	619.5	0.185	312.2	471.1	0.183
300	0	459.8	619.0	0.212	312.0	470.5	0.193
	0.27	460.7	618.7	0.236	311.8	470.6	0.236
	0.8	460.4	619.1	0.235	311.9	470.0	0.229
	3	459.3	619.4	0.201	311.5	470.4	0.193

alternating wet and dry conditions. The difference in the flexural strength loss rate of the specimens was small for the test environments with the boric acid concentration of 0.27% and 0.8%. The flexural strength loss rate is basically the same in the alternating environment of 0.27% concentration and the immersion environment of 0.8% concentration but showed large fluctuations in the later part of the test at a 3% boric acid concentration environment.

The loss rate of bond strength of specimens was small. The maximum loss rate of bond strength occurred at 240 days of corrosion under the wet and dry alternation, but the maximum value was only 1.83%, and the loss rate of bond strength tended

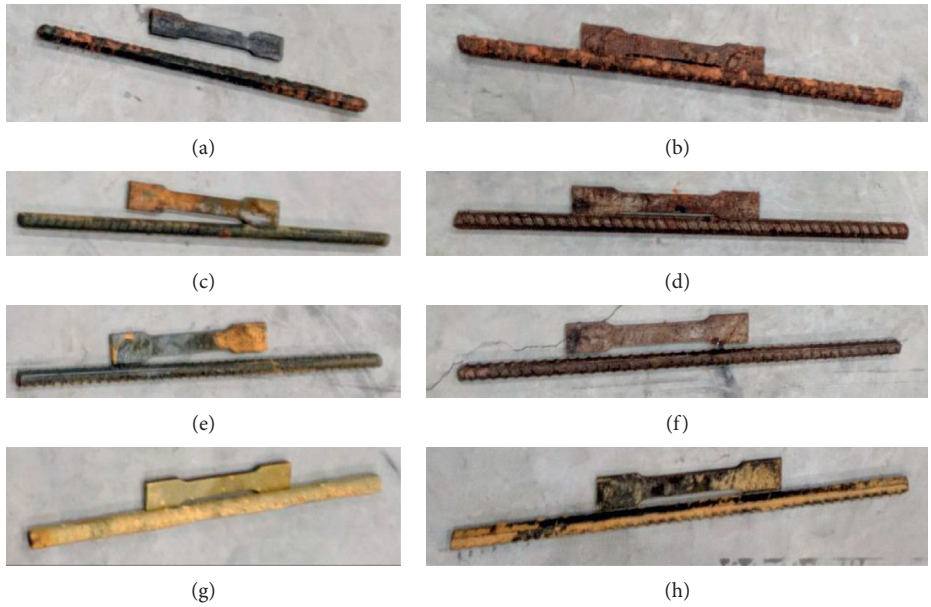

Figure 4: Steel bar and steel plate specimens after 300 d of corrosion: (a) immersion 0%, (b) dry-wet 0%, (c) immersion 0.27%, (d) dry-wet 0.27%, (e) immersion 0.8%, (f) dry-wet 0.8%, (g) immersion 3.0%, and (h) dry-wet 3.0%.

Table 5: Mechanical properties of reinforced concrete.

Test environment		Immersion		Dry-wet cycles	
Age (d)	Concentration (%)	Bond strength (MPa)	Flexural strength (kN)	Bond strength (MPa)	Flexural strength (kN)
60	0	7.62	21.6	7.56	20.8
	0.27	7.61	21.6	7.56	20.6
	0.8	7.61	21.4	7.54	20.7
	3	7.59	21.3	7.54	20.5
120	0	7.87	24.2	7.70	23.7
	0.27	7.85	24.0	7.67	23.4
	0.8	7.82	23.9	7.64	23.3
	3	7.79	23.6	7.60	23.0
180	0	8.05	25.4	7.96	25.2
	0.27	8.02	25.1	7.91	24.8
	0.8	7.96	24.0	7.88	24.6
	3	7.93	24.6	7.82	24.3
240	0	8.21	25.8	8.18	25.5
	0.27	8.17	24.5	8.12	25.0
	0.8	8.10	25.3	8.06	24.9
	3	8.08	25.0	8.03	24.6
300	0	8.27	25.6	8.28	25.7
	0.27	8.23	25.2	8.23	25.2
	0.8	8.20	25.1	8.19	25.1
	3	8.15	24.7	8.13	24.9

to be fixed at the later stage of corrosion. The bond strength of reinforced concrete was weakly affected by boric acid.

The test specimens of flexural strength and bond strength after 300 days of boric acid corrosion are shown in Figures 6 and 7. When the test specimens of flexural strength were split and sprayed with phenolphthalein solution, except for the surface location where no color indication appeared, the interior of the test specimens still maintained the high alkaline environment turning the phenolphthalein solution to red, and the internal reinforcement of the test specimens still maintained the polished luster. The internal reinforcement of the bond strength specimen also maintained the same pitting luster. The effect of boric acid corrosion on reinforced concrete specimens occurred only on the surface location of the specimen, and the internal reinforcement was not affected by the boric acid solution.

The electrochemical impedance spectra of the steel bars in flexural specimens of different ages under each corrosive

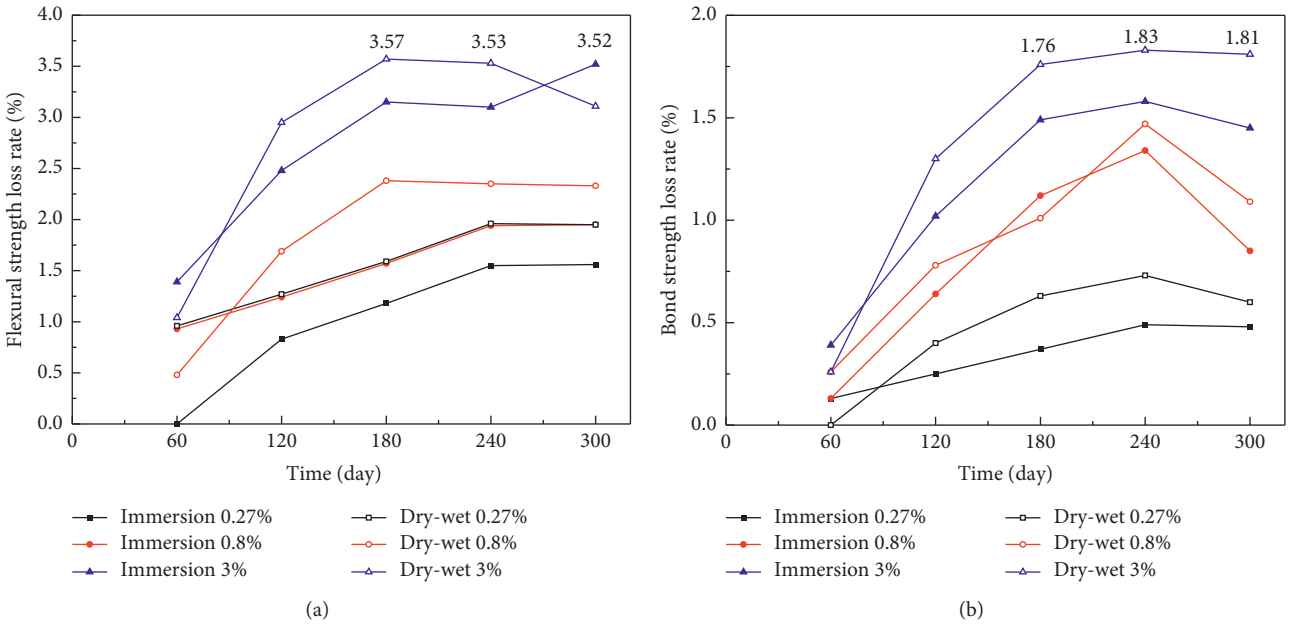

Figure 5: Loss rate of mechanical properties of reinforced concrete.

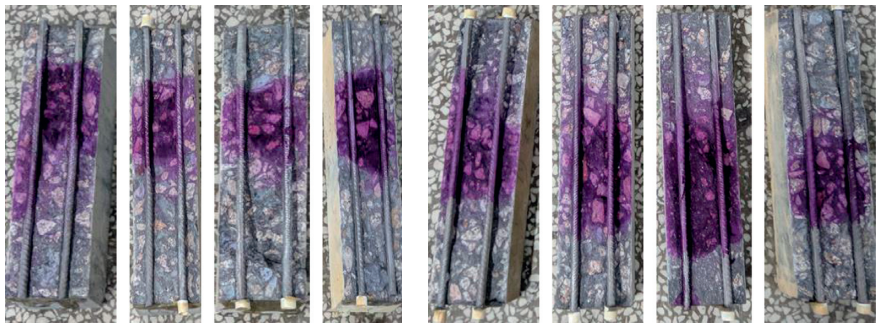

Figure 6: Flexural strength specimens after 300 days of corrosion: (a) immersion (0%, 0.27%, 0.8%, and 3%) and (b) dry-wet (0%, 0.27%, 0.8%, and 3%).

environment were recorded and analyzed. Figure 8 shows the Nyquist diagram of the internal reinforcement of the flexural specimen under the test environment, exhibiting only two capacitive resistance arcs in the high- and low-frequency regions.

The larger the radius of the low-frequency band capacitive arc, the greater the passivation film resistance of the steel surface [17, 18]. The intersection of the high- and low-frequency regions of the capacitive arc indicates the transfer resistance of the corrosive material to the surface of the reinforcement through the protective layer of concrete [19, 20].

The Nyquist diagram of the low-frequency band capacitive arc shows that under different corrosive environments, the slope of the low-frequency band capacitive arc resistance of the corrosion age of 60 days is significantly smaller than that after 120 days of corrosion. When the corrosion age reaches 120 days, there is no significant change in the slope of the low-frequency band capacitive arc resistance in different ages and corrosion environments. This result is consistent with the change in the cross-point position of the two capacitive resistance arcs in the real part of the Nyquist plot at different corrosion ages, probably because in the early stage of corrosion, relatively more cement is not fully hydrated inside the concrete, and the passivation film on the outer surface of the reinforcement is under a relatively weak alkaline environment. With increasing corrosion time, the internal cement hydrates more completely, providing a better alkaline environment for the internal reinforcement and the formation of a more complete passivation film on the surface of the reinforcement.

However, even in the early stages of corrosion, the low-frequency segment of the Nyquist plot in different corrosive environments does not show a flattened semicircular arc but a straight line with an inclination angle much greater than 45°. Similar test results were reported

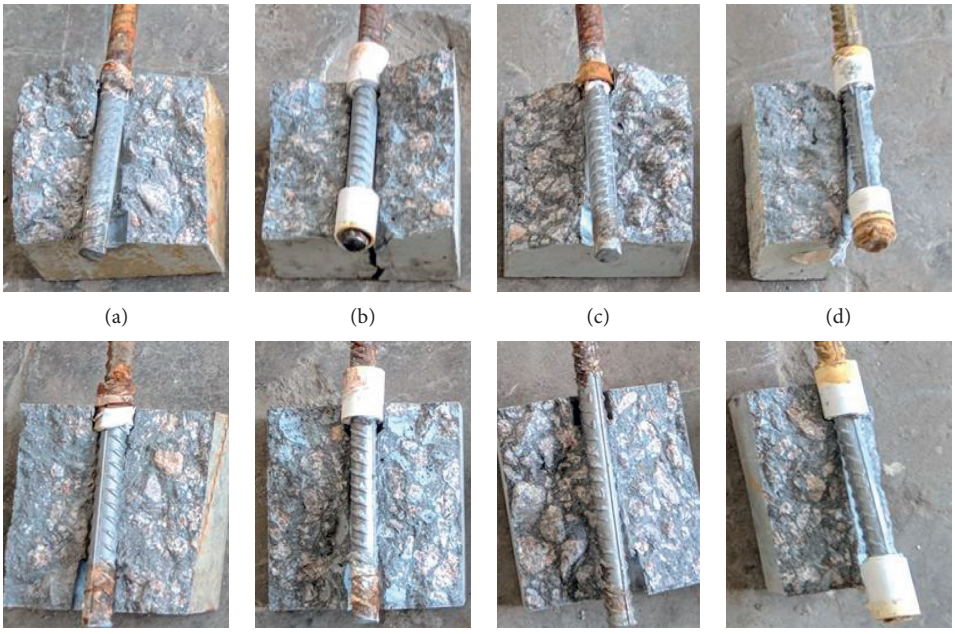

Figure 7: Bond strength specimens after 300 days of corrosion: (a) immersion 0%, (b) immersion 0.27%, (c) immersion 0.8%, (d) immersion 3%, (e) dry-wet 0%, (f) dry-wet 0.27%, (g) dry-wet 0.8%, and (h) dry-wet 3%.

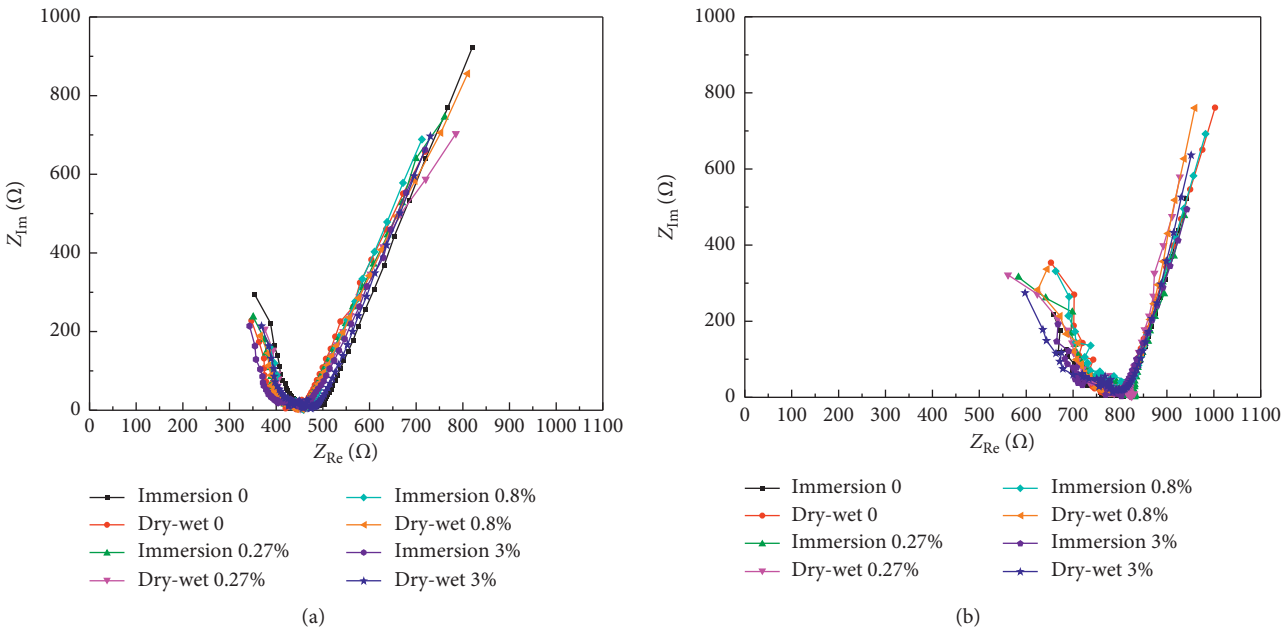

Figure 8: Continued.

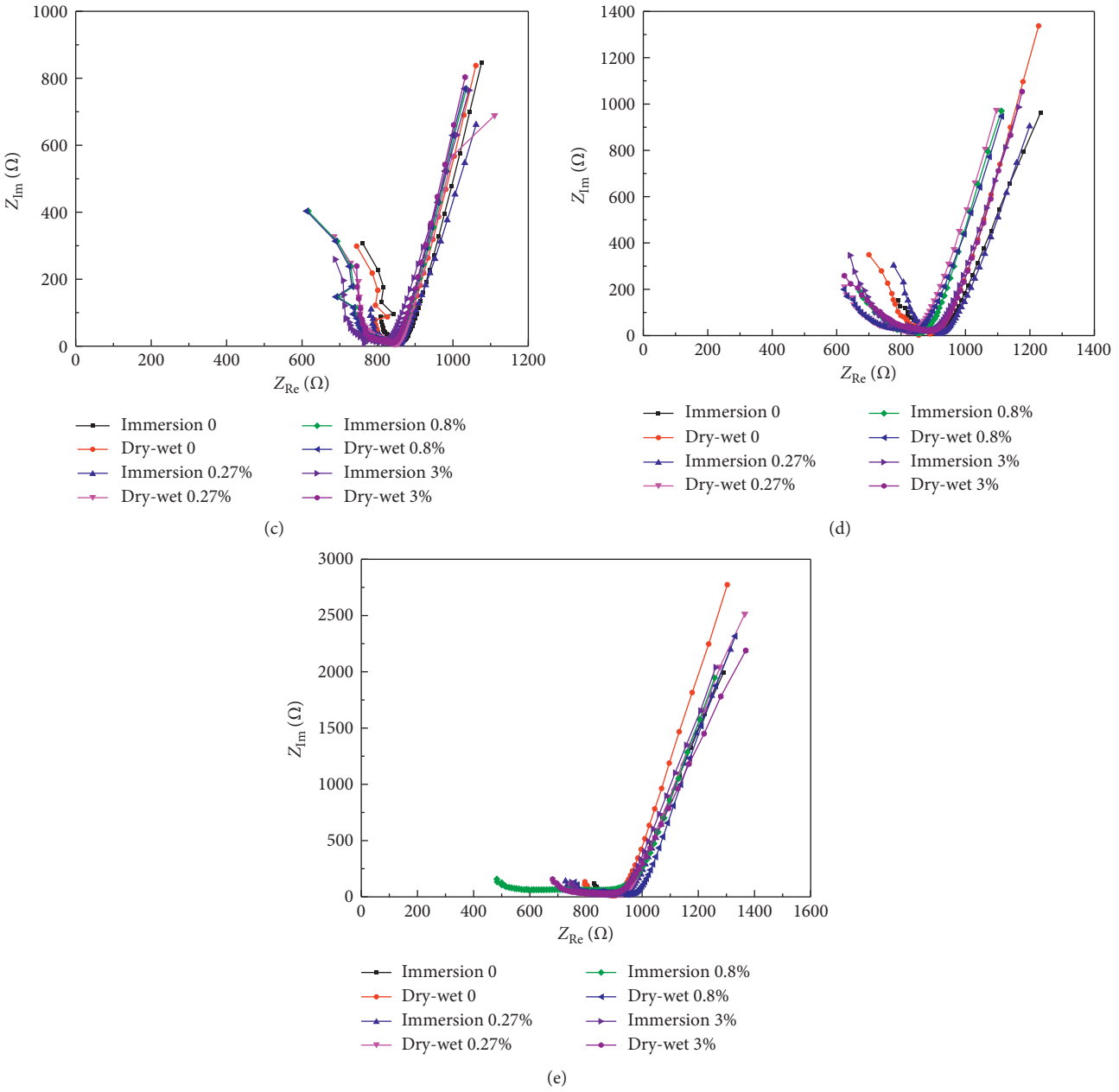

Figure 8: Nyquist diagram of reinforcement for flexural specimens at each age: (a) 60 days, (b) 120 days, (c) 180 days, (d) 240 days, and (e) 300 days.

by numerous scholars, indicating a typical feature of reinforcing steel in concrete in a passivated state [21–24]. Therefore, complete passivation film formed on the surface of the reinforcement concrete, and the reinforcement inside the flexural specimens at different corrosion ages and under different corrosion environments did not show any rusting. Comparing the Nyquist plot of the same age and different corrosive environments in the low-frequency band tolerance arc shows that the slope of the low-frequency band tolerance arc is basically the same, but the highest point of the low-frequency band tolerance arc is not significantly related to the concentration of boric acid corrosion solution, that is, the integrity of the passivation film on the surface of the steel is not affected by the concentration of the corrosion solution.

4.4. Effect on the Microstructure of Concrete. The sampled concrete powder was analyzed by X-ray diffraction (XRD) using a D8 ADVANCE X-ray diffractometer. A reinforced concrete specimen with a corrosion age of 300 days was selected and sampled on the surface and at 2 cm depth. Figure 9 shows the XRD analysis result. The XRD diffraction pattern shows that the corrosion product on the surface (0 cm) includes metaborate ($Ca(B0_2)_2$) and polyborate products (CaB_6O_{10}-$4H_2O$, CaB_4O_{10}). No significant

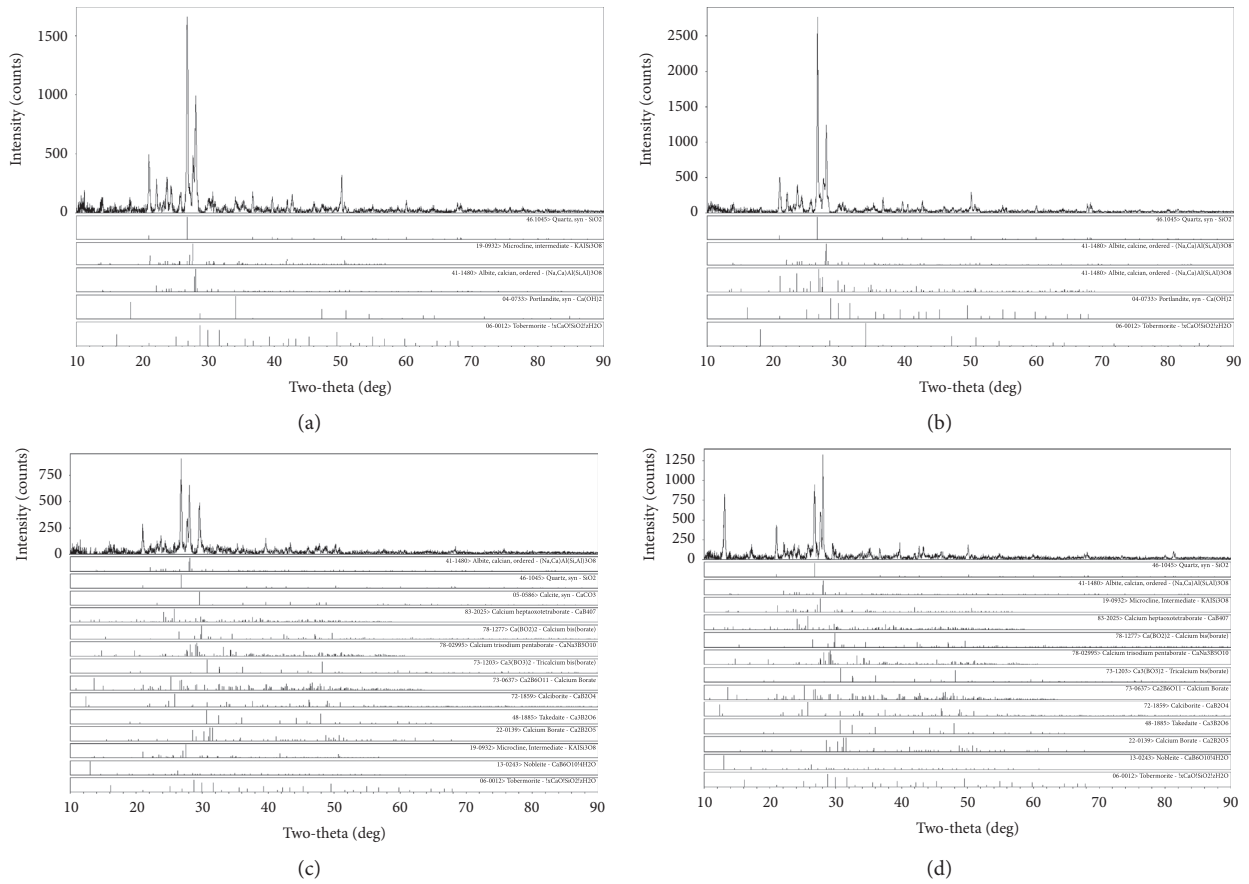

Figure 9: XRD analysis at 300 days of corrosion: (a) immersion 0.8% (2 cm), (b) immersion 3% (2 cm), (c) dry-wet 0.8% (0 cm), and (d) dry-wet 3% (0 cm).

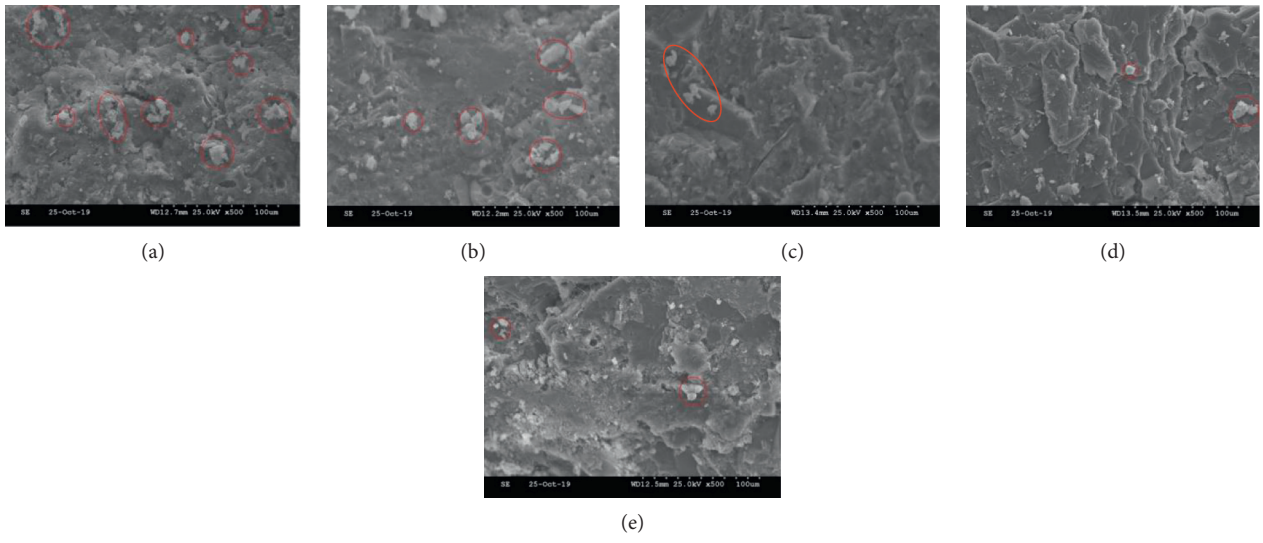

Figure 10: Electron microscopy scans of specimens at 300 days of corrosion: (a) immersion 0.8% (0 cm), (b) immersion 3% (0 cm), (c) immersion 0.27% (0 cm), (d) dry-wet 0.8% (2 cm), and (e) immersion 3% (2 cm).

corrosion products were detected in the diffraction pattern of the concrete internal specimens (2 cm). According to the relevant literature, boric acid produces metaborates with alkaline substances in an alkaline environment and polyborates with alkaline substances in an acidic environment. Boric acid mainly reacts with alkaline leaching solution and

has a weak corrosive effect on concrete specimens. The X-ray scan analysis results are consistent with the phenolphthalein solution color development results shown in Figure 6.

The concrete specimens were analyzed by scanning electron microscopy using an S-3500N series electron scanning microscope. Figure 10 shows the electron microscope scanning images of concrete specimens, indicating 0.8%, 3%, and 0.27% crystalline content of white corrosion products on the surface of the specimen under the immersion environment. The main reason is that the corrosion crystals attached to the surface of the specimen in the boric acid concentration of 3% environment inhibited the further corrosion of concrete. The concrete specimens did not show obvious corrosion crystallization products at 2 cm inside the specimen, allowing assuming that the corrosion of concrete by the boric acid mainly occurred on the concrete surface.

5. Conclusions

In conclusion, the corrosive effect of boric acid solution on reinforced concrete was systematically studied under two test environments, immersion and alternating wet-dry, to simulate the actual situation of nuclear power plant operation. The effects of boric acid corrosion on reinforced concrete were studied, leading to the following conclusions:

(1) The effect of the boric acid solution on the compressive strength, splitting tensile strength, elastic modulus, flexural strength, and bond strength of reinforced concrete specimens was found to be small. The corrosion effect is related to the concentration of the boric acid solution, but the effect is not significant. The corrosion degree of the specimens is mainly determined by the corrosion age.

(2) The effect of the boric acid solution on the yield strength, ultimate strength, and rust rate of steel bars and steel plates is weak, and the mechanical properties of the specimens after corrosion still met the strength requirements during the service.

(3) For concrete, the degradation of mechanical properties is slightly higher in alternating wet and dry environments than in the immersion environments; for example, the loss rate of compressive strength in these environments was 5.04% and 4.07%, respectively. However, steel specimens did not show this pattern.

(4) Corrosion occurs only at 2 cm inside the specimen under the action of boric acid.

(5) With increasing corrosion age, uneven corrosion products began to cover the surface of the specimen that inhibits further corrosion.

(6) The corrosion of reinforced concrete structures by boric acid has minimal impact on the safety of nuclear power plants, and thus, this study provides a reference for nuclear power plant operation and maintenance.

Data Availability

The data used to support the findings of this study are included within the article and also available from the corresponding author upon request.

Conflicts of Interest

The authors declare that they have no conflicts of interest.

Acknowledgments

This project was supported by the High-Level Talent Research Fund of Qingdao Agricultural University (663/1120050).

References

[1] Y. H. Zheng, *40 Years, Write a Brilliant Chapter in the Use of Nuclear Energy*, China Energy News, Zhejiang, China, 2018.

[2] L. Wang, T. S. He, Y. X. Zhou et al., "The influence of fiber type and length on the cracking resistance, durability and pore structure of face slab concrete," *Construction and Building Materials*, vol. 282, Article ID 122706, 2021.

[3] S. M. Abd El Haleem, S. Abd El Wanees, E. E. Abd El Aal, and A. Diab, "Environmental factors affecting the corrosion behavior of reinforcing steel II. Role of some anions in the initiation and inhibition of pitting corrosion of steel in $Ca(OH)_2$ solutions," *Corrosion Science*, vol. 52, no. 2, pp. 292–302, 2010.

[4] Z. S. Yao, Y. Fang, W. H. Kong, X. W. Huang, and X. S. Wang, "Experimental study on dynamic mechanical properties of coal gangue concrete," *Advances in Materials Science and Engineering*, vol. 2020, Article ID 8874191, 16 pages, 2020.

[5] C. Muñoz-Ruiperez, A. Rodríguez, C. Junco, F. Fiol, and V. Calderon, "Durability of lightweight concrete made concurrently with waste aggregates and expanded clay," *Structural Concrete*, vol. 19, no. 5, pp. 1309–1317, 2018.

[6] M. Kumar, A. K. Sinha, and J. Kujur, "Mechanical and durability studies on high-volume fly-ash concrete," *Structural Concrete*, vol. 22, no. 1, pp. 1–14, 2020.

[7] D. Chen, K. J. Howe, J. Dallman et al., "Experimental analysis of the aqueous chemical environment following a loss-of-coolant accident," *Nuclear Engineering and Design*, vol. 237, no. 20-21, pp. 2126–2136, 2007.

[8] W. Ramm and M. Biscoping, "Autogenous healing and reinforcement corrosion of water-penetrated separation cracks in reinforced concrete," *Nuclear Engineering and Design*, vol. 179, no. 2, pp. 191–200, 1998.

[9] A. Demirbaş and S. Karslioğlu, "The effect of boric acid sludges containing borogypsum on properties of cement," *Cement and Concrete Research*, vol. 25, no. 7, pp. 1381–1384, 1995.

[10] C. Z. Wu, R. F. Zhu, J. P. Lin et al., "Selection and application of AP1000 WIRST material," *Hot Working Techmolog*, vol. 44, no. 14, pp. 120–125, 2015.

[11] H. Huang, N. G. Jin, G. Y. Zheng et al., "Study on the influence of boric acid on the corrosion of concrete," *China Concrete and Cement Products*, vol. 3, pp. 14–16, 2006.

[12] H. Rong, L. Yang, J. W. Li et al., "Research on the corrosion effect on the durability of concrete structure of a nuclear power plant by boric acid," *Industrial Construction*, vol. 47, no. 9, pp. 35–38, 2017.

[13] L. Wang, M. M. Jin, Y. H. Wu et al., "Hydration, shrinkage, pore structure and fractal dimension of silica fume modified low heat Portland cement-based materials," *Construction and Building Materials*, vol. 272, Article ID 121952, 2021.

[14] L. Wang, R. Luo, and W. Zhang, "Effects of fineness and content of phosphorus slag on cement hydration, permeability, pore structure and fractal dimension of concrete," *Fractals*, vol. 29, no. 2, Article ID 2140004, 2021.

[15] L. J. Jiang, M. F. Chang, and Z. Q. Wen, "Experimental study on mechanical properties of corroded steel bars," *Low Temperature Architecture Technology*, vol. 33, no. 3, pp. 62–64, 2011.

[16] G. Xu, Z. W. Yang, R. Zhang et al., "Corrosion characteristics of rebar in two surface states under chloride environment," *Journal of Building Materials*, vol. 22, no. 2, pp. 254–259, 2019.

[17] Z. Y. Ai, J. Y. Jiang, W. Sun et al., "Passive behaviour of Cr_8Ni_2 alloy corrosion-resistant steel in simulating concrete pore solutions with different pH values," *Journal of Southeast University (Natural Science Edition)*, vol. 46, no. 1, pp. 152–159, 2016.

[18] S. Joiret, M. Keddam, X. R. Nóvoa, M. C. Pérez, C. Rangel, and H. Takenouti, "Use of EIS, ring-disk electrode, EQCM and Raman spectroscopy to study the film of oxides formed on iron in 1 M NaOH, ring-disk electrode, EQCM and Raman spectroscopy to study the film of oxides formed on iron in 1 M NaOH," *Cement and Concrete Composites*, vol. 24, no. 1, pp. 7–15, 2002.

[19] L. Yang, Z.-Q. Jin, and H. Zhang, "Steel corrosion electrochemical research under the condition of wet and dry cycle," *Concrete*, vol. 4, pp. 27–29, 2014.

[20] C. Xu, Z. Y. Li, and W. L. Jin, "Electrochemical impedance spectroscopy characteristics of corrosion behavior of rebar in concrete," *Corrosion Science and Protection Technology*, vol. 23, no. 5, pp. 393–398, 2011.

[21] G. Qiao and J. Ou, "Corrosion monitoring of reinforcing steel in cement mortar by EIS and ENA," *Electrochimica Acta*, vol. 52, no. 28, pp. 8008–8019, 2007.

[22] L. Wang, F. X. Guo, and Y. Q. Lin, "Comparison between the effects of phosphorous slag and fly ash on the C-S-H structure, long-term hydration heat and volume deformation of cement-based materials," *Construction and Building Materials*, vol. 250, Article ID 118807, 2020.

[23] M. Stern and A. Geary, "Electrochemical polarization I. A theoretical analysis of the shape of polarization curves," *Journal of the Electrochemical Society*, vol. 1, no. 104, pp. 56–63, 1957.

[24] S. G. Millard, D. Law, J. H. Bungey, and J. Cairns, "Environmental influences on linear polarisation corrosion rate measurement in reinforced concrete," *NDT & E International*, vol. 34, no. 6, pp. 409–417, 2001.

Hindawi
Advances in Materials Science and Engineering
Volume 2021, Article ID 5543286, 13 pages
https://doi.org/10.1155/2021/5543286

Research Article

Influence of Crack on Concrete Damage in Salt-Freezing Environment

Guangyan Liu[1,2] **Song Mu**[1,2] **Jingshun Cai**[1,2] **Deqing Xie**[1,2] **Ying Zhou**[1,2] **and Xiaocheng Zhou**[1,2]

[1]*State Key Laboratory of High Performance Civil Engineering Material, Jiangsu Research Institute of Building Science, Nanjing 210008, China*
[2]*Jiangsu Sobute New Materials Co. Ltd., Nanjing 211103, China*

Correspondence should be addressed to Song Mu; musong@cnjsjk.cn

Received 18 January 2021; Revised 22 April 2021; Accepted 7 June 2021; Published 16 June 2021

Academic Editor: Peng Zhang

The damage development trend of concrete with cracks in salt-freezing environment is systematically studied. The cracks are also tested in intact concrete for comparison, and crack characterization is introduced. The mass loss, the relative dynamic elastic modulus, and the change of crack width are analyzed. Results show that the crack width increases as the salt-freezing cycle progresses. Following the development trend of the cracks, concrete cracks can be divided into three categories: 0–40, 40–100, and 100–150 μm. The mass loss increases significantly, and the change of relative dynamic elastic modulus decreases in concrete with an initial crack compared with the intact concrete. When the crack width is 80 μm, a maximum mass loss rate of 0.19% and a minimum relative dynamic elastic modulus of 75.81% can be obtained. These test results prove that crack and freeze-thaw coupling can influence each other and accelerate the failure of concrete. Overall, this study can serve as a basis for the durability design and life improvement of concrete structures.

1. Introduction

With the construction of cross-sea bridges, concrete has been increasingly used in marine environments. Thus, the improvement of the durability of concrete material is a significant scientific issue for civil structure design [1]. In some cold areas, such as in northern China, the temperature is usually less than 0°, leading to the rapid degradation of the concrete. Frost attack on concrete is distress resulting from the phase transformation associated with the freezing of internal moisture. This phenomenon directly leads to the reduction of the cover and rusting of steel, affecting the service life of the concrete. In environments characterized by the presence of chloride ions, such as coastal environments and areas where deicing salts are used, the combination of freeze-thaw cycles and deicer salt application can seriously damage concrete [2, 3]. The damage mechanism of salt-freezing is different from freezing and thawing damage. Deicing salt, employed to reduce the freezing point of water, alters the degree of saturation [4, 5] and reacts with the hydrated ordinary Portland cement (OPC), creating expansive reaction products that lead to cracking and distress [6–11]. The deterioration due to the erosive effect of deicing salt can develop rather rapidly than the destructive effect of normal freezing and thawing cycle on concrete. Consequently, the performance degradation of concrete is more serious under salt-freezing circumstances. The extensive use of deicing salts can result in the deterioration of concrete structures, such as pop-outs, exfoliations, and cracks, significantly affecting the service life of structures [12–15].

For concrete, cracks can form in various ways, including applied external force, temperature changes leading to volumetric mismatch, and internal chemical reactions usually caused by the ingress of aggressive chemicals [16–19]. Once cracks take form, they can provide a way for the chloride transport to the concrete [20–22]. Ingress of steel corrosive agents, such as water and air, will also accelerate, leading to higher chances of initiating corrosion

[23, 24]. Thus, many scholars investigated the effect of cracks on chloride ion transport. Jang et al. [25] studied the influence of cracks on chloride ion diffusion behavior in concrete. They found that the diffusion coefficient of chloride ion would not increase with the increase of the crack width until the so-called critical crack width is reached. When the crack width is larger than the critical value, the diffusion coefficient increases with the increase of the width, and the critical crack width obtained by the test varies from 55 μm to 80 μm. Wang et al. [26] showed that when the crack width is between 100 and 400 μm, the diffusion coefficient of chloride ions in the crack increases rapidly with the increase of the crack width. Otherwise, the crack width has no obvious effects on chloride diffusion. Djerbi et al. [27] compared the influence of cracks on ordinary concrete and high-performance concrete by simulating chloride ion penetration in concrete. They proved that the diffusion coefficient of chloride ions in the crack increases with the increase of the crack width. When the crack width is greater than 80 μm, the diffusion coefficient of chloride ion in the crack is equal to the diffusion coefficient of chloride ion in water, which is independent of the concrete mix ratio.

The above studies were only a few of the increasing investigations on the salt frost damage on concrete. However, concrete with cracks has not yet been considered, and the factors leading to its rapid degradation in a marine environment remain unclear. Therefore, the frost damage resistance of concrete under cracking conditions requires further examination, which is helpful for the material's durability design and life prediction. The present study aims to determine how the development process of salt frost will damage concrete with crack and how the cracks influence salt frost damage. Specifically, the salt-freeze cycle is applied to the concrete specimens with initial cracks. After analyzing the mass loss of concrete, relative dynamic elastic modulus, and the change of crack width, the development trend of concrete damage under the coupled action of crack and the salt-freezing cycle is obtained.

2. Preparation of Test Specimens and Applied Test Methods

2.1. Materials. Type II52.5 OPC provided by Jiangnan-Xiaoyetian Cement Co., Ltd., was used in the experiment. Fly ash (FA) and ground slag (SL) were also used to replace part of the cement as supplementary cementitious materials. FA and SL had replacement rates of 15% and 35%, respectively. The chemical compositions were determined using X-ray fluorescence (XRF; Thermo Fisher Scientific ARL QUANTX), as shown in Table 1.

Fine aggregate was natural sand with a fineness modulus of 2.6 and an apparent density of 2640 kg/m^3. The basalt with particle size ranging from 5 mm to 15 mm and an apparent density of 2800 kg/m^3 was used as coarse aggregate. A 20% solid superplasticizer was applied to adjust the workability of fresh concrete. The air-entraining agent was also used to regulate 5%–6% of the air content. The above materials were provided by Jiangsu Sobute New Materials Co. Ltd.

Poremaster GT-60 produced by Quantachrome Instruments was used to test concrete porosity. Quanta 250 scanning electron microscopy (SEM) manufactured by FEI Company was employed to conduct microscopic analysis of the samples obtained after the salt-freezing cycle.

2.2. Sample Preparation. The w/b used for concrete was 0.35. The concrete mix proportion is shown in Table 2.

The concrete was mixed as follows. The cementitious materials and aggregate were added and mixed for 1 min. Then, the superplasticizer and air-entraining agent were placed and stirred continuously for 2 mins. After stirring, the concrete samples with dimensions of $100 \times 100 \times 100$ mm and φ of 100×200 were cast. The cube samples were used to test the compressive strength, and the cylindrical samples were examined. The samples were removed from their mold on the next day. They were cured for another 28 days in $20 \pm 2^{\circ}$C, under 95% RH following the GB/T50081-2019. Subsequently, the compressive strength of the sample was determined using the pressure testing machine. The compressive strength of concrete was 56.9 MPa. The cylindrical samples were finally tested.

2.3. Preparation and Characterization of Cracks. Various methods can be used to prepare concrete cracks, such as the Brazilian splitting test, wedge splitting test, and three-point bending mode. Here, the method proposed by Toshiki on the basis of the Brazilian splitting test was employed. The Brazilian splitting test is simple and convenient, and thus, it is accepted by the majority [25, 28, 29]. However, due to the heterogeneity of concrete, controlling the formation and development of cracks in the loading process would be difficult, and the specimen might easily develop a fracture. In the present experiment, the method would use the PVC pipes to prevent specimen fracture.

After curing for 28 days, the samples with dry surfaces were put in PVC pipes whose one end was closed, as presented in Figures 1(a) and 1(b). Then, a low viscosity epoxy resin was used to fill the gap between PVC pipes and samples. A sample slice with a height of 50 mm was obtained for crack preparation. The details of the production process are presented in Figure 1. On the basis of the Brazilian splitting test, a linear variable differential transformer (LVDT) was used to monitor the crack width during the whole process, as shown in Figure 1(e). When the width reached the design value, the sample was removed, and the fracture parameters were characterized after 15 min [30] as the crack width would shrink after unloading.

After completing the crack preparation, the exact crack width was tested as follows: first, a glass slide with a size of 24.5×76 mm was chosen as a reference. Then, a photograph of the crack was taken with the reference, as shown in Figure 2(a). Next, the reference and the cracking area were selected and binarized. Finally, the number of pixels of the selected area was determined. In the same photograph, the ratio of the cracking area was equal to the ratio of pixels. The pixel of the crack and reference and the area of the reference were obtained. Accordingly, the area of the reference was calculated. For simplicity, the length of the crack was assumed to be the diameter of the specimen, which was

Table 1: Chemical compositions of the binder (%).

Type	SiO_2	CaO_2	Al_2O_3	Fe_2O_3	MgO	K_2O	Na_2O	SO_3	Others
OPC	19.86	67.24	4.79	2.94	1.26	0.67	0.12	2.81	0.31
FA	40.00	12.50	33.10	5.61	0.65	0.96	0.38	3.30	3.5
SL	32.20	41.10	14.4	1.04	6.38	0.53	0.35	2.23	1.77

Table 2: Concrete mix proportion (kg/m^3).

Cement	SL	FA	Water	Sand	Aggregate	Superplasticizer	Air-entraining agent
240.00	168.00	72.00	168.00	735.84	1625.86	2.68	0.04

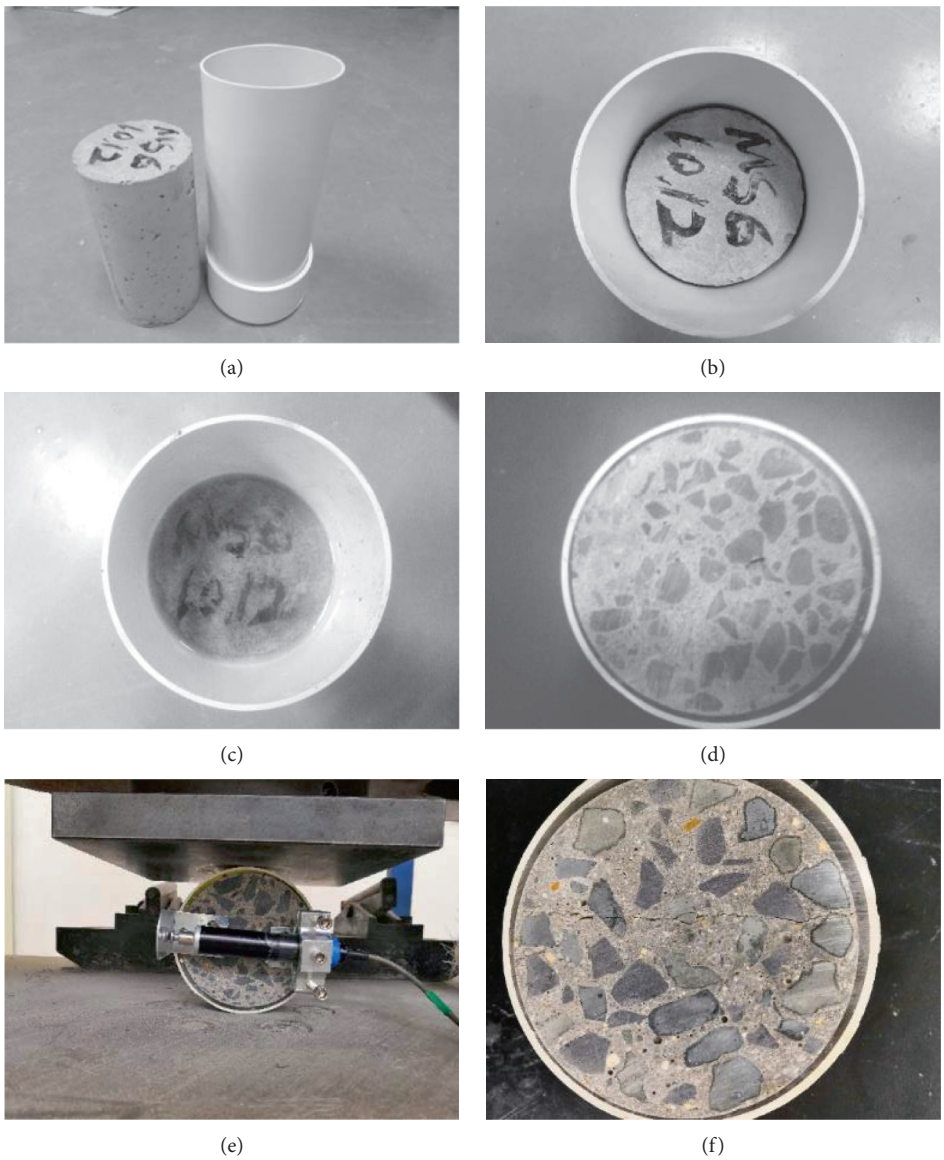

Figure 1: Preparation process of cracks in concrete specimens.

100 mm. Thus, the width of the crack was equal to the area divided by the length.

On the basis of the above method, the final crack width was divided into seven groups: 20, 40, 60, 80, 100, 130, and 150 μm. In the subsequent test, the width of each group was considered to be the actual crack width. The width error of each group was 5 μm. The detailed grouping is shown in Table 3.

(a) (b)

Figure 2: Fracture characterization process.

Table 3: Grouping of cracks of different widths.

Group width (μm)	20	40	60	80	100	130	150
Actual crack width (μm)	15–25	35–45	55–65	75–85	95–105	125–135	145–155

2.4. Salt-Freezing Testing Procedure. These tests were run following the GB/T50082-2009 Chinese standard. In this case, the sodium chloride (NaCl) solution had a similar mass concentration of 3% as the freeze-thaw solution. The test surfaces of the samples were placed in 3% NaCl solution for seven days for solution uptake by capillary suction. The temperature in the box varied between +20°C and −20°C. A cycle of freezing and thawing lasted for 12 h, and the test only started when the temperature in the box was 20°C. In the first cycle, the samples were cooled at 10°C per hour for 4 h until the temperature was −20°C. This setup was maintained for 3 h. Then, they were heated up at a rate of 10°C per hour. Finally, the temperature was kept at 20°C for 1 h to complete the cycle. The temperature change during a cycle is shown in Figure 3. The specimens were characterized by the crack width and number of freeze-thaw cycles. For example, D28C8 indicates that the specimens had a crack width of 80 μm and were exposed to freeze-thaw cycles 28 times.

Following the GB/T50082-2009 standard, the related parameters were tested every four cycles (two days). The damage of specimens was reflected by the relative dynamic elastic modulus and scaling mass. After four cycles, the flaking material was collected, dried, and weighed. The measurement of ultrasonic transit time was a standardized test method used to determine the variation in the relative dynamic elastic modulus with time. Ultrasonic transducers were positioned to arrange the axis of the ultrasonic transit path perpendicular to the specimen surface and parallel to the crack depth direction. The transit time in the coupling medium was calculated from the velocity of the ultrasonic signal and the transit length in the coupling medium. In this experiment, ZBL-U510 nonmetallic ultrasonic detector was used to test the ultrasonic transmission time.

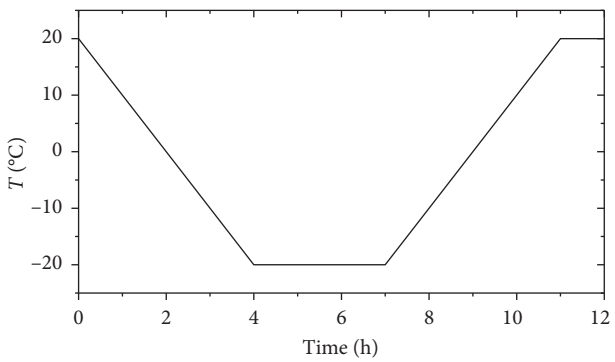

Figure 3: Salt-freezing cycle temperature system.

The relative dynamic elastic modulus was determined using the following equations:

$$\tau_n = \frac{t_0 - t_c}{t_n - t_c} \times 100,$$
$$E_d = \tau_n^2 \times 100, \quad (1)$$

where E_d is the relative dynamic elastic modulus of the specimen (%), τ_n is the ultrasonic wave relative propagation

time of the specimen (%), t_0 is the total propagation time of ultrasonic wave in the specimen and coupling agent (μs), t_n is the total propagation time of ultrasonic wave in the specimen and coupling agent after n cycles (μs), and t_c is the propagation time of ultrasonic waves in the coupling agent.

At the same time, a camera was used to take photos of the specimen. The photographs were processed to observe the changes in the crack width and sampling for porosity and microscopic testing.

3. Results and Discussion

3.1. Crack Width. The effect of salt-freezing cycles on the crack width of concrete is presented in Figure 4. The initial crack width was roughly 60 μm, as shown in Figure 4(a). After the 8th, 16th, and 28th cycles, the crack widths indicated in Figure 4 were increased to 164.51, 193.58, and 268.01 μm. In other words, the crack width increased with the extension of the cycle period.

The damage development of the crack width with the increase in salt-freezing cycle periods is shown in Figure 5. The initial crack width of less than 40 μm gradually increased at the early and late stages, with the increase of the cycle period. In the initial stage, due to the small crack widths, considering, self-healing and other factors, the increase of crack width was relatively slow. However, with the continuous increase of the crack width, the self-healing ability was weakened. The bigger the crack width, the easier it for the solution to be absorbed by the concrete, leading to internally and externally salt-induced freezing damage and a significant increase in the crack width.

In the later period of salt-freezing cycle, concrete cracks tended to shrink. The identification and detection of cracks were mainly based on the software. With the development of salt-freezing cycle, on the one hand, flaking led to particles blocking cracks. On the other hand, the damage range of the specimen generally extended from the fracture area to both sides, making it difficult to identify fractures. Consequently, the crack width obtained by the test was reduced. For specimens with crack width less than 40 μm, the initial crack width was small, and the damage caused by salt-freezing was not serious, so this phenomenon did not occur at all.

Following the development trend of cracks, concrete cracks could be concluded as three categories. For the crack width of less than 40 μm, the salt-freezing cycle almost did not affect the crack development at the early stage. However, it caused a rapid growth for the crack width at the later stage. For the crack widths ranging from 40 μm to 100 μm, the salt-freezing cycle resulted in rapid growth at the first 20 cycles. The crack width remained stable or gradually decreased after 20 cycles. For the crack widths greater than 100 μm, the development trend of the cracks was similar, and the width was almost identical. To sum up, no obvious effect was observed on the crack development when the crack width was more than 100 μm. Moreover, for the cracks at different widths to reach the maximum growth rate of the crack widths, the number of salt-freezing cycles required is gradually reduced. For the crack widths of 40, 80, and 130 μm, the number of cycles required to achieve the maximum growth rate of the crack width was 28, 20, and 16 times, respectively.

3.2. Mass Loss Rate. The mass loss rate of the specimen after 28 salt-freezing cycles is shown in Figure 6. At the stage where the crack width was less than 20 μm, no obvious effect was observed on its mass loss rate. When the crack width was ranging from 20 μm to 80 μm, the mass loss rate sharply increased. The maximum mass loss rate was 0.19%, which was obtained when the crack width was 80 μm. Afterward, the curve slowly decreased. The mass loss of surface undamaged concrete (crack width of 0 μm) was minimal, indicating that the surface cracks could significantly affect the salt-freezing resistance and reduce the durability of the specimen. Moreover, the increase of the crack width and contact parts between the specimen surface and salt solution increased the scaling mass.

The mass loss of the specimens with different crack widths along with the salt-freezing cycle is shown in Figure 7. With the increase of the crack width, the mass loss gradually increased. At the early stage of the salt-freezing cycle, the mass scaling of concrete specimens was not obvious, and the mass scaling rate was low. With the increase of the salt-freezing cycle period, the quality loss of the specimen increased gradually. The mass loss also increased when the freeze-thaw cycle was more than eight times. With the continuous salt-freezing cycle, the peeling quality gradually increased, and the mass loss rate increased. The reason might be the gradual accumulation of the damage of the specimen. Given the existence of cracks, the salt solution could enter into the concrete through the cracks and cause damage. At the early stage of the salt-freezing cycle, no significant differences were observed in the scaling quality between specimens with different fracture widths, indicating that the effect of fracture width on the scaling quality was not obvious at this time. As the number of salt-freezing cycles went on, the effect of the fracture width on the scaling quality gradually increased.

3.3. Relative Dynamic Modulus of Elasticity. The propagation of ultrasonic waves in concrete was affected by the matrix compactness and microcracks. The damage of concrete was determined by testing the change of ultrasonic wave transmission time in concrete. Ultrasonic testing of concrete was carried out in a direction perpendicular to the crack, as shown in Figure 8.

The change of the relative dynamic elastic modulus of the specimen with the salt-freezing cycle under different fracture conditions is displayed in Figure 9.

When the crack width was less than 20 μm, the relative dynamic elastic modulus of concrete decreased slightly, and the damage occurred only in the later stages of the salt-freezing cycle. In Figures 9(c) and 9(d), the relative dynamic elastic modulus of concrete dropped sharply, whose crack width was 60 and 80 μm by 75.92% and 75.81%. However, when the crack width was 100 and 130 μm, the relative dynamic modulus was only slightly reduced. By contrast, when the crack width was 80 μm, the relative dynamic

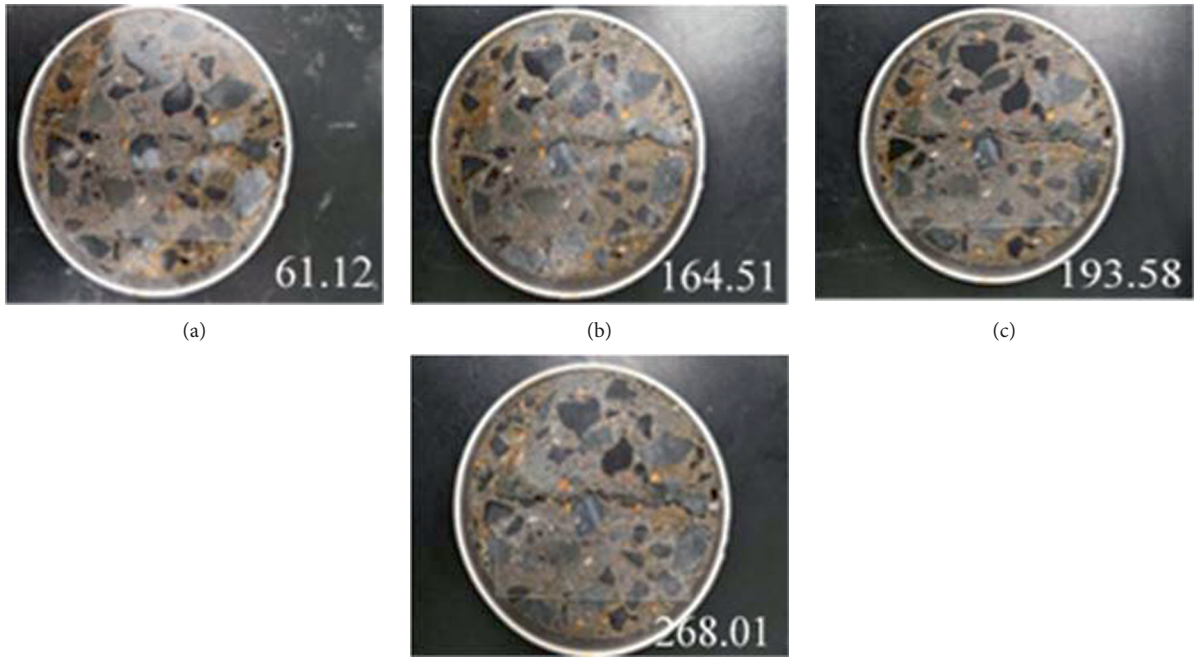

Figure 4: The development of concrete damage under different salt-freezing cycle periods: (a) 0, (b) 8th, (c) 16th, and (d) 28th cycles.

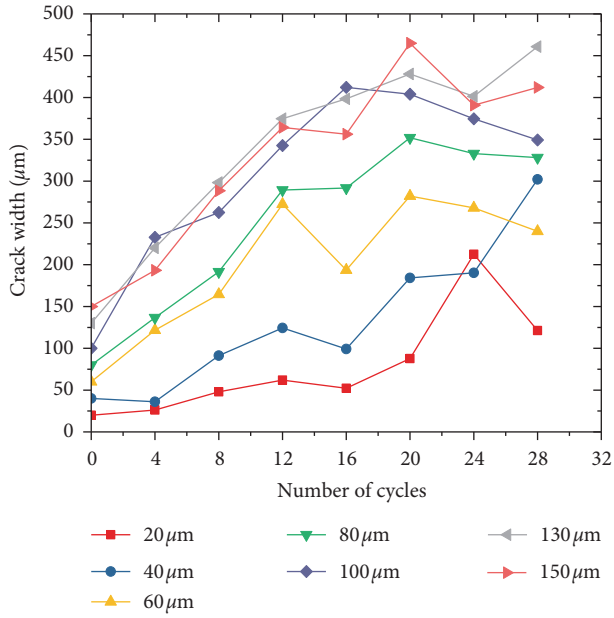

Figure 5: The fracture development of the specimens under different salt-freezing cycles.

modulus did not continue to reduce as the crack width increases. Given the gradual damage accumulation, the relative dynamic modulus of all the specimens did not excessively change. The maximum change was only 92.96% when the width was 60 μm during the first eight salt-freezing cycles. In the early stage of the salt-freezing cycle, the microcracks were produced in the sample, and the relative dynamic elastic modulus did not change significantly. As the cycle progresses, the damage of the sample and the peeling were intensified. Macroperformances decreased in relative dynamic modulus of elasticity.

The relative dynamic elastic modulus of the sample after completion of all salt-freezing cycles under different initial crack widths is shown in Figure 10. Without any produced cracks, the relative dynamic modulus of the specimen was 93% after 28 salt-freezing cycles. However, the relative

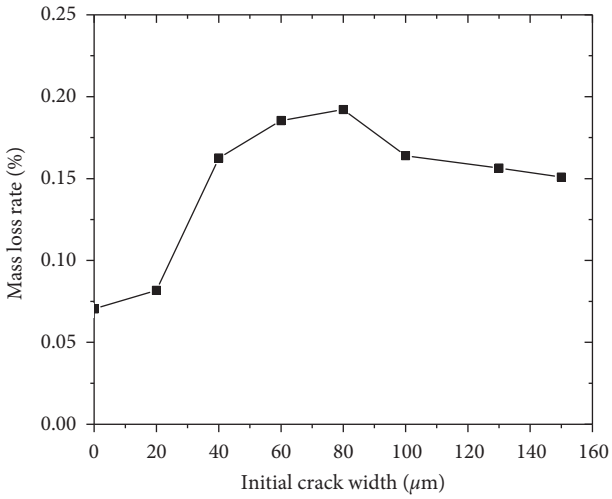

Figure 6: The mass loss rate of the specimens after 28 salt-freezing cycles.

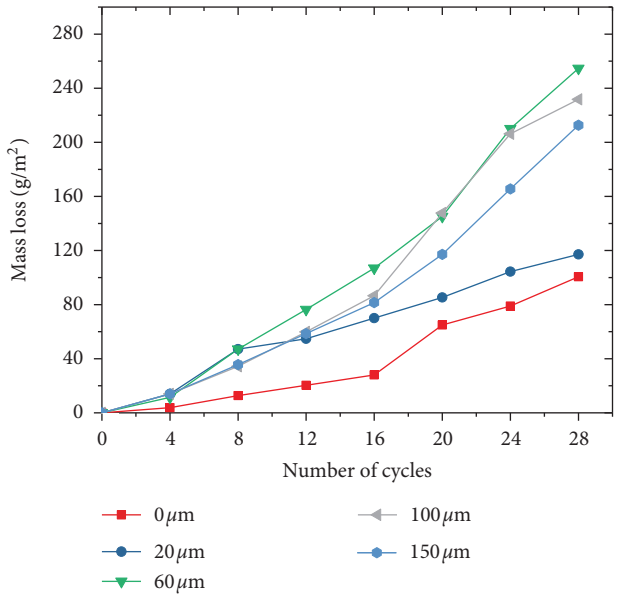

Figure 7: Mass loss of specimens with different salt-freezing cycles.

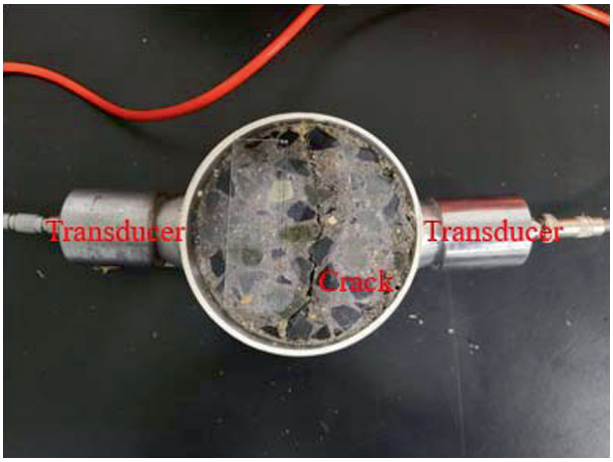

Figure 8: Diagram of the ultrasonic test.

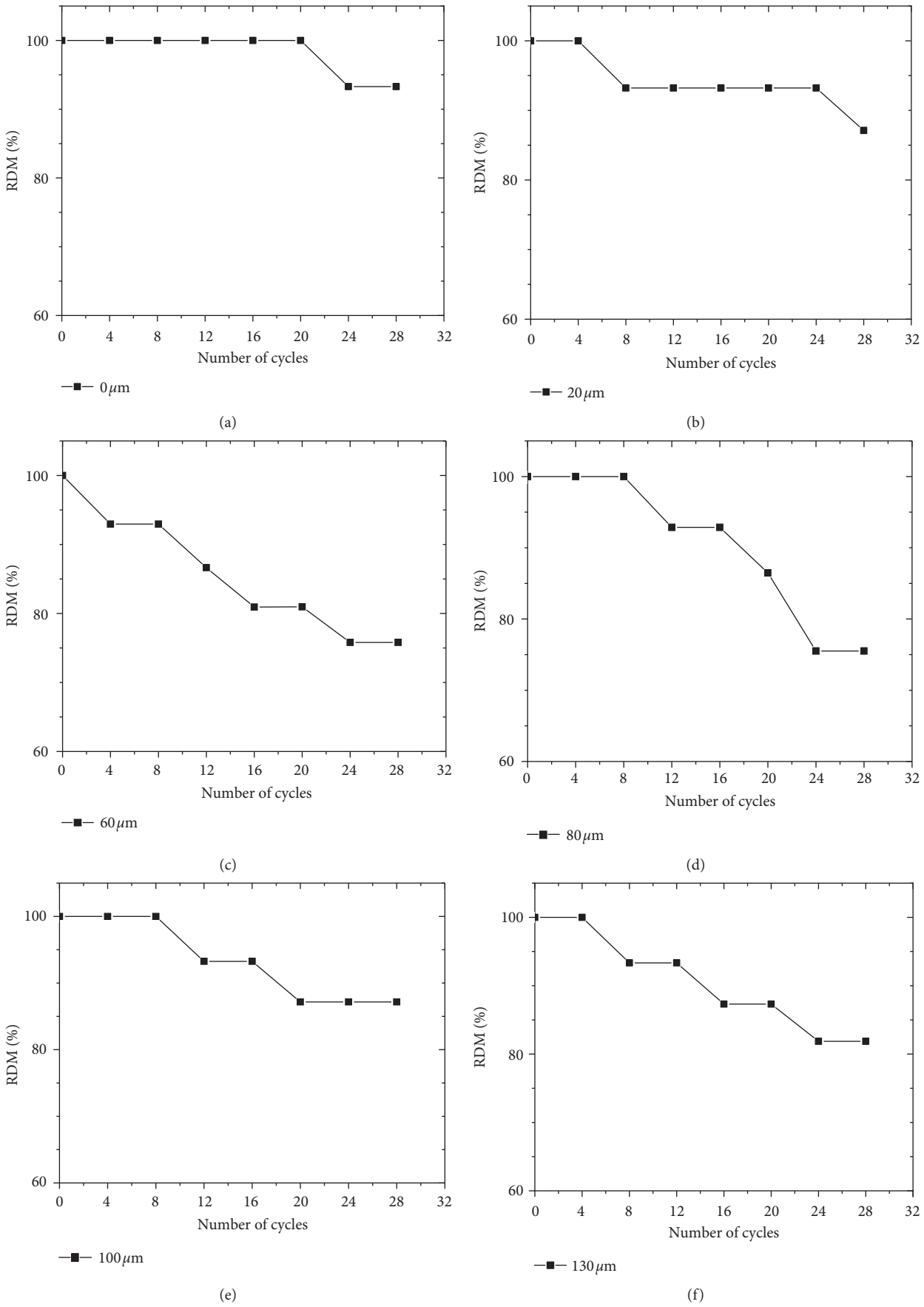

Figure 9: Changes in the relative dynamic elastic modulus of the specimens with the salt-freezing cycle: (a) 0, (b) 20, (c) 60, (d) 80, (e) 100, and (f) 130 μm.

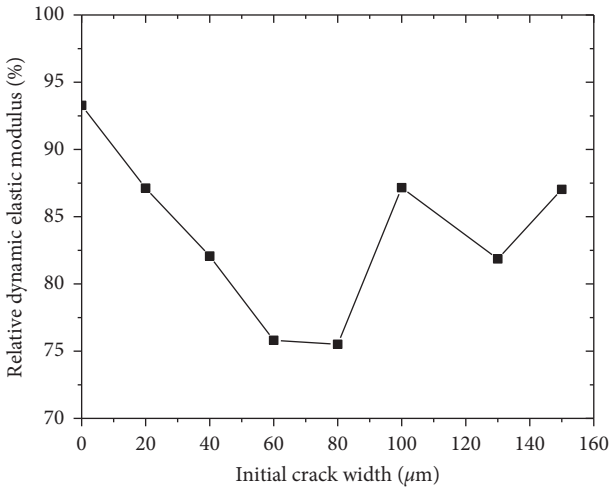

Figure 10: Changes in the relative dynamic elastic modulus of concrete after 28 salt-freezing cycles.

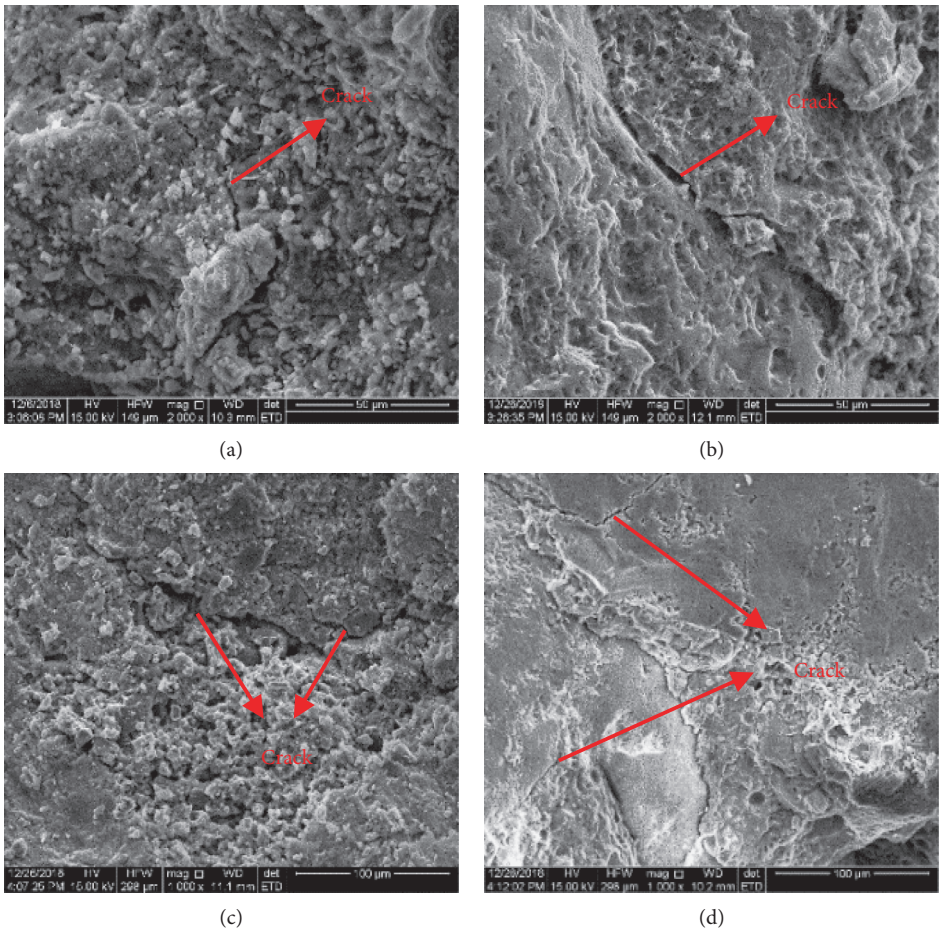

(a) (b)

(c) (d)

Figure 11: Continued.

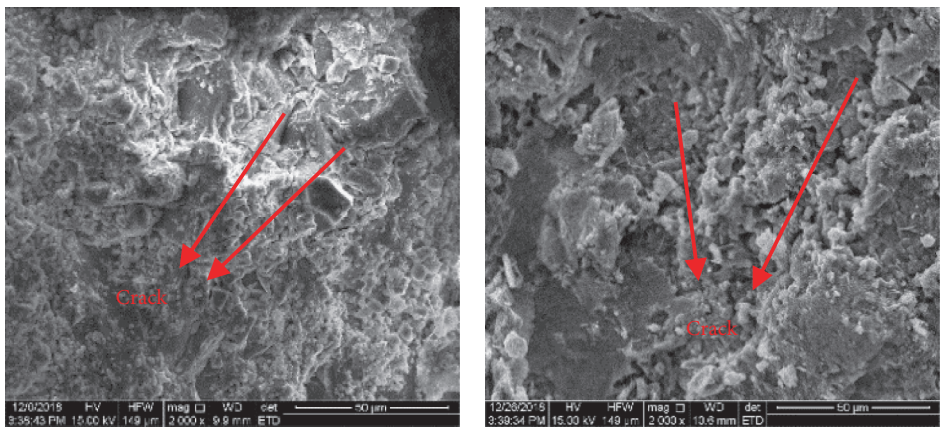

(e) (f)

Figure 11: SEM photographs of the concrete under different salt-freezing cycles. (a) D0C0, (b) D28C2, (c) D28C6, (d) D28C8, (e) D28C10, and (f) D8C13.

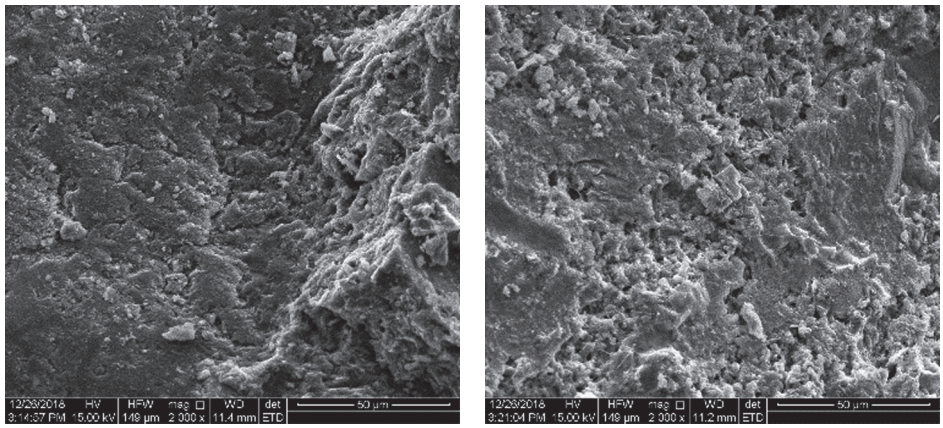

(a) (b)

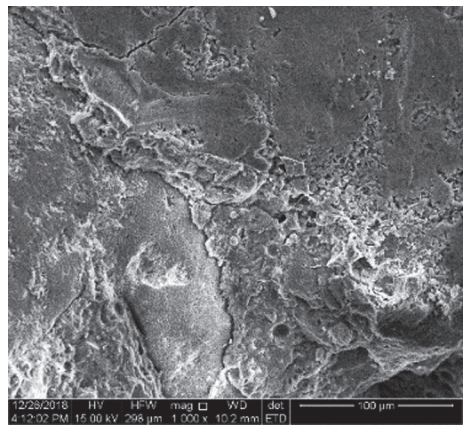

(c)

Figure 12: SEM photographs of the concrete under different salt-freezing cycles. (a) D8C8, (b) D16C8, and (c) D28C8.

dynamic modulus was 87.12%, 82.07%, 75.92%, 75.81%, 87.16%, 81.86%, and 87.03% for the sample with the crack widths of 20, 40, 60, 80, 100, 130, and 150 μm, respectively. The existence of cracks led to simultaneous surface and internal damage. Therefore, after completing all the salt-freezing cycles, the relative dynamic elastic modulus was markedly reduced compared with the intact concrete sample. Considering that the relative dynamic elastic modulus mainly represented the internal damage degree of the specimen, the cracks in the specimen led to the increase

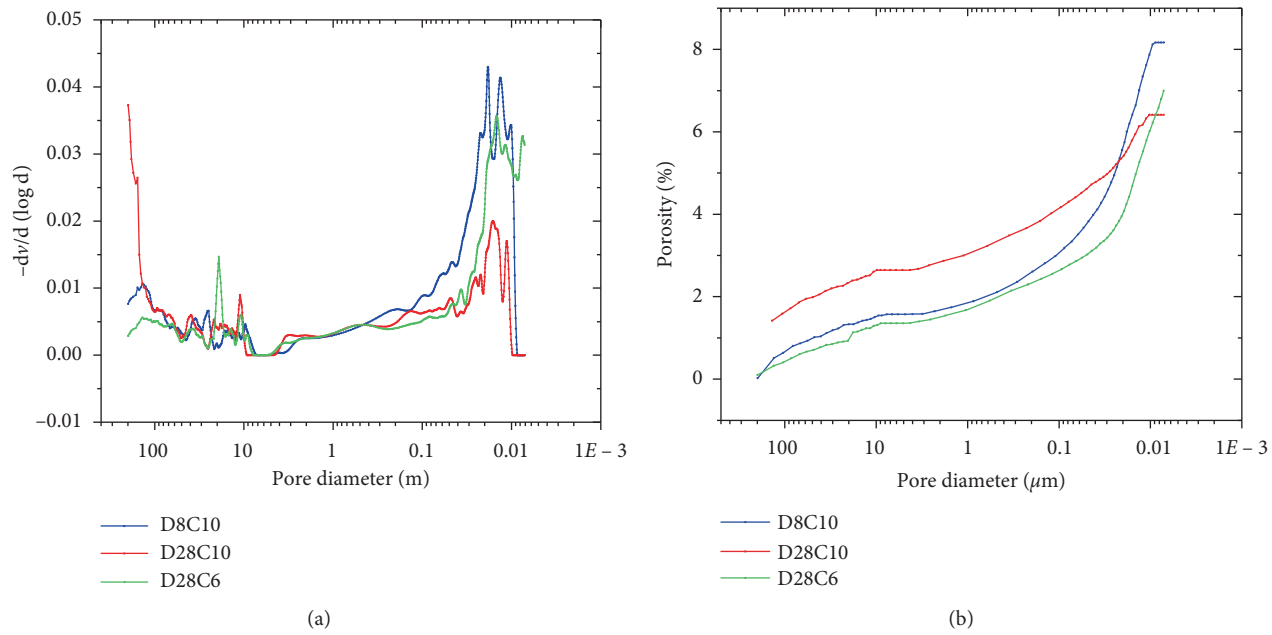

Figure 13: Pore size distribution of specimens with different crack widths and salt-freezing cycles: (a) most probable pore radius and (b) porosity.

of the internal damage degree. When the crack width was less than 80 μm, the larger the crack width, the more obvious the decrease of the relative dynamic modulus of the specimen. The specimen would be more easily damaged in the salt-freezing cycle. However, at the stage where the crack width was greater than 80 μm, the relative dynamic elastic modulus exhibited the opposite trend, except when the crack width was 100 μm.

For the mass loss, obvious damage was produced in concrete specimens with an initial crack after eight salt-freezing cycles. When the crack width was 80 μm, the concrete was most likely to be damaged, and the destruction was the most serious in a salt-freezing environment.

3.4. Microstructure and Porosity. The SEM images of the samples with the initial crack after 28 salt-freezing cycles are shown in Figure 11. Although cracks were observed in the concrete that did not undergo the salt-freezing cycle, their number was small, and the CSH gel was relatively complete and dense. After completing the salt-freezing cycle, the integrity of the specimen was damaged, and the peeling of small particles led to internal potholes and increased mass loss. When the crack width was 20 μm, the CSH gel was pitted, and the integrity was damaged. As the crack width increases, the damage to the specimen increases. For example, in the stage where the crack width was ranging from 60 μm to 80 μm, the microcracks inside the specimen significantly increased, and the crack expansion caused the specimen to peel. The damage of the specimen was the most serious when the crack width was 130 μm, and the CSH gel produced microholes. The damage caused by freezing and thawing resulted in many microcracks in the specimen. These damages led to the scaling of the specimen. As a new transmission channel, microcracks accelerated the entry of chloride ions and water into the specimen. Thus, they could aggravate the damage degree of the next freeze-thaw cycle. The larger the crack width, the more serious was the microstructure damage and the more evident the damaging effect would be. Given the damage, more solutions entered the pores, further leading to the degradation of concrete. This coupling effect was also one of the reasons why the damage of cracked concrete was worse than that of intact concrete.

The SEM images of the specimens with the same crack width at the 8th, 16th, and 28th salt-freezing cycles are shown in Figure 12. The damage of concrete increased gradually with the salt-freezing cycle. Similarly, the degree of surface scaling aggravation and the number of microcracks increased. The increase in the salt-freezing cycle periods gradually accumulated damage to the specimens aggravated.

The changes in the void fraction during the salt-freezing cycle are shown in Figure 13. The samples with a crack width of 100 μm had the most probable pore radius increase and porosity diminution after completing all the salt-freezing cycles compared with only eight cycle periods. Salt-freezing caused the generation of tiny cracks. Many small damages, whether newly generated or originally in the specimen, increased gradually. Consequently, the most probable pore radius also increased. The voids grew and communicated with one another to form large damage, causing a decrease in porosity. For the specimen with a crack width of 60 μm, the most probable pore radius increased significantly after 28 cycles, but the change in the void fraction was not obvious compared with the specimens with a crack width of 100 μm. Yet, the porosity and most probable pore radius of D28C10 slightly changed in contrast to sample D8C10. This result proved that the influence of the crack width on concrete was

greater than that of the freeze-thaw cycle, which was more likely to cause pore size increase and concrete damage.

4. Conclusion

In this study, the damage development trend of concrete with initial cracks in a salt-freezing environment was systematically examined. The development of cracks in concrete, the mass loss, the change of relative dynamic elastic modulus, and the change of microstructure and void ratio were tested. On the basis of the test results, the following conclusions can be drawn:

(1) The crack width increases with salt-freezing. The larger the initial crack width, the larger the crack width will be. For the specimens with a crack width of less than 40 μm, the crack width develops slowly in the initial stage but rapidly at the later stage. The crack widths ranging from 40 to 100 μm have exhibited rapid growth. However, for the specimens with a crack width greater than 100 μm, under the same salt-freezing cycle, the crack width is almost the same, indicating that the influence of the initial crack width can be ignored.

(2) Under cracking conditions, the salt-free cycle exacerbates the damage of concrete. The mass loss and the relative dynamic elastic modulus have obvious changes compared with the intact concrete. In addition, the influence of the crack width on concrete damage is greater, and the acceleration effect on the concrete failure is more obvious than the salt cycles.

(3) The SEM results show that the damage of concrete increases gradually with a continuous salt-freezing cycle. The peeling of small particles leads to internal potholes and mass loss. The larger the crack width is, the more serious the microstructure damage and the more evident the damaging effect. Salt-freezing also leads to the most probable pore radius increase and porosity diminution.

(4) The concrete with an initial crack has developed internal and surface damage compared with the intact concrete. Therefore, the surface and internal cracks and the pores of the specimen tend to fall off and increase, respectively. In other words, corrosive substances, such as chloride ions, can diffuse into the concrete through the surface and pass through the cracks. Consequently, substances can easily enter the concrete, causing durability problems, such as steel corrosion, and affecting the service life.

Data Availability

The data and charts used to support the findings of this study are available within in the article.

Conflicts of Interest

The authors declare that they have no conflicts of interest.

Acknowledgments

The authors are grateful for the financial support provided by the National Natural Science Foundation of China (U1706222) and the China Railway First Survey and Design Institute Group Co., Ltd. (20-16-2).

References

[1] S. Jacobsen, H. C. Gran, E. J. Sellevold, and J. A. Bakke, "High strength concrete—freeze/thaw testing and cracking," *Cement and Concrete Research*, vol. 25, no. 8, pp. 1775–1780, 1995.

[2] A. B. Harnik, U. Meier, and A. Rosw, "Combined influence of freezing and delcing salt on concrete – physical aspects," *Durability of Building Materials and Components ASTMSTP*, vol. 69, pp. 474–484, 1980.

[3] J. Deja, "Freezing and de-icing salt resistance of blast furnace slag concretes," *Cement and Concrete Composites*, vol. 25, no. 3, pp. 357–361, 2003.

[4] R. P. Spragg, J. Castro, W. Li, M. Pour-Ghaz, P. T. Huang, and J. Weiss, "Wetting and drying of concrete using aqueous solutions containing deicing salts," *Cement and Concrete Composites*, vol. 33, no. 5, pp. 535–542, 2011.

[5] C. Villani, R. Spragg, M. Pour-Ghaz, and W. Jason Weiss, "The influence of pore solutions properties on drying in cementitious materials," *Journal of the American Ceramic Society*, vol. 97, no. 2, pp. 386–393, 2014.

[6] Y. Farnam, D. Bentz, A. Hampton, and W. J. Weiss, "Acoustic emission and low-temperature calorimetry study of freeze and thaw behavior in cementitious materials exposed to sodium chloride salt," *Transportation Research Record: Journal of the Transportation Research Board*, vol. 2441, no. 1, pp. 81–90, 2014.

[7] Y. Farnam, H. Todak, R. Spragg, and J. Weiss, "Electrical response of mortar with different degrees of saturation and deicing salt solutions during freezing and thawing," *Cement and Concrete Composites*, vol. 59, pp. 49–59, 2015.

[8] Y. Farnam, D. Bentz, A. Sakulich, D. Flynn, and J. Weiss, "Measuring freeze and thaw damage in mortars containing deicing salt using a low-temperature longitudinal guarded comparative calorimeter and acoustic emission," *Advances in Civil Engineering Materials*, vol. 3, pp. 316–337, 2014.

[9] Y. Qian, Y. Farnam, and J. Weiss, "Using acoustic emission to quantify freeze–thaw damage of mortar saturated with nacl solutions," in *Proceedings of the International Conference on the Durability of Concrete Structures*, pp. 32–37, West Lafayette, IN, USA, July 2014.

[10] Y. Farnam, S. Dick, A. Wiese, J. Davis, D. Bentz, and J. Weiss, "The influence of calcium chloride deicing salt on phase changes and damage development in cementitious materials," *Cement and Concrete Composites*, vol. 64, pp. 1–15, 2015.

[11] Y. Farnam, A. Wiese, D. Bentz, J. Davis, and J. Weiss, "Damage development in cementitious materials exposed to magnesium chloride deicing salt," *Construction and Building Materials*, vol. 93, pp. 384–392, 2015.

[12] X. Shi, L. Fay, M. M. Peterson, and Z. Yang, "Freeze-thaw damage and chemical change of a portland cement concrete in the presence of diluted deicers," *Materials and Structures*, vol. 43, no. 7, pp. 933–946, 2010.

[13] J. J. Valenza and G. W. Scherer, "A review of salt scaling: I. Phenomenology," *Cement and Concrete Research*, vol. 37, no. 7, pp. 1007–1021, 2007.

[14] K. Wang, D. E. Nelsen, and W. A. Nixon, "Damaging effects of deicing chemicals on concrete materials," *Cement and Concrete Composites*, vol. 28, no. 2, pp. 173–188, 2006.

[15] W. Sun, R. Mu, X. Luo, and C. Miao, "Effect of chloride salt, freeze–thaw cycling and externally applied load on the performance of the concrete," *Cement and Concrete Research*, vol. 32, no. 32, pp. 1859–1864, 2002.

[16] Z. Li and S. P. Shah, "Localization of microcracking in concrete under uniaxial tension," *ACI Materials Journal*, vol. 91, pp. 372–381, 1994.

[17] H. Zhao, K. Jiang, B. Hong et al., "Experimental and numerical analysis on coupled hygro-thermo-chemo-mechanical effect in early-age concrete," *Journal of Materials in Civil Engineering*, vol. 33, no. 5, Article ID 04021064, 2021.

[18] H. Zhao, X. Wu, Y. Huang, P. Zhang, Q. Tian, and J. Liu, "Investigation of moisture transport in cement-based materials using low-field nuclear magnetic resonance imaging," *Magazine of Concrete Research*, vol. 73, no. 5, pp. 252–270, 2021.

[19] H. Zhao, K. Jiang, R. Yang, Y. Tang, and J. Liu, "Experimental and theoretical analysis on coupled effect of hydration, temperature and humidity in early-age cement-based materials," *International Journal of Heat and Mass Transfer*, vol. 146, Article ID 118784, 2020.

[20] C. M. Aldea, S. P. Shah, and A. Karr, "Effect of cracking on water and chloride permeability of concrete," *Journal of Materials in Civil Engineering*, vol. 11, no. 3, pp. 181–187, 1999.

[21] M. Hoseini, V. Bindiganavile, and N. Banthia, "The effect of mechanical stress on permeability of concrete: a review," *Cement and Concrete Composites*, vol. 31, no. 4, pp. 213–220, 2009.

[22] M. B. Otieno, M. G. Alexander, and H.-D. Beushausen, "Corrosion in cracked and uncracked concrete - influence of crack width, concrete quality and crack reopening," *Magazine of Concrete Research*, vol. 62, no. 6, pp. 393–404, 2010.

[23] B. Pease, M. Geiker, H. Stang, and J. Weiss, "The design of an instrumented rebar for assessment of corrosion in cracked reinforced concrete," *Materials and Structures*, vol. 44, no. 7, pp. 1259–1271, 2011.

[24] F. Hiemer, S. Keßler, and C. Gehlen, "Development of chloride induced reinforcement corrosion in cracked concrete after application of a surface protection system," in *Proceedings of the Concrete Solutions 6th International Conference on Concrete Repair*, Thessaloniki, Greece, June 2016.

[25] S. Y. Jang, B. S. Kim, and B. H. Oh, "Effect of crack width on chloride diffusion coefficients of concrete by steady-state migration tests," *Cement and Concrete Research*, vol. 41, no. 1, pp. 9–19, 2011.

[26] H. L. Wang, J. G. Dai, X. Y. Sun, and X. L. Zhang, "Characteristics of concrete cracks and their influence on chloride penetration," *Construction and Building Materials*, vol. 107, pp. 216–225, 2016.

[27] A. Djerbi, S. Bonnet, A. Khelidj, and V. Baroghel-Bouny, "Influence of traversing crack on chloride diffusion into concrete," *Cement and Concrete Research*, vol. 38, no. 6, pp. 877–883, 2008.

[28] S. S. Park, S. J. Kwon, and S. H. Jung, "Analysis technique for chloride penetration in cracked concrete using equivalent diffusion and permeation," *Construction and Building Materials*, vol. 29, pp. 183–192, 2012.

[29] O. G. Rodriguez and R. D. Hooton, "Influence of cracks on chloride ingress into concrete," *ACI Materials Journal*, vol. 100, no. 2, pp. 120–126, 2003.

[30] V. Picandet, A. Khelidj, and H. Bellegou, "Crack effects on gas and water permeability of concretes," *Cement and Concrete Research*, vol. 39, no. 6, pp. 537–547, 2009.

Hindawi
Advances in Materials Science and Engineering
Volume 2021, Article ID 5598576, 7 pages
https://doi.org/10.1155/2021/5598576

Research Article

Experimental Study on the Effect of Expansive Agent on the Durability of Concrete in Civil Air Defense Engineering

Junbo Zhang,[1] Jigang Zhang ,[1,2] Weiwei Xiao,[1] Qianying Wang,[3] and Feng Shao[4]

[1]*School of Civil Engineering, Qingdao University of Technology, Qingdao 266033, China*
[2]*Qingdao University of Technology, Cooperative Innovation Center of Engineering Construction and Safety in Shandong Blue Economic Zone, Qingdao 266033, China*
[3]*School of Architecture Engineering, Qingdao Agricultural University, Qingdao 266033, China*
[4]*College of Architecture and Urban Planning, Qingdao University of Technology, Qingdao 266033, China*

Correspondence should be addressed to Jigang Zhang; jigangzhang@126.com

Received 19 February 2021; Accepted 25 April 2021; Published 12 May 2021

Academic Editor: Peter Majewski

In this study, the effect of 8% UEA the reason why the UEA content is 8% is as follows: the expansion agent content in the actual mix proportion of the project is 8%, which is selected in this test to fit the reality better. expansion agent on the compressive strength, chloride ion penetration resistance, and carbonation resistance of civil air defense concrete were studied by simulating the rapid carbonation and chloride solution immersion of concrete structure in coastal civil air defense engineering environment. The results of this study show that the early compressive strength of concrete decreased by adding the UEA expansion agent and was also affected by the curing time. Moreover, the addition of UEA expansion agent decreased the content of free chloride ions and calcium carbonate in concrete and reduced the early compressive strength of concrete.

1. Introduction

In the construction of civil air defense projects in coastal cities, the reinforced concrete structures often face the steel corrosion caused by water leakage due to the high underground water pressure and groundwater infiltration. Therefore, the domestic civil air defense projects have strict requirements for the impermeability grade of concrete. Engineering leakage water generally comes from concrete structure cracks, mainly caused by the volume changes in concrete because of the temperature changes and chemical reactions. To reduce concrete cracks and improve the impermeability of engineering, various types of expansion agents have emerged with time.

The principle of the expander is to produce some expansion crystals by the hydration of expansion components to compensate for the volume shrinkage of concrete, and the expansion crystals will affect the internal structure of concrete.

Concrete expansion agent [1–3] can compensate the shrinkage of concrete and improve the compactness, impermeability, waterproof, and crack resistance of concrete. The studies on expansion agents mainly focused on the expansion rate, shrinkage compensation, and limiting conditions of expansion agents [4, 5]. For example, Huang et al. [6] applied HCSA expansion agent and domestic traditional U-type expanding agent (UEA) to ultra-high performance concrete (UHPC) paste without fiber and compared their shrinkage reduction effects; Park et al. [7] studied the effect of CSA expansive agent and metolatp 860 shrinkage reducer on the shrinkage of UHPC doped with steel fiber; Zheng et al. [8] studied the effect of sirenps100 and f17a on the shrinkage properties of UHPC without fiber; Wang et al. [9] investigated the characteristics of strength and expansion as well as coordination between strength and expansion of superplasticized middle-strength and high-strength concrete. Deng et al. [10] studied the effect of expansion agent and shrinkage reducing agent on the

autogenous shrinkage of UHPC. Chen et al. [11] studied improving crack-resistance property of cement-stabilized aggregate mixtures with expansion agent.

Zhao and Liu [12] studied the effect of additives and cement varieties on the expansion performance of HCSA expansion agents, and Tao [13] studied the effect of type of expansion agent, dosage, and curing conditions on the expansion rate. Besides, a few studies investigated the effect of expansion agents on concrete durability. Zhang et al. [14] studied the effect of microexpansive preservatives on the mechanical properties and durability of cement concrete.

In this study, the effect of UEA expansion agent on the compressive strength, free chloride ion content, and calcium carbonate content of civil air defense engineering concrete was studied by the actual concrete mix proportion.

2. Experimental

2.1. Preparation of Concrete. The cement selected in this test is Zhonglian P.O 42.5 ordinary Portland cement produced by Qingzhou Zhonglian cement company. The grade II fly ash is produced by Weifang Electric Power Plant. The S95 grade ore powder is produced by Qingdao Zhongkuang Hongyuan Industry and Trade Co., Ltd.; Qingdao river sand was used in the experiment after passing through a 5 mm sieve, with a fineness modulus of 2.6. The coarse aggregate is in the range 5–20 mm continuous graded crushed stone. The UEA expansion agent produced by Shanghai Sanjia Building Materials Technology Co., Ltd., was selected. Polycarboxylate superplasticizer was selected, and tap water was used for mixing.

Two concrete mix proportions are used in this test, as listed in Table 1.

2.2. Experimental Plan. To simulate the service environment of civil air defense engineering concrete in the real marine atmosphere environment, rapid carbonation and chloride solution immersion drying and wetting cycle (drying-wetting cycle) test were used in this experiment. The drying-wetting cycle system is shown in Table 2.

The nonstandard specimen with a cube size of 100 mm × 100 mm × 100 mm was used for measuring the concrete compressive strength test, and the compressive strength and load values of 100 mm cubes with the curing ages of 7, 28, and 56 days were measured. The final concrete cube compressive strength was obtained by multiplying the measured strength value by the conversion factor of 0.95.

In the wetting-drying cycle test of rapid carbonization and chloride salt immersion, the prism test block with a size of 100 mm × 100 mm × 400 mm and the length-width ratio of 4 was used, meeting the requirements of Standard for Test Methods of Long-Term Performance and Durability of Ordinary Concrete (GB/T 50082–2009). The carbonization test was carried out in a fast carbonization chamber. The parameters of the carbonization chamber were set as follows: CO_2 concentration, 20 ± 3%; relative humidity, 70 ± 5%; temperature, 20 ± 2°C.

The concrete test block was cured with formwork for 48 h and then put in a standard curing room for 28 days. After curing, the test block was taken out, and its two opposite rectangular sides were reserved, and the other sides were sealed with epoxy resin. The sealed concrete blocks were used in a ventilated place for 48 h and then soaked in a 3.5% (seawater concentration) chloride solution. After soaking for four days, the samples were taken out and kept in an oven for two days at a temperature of 50 ± 2°C. After drying, the samples were taken out. Then the samples were cooled to room temperature and kept in a carbonization oven for rapid carbonization. The carbonization process conforms to the corresponding cycle system degree. This series of steps serves as a cycle. Because one cycle test is momentary, the test data after six cycles was used in this study.

After the test block completed the specified cycle, the concrete mill was used to grind the test block from the surface of the solution. When the grinding range is within the first 10 mm and in the range of 10–20 mm, sample every 1 and 2 mm, respectively. When sampling, the ground powder was passed through a 0.63 mm sieve. The sieved powder was placed in an oven for 120 min, and the oven temperature was set at 105 °C ± 2°C. After drying, the samples were immediately placed in a drying oven.

2.3. The Method of Experiments

2.3.1. Compressive Strength. The compressive strength of concrete was measured using an electrohydraulic servo universal pressure testing machine in the Civil Engineering Materials Laboratory of Qingdao University of Technology, according to the Standard of Test Methods for Mechanical Properties of Ordinary Concrete (GB/T 50081–2002).

2.3.2. Free Chloride Concentration and Calcium Carbonate Content. The free chloride concentration was measured according to the Specification of Test Code for Concrete of Water Transport Engineering (JTJ270-98); the content of calcium carbonate was measured using a DRB-C1 precise concrete carbonation measuring instrument. The measuring principle was to convert the pressure of carbon dioxide gas generated by a chemical reaction between calcium carbonate and excess hydrochloric acid into the digital display using a pressure transmitter. The corresponding mass fraction of calcium carbonate in the concrete was obtained by the pressure value table.

3. Results and Discussion

3.1. Compressive Strength. To analyze the effect of UEA expansion agent on the compressive strength of concrete under standard curing conditions, the compressive strength tests of two types of concrete blocks under standard curing conditions of 7, 28, and 56 days were measured. The test results are listed in Table 3.

Table 1: Concrete mix proportion (kg/m^3).

Concrete number	Cement	Fly ash	Mineral powder	Stone	Sand	Expansive agent	Water reducer	Water
P	240	67	33	991	811	30	7.4	162
M	270	67	33	991	811	0	7.4	162

Table 2: Drying and wetting cycle system.

Circular system number	Experimental plan			
S1	Soaked in 3.5% NaCl for 4 days	Dry for 2 days	Carbonized for 3 days	Cycle 6 times
S2	Soaked in 3.5% NaCl for 4 days	Dry for 2 days	Carbonized for 5 days	Cycle 6 times
S3	Soaked in 3.5% NaCl for 4 days	Dry for 2 days	Carbonized for 0 days	Cycle 6 times

Table 3: Concrete cube compressive strength value.

Age	Specimen (MPa)	Specimen size (mm × mm × mm)	Peak load (kN)	Measured value of compressive strength (MPa)	Average compressive strength
M-7d	C30-1	100 × 100 × 100	247.75	23.5	24.6
	C30-2	100 × 100 × 100	281.53	26.7	
	C30-3	100 × 100 × 100	258.67	23.4	
P-7d	C30-1	100 × 100 × 100	228.42	21.7	21.1
	C30-2	100 × 100 × 100	217.89	20.7	
	C30-3	100 × 100 × 100	220.00	20.9	
M-28d	C30-4	100 × 100 × 100	414.75	39.4	40.1
	C30-5	100 × 100 × 100	408.07	38.8	
	C30-6	100 × 100 × 100	444.88	42.3	
P-28d	C30-4	100 × 100 × 100	417.89	39.7	38.6
	C30-5	100 × 100 × 100	394.74	37.5	
	C30-6	100 × 100 × 100	406.32	38.6	
M-56d	C30-7	100 × 100 × 100	454.85	43.2	45.3
	C30-8	100 × 100 × 100	465.81	44.3	
	C30-9	100 × 100 × 100	507.97	48.3	
P-56d	C30-1	100 × 100 × 100	467.37	44.4	44.6
	C30-2	100 × 100 × 100	491.58	46.7	
	C30-3	100 × 100 × 100	449.47	42.7	

The change curve of concrete compressive strength as shown in Figure 1 was obtained from the data listed in Table 3.

Figure 1 shows that the addition of an expansion agent has an obvious effect on the compressive strength of concrete at 7 days, 28 days, and 56 days under the same standard curing time. The test data show that, under different curing ages, the compressive strength of concrete with the expansion agent is less than that of concrete without the expansion agent, but with increasing curing time, the strength gap gradually narrowed down. In the test of compressive strength with the curing time of 7, 28, and 56 days, the compressive strength of concrete with an expansion agent is 85.7%, 96.26% and 98.45% of that of the reference concrete, respectively. For C30 low-grade concrete, the compressive strength of concrete decreases with the addition of expansion agent but is greatly affected by the curing age. At the age of 7 and 28 days, the compressive strength decreases by 14.23% and 3.7%, respectively; at the age of 56 days, the compressive strength is almost the same as that of the reference concrete.

The reason for this phenomenon may be attributed to the fact that the UEA expansion agent is a sulphoaluminate type expansion agent. In the process of concrete formation, the calcium hydroxide of the cement hydration product will react with some components in the expansion agent to form calcium sulphoaluminate hydrate (ettringite). Ettringite is a type of needle-like crystal, which will gradually grow and extend with the progress of the reaction, destroying the small pores and making it larger. The concrete blocks used in this experiment are only cured with mold for two days after forming and then demolded and standard cured for two days under standard conditions. Therefore, the growth of ettringite is not limited, and the concrete structure will become bulkier and bulkier, which will eventually decrease the concrete pressure resistance. However, this expansion

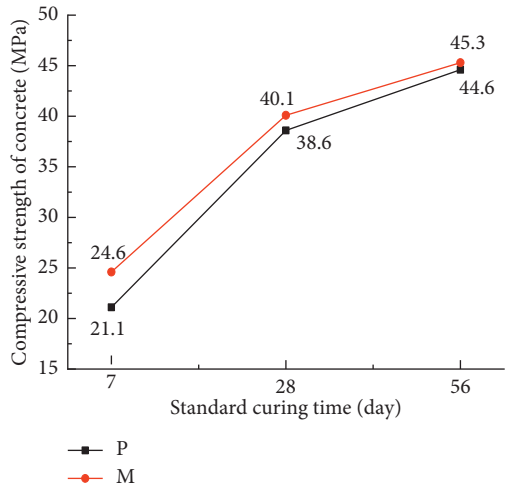

Figure 1: Curve of concrete compressive strength.

effect is more obvious in the early stage of strong growth, when the curing time is 28 days later. Therefore, the compressive strength after 56 days is the same as that of the reference concrete.

3.2. Free Chloride Concentration. This test does not consider the chloride ion in the concrete specimen due to external factors and test raw materials in the production process and takes the initial chloride ion content of the concrete specimen as 0. Figure 2 shows the distribution of free chloride ion content in the concrete specimens under the cyclic system of this experimental design.

Due to the short cycle time of a single cycle, this study analyzed the effect of UEA expansion agent on the content of free chloride ions in the concrete by using the test data of test blocks after six cycles.

Figures 2(a), 2(b), and 2(c) show that, under the condition of the same cycle system and the same cycle period, the distribution of chloride ions in the carbonated concrete can be divided into three stages: convection zone, diffusion zone, and stable zone. There are two peaks in the convection zone. The analysis indicates that the formation of the first peak content is because of the initial precipitation of concrete under a dry environment. The chloride ion in the solution gradually infiltrates into the concrete under the action of capillary adsorption, so the convection direction of chloride ion is from the outside to the inside. However, the formation of the second peak content is more complex. The dried concrete sample was further soaked in the chloride solution for the designated period and further dried in the oven at 60°C for 48 h. At this time, the concrete surface changes from the saturated state to the dry state. However, because of the presence of some liquid in the pores of the concrete, this part of pore liquid migrates outward due to the evaporation of the surface solution. The presence of postcondition will only affect the surface pore saturation of the concrete block and not the deeper pore saturation of concrete; therefore, the convection direction of chloride ions in the surface part is from the inside to the outside. In contrast, in the deeper part of the concrete, the chloride ions penetrating the surface of concrete diffuse to the interior of the concrete due to the concentration difference. Under both actions combined, the chloride ion content in the surface layer of concrete accumulates because of the convection effect, and the peak's value in the depth of the concrete also forms due to the diffusion effect. In contrast, there is a slight difference between the content of two peaks, because at this peak content, the concrete is in a saturated state, and the pore structure at different depths of the concrete is slightly different. However, there is a certain position between the two peaks of chloride ion content. At this position, some chloride ions diffuse from the inside to the outside and some from the outside to the inside, reducing the chloride ion content around this position and thus forming a low content. According to the analysis of Figures 2(a), 2(b), and 2(c), the depth of the convection zone in the concrete is approximately 6–11 mm, which is slightly lower than the average reported depth of 10 mm. The analysis indicates that the test period is too short and chloride ion penetration is limited; therefore, the depth of convection zone formed in this time is short.

The distribution curve of free chloride ion content in concrete with an expansion agent is similar to that in the control group, and the chloride ion distribution has three stages. However, the content of free chloride ion in the concrete mixed with the expansion agent is lower than that in the control group, probably because the curing of the concrete block for the drying–wetting cycle test was completed after 28 days. At this time, the effect of the expansion agent was saturated, and the crystalline expansion products filled the pores of the concrete, increasing the internal

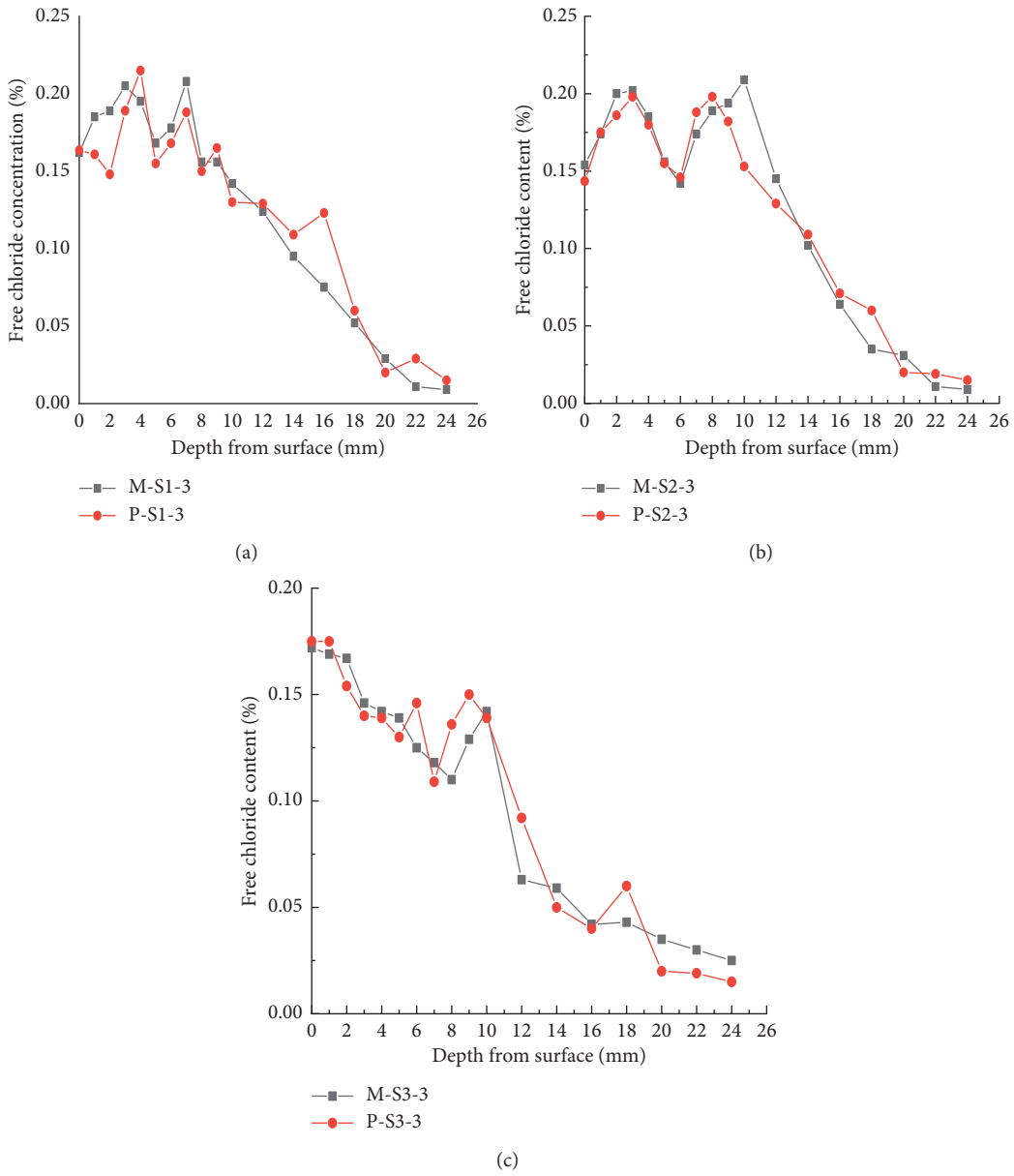

Figure 2: Distribution of free chloride ion content in concrete with different mix proportions and different systems. (a) Free chloride content diagram under S1 system. (b) Free chloride content diagram under S2 system. (c) Free chloride content diagram under S3 system.

compactness of the concrete and making it difficult for the chloride ions to recover from the inner penetration, which in turn decreases the free chloride ion content in the concrete and improves the anti-chloride ion penetration ability of concrete.

3.3. Calcium Carbonate Content of Concrete. The method of measuring the carbonation depth of concrete blocks by phenolphthalein reagent method is simple and easy to operate, but the measurement results are discrete and only roughly reflect the carbonation degree with poor accuracy. Therefore, according to the principle of carbon dioxide and calcium hydroxide reaction to form calcium carbonate precipitate, this test reflects the internal carbonation of concrete by measuring the content of calcium carbonate at each depth of concrete. The disadvantage of this method is that the ground powder samples of concrete test block must be taken and reacted with hydrochloric acid using specific instruments for measurement. This operation is more complex, but the accuracy is higher and thus this procedure truly reflects the carbonation degree of concrete. The distribution of calcium carbonate content in concrete with different cycle systems is shown in Figure 3.

In Figures 3(a) and 3(b) are the distributions of calcium carbonate content of two different mix proportion concrete under the S1 and S2 systems after six cycles, indicating that the distribution trend of calcium carbonate content in concrete mixed with the expansion agent under the same system is roughly the same as that in the ordinary

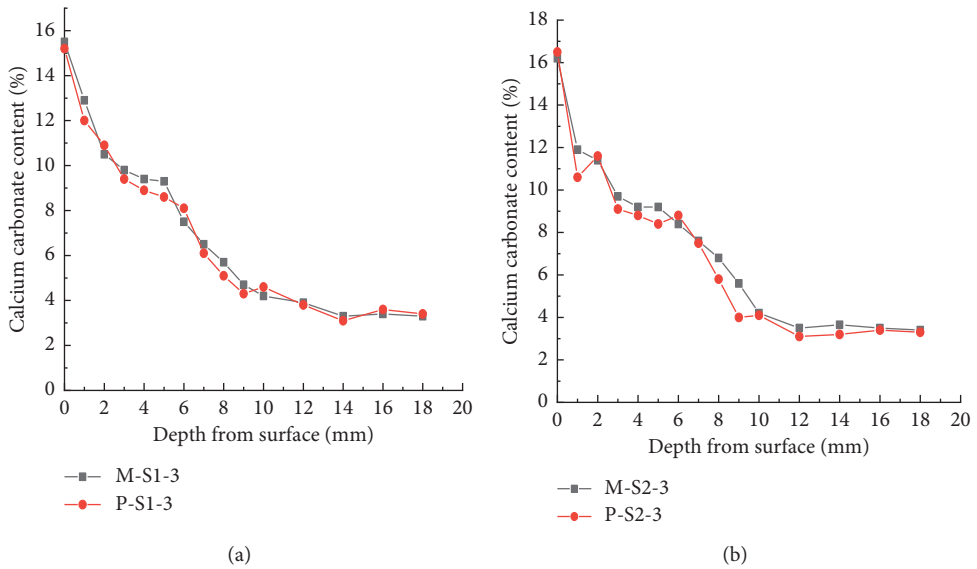

Figure 3: Distribution diagram of calcium carbonate content in different mix proportion. (a) Figure of calcium carbonate content in S1 system. (b) Figure of calcium carbonate content in S2 system.

concrete. There are four stages of concrete formation and drying: surface laitance zone, complete carbonation zone, partial carbonation zone, and noncarbonation zone. However, in the laitance zone, the calcium carbonate content of the concrete with an internal expansion agent is not different from that of the ordinary concrete, but the length of the complete carbonation zone of concrete with an internal expansion agent is less than that of the ordinary concrete. At the same depth of the partial carbonation zone, the calcium carbonate content of concrete with an internal expansion agent is lower than that of the ordinary concrete, and it enters a stable stage earlier. The reason may be that the carbonation of concrete is mainly affected by two aspects: the diffusion rate of carbon dioxide and the carbonate substances in the concrete. The diffusion rate of carbon dioxide is not only related to the external concentration, but also to the internal compactness of concrete. When the expansion agent is mixed in the concrete, the sulphoaluminate expansion agent will react with calcium hydroxide, the hydration product of early cement, to form ettringite (swelling source). This process consumes calcium hydroxide and reduces the carbonizable substances in the concrete, thus accelerating the carbonation of concrete. However, ettringite, which comates the expansion effect, will fill in the coarse pores in the concrete and will greatly improve the internal structure of the concrete and increase the density of concrete. With increasing density of concrete, the diffusion rate of carbon dioxide in the concrete decreases; therefore, the carbonation resistance of concrete depends on the leading factor. Zhao et al. [15] confirmed that, using the same amount of expansion agent as in this study, the expansion agent is the main factor leading to the change in the internal structure of concrete, thus improving the anticarbonation ability of concrete.

4. Conclusion

The effect of UEA expansion agent on the compressive strength, chloride ion penetration resistance, and carbonation resistance of civil air defense engineering concrete was studied by simulating the real service environment of civil air defense engineering in coastal cities by the method of rapid carbonation, chloride salt immersion drying, and wetting cycles. The experimental data of this study lead to the following conclusions:

(1) For low-grade concrete such as C30, under the condition of no mold limit, 8% UEA expansion agent reduced the early compressive strength of concrete, and the compressive strength at 7-day curing age is 14.23% lower than that of the control group, but with increasing curing time, the reduction range is small and is the same as that of the reference concrete at 56 days.

(2) When the curing age reaches 28 days, the trend of free chloride ion content and calcium carbonate content in the concrete with an expansion agent is the same as that in the control group, but the internal content decreases.

(3) At 8% UAE content expansion agent, the concrete strength decreases, but it meets the strength grade requirements and effectively improves the chloride ion penetration resistance and carbonation resistance of the concrete structure. Therefore, the expansion agent with 8% UAE content has a wide application prospect for civil air defense engineering.

Data Availability

The data used to support the findings of this study have been deposited in the [figure] repository. Previously reported

[PDF] data were used to support this study and are available at [reference file]. These prior studies (and datasets) are cited at relevant places within the text as references [2–5]. The data used to support the findings of this study are included within the article.

Conflicts of Interest

The authors declare that they have no conflicts of interest.

References

[1] C. Chen and D. Wang, "Experimental study on the shear performance of self-compacting concrete beam," *Sichuan Building Science*, vol. 46, no. 2, pp. 50–56, 2020.

[2] P. Yan, H. Lian, and Q. Xiao, "Several issues in the manufacture of shrinkage_compensating concrete us-ing expansive agent," *Journal of the Chinese Ceramic Society*, vol. 28, no. Supplement, pp. 42–45, 2000.

[3] J. Liu, Q. Tian, and M. Tang, "Influence of expansion agent and shrinkage reducing agent on shrinkage cracking of high performance concrete," *Journal of Southeast University (NATURAL SCIENCE EDITION)*, vol. 36, no. Sup(II), pp. 195–199, 2006.

[4] Z. Wu, *Zhang Hongzhi. Expansive Concrete*, China Machine Press, Beijing, 2004.

[5] Li Fei and W. Qin, "Experimental study on the effect of HCSA expansive agent in high content fly ash concrete[J]," *Expansive Agent and Expansive Concrete*, vol. 19, no. 2, pp. 6–8, 2009.

[6] Z. Huang, Y. Liu, and C. Li, "Performance research of Ultra high performance concrete incorporating HCSA expansion agent," *Materials Guide*, vol. 29, no. 4, pp. 116–121, 2015.

[7] J.-J. Park, D.-Y. Yoo, S.-W. Kim, and Y.-S. Yoon, "Benefits of using expansive and shrinkage-reducing agents in UHPC for volume stability," *Magazine of Concrete Research*, vol. 66, no. 14, 2014.

[8] X. Zheng, N. Guocai, and H. Zhang, "Research on influence of shrinkage-reducing agentand expansive agent for shrinkage performance of UHPC," *Concrete*, vol. 9, no. 9, pp. 76–79, 2017.

[9] D. Wang, H. Chen, and S. Ouyang, "Investigation on mechanical property and expansion behavior of high strength superplasticized expansive concrete," *Journal of The Chinese Ceramic Society*, vol. 32, no. 4, pp. 454–459, 2004.

[10] Z. Deng, Y. Lian, and L. Zhao, "Influence of expansion agent and shrinkage reducing agent on autogenous shrinkage of UHPC," *Journal of Beijing University of Technology*, vol. 47, no. 1, pp. 61–69, 2021.

[11] D. Chen, "Study on crack-resistance property of cement-stabilized aggregate mixtures with expansion agent," *Heb Jiaotong ence and Technology*, 2005.

[12] S. Zhao and Li Liu, "Study on Adaptability of HCSA expansive agent with chemical admixture and cement," in *Proceedings of the 4th National Symposium on Concrete Expansive Agents*, no. 2, pp. 1–5, China Silicate Society, Shenzhen, China, 2006.

[13] X. Tao, "Factors influencing the expansion rate of cement-based cementitious materials with expansion agent," *Fujian Jianshe Science and Technology*, vol. 5, no. 5, pp. 39–41+48, 2009.

[14] X. Zhang, Y. Liu, X. Li, W. Wu, and H. Yang, "Effect of micro-expansion preservatives on the durability of cement concrete," *New Building Materials*, vol. 47, no. 12, pp. 15–18+34, 2020.

[15] S. Zhao and L. Liu, "Effect of expansive agent on carbonation of concrete with fly ash and its mechanism," in *Proceedings of the 4th National Symposium on Concrete Expansive Agents*, no. 2, pp. 17–22, Hangzhou, China, 2008.

Hindawi
Advances in Materials Science and Engineering
Volume 2021, Article ID 5542072, 9 pages
https://doi.org/10.1155/2021/5542072

Review Article

Expansion Mechanism and Properties of Magnesium Oxide Expansive Hydraulic Cement for Engineering Applications

Siqi Li, Yecheng Feng, and Jinbo Yang

School of Civil Engineering, College of Water Conservancy and Civil Engineering, Shandong Agricultural University, Taian 271018, Shandong, China

Correspondence should be addressed to Jinbo Yang; yangjinbo@tsinghua.org.cn

Received 4 February 2021; Revised 5 April 2021; Accepted 26 April 2021; Published 5 May 2021

Academic Editor: Robert Cerny

The expansion mechanism of magnesium oxide expansive hydraulic cement as a novel expansive hydraulic cement was reviewed. Anisotropic crystallization results in crystal growth pressure, causing volume expansion while also increasing the porosity of the whole system. The theoretical relationship between porosity and expansion was analyzed. A basic method is given for predicting the expansion rate considering the expansive agent content in MgO expansive hydraulic cement. A concise equation is proposed for calculating the ultimate expansion. A theoretical relationship between porosity and expansion is presented. The compressive strength and durability of magnesium oxide expansive hydraulic cement were analyzed considering porosity changes and compared with hydraulic cement. If the expansion rate exceeds 0.8%, the mechanical properties and durability changes caused by porosity should be considered. If magnesium oxide expansive concrete is used with restraining in real structure, extra compressive stress is generated and the porosity decreases, compared with that during free expansion. In particular, for strain-hardening cementitious composites, expansion confined with the fibers present in the composite is beneficial for refining cracks and improving the self-healing ability of these materials whenever exposed to humid environments. This paper describes the expansion mechanism and properties of magnesium oxide expansive hydraulic cement for engineering applications.

1. Introduction

The elimination of cracks in hydraulic cement concrete structures is a global issue; eliminating cracks is necessary for improving the durability of these structures and saving maintenance and repair costs. Hydraulic cement commonly refers to Portland cement and slag cement; it has an extremely wide range of applications throughout the world and is expected to be used extensively in future as well. This cement sets and hardens via chemical reactions with water and is capable of doing so underwater. Concrete containing hydraulic cement has a minor underwater volume expansion. However, when exposed to atmospheric conditions and restrained internally or externally, it always produces cracks caused by thermal contraction or drying shrinkage; these cracks might cause problems in terms of the structural stability and durability at different levels [1]. Thermal contraction and drying shrinkage resulting from hydration and water evaporation (or consuming) are hardly eliminated as concrete contains water.

To maintain the volume stability of concrete or reduce drying shrinkage (or thermal contraction), expansive hydraulic cement containing expansive agents or an expansive component was studied and utilized over the past half-century; in particular, shrinkage-compensating concrete is used worldwide [2–10]. The three common expansive portions in expansive hydraulic cement are based on calcium sulfoaluminate ($4CaO{\cdot}3Al_2O_3{\cdot}SO_3$), calcium oxide (CaO), and magnesium oxide (MgO). Calcium sulfoaluminate expansive hydraulic cement has been studied since many years [3, 11–14]. Yan et al. [15, 16] found that the shrinkage-compensating effect of calcium sulfoaluminate when used in massive concrete structures cannot be completely utilized when the curing temperature is higher than 70°C because of the decomposition of ettringite, which is the main hydration product of calcium sulfoaluminate expansive agents.

Compared with CaO expansive agents, MgO expansive agents have a significant advantage owing to their designable expansion properties [17] because the hydration rate of MgO is relatively easier to control by controlling different calcination conditions during the manufacturing process. Since the 1970s, MgO is being used as an expansive agent to compensate for the thermal contraction of mass concrete, particularly in dam concrete used in China; it is extensively used both in research activities and industrial applications [17–19]. Moreover, expansive agents are mineral admixture used for enhancing the performance for self-healing concrete mainly because of their expansion effect [20]. Furthermore, it was proved that the utilization of appropriate dosages of MgO expansive agents has high potential as a new self-healing method for cracked concrete [21–23]. Moradpour et al. [24] found that adding nano-MgO increased the mechanical strength of cement composites during aging to a certain extent and decreased the permeability of these materials. This is because the microstructures of the cement composites with nano-MgO were more compact and homogeneous than those of normal composites because of expansive effect of nano-MgO.

Therefore, the expansion mechanism and dynamics of MgO expansive hydraulic cement should be understood thoroughly to determine the optimal dosages of MgO for use during actual construction and avoid overdose to avoid damages to concrete structures. The mechanism for the expansion of dead-burnt MgO and CaO was first studied by Chatterji based on the crystal growth pressure, solubility of hydroxide crystals, their growth patterns, and diffusion of ions through the electrical double layer formed around the cement hydration products [25, 26]. According to the above mechanism, Mo et al. built an image model of an MgO expansive agent considering the inner pore structure of the expansive agent but could not simulate the expansive process and expansion mechanism in MgO expansive agent concrete [17, 27]. The expansive process and expansion mechanism need to be stated clearly to identify the main design parameters for shrinkage-compensating concrete, which are mainly dependent on the type and content of the expansive agent, the hydraulic cement matrix, and environmental conditions of real concrete structures [28, 29]. Likewise, the relationship between expansion and mechanical properties and durability should be studied.

This article discusses not only the crystallization pressure theory for explaining the expansion mechanism of MgO expansive hydraulic cement but also a basic method for predicting the expansion rate considering the expansive agent content in MgO expansive hydraulic cement. A concise equation is proposed for calculating the ultimate expansion. Autoclave tests are discussed for determining the ultimate expansion. A theoretical relationship between porosity and expansion is presented. Based on this, the connection between expansion, mechanical properties, and durability is discussed. Further studies on concrete under restrained conditions and empirical research will follow.

2. MgO Expansive Agent

MgO expansive hydraulic cement is a mixture of hydraulic cement and MgO expansive agent, which is responsible for expansion. Mixing of the hydraulic cement and MgO expansive agent could be carried out during cement manufacture or during concrete mixing. As the MgO expansive agent is very sensitive to calcination conditions, particularly the calcining temperature, precisely controlling the temperature and residence time and homogeneously heating the magnesite are extremely important for maintaining the quality of MgO expansive agent [17]. For manufacturing MgO expansive hydraulic cement or shrinkage-compensating concrete, MgO expansive agent must be manufactured separately, complying with standards. The first and latest standard for MgO expansive agent for use in concrete was issued by the China Building Materials Federation and China Concrete and Cement-Based Products Association in 2017 [30]. According to this standard, the product shall conform to the chemical and physical requirements prescribed in Table 1.

3. Expansion

3.1. Mechanism of Expansion. Hydration products of MgO expansive cement include hydration products of hydraulic cement and magnesium hydroxide ($Mg(OH)_2$) because the hydration reactions of hydraulic cement and MgO expansive agent are relatively independent. Hydration of MgO proceeds according to the following equation, and the volume change is calculated as follows:

$$\begin{array}{ccccc} \mathrm{MgO} & + & \mathrm{H_2O} & = & \mathrm{Mg(OH)_2}, \\ 40.3\,\mathrm{g} & & 18.0\,\mathrm{g} & & 58.3\,\mathrm{g} \\ 11.2\,\mathrm{cm^3} & & 18.0\,\mathrm{cm^3} & & 25.3\,\mathrm{cm^3}. \end{array} \quad (1)$$

The specific gravity values of MgO and $Mg(OH)_2$ used in the calculation are 3.6 and 2.3. It was found that the system as a whole undergoes a net volume contraction of approximately 13%, and the solid volume increases by approximately 126%. After mixing with water and cement, MgO particles having micrometer diameters will contact with water and be covered with a water film. When in contact with water, MgO dissolves in water first. Dissolution of MgO will increase the concentration of magnesium ions in the water film, and $Mg(OH)_2$ crystals will grow when supersaturation is reached. Neglecting the dissolution of $Mg(OH)_2$, which has a solubility of approximately 0.00064 g/100 mL (25°C) in water, all MgO that undergoes hydration to form $Mg(OH)_2$ needs a water–MgO mass ratio more than 0.45 according to equation (1). Crystallization of $Mg(OH)_2$ may occur randomly on the surfaces of MgO particles, cement particles, or the cement hydration gel. The crystal size of $Mg(OH)_2$ will be in the nanometer range initially and then increases to micrometer levels [6]. If an $Mg(OH)_2$ crystal is confined, the volume increases or crystallization pressure will cause expansion of the hardened cement paste. Steiger [31, 32] provided the following thermodynamically consistent equation for the calculation of the pressure generated during crystal growth in porous materials:

$$\Delta p_i = \frac{\mathrm{RT}}{V_m} \ln \frac{a}{a_\infty} - \gamma_{cl,i} \frac{\mathrm{d}A_i}{\mathrm{d}V}, \quad (2)$$

Table 1: Chemical and physical requirements for MgO expansive agent [30].

Items			Requirements		
			R (rapid type)	*M* (medium type)	*S* (slow type)
MgO mass content (%)		≥		80.0	
Loss on ignition (%)		≤		4.0	
Water content (%)		≤		0.3	
Reaction time ∗ (s)			<100	≥100 and <200	≥200 and <300
Fineness	80 μm square hole sieve residue (%)	≤		5.0	
	1.18 mm square hole sieve residue (%)	≤		0.5	

Reaction time ∗ is the time required for completing the neutralization reaction between magnesium oxide expansive agent and citric acid solution with definitive concentration

where Δp_i is the crystal growth pressure at crystal face i, R is the gas constant, T is the absolute temperature, V_m is the mole volume of magnesium hydroxide, a is the equilibrium activity of the crystal under pressure Δp_i, a_∞ is the equilibrium activity of the large reference crystal under ambient pressure, $\gamma_{cl,i}$ is the surface-free energy of the crystal-liquid interface at the ith crystal face, and dA_i and dV are the area of the surface created and the volume transformed during growth at the ith crystal face, respectively. In the limiting case of a very large crystal size greater than approximately 0.1–1 μm, the interfacial energy term vanishes.

Equation (2) indicates that the crystal growth pressure is the main reason for expansion. Crystallization will occur randomly where the solution is supersaturated; later, as crystal volume increases, the crystal growth pressure increases. According to Steiger's explanation [31, 32], a solution film must exist, separating the loaded face of a crystal from its constraint; growth on the loaded face of a crystal can only exert pressure if this face is in contact with a supersaturated solution. The crystal growth pressure theory is effectively utilized to understand the mechanism of expansion, but it is difficult to connect microcosmic crystal properties with macroscopic hardened cement paste or concrete properties directly. Moreover, estimating the degree of supersaturation in pore solutions is apparently unrealistic for calculating crystallization pressures.

Based on crystallization pressure theory, there are three main stages in the hydration of MgO. In the first stage, crystallization occurs when the cement paste or concrete is plastic; in the next stage, crystallization occurs without restraining because the crystal dimensions are relatively small. The above two stages will not cause expansion of the cement system. In the third stage, while the cement paste or concrete is hardened and $Mg(OH)_2$ crystals are restrained, crystallization pressure is caused, leading to expansion.

3.2. Dynamics of Expansion. The hydration dynamics of MgO in a hydraulic cement system is highly complicated because it is combined with the hydration of cement and influenced by environmental factors such as the pore solution, temperature, and humidity and strongly depends on the concentration of surface defects on MgO crystals [17, 33, 34]. Different types of MgO, which are calcined at different temperatures, will show different hydration performances with various hydration reactivities. MgO with high reactivity commonly calcined at approximately 600°C undergoes hydration rapidly and thus causes fast expansion at an early age, and the expansion then ceases within a short time approximately 14 d [17]. According to the experiments of Kasselouris et al. [35], the hydration of periclase, or dead-burned MgO, commonly calcined at approximately 1450°C with very low reactivity in cement pastes reached a limited value of 73.4% at a water curing age of about six years. As the pozzolanic activity of the materials with good pozzolanic activity is increased, the hydration of MgO is reduced. Majumdar and Rehsi [36] stated that the precise mechanism through which the addition of pulverized fly ash or other similar active silica materials reduces the autoclave expansion of Portland cements containing large percentages of MgO to permissible levels remains unclear. If the hydration environment of MgO is stable, the expansion should be a continuous process through which expansion will infinitely approach the maximum value assuming that hydration of MgO will finally reach 100%. Yuan [37] proposed a hyperbolic model for simulating the expansion process for MgO-based expansive hydraulic cement concrete, as shown in the following equation:

$$\varepsilon_t = \frac{t}{\alpha + (1/\varepsilon_{\max})t}, \tag{3}$$

where ε_t is the expansion at time t, t is the time, $\varepsilon_{\max}$ is the ultimate expansion, and α is a factor controlled by the expansive agent type, hydraulic cement matrix, and environment conditions.

In real concrete structures, hydration of reactive magnesium oxide is an infinite process like the hydration of cement. If the ultimate expansion could be determined, expansion of MgO expansive hydraulic cement concrete can be approximately calculated at any time using equation (3).

3.3. Ultimate Expansion. Expansion of MgO expansive hydraulic cement is driven by two forces, namely, the crystallization pressure caused by supersaturation and crystallization amount, which are both relative to the expansion agent content according to the above analysis. A possible equation for calculating expansion rate is as follows:

$$\varepsilon_{\max} = \beta C^2, \tag{4}$$

where $\varepsilon_{\max}$ is the ultimate expansion (%), β is a factor controlled by the expansive agent type and category, hydraulic cement matrix, and environment conditions, and C is the expansion agent content in terms of mass (%).

Hydration of the MgO expansive agent will be triggered when it is mixed with water. During the plastic stage of fresh concrete, crystallization will not cause pressure without confinement. This is the reason that CaO expansive agents have the disadvantages of an extremely fast reaction rate when mixed with water and lower storage stability when exposed to the atmosphere; this reduces its expansion efficiency in shrinkage-compensating concrete [38]. Generally, the ultimate expansion will increase with the increase in expansion agent content. When the ultimate expansion exceeds a particular value or the expansive agent content increases to some value, the whole gel system will disintegrate and lose strength.

3.4. Determining Ultimate Expansion. Hydration of MgO is a long-term reaction like the hydration of hydraulic cement, making it generally impossible to measure the ultimate expansion. To accelerate the hydration process, extra pressure and high temperature should be applied. Till date, for testing the soundness of hydraulic cement, the autoclave expansion test (216°C, 2 MPa, and 3 h) is used to determine the potential delayed expansion caused by the hydration of CaO or MgO, or both, when present in hydraulic cement [39, 40]. Owing to potential safety hazards and the fact that not all testing laboratories have access to testing equipment, Michelle [41] found that a very good correlation exists between the standard ASTM C151 autoclave results and both the 3-h boiling and 80°C (176°F) water-curing expansion values. However, small expansion values would introduce difficulties in terms of the precision and accuracy of the method and the inherent variability of multiple prisms produced using the same mixture. Although Mo et al. [42] concluded that a curing temperature of 80°C (176°F) was much lower than 216°C (420.8°F), less internal thermal stress may be induced in concrete and no serious destruction of the cement hydration products will be caused; therefore, the test results obtained from this accelerated experiment may be more reliable. Nevertheless, the autoclave expansion test is still the most suitable test for determining the ultimate expansion of MgO expansive hydraulic cement or concrete according to the experimental results of Gao et al. [43]. According to autoclave test results for cement pastes obtained by Michelle [41] and those for concrete obtained by Gao et al. [43], equation (4) is applied to obtain the relationship between expansion and MgO content, and the fitted curves are shown in Figure 1 with R-square values of 0.99 and 0.94, respectively. In fact, even in the autoclave test, the hydration reaction will not reach 100% completion. Assuming that the ultimate expansion determined via autoclave tests is close to that under real situations, equation (4) is acceptable for calculating the ultimate expansion rate while factor β is confirmed.

Equation	$y = A^*X^2$		
Adj. R-square	0.98816	0.94183	
		Value	Standard error
Paste	A	0.50742	0.02316
Concrete	A	0.03342	0.00453

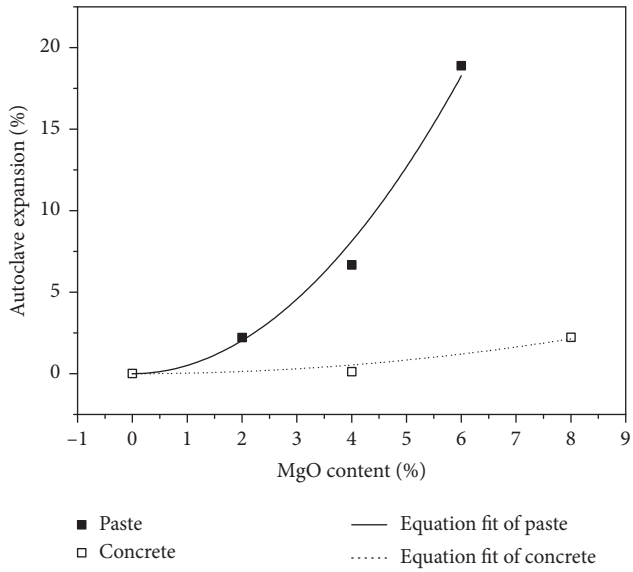

Figure 1: Relationship between autoclave expansion and reactive magnesium oxide content.

4. Properties

4.1. Expansion and Porosity. During the process of MgO hydration, there are three main stages that may occur at the same time but be dominant at different times. In the first two stages, reactive MgO particles dissolve and leave pores in the whole system, and then minor $Mg(OH)_2$ crystal grows freely to fill these pores without generating crystal growth pressure. The third stage is dominated by confined crystallization, and expansion is mainly caused by microcracks induced by the crystal growth pressure in the whole system. This stage will increase the pore volume. This assumption that there is an increase in porosity causes the volume of the entire system to increase, as shown in the following equation:

$$V_0 p_0 + V_0 (1+\varepsilon)^3 - V_0 = V_0 (1+\varepsilon)^3 p_e, \tag{5}$$

where V_0 is the volume of the system before expansion, p_0 is the original porosity of the system before expansion, p_e is the porosity after expansion, and ε is the expansion rate after expansion. Porosity p_e in equation (5) is determined as follows:

$$p_e = 1 - \frac{1 - p_0}{(1+\varepsilon)^3}. \tag{6}$$

This equation indicates that expansion will increase the number of pores in the system. According to ASTM C151, the expansion rate limit for maintaining the soundness of

cement is at 0.8%. Assuming that the original porosity is 10%, after expansion with at a rate of 0.8%, the porosity is 12.12%, as calculated using equation (6). The porosity increase rate after expansion at a rate of 0.8% is 21.2%. If the expansion rate exceeds 0.8%, the mechanical properties and durability changes caused by porosity should be considered. The relationships between porosity and expansion rate with different original porosities are shown in Figure 2.

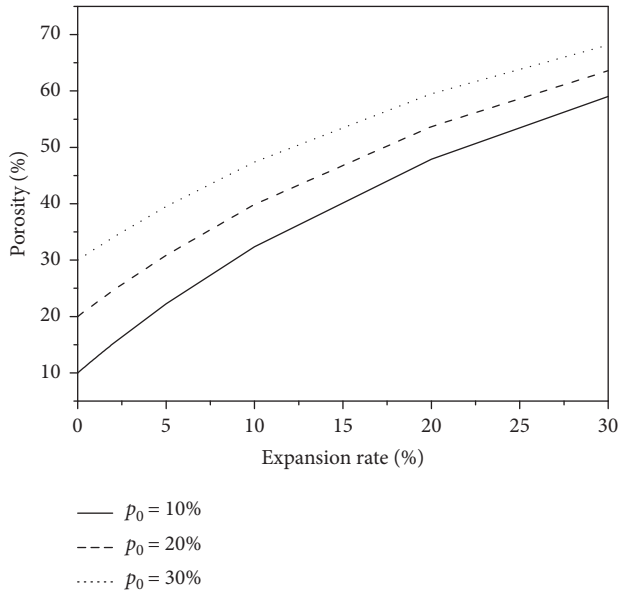

Figure 2: Relationships between porosity and expansion rate with different original porosities.

4.2. Expansion and Compressive Strength. The fact that a reduction in the porosity of a solid material increases its strength in general and the strength of cement-based materials in particular was recognized long ago [44, 45]. As expansion increases porosity, it should have a role in determining the relationship between the mechanical properties of concrete. Chen et al. [44] evaluated the porosity-strength relationship of cement mortar using the following equation:

$$\sigma = \sigma_0 \left[\left(\frac{p_c - p}{p_c} \right)^{1.85} \left(1 - p^{2/3} \right) \right]^{1/2}, \tag{7}$$

where σ is the compressive strength, σ_0 is the compressive strength at zero porosity, p_c is the percolation porosity at the failure threshold, and p is the porosity of the system. The application of the theoretical equation to experimental data yields constants σ_0 equal to 69.4 and p_c equal to 56.2% for cement mortar.

While the porosity is 56.2%, the cement matrix disintegrates as shown in Figure 3 and the expansion rate calculated using equation (6) is 21%, assuming the original porosity to be 25% (the mortar compressive strength is 30 MPa with a porosity of 25% calculated using equation (7)). It is close to the autoclave results obtained in another study [41]; when the expansion rate exceeded 18.89%, the specimen was crushed. By combining equations (6) and (7), the compressive strength of mortar after expansion, σ_e , is given as in the following equation:

$$\sigma_e = \sigma_0 \left[\left(\frac{p_c - \left(1 - \left((1 - p_0)/(1 + \varepsilon)^3 \right) \right)}{p_c} \right)^{1.85} \left(1 - \left(1 - \frac{1 - p_0}{(1 + \varepsilon)^3} \right)^{2/3} \right) \right]^{1/2}. \tag{8}$$

Equation (8) shows the relationship between the expansion rate and compressive strength after expansion. An increasing expansion rate will decrease the compressive strength of hydraulic cement systems. This equation does not consider the hydration of cement, which will continue for a long time and will refine the pore structure, decrease the porosity, and then increase the compressive strength on some levels.

4.3. Expansion and Durability. From the viewpoint of the three stages of MgO hydration discussed above, hydration of MgO makes the pore structure partially dense or increases the tortuosity of pores, which will improve durability; further, if high expansion occurs, high porosity will reduce durability. Choi et al. investigated the durability properties, including carbonation, freezing-thawing, chloride penetration, and sulfate resistance, of fly ash concrete containing 5% MgO by mass of binders as an expansive agent [46]. Experimental results indicated that the compressive strength and durability characteristics of concrete during long-term aging were slightly improved. Gao et al. [47] observed that during the freezing-thawing test performed using the procedure given in ASTM C666, when the content of MgO expansive agent was increased from 0% to 4% and 8%, the strength and mass losses of roller-compacted concrete decreased. When the content of MgO expansive agent increased from 8% to 12%, the strength and mass losses of roller-compacted concrete increased. While the MgO content is relatively low, less than 5% by mass of binders, most hydration products from the reactive MgO act as fillers for the concrete pores and increase the tortuosity of pores. Gao et al. [48] also found that fly ash may inhibit the autogenous volume expansion of concrete with MgO expansive agent, and the effect became more significant on increasing the fly ash content. They concluded that microexpansion caused by MgO closed the pores of the concrete paste and made the structure denser; this might compensate for the shrinkage of concrete, decrease cracking in concrete works, and improve the durability of concrete. Gonçalves et al. found an overall

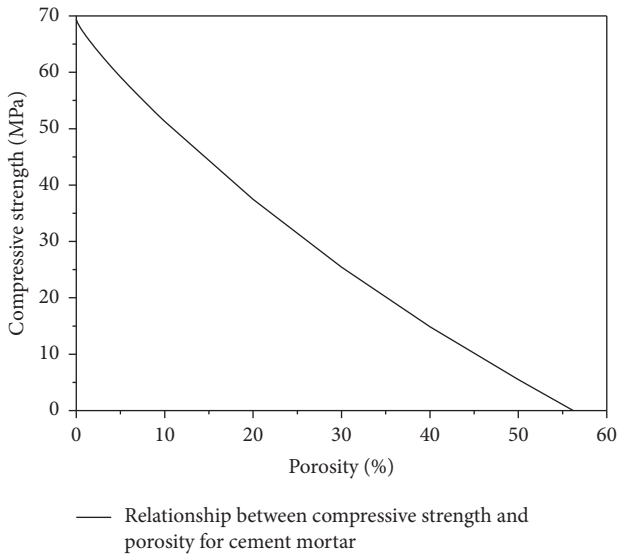

Figure 3: Relationship between compressive strength and porosity for cement mortar.

decline in mechanical and durability-related performance with the use of both MgO and fine recycled concrete aggregates but enhanced shrinkage behaviour was observed in all MgO-containing specimens [49]. Runxiao Zhang and Daman K. Panesar found that reactive magnesium oxide as a replacement of Portland cement not only brings potential to reduce the embodied carbon in construction materials but also brings uncertainties in the volumetric stability of carbonated MgO-Portland cement systems during carbonation curing and sulfate exposure [50].

For shrinkage-compensating concrete or expansive concrete, more expansion is needed to compensate for shrinkage or contraction and the MgO content should be higher than 5%. However, it appears that the suitable dosage of MgO for improving durability is less than 5%. Further experiments are required to confirm this, and more experiments are needed to study the durability performance of MgO expansive concrete under combined loadings [51–58].

5. Expansion via Restraining

In real concrete structures, expansion of concrete material is always restrained by reinforcements in concrete. On the one hand, a restraining will reduce expansion and decrease porosity when compared with free expansion. Hu and Li [59] studied high-performance expansive fly ash concrete (with an alunite- and gypsum-based expansive agent) and found that confined curing could improve the microstructure of expansive concrete, particularly by intensifying and densifying the paste-aggregate interface. On the other hand, constraining will cause stress, commonly called compressive stress, in concrete materials during the service life of the concrete structure. Wittmman et al. [60] found that application of a moderate compressive stress, a stress up to 35% of the ultimate stress, decreases the diffusion coefficient of chloride ions in concrete. In summary, expansion under restraining is expected to compact the pore space and close micropores. Likewise, considering the physical process of moisture transport in cement-based materials, which has a direct influence on both service life and durability [61, 62], expansion under constraint retards moisture transportation. Furthermore, for strain-hardening cementitious composite (SHCC) materials, having high strain capacity and resistance against steel rebar corrosion [63, 64], fibers will cause an internal constraint similar to that caused by adding reinforcements. Zhang et al. found that MgO expansive agents can significantly improve the crack healing efficiency of SHCC under water fog curing conditions [65]. With the designable expansion of MgO expansive agent, improving the self-healing ability of SHCCs using MgO expansive hydraulic cement is possible [66]. It is predicted that regulating expansion of cementitious materials with MgO expansive agent combined with fibers is a novel and promising approach to improve the self-healing ability and durability of SHCCs. In summary, if expansive concrete is restrained, extra compressive stress will be generated and porosity will decrease compared with that during free expansion. Obviously, suitable dosages of MgO should be determined for use in expansive concrete [67–72].

6. Conclusions

(1) Based on the crystallization pressure theory, there are at least three main stages in the hydration of MgO. In the first stage, crystallization occurs when the cement paste or concrete is plastic; in the following stage, crystallization occurs without restraining because the crystal dimensions are relatively small. The above two stages will not cause expansion of the cement system. In the third stage, the cement paste or concrete hardens and crystals are restrained, producing crystallization pressure and thus leading to expansion.

(2) In real concrete structures, hydration of MgO is an infinite process like the hydration of cement. If the ultimate expansion could be determined, the expansion of MgO expansive concrete can be predicted approximately at any time using equation (3). Generally, the ultimate expansion rate will increase with the increase in the content of the expansion agent. When the ultimate expansion exceeds some value or the expansion content increases to some value, the whole gel system will disintegrate. The autoclave expansion test is currently the most suitable test for determining the ultimate expansion rate of MgO expansive hydraulic cement or concrete.

(3) A model for explaining the relationship between the porosity after expansion and expansive rate is presented, along with the equation for calculating the compressive strength of mortar after expansion while considering porosity.

(4) From the viewpoint of the three stages of MgO hydration, hydration of MgO will make the pore structure partially dense or increase the tortuosity of the pores, which will improve durability properties;

however, if high expansion occurs, a high porosity will induce durability properties. If the expansion rate exceeds 0.8%, the mechanical properties and durability changes caused by porosity should be considered. Further experimental studies should be carried out for different types of MgO expansive agent to verify the expansion mechanism, identify the ultimate expansive rate, and propose suitable MgO dosage for MgO expansive hydraulic cement or concrete.

Data Availability

The data used to support the findings of this study are available from the corresponding author upon request.

Conflicts of Interest

The authors declare that they have no conflicts of interest regarding the publication of this paper.

Authors' Contributions

Jinbo Yang conceived and designed the article. Jinbo Yang and Siqi Li analyzed the data. Siqi Li, Yecheng Feng, and Jinbo Yang wrote the paper.

Acknowledgments

This study was supported by the National Natural Science Foundation of China (51208013).

References

[1] A. Damgaard Jensen and S. Chatterji, "State of the art report on micro-cracking and lifetime of concrete-part 1," *Materials and Structures*, vol. 29, no. 1, pp. 3–8, 1996.

[2] ASTM C845-04, *Standard Specification for Expansive Hydraulic Cement*, ASTM International, West Conshohocken, PA, USA, 2004, http://www.astm.org.

[3] S. Nagataki and H. Gomi, "Expansive admixtures (mainly ettringite)," *Cement and Concrete Composites*, vol. 20, no. 2-3, pp. 163–170, 1998.

[4] ACI 223, *Guide for the Use of Shrinkage-Compensating Concrete*, ACI Committee 223R-10, Farmington Hills, MI, USA, 2010.

[5] J. L. García Calvo, D. Revuelta, P. Carballosa, and J. P. Gutiérrez, "Comparison between the performance of expansive SCC and expansive conventional concretes in different expansion and curing conditions," *Construction and Building Materials*, vol. 136, pp. 277–285, 2017.

[6] P. Gao, X. Lu, F. Geng et al., "Production of MgO-type expansive agent in dam concrete by use of industrial by-products," *Building and Environment*, vol. 43, no. 4, pp. 453–457, 2008.

[7] M. Collepardi, R. Troli, M. Bressan, F. Liberatore, and G. Sforza, "Crack-free concrete for outside industrial floors in the absence of wet curing and contraction joints," *Cement and Concrete Composites*, vol. 30, no. 10, pp. 887–891, 2008.

[8] C. Maltese, C. Pistolesi, A. Lolli, A. Bravo, T. Cerulli, and D. Salvioni, "Combined effect of expansive and shrinkage reducing admixtures to obtain stable and durable mortars," *Cement and Concrete Research*, vol. 35, no. 12, pp. 2244–2251, 2005.

[9] L. Mo, M. Deng, and A. Wang, "Effects of MgO-based expansive additive on compensating the shrinkage of cement paste under non-wet curing conditions," *Cement and Concrete Composites*, vol. 34, no. 3, pp. 377–383, 2012.

[10] F. Liu, S.-L. Shen, D.-W. Hou, A. Arulrajah, and S. Horpibulsuk, "Enhancing behavior of large volume underground concrete structure using expansive agents," *Construction and Building Materials*, vol. 114, pp. 49–55, 2016.

[11] M. Ish-Shalom and A. Bentur, "Properties of type *K* expansive cement of pure components I. hydration of unrestrained paste of expansive component-results," *Cement and Concrete Research*, vol. 4, no. 4, pp. 519–532, 1974.

[12] A. Bentur and M. Ish-Shalom, "Properties of type *K* expensive cement of pure components II. proposed mechanism of ettringite formation and expansion in unrestrained paste of pure expansive component," *Cement and Concrete Research*, vol. 4, no. 5, pp. 709–721, 1974.

[13] M. Ish-Shalom and A. Bentur, "Properties of type *K* expansive cement of pure components III. hydration of pure expansive component under varying restraining conditions," *Cement and Concrete Research*, vol. 5, no. 2, pp. 139–152, 1975.

[14] M. Deng and M. Tang, "Formation and expansion of ettringite crystals," *Cement and Concrete Research*, vol. 24, no. 1, pp. 119–126, 1994.

[15] P. Yan and X. Qin, "The effect of expansive agent and possibility of delayed ettringite formation in shrinkage-compensating massive concrete," *Cement and Concrete Research*, vol. 31, no. 2, pp. 335–337, 2001.

[16] P. Yan, F. Zheng, J. Peng, and X. Qin, "Relationship between delayed ettringite formation and delayed expansion in massive shrinkage-compensating concrete," *Cement and Concrete Composites*, vol. 26, no. 6, pp. 687–693, 2004.

[17] L. Mo, M. Deng, M. Tang, and A. Al-Tabbaa, "MgO expansive cement and concrete in China: past, present and future," *Cement and Concrete Research*, vol. 57, pp. 1–12, 2014.

[18] L. Zheng, C. Mingshu, and M. Tang, "Hydration and setting time of MgO-type expansive cement," *Cement and Concrete Research*, vol. 22, no. 1, pp. 1–5, 1992.

[19] L. Mo, M. Deng, and M. Tang, "Effects of calcination condition on expansion property of MgO-type expansive agent used in cement-based materials," *Cement and Concrete Research*, vol. 40, no. 3, pp. 437–446, 2010.

[20] T.-H. Ahn and T. Kishi, "Crack self-healing behavior of cementitious composites incorporating various mineral admixtures," *Journal of Advanced Concrete Technology*, vol. 8, no. 2, pp. 171–186, 2010.

[21] T. S. Qureshi and A. Al-Tabbaa, "Self-healing of drying shrinkage cracks in cement-based materials incorporating reactive MgO," *Smart Materials and Structures*, vol. 25, no. 8, Article ID 084004, 2016.

[22] M. A. A. Sherir, K. M. A. Hossain, and M. Lachemi, "Development and recovery of mechanical properties of self-healing cementitious composites with MgO expansive agent," *Construction and Building Materials*, vol. 148, pp. 789–810, 2017.

[23] M. A. A. Sherir, K. M. A. Hossain, and M. Lachemi, "The influence of MgO-type expansive agent incorporated in self-healing system of Engineered cementitious Composites," *Construction and Building Materials*, vol. 149, pp. 164–185, 2017.

[24] R. Moradpour, E. Taheri-Nassaj, T. Parhizkar, and M. Ghodsian, "The effects of nanoscale expansive agents on

the mechanical properties of non-shrink cement-based composites: the influence of nano-MgO addition," *Composites Part B: Engineering*, vol. 55, pp. 193–202, 2013.

[25] S. Chatterji and J. W. Jeffery, "The volume expansion of hardened cement paste due to the presence of "dead-burnt" CaO," *Magazine of Concrete Research*, vol. 18, no. 55, pp. 65–68, 1966.

[26] S. Chatterji, "Mechanism of expansion of concrete due to the presence of dead-burnt CaO and MgO," *Cement and Concrete Research*, vol. 25, no. 1, pp. 51–56, 1995.

[27] F. Cao, M. Miao, and P. Yan, "Hydration characteristics and expansive mechanism of MgO expansive agents," *Construction and Building Materials*, vol. 183, pp. 234–242, 2018.

[28] L. Mo, J. Fang, W. Hou et al., "Synergetic effects of curing temperature and hydration reactivity of MgO expansive agents on their hydration and expansion behaviours in cement pastes," *Construction and Building Materials*, vol. 207, pp. 206–217, 2019.

[29] F. Cao and P. Yan, "The influence of the hydration procedure of MgO expansive agent on the expansive behavior of shrinkage-compensating mortar," *Construction and Building Materials*, vol. 202, pp. 162–168, 2019.

[30] CBMF 19-2017, *Magnesium Oxide Expansive Agent for Concrete*, China Building Materials Federation and China Concrete & Cement-based Products Association, Beijing, China, 2017, in Chinese.

[31] M. Steiger, "Crystal growth in porous materials—I: the crystallization pressure of large crystals," *Journal of Crystal Growth*, vol. 282, no. 3-4, pp. 455–469, 2005.

[32] M. Steiger, "Crystal growth in porous materials—II: influence of crystal size on the crystallization pressure," *Journal of Crystal Growth*, vol. 282, no. 3-4, pp. 470–481, 2005.

[33] J. A. Mejias, A. J. Berry, R. Keith, and D. G. Fraser, "The kinetics and mechanism of MgO dissolution," *Chemical Physics Letters*, vol. 314, no. 5-6, pp. 558–563, 1999.

[34] D. Filippou, N. Katiforis, N. Papassiopi, and K. Adam, "On the kinetics of magnesia hydration in magnesium acetate solutions," *Journal of Chemical Technology & Biotechnology*, vol. 74, no. 4, pp. 322–328, 1999.

[35] V. Kasselouris, C. Ftikos, and G. Parissakis, "On the hydration of MgO in cement pastes hydrated up to eight years," *Cement and Concrete Research*, vol. 15, no. 5, pp. 758–764, 1985.

[36] A. J. Majumdar and S. S. Rehsi, "The mechanism of stabilization of highmagnesia Portland cements by reactive silica under autoclave conditions," *Magazine of Concrete Research*, vol. 21, no. 68, pp. 141–150, 1969.

[37] M. Yuan, "Study on deformation characteristics of micro expansion concrete of MgO-admixed," pp. 81–109, Wuhan University, Wuhan, China, 2013, Ph. D. dissertation.

[38] R. Wang, Q. Tian, S. Zhang et al., "Improving efficiency of calcium oxide expansive additives by polylactic acid film," *Magazine of Concrete Research*, vol. 68, no. 20, pp. 1070–1078, 2016.

[39] ASTM C151/C151M-18, *Standard Test Method for Autoclave Expansion of Hydraulic Cement*, ASTM International, West Conshohocken, PA, USA, 2018, http://www.astm.org.

[40] R. Helmuth and P. B. West, "Reappraisal of the autoclave expansion test," *Cement, Concrete and Aggregates*, vol. 20, no. 1, pp. 194–219, 1998.

[41] R. Michelle, "Nokken, Expansion of MgO in cement pastes measured by different methods," *ACI Materials Journal*, vol. 107, no. 1, pp. 80–84, 2010.

[42] L. Mo, M. Deng, and M. Tang, "Potential approach to evaluating soundness of concrete containing MgO-based expansive agent," *ACI Materials Journal*, vol. 107, no. 2, pp. 99–105, 2010.

[43] P.-w. Gao, S.-x. Wu, X.-l. Lu et al., "Soundness evaluation of concrete with MgO," *Construction and Building Materials*, vol. 21, no. 1, pp. 132–138, 2007.

[44] X. Chen, S. Wu, and J. Zhou, "Influence of porosity on compressive and tensile strength of cement mortar," *Construction and Building Materials*, vol. 40, pp. 869–874, 2013.

[45] R. Kumar and B. Bhattacharjee, "Porosity, pore size distribution and in situ strength of concrete," *Cement and Concrete Research*, vol. 33, no. 1, pp. 155–164, 2003.

[46] S.-w. Choi, B.-s. Jang, J.-h. Kim, and K.-m. Lee, "Durability characteristics of fly ash concrete containing lightly-burnt MgO," *Construction and Building Materials*, vol. 58, pp. 77–84, 2014.

[47] P.-w. Gao, S.-x. Wu, P.-h. Lin, Z.-r. Wu, and M.-s. Tang, "The characteristics of air void and frost resistance of RCC with fly ash and expansive agent," *Construction and Building Materials*, vol. 20, no. 8, pp. 586–590, 2006.

[48] P.-w. Gao, S.-y. Xu, X. Chen, J. Li, and X.-l. Lu, "Research on autogenous volume deformation of concrete with MgO," *Construction and Building Materials*, vol. 40, pp. 998–1001, 2013.

[49] T. Gonçalves, R. V. Silva, J. de Brito, J. M. Fernández, and A. R. Esquinas, "Mechanical and durability performance of mortars with fine recycled concrete aggregates and reactive magnesium oxide as partial cement replacement," *Cement and Concrete Composites*, vol. 105, Article ID 103420, 2020.

[50] R. Zhang and K. P. Daman, "Longitudinal deformation of mortar bars containing reactive MgO during carbonation curing and sulfate solution immersion," *Journal of Materials in Civil Engineering*, vol. 31, no. 11, Article ID 04019275, 2019.

[51] P. Zhang, F. H. Wittmann, M. Vogel, H. S. Müller, and T. Zhao, "Influence of freeze-thaw cycles on capillary absorption and chloride penetration into concrete," *Cement and Concrete Research*, vol. 100, no. 10, pp. 60–67, 2017.

[52] P. Zhang, D. Li, Y. Qiao, S. Zhang, C. T. Sun, and T. Zhao, "The effect of air entrainment on the mechanical properties, chloride migration and microstructure of ordinary concrete and fly ash concrete," *ASCE Journal of Materials in Civil Engineering*, vol. 30, no. 10, Article ID 04018265, 2018.

[53] Y. Wang, Y. Cao, P. Zhang et al., "Water absorption and chloride diffusivity of concrete under the coupling effect of uniaxial compressive load and freeze-thaw cycles," *Construction and Building Materials*, vol. 209, pp. 566–576, 2019.

[54] Q. Song, H. Zhao, J. Jia et al., "Pyrolysis of municipal solid waste with iron-based additives: a study on the kinetic, product distribution and catalytic mechanisms," *Journal of Cleaner Production*, vol. 258, Article ID 120682, 2020.

[55] Y. Tian, P. Zhang, K. Zhao, Z. Du, and T. Zhao, "Application of Ag/AgCl sensor for chloride monitoring of mortar under dry-wet cycles," *Sensors*, vol. 20, no. 5, p. 1394, 2020.

[56] J. W. Bao, S. B. Xue, P. Zhang, Z. Dai, and Y. F. Cui, "Coupled effects of sustained compressive loading and freeze-thaw cycles on water penetration into concrete," *Structural Concrete*, vol. 22, no. S1, 2020.

[57] K. Zhao, Y. Qiao, P. Zhang, J. Bao, and Y. Tian, "Experimental and numerical study on chloride transport in cement mortar during drying process," *Construction and Building Materials*, vol. 258, Article ID 119655, 2020.

[58] J. Bao, S. Li, P. Zhang et al., "Influence of the incorporation of recycled coarse aggregate on water absorption and chloride

penetration into concrete," *Construction and Building Materials*, vol. 239, Article ID 117845, 2020.

[59] S. Hu and Y. Li, "Research on the hydration, hardening mechanism, and microstructure of high performance expansive concrete," *Cement and Concrete Research*, vol. 29, no. 7, pp. 1013–1017, 1999.

[60] F. H. Wittmann, F. Jiang, T. Zhao, and Y. Wang, "Influence of an applied compressive stress on service life of reinforced concrete structures in marine environment," *Restoration of Buildings and Monuments*, vol. 19, no. 1, pp. 3–10, 2013.

[61] P. Zhang, F. H. Wittmann, P. Lura, H. S. Müller, S. Han, and T. Zhao, "Application of neutron imaging to investigate fundamental aspects of durability of cement-based materials: a review," *Cement and Concrete Research*, vol. 108, pp. 152–166, 2018.

[62] S. Xue, P. Zhang, J. Bao, L. He, Y. Hu, and S. Yang, "Comparison of mercury intrusion porosimetry and multi-scale X-ray CT on characterizing the microstructure of heat-treated cement mortar," *Materials Characterization*, vol. 160, Article ID 110085, 2020.

[63] P. Zhang, P. Wang, D. Hou, Z. Liu, M. Haist, and T. Zhao, "Application of neutron radiography in observing and quantifying the time-dependent moisture distributions in multi-cracked cement-based composites," *Cement and Concrete Composites*, vol. 78, pp. 13–20, 2017.

[64] P. Zhang, Z. Liu, Y. Wang, J. Yang, S. Han, and T. Zhao, "3D neutron tomography of steel reinforcement corrosion in cement-based composites," *Construction and Building Materials*, vol. 162, pp. 561–565, 2018.

[65] P. Zhang, Y. Dai, W. Wang et al., "Effects of magnesia expansive agents on the self-healing performance of microcracks in strain-hardening cement-based composites (SHCC)," *Materials Today Communications*, vol. 25, Article ID 101421, 2020.

[66] H. Wu, J. Yu, Y. Du, and V. C. Li, "Mechanical performance of MgO-doped engineered cementitious composites (ECC)," *Cement and Concrete Composites*, vol. 115, Article ID 103857, 2021.

[67] F. Jiang, Z. Mao, M. Deng, and D. Li, "Deformation and compressive strength of steel fiber reinforced MgO concrete," *Materials*, vol. 12, no. 21, p. 3617, 2019.

[68] H. Kabir and R. D. Hooton, "Evaluating soundness of concrete containing shrinkage-compensating MgO admixtures," *Construction and Building Materials*, vol. 253, Article ID 119141, 2020.

[69] H. Kabir, R. D. Hooton, and N. J. Popoff, "Evaluation of cement soundness using the ASTM C151 autoclave expansion test," *Cement and Concrete Research*, vol. 136, Article ID 106159, 2020.

[70] J. Guo, T. Guo, S. Zhang, and Y. Lu, "Experimental study on freezing and thawing cycles of shrinkage-compensating concrete with double expansive agents," *Materials*, vol. 13, no. 8, p. 1850, 2020.

[71] R. Hay and K. Celik, "Hydration, carbonation, strength development and corrosion resistance of reactive MgO cement-based composites," *Cement and Concrete Research*, vol. 128, Article ID 105941, 2020.

[72] S. Li, S. Cheng, L. Mo, and M. Deng, "Effects of steel slag powder and expansive agent on the properties of ultra-high performance concrete (UHPC): based on a case study," *Materials*, vol. 13, no. 3, p. 683, 2020.

Hindawi
Advances in Materials Science and Engineering
Volume 2021, Article ID 6637014, 15 pages
https://doi.org/10.1155/2021/6637014

Research Article

Collapse Behaviour of a Concrete-Filled Steel Tubular Column Steel Beam Frame under Impact Loading

Lian Song,[1,2] Hao Hu,[1,3] Jian He,[1] Xu Chen,[2] and Xi Tu[4]

[1]*School of Civil Engineering, Chongqing University of Arts and Sciences, Chongqing 402160, China*
[2]*Infrastructure Department, Chongqing University of Arts and Sciences, Chongqing 402160, China*
[3]*Institute of Civil Engineering Disaster Prevention and Reduction, Chongqing University of Arts and Sciences, Chongqing 402160, China*
[4]*School of Civil Engineering, Chongqing University, Chongqing 400045, China*

Correspondence should be addressed to Hao Hu; hhxkfy@126.com

Received 29 October 2020; Revised 11 December 2020; Accepted 10 April 2021; Published 23 April 2021

Academic Editor: Robert Cerný

The progressive collapse of a concrete-filled steel tubular (CFST) frame structure is studied subjected to impact loading of vehicle by the finite-element software ABAQUS, in the direct simulation method (DS) and alternate path method (AP), respectively. Firstly, a total of 14 reference specimens including 8 hollow steel tubes and 6 CFST specimens were numerically simulated under transverse impact loading for verification of finite-element models, which were compared with the existing test results, confirming the overall similarity between them. Secondly, a finite-element analysis (FEA) model is established to predict the impact behaviour of a five-storey and three-span composite frame which was composed of CFST columns and steel beams under impact vehicle loading. The failure mode, internal force-time curve, displacement-time curve, and mechanical performance of the CFST frame were obtained through analyzing. Finally, it is concluded that the result by the DS method is closer to the actual condition and the collapse process of the structure under impact load can be relatively accurately described; however, the AP method is not.

1. Introduction

Concrete-filled steel tubular (CFST) structures are widely encountered in civil engineering structures, such as composite frames, whose columns are the concrete-filled steel tubular (CFST), while beams are steel. Such structures are commonly exposed to accidental impact loads during the service. In recent years, there have been some successive structural collapses because of natural disasters and terrorist attacks around the world [1–3]. However, the continuous collapses due to accidental impact loads except some normal loads have not been considered in existing design specifications for safety of structure design [4–9].

So far, a number of researchers have studied the continuous collapses of structures in some occasional cases [10-11]. A new partial distributed damage method to capture loss of stability phenomena is described for steel moment frames by Gerasimidis [12]. Salloum [13] demonstrated the vulnerability of a typical medium-rise circular RC building against progressive collapse as a result of blast generated waves. Ding [14] studied the failure probability of steel frame structures against terrorist attack. Jiang [15] presented progressive collapse resistance of three-dimensional steel frames with reinforced concrete slabs exposed to localized fire. The influence of building height on the robustness of reinforced concrete frame buildings to resist progressive collapse is investigated by Shan [16]. Wang [17] studied the analysis of stainless steel composite beam-to-column joint submodels and moment-resisting frames with the column removed. Kong [18] presented the results of a large-scale test on a three-dimensional (3D) composite floor specimen under the scenario of removed internal column. In [19], the influence of different span length of precast beams was studied under different column removal scenarios. Zhou [20] conducted the progressive collapse performance on three half-scale moment substructures, including a

conventional RC specimen and two PC specimens using dowel bars and corbel. These studies provide useful information on the progressive collapse of different structures or components for the specific types of disasters concentrated in the explosion and fire but produce little data about composite frames by impact loads. Considering the dynamic effect via the impact loads on structures, it is very significant to make valid conclusions and recommendations on reasonable structure design for strengthening the ability of buildings to resist progressive collapse and ensure structural stability in the short time.

This research studies the continuous collapse performance and analysis method of a typical composite frame with concrete-filled steel tubular (CFST) columns and steel beams by accidental impact load of vehicle through the finite-element software ABAQUS. In this paper, the results of the finite-element model for a single member under dynamic impacts are coincident with that of existing experiments. The performance of this collapsed composite frame by the direct simulation method (DS) is compared with that by the alternate path method (AP) [21] in terms of displacement of the failure column top node and axial force of the adjacent columns.

2. Verification of the Finite-Element Model

2.1. Introduction of the Impact Test. As the basis for the verification of the planar frame, the simplest and most important model is the confined axial column subjected to lateral impact. Firstly, based on the ABAQUS software platform, a series of numerical analysis models for the existing tests of steel and CFST columns under lateral impact load are established. The verification tests consisted of 6 concrete-filled steel tubes and 8 hollow steel tube concrete tests. Detailed information is summarized in Table 1, where the symbol B is the nominal external depth, D is the outer diameter of the steel tube, t_s is the thickness of the steel tube, L is the length of the specimen, V is the lateral impact velocity, and M is the quality of the drop hammer.

2.2. The Finite-Element Model. In the finite-element model, four parts were built: a steel column, core concrete column, drop hammer, and endplate. The 4-node finite film strain linear reduced integral shell element (S4R) given in the finite-element program ABAQUS was used in this study to model the steel pipe. The 8-node 3D linear reduction integral entity unit (C3D8R) was used to model the concrete.

In order to improve the computational efficiency, the 4-bus unit of three-dimensional rigid body (R3D4) was used to model drop hammer and endplate because the stiffness of the hammer is larger than that of the impact column and its deformation hardly occurs. In the constitutive relation of materials, steel adopted with the bilinear model, core concrete adopted with the concrete damage plasticity model, and both are separately considering strain rate effect. The grid divided in the impact area is very dense, while that in the other parts is relatively sparse. Two ends of the steel pipe column were connected with the rigid end plates by command of Tie. The reference point established in the end plate was exerted by both the boundary constraint and axial force. The contact between the concrete-filled steel tubular column and drop hammer was built by surface-to-surface contact (Explicit). In addition, tangential behavior is used to consider the cohesive force because of tangential bond stress on the surfaces of concrete and steel pipe [25]. At this time, the relative sliding of the interface is simulated by the Columbia Friction Model, and the value of friction coefficient is 0.6.

2.3. Result Verification. The failure modes obtained from the finite-element analysis (FEA) and tests are compared in Figure 1. The tests are from references [22–24], respectively. It can be seen that the simulated failure modes and deformation of the specimens are in good agreement with the experimental results. Both lateral displacement and impact force are compared as shown in Figures 2 and 3, respectively. Good agreement between the FEA and test results is achieved, as presented in Figure 2. Both the overall trend and numerical value are close to that of tests in Figure 3. Δ, P, and T are the lateral displacement, impact force, and impact time, respectively. It can be concluded that the typical results obtained from finite-element analysis are verified by that observed in the experimental investigation. Based on the model of extension, analysis of mechanical properties of CFST frames under impact load is carried out in Section 3.

3. FEA of Progressive Collapse for the Planar Composite Frame

3.1. Multiscale Finite-Element Model. Frame steel structures are commonly used in public buildings, multistorey industrial factories, and some special-purpose buildings, such as theatres, shopping malls, stations, exhibition halls, parking lots, and light industry workshops. According to the relevant standard [9], a typical planer frame structure with concrete-filled steel tubular column steel beam for 5 floors and 3 spans is designed as shown in Figure 4, which meets the design of the normal use requirements. The joints of the planer frame are external ring-plate-type-included intermediate and exterior joints, whose strengthened ring width is 100 mm and thickness is 12 mm, as shown in Figure 5. This paper conducts a comparative study taking into account the failure of the underlying middle column B. Also, the basic information of the model as follows:

Building general information: column spacing of 6 meters, 3.6 meters height, column feet, and foundation consolidation

Frame column: O-360×6 mm

Frame beams: I$-300 \times 250 \times 8 \times 12$ mm (height $\times$ width $\times$ belly $\times$ wing)

Material information: steel tubes and steel beams using steel S355, the yield stress of steel f_y is 355 MPa, the ultimate strength of steel f_u is 470 MPa, and the cube strength of concrete f_{cu} is 50 MPa

Table 1: Detail information of the testing specimens.

Specimen label	Boundary condition	$D(B) \times t_s \times L$ (mm × mm × mm)	V (m/s)	M (kg)	Preloading (kN)	Reference
*MSH	Pinned-pinned	□100 × 2 × 2500	3.57	592	288	[22]
*Pd1	Fixed-sliding	○100 × 2 × 1000	7.006	25.45	0	[23]
*Pd2	Fixed-sliding	○100 × 2 × 1000	6.998	25.45	88	
*Pd3	Fixed-sliding	○100 × 2 × 1000	6.995	25.45	163	
*Pd4	Fixed-sliding	○100 × 2 × 1000	7.012	25.45	196	
*Pd6	Fixed-sliding	○100 × 2 × 1000	7.006	25.45	228	
*HCC	Fixed-fixed	○180 × 3.65 × 1940	7.73	465	0	[24]
CC1	Fixed-fixed	○180 × 3.65 × 1940	9.21	465	0	
CC2	Fixed-fixed	○180 × 3.65 × 1940	6.4	920	0	
CC3	Fixed-fixed	○180 × 3.65 × 1940	9.67	465	0	
*HSS	Pinned-pinned	○180 × 3.65 × 2800	4.25	465	0	
SS1	Pinned-pinned	○180 × 3.65 × 2800	8.05	465	0	
SS2	Pinned-pinned	○180 × 3.65 × 2800	5.69	920	0	
SS3	Pinned-pinned	○180 × 3.65 × 2800	8.93	465	0	

The specimens with asterisk in label are hollow steel tubes.

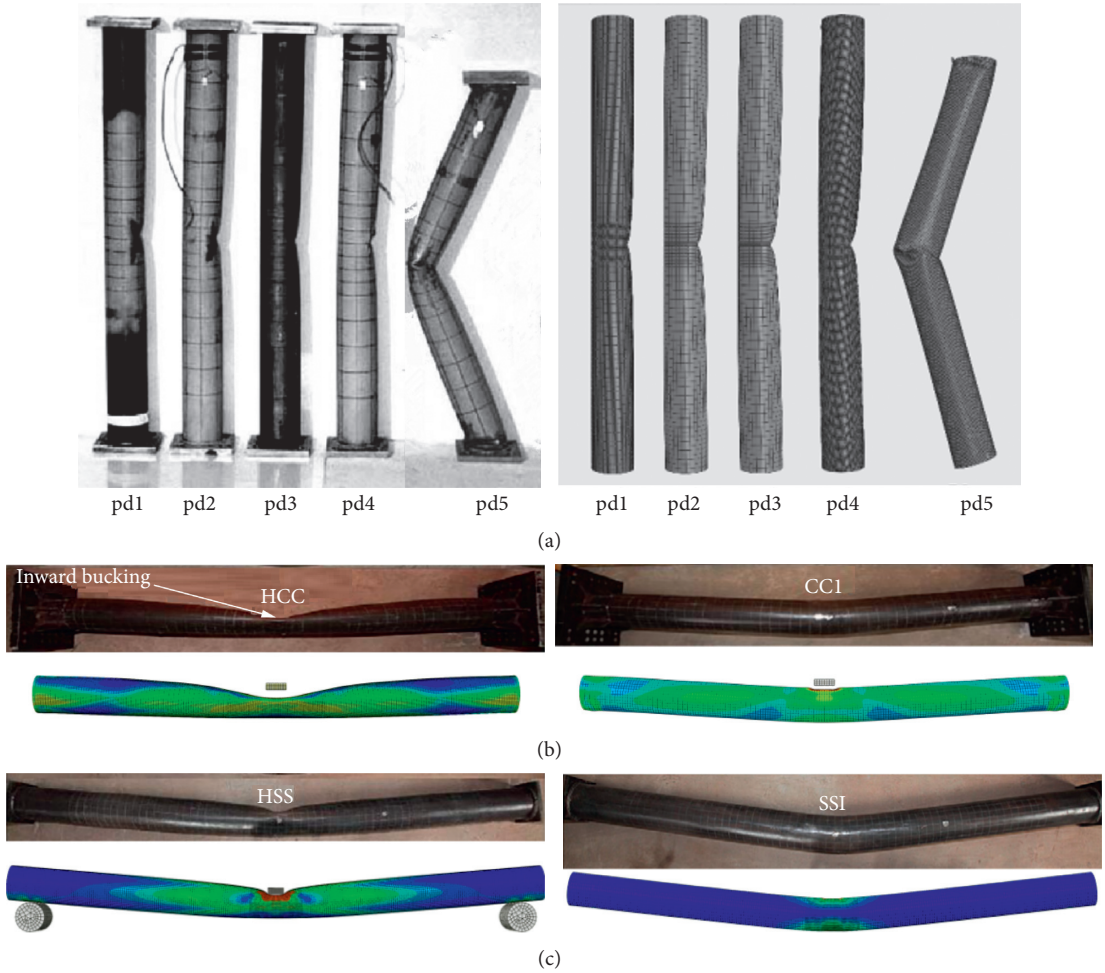

Figure 1: Failure mode comparison tests and FEA. (a) Failure tests from [22]. (b) Failure tests from reference [23]. (c) Failure tests from [24].

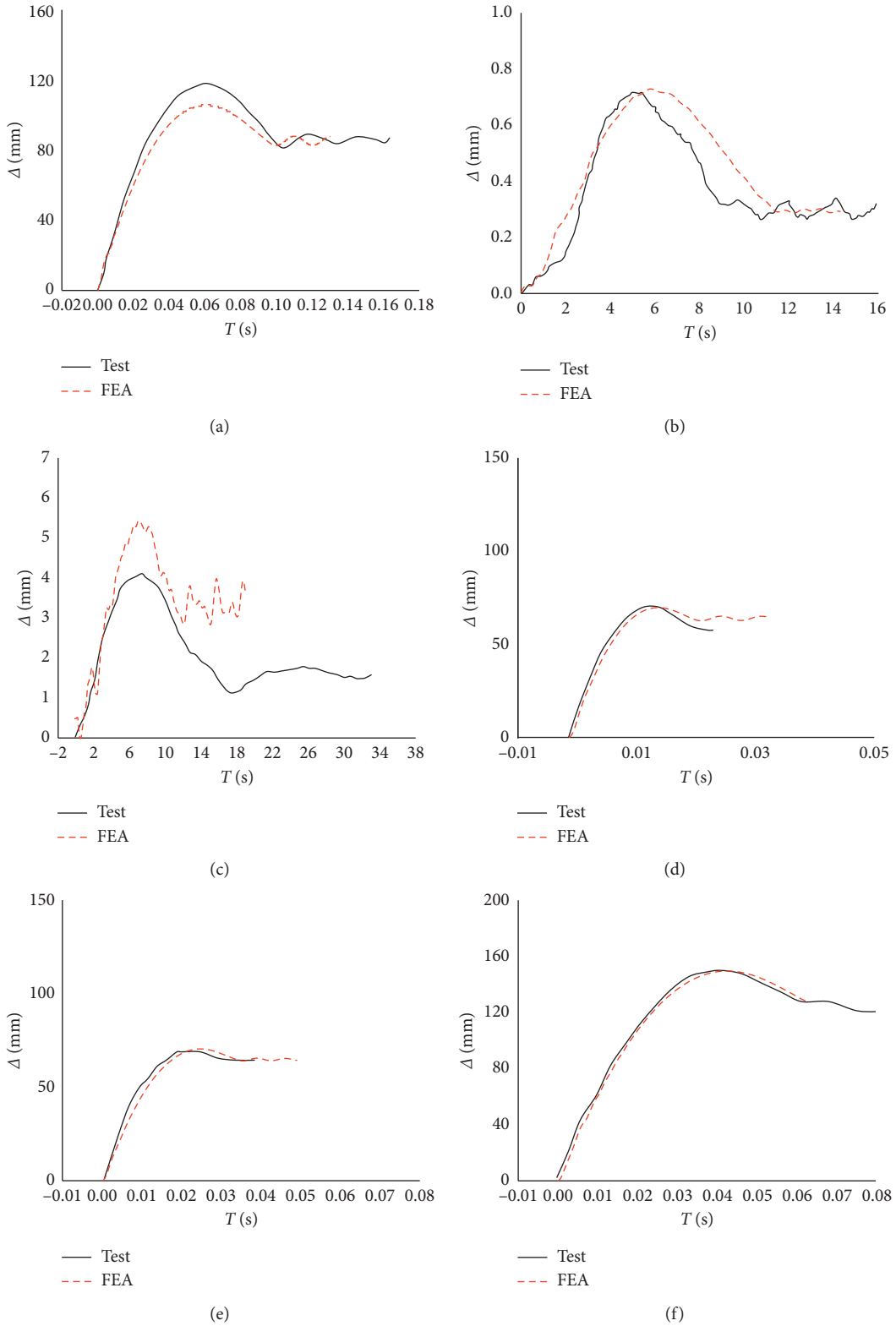

Figure 2: Continued.

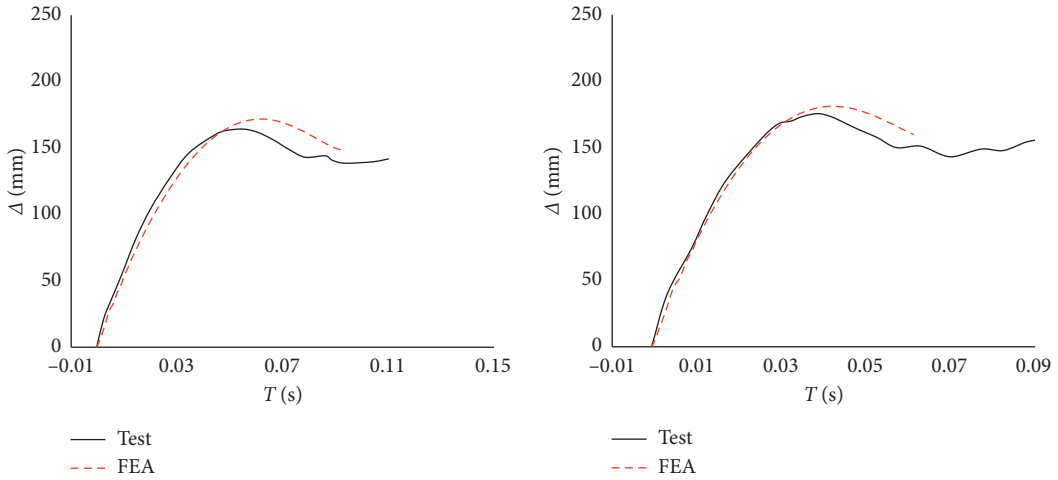

Figure 2: Lateral displacement (Δ) versus time (T) curves. (a) MSH, (b) Pd1, (c) Pd2, (d) CC1, (e) CC2, (f) SS1, (g) SS2, and (h) SS3.

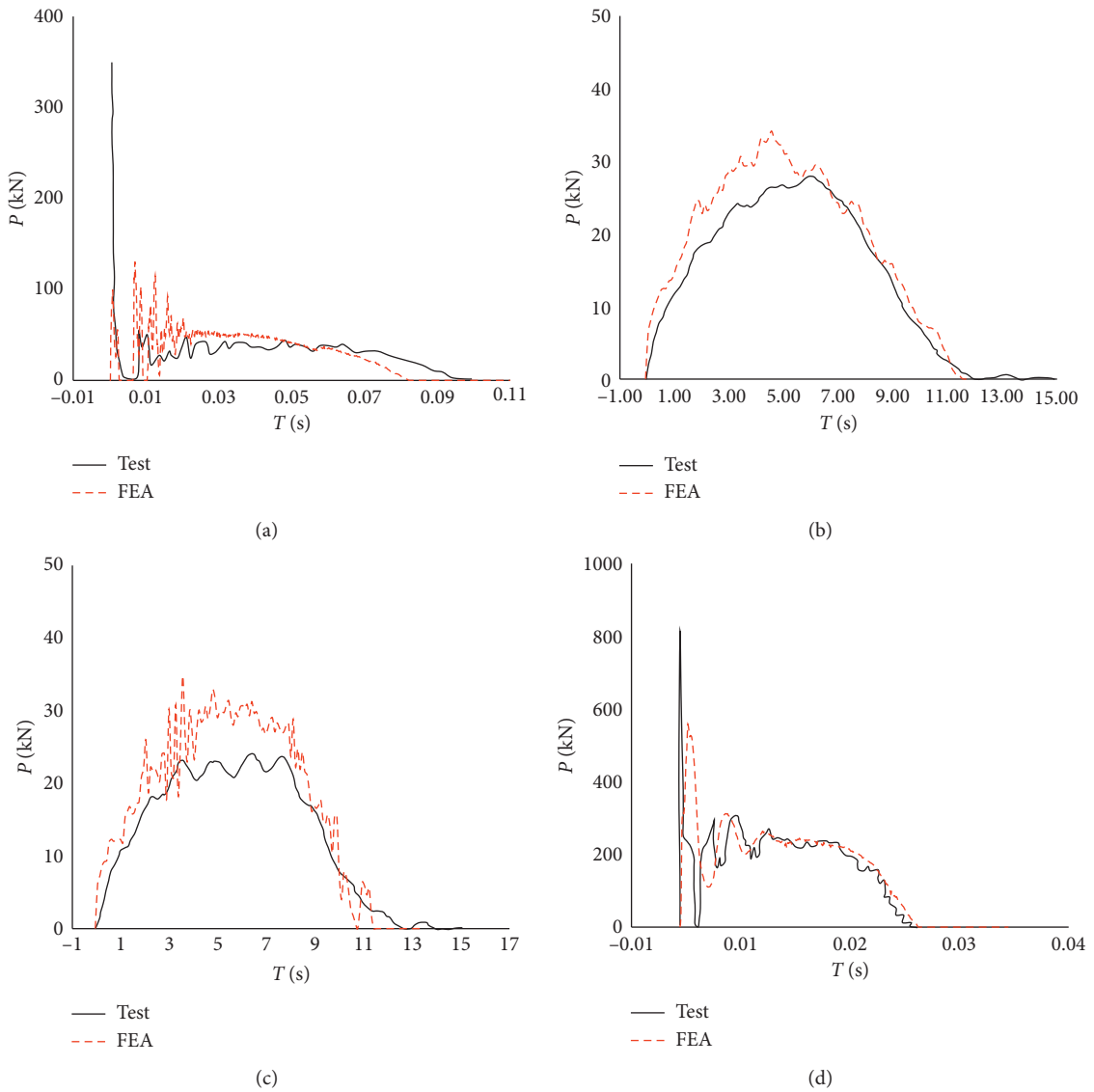

Figure 3: Continued.

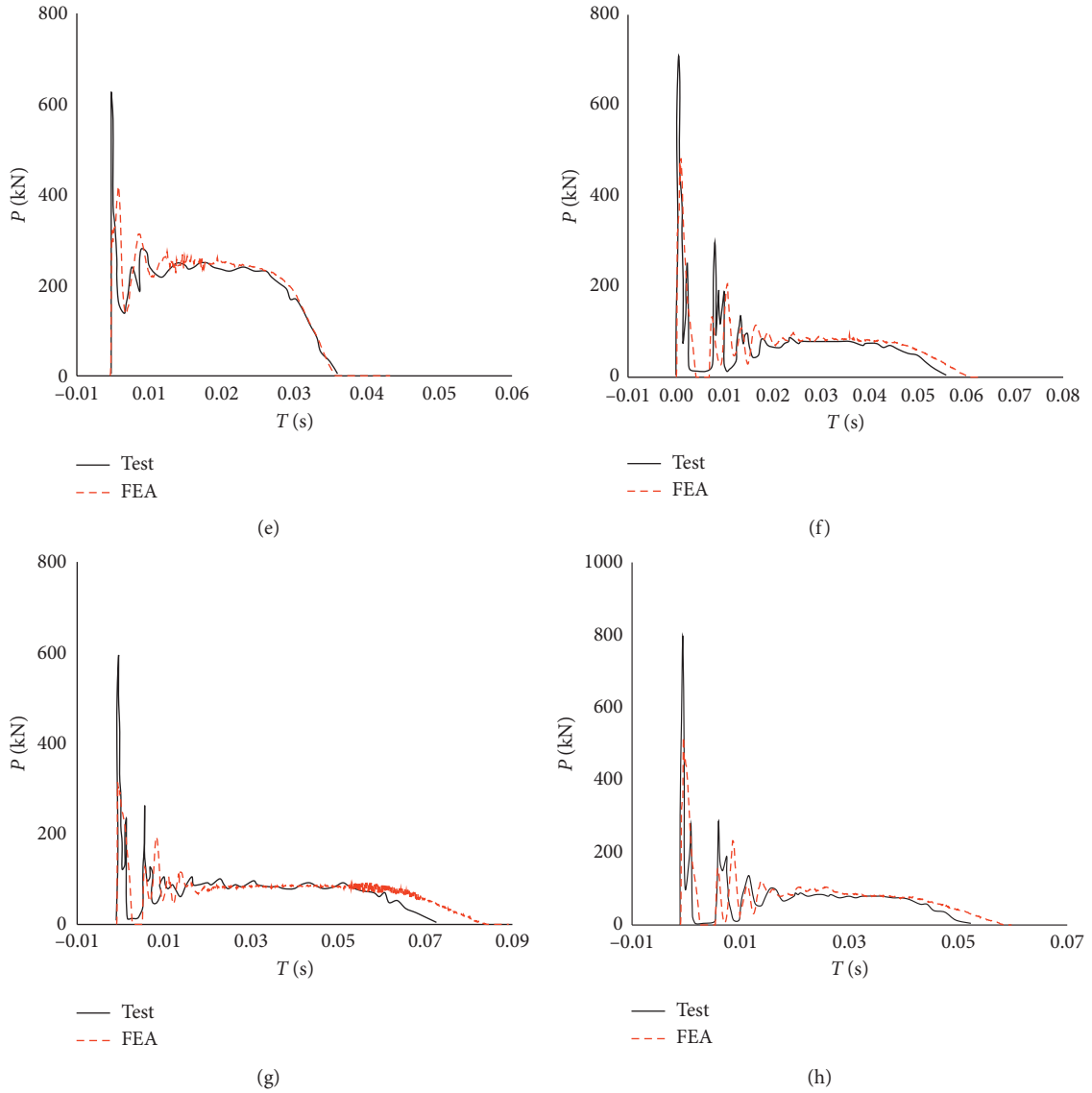

Figure 3: Impact force (P) versus time (T) curves. (a) MSH, (b) Pd1, (c) Pd2, (d) CC1, (e) CC2, (f) SS1, (g) SS2, and (h) SS3.

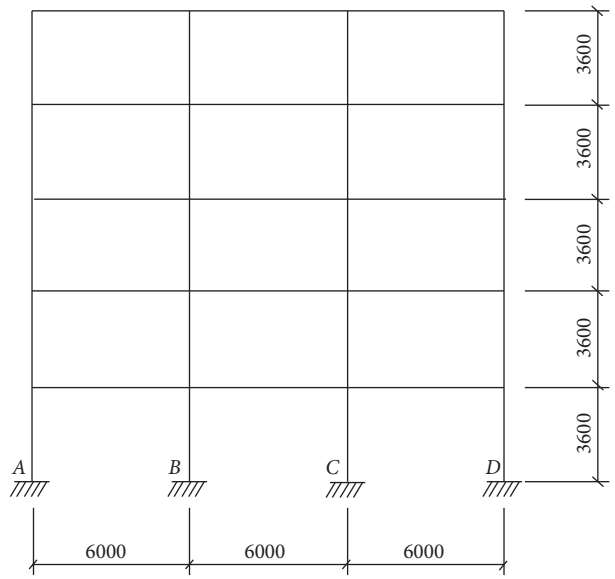

Figure 4: Elevation drawing of the plane frame (unit: mm).

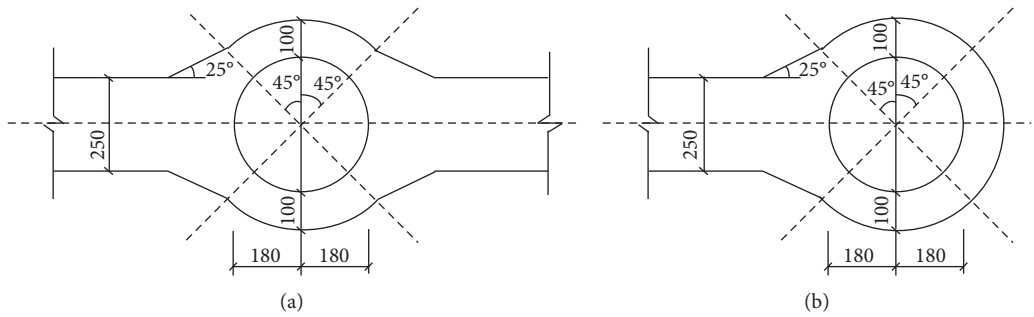

Figure 5: Joint construction (unit: mm). (a) Intermediate joint. (b) Exterior joint.

Loads: the vertical uniform load on all beams is 45 kN/m, and weight of the structure additionally is applied

3.2. Method for Analysis of Progressive Collapse. Considering the computational precision and cost, this paper presents a hybrid multiscale model including a beam element, shell element, and solid element. The couple function of interaction in ABAQUS is used to deal with the interface of different units and realize the connection between the fine model and the macroscopic model. The fine models of the impact column and the joint and the overall multiscale frame work for the direct simulation method (DS) and alternate path method (AP) are shown in Figure 6.

3.2.1. Direct Simulation Method (DS). The AP method does not need to consider the cause of column failure. Compared with the AP method, the impact condition which causes component failure is taken into account. There are many forms of accidental impact loads on building structures. The DS model considers the accidental impact conditions of the car crashing into the bottom column of the parking lot and specifically studies the impact degree of structural damage caused by such impact on the residual structure's resistance to continuous collapse.

Vehicle impact is one of the accidental loads with high uncertainty in the United States, according to the gross vehicular weight rating (GVWR), i.e., light-duty, medium-duty, and heavy-duty trucks. As shown in Figure 7(a), a medium-duty truck (F800 truck) is selected as the reference truck. This category and specific truck type are selected because (1) light trucks usually do not cause column damage; (2) F800 trucks are close to the lower bound of the heavy truck category when fully loaded. In addition, the truck may be overloaded, and it may cover certain aspects of the heavy truck category [26]; and (3) studies have shown that an overloaded F800 truck has the same serious impact effect as a heavy truck. Among the publically available finite-element truck models, the F800 truck model has been widely used and validated by many scholars [27, 28].

Chen [29] established an equivalent frame to simulate the impact of F800 truck and column collisions, and verified the validity of the model by comparing their deformation and internal energy relationship. The F800 truck is the equivalent of a frame, which is divided into a chassis channel, engine, and cargo, as shown in Figure 7(b). Three major impact parameters were selected to reflect the uncertainty of vehicle impact, including impact load, velocity, and height of the impact point of the F800 truck. In order to facilitate the comparison of various factors, 5 values are taken for each parameter. A total of 125 trials would be carried out; furthermore, calculation will be large if all the research combinations of each parameter are fully considered. It is necessarily simulated through a combination of noncomprehensive parameters and selecting representative test points, by which the reasonable influence of parameters can be shown. Therefore, each parameter value of analysis is used from the orthogonal test method as seen in Table 2.

3.2.2. Alternate Path Method (AP). The AP method is suitable for the analysis of structural collapse under blast and impact loads, which is based on the assumption that the failure of one or several main vertical members of the structure can be used to calculate the residual structural response.

3.2.3. Collapse Criterion. In this paper, the nonlinear dynamic collapse analysis of CFST plane frame structure is studied, and the failure criterion of limiting rotation angle value 12 of the steel beam is used from the code GSA [4]. The collapse occurred when the vertical displacement of the failed node is greater than 1275 mm which is the limiting displacement value corresponding to this frame.

3.3. Comparative Analysis

3.3.1. Collapse Mechanism. From Figure 8, it can be seen that there are two deformation modes of the failure column under impact load. The one is the local deformation of columns as shown in Figures 8(a) and 9(a), and the other is large deformation when the columns feet are destroyed as shown during the impact process in Figures 8(b), 8(c), 9(b), and 9(c). In addition, in the impact contact sites and the opposite sides of the steel pipes, there is stress centralization and partial steel pipes appeared with fracture; the relative obvious local deformation also occurred in the joint zone, as shown in Figure 9(c).

It can be known from Figures 8(a) and 8(b) separately that if the impact energy is low in the DS method, there is

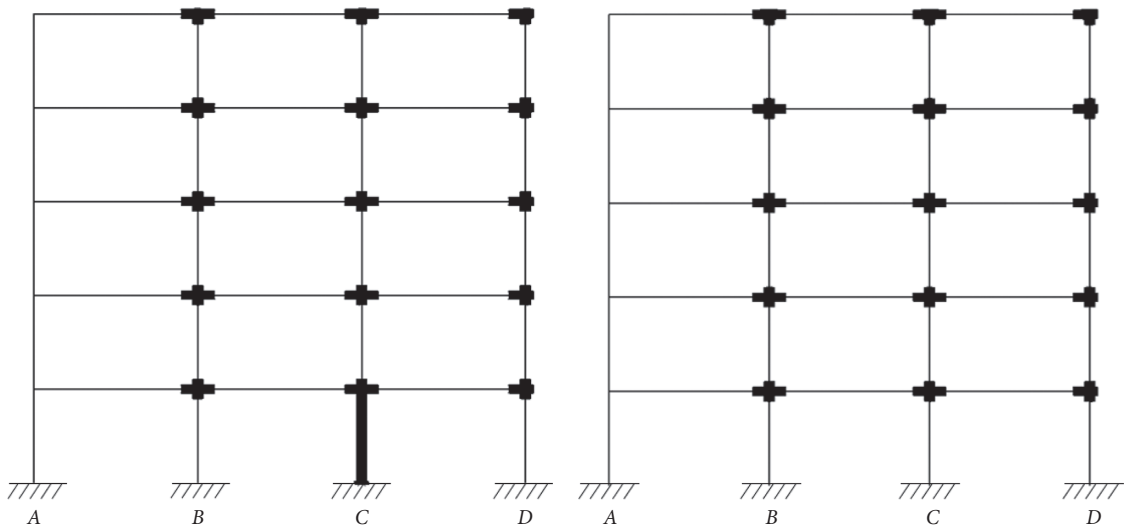

(a) (b)

Figure 6: CFST plane frame structure model. (a) Model via the DS method. (b) Model via the AP method.

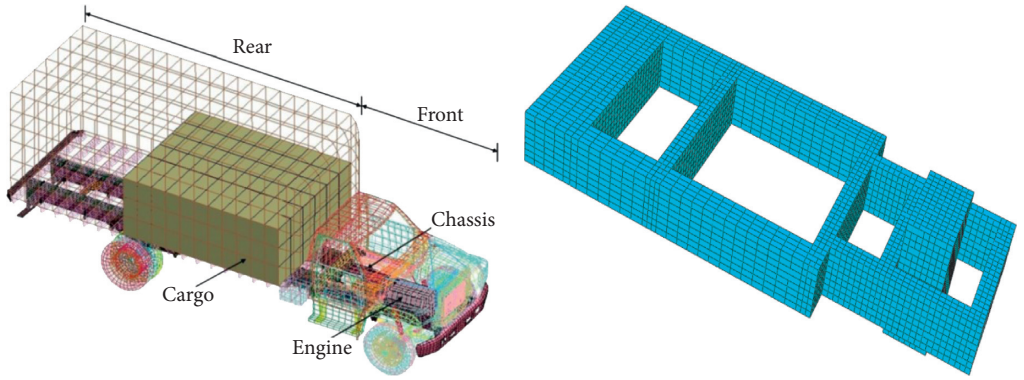

(a) (b)

Figure 7: The car model. (a) 1995 Ford F800 truck. (b) Equivalent frame.

hardly any deformation in the remaining frame structure except for the small bending deformation of the impacted column; moreover, this column can still work. If the impacted column failed, the vertical displacement of beam ends and joints of this column is large, and there is scarcely any deformation in the remaining frame structure too. However, the internal force of the surplus structure is redistributed, and the integer collapse did not occur. As shown in Figure 8(c), the results of the AP method are similar to that of the DS method in Figure 8(b). After the destruction of the impacted column, the internal force is redistributed and a new equilibrium state of the frame finally appears due to the good deformation ability, ductility, and, furthermore, suspended cable effect of the steel beams.

3.3.2. Axial Force of Adjacent Columns. The axial-force-time-history curves of the *A*, *B*, and *D* bottom columns under different conditions are shown in Figures 10(a), 10(b), and 10(c). It can be seen that the forced state of the *B* column is more unfavorable than that of the *A* and *D* columns. The change trends of axial force for *A*, *B*, and *D* columns by the DS method are similar for each impact combination case. The axial force is significantly increased firstly as a result of the reverse vibration structure, and it decreases when time increases and then keeps a value in some level.

In the worst case, the maximum axial force of the *B* column is 2.12 times of that of the AP method. More axial force is produced by the *B* column as one of the adjacent columns because the impacted column is destroyed. In Figure 10, the result obtained by the AP method is generally close to the intermediate value of that of the DS method, and this only represents one of the impact combinations without practical significance. So, it is not reliable and, furthermore, insecure to evaluate the dynamic effect of the structure under the impact load by the AP method.

3.3.3. The Displacement of the Failure Point. As shown in Figure 11, the maximum displacement obtained by the AP method is 322 mm lower than 1275 mm, which is the

Table 2: Summary of research on transverse impact tests.

No.	Impact velocity (km/h)	Impact mass (t)	Impact position (m)
$c1$	40	1.5	0.7
$c2$	40	4.5	1.2
$c3$	40	7.5	1.5
$c4$	40	12	1.8
$c5$	40	20	2.5
$c6$	60	1.5	1.2
$c7$	60	4.5	1.5
$c8$	60	7.5	1.8
$c9$	60	12	2.5
$c10$	60	20	0.7
$c11$	80	1.5	1.5
$c12$	80	4.5	1.8
$c13$	80	7.5	2.5
$c14$	80	12	0.7
$c15$	80	20	1.2
$c16$	100	1.5	1.8
$c17$	100	4.5	2.5
$c18$	100	7.5	0.7
$c19$	100	12	1.2
$c20$	100	20	1.5
$c21$	120	1.5	2.5
$c22$	120	4.5	0.7
$c23$	120	7.5	1.2
$c24$	120	12	1.5
$c25$	120	20	1.8

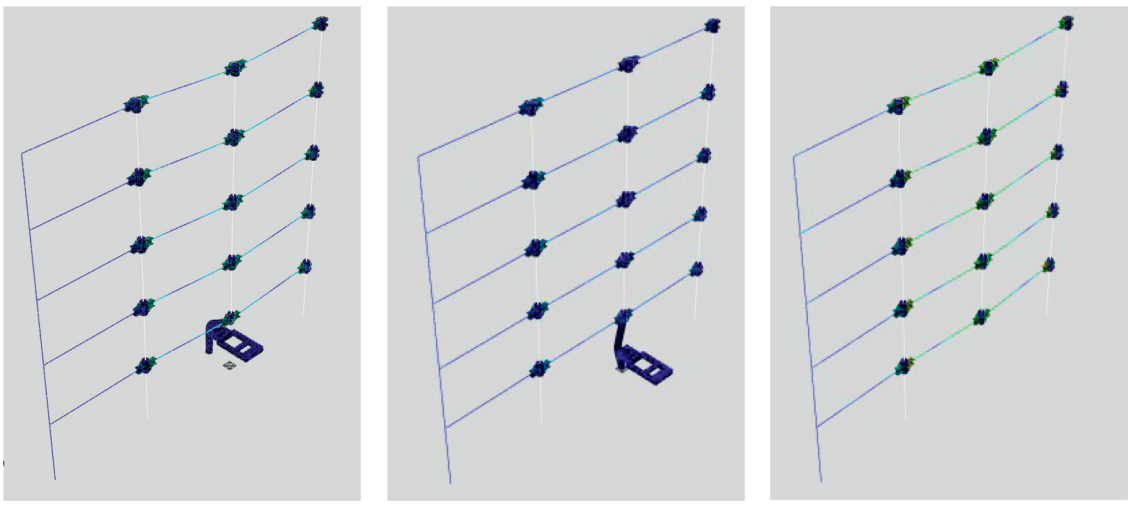

(a) (b) (c)

Figure 8: Deformation of the planer frame with the middle column removed. (a) Model c1 via the DS method. (b) Model c25 via the DS method. (c) Model via the AP method.

limiting displacement from the displacement-time-history curve of the failure point. It shows that the progressive collapse can be resisted by the five-layer plane frame structure. In the DS method, on the different impacted condition, the maximum value of the displacement variation is relatively larger, in the range of 17 mm–1274 mm. However, compared with the AP method, the maximum displacement of the worst case in the DS method is 1274 mm, basically reaching 1275 mm, and the collapse may appear. It can be predicted that the DS method is more accurate than the AP method for analysis on collapse of frame structures.

3.3.4. Data Analysis. According to Figure 10, it can be concluded that the axial force of the B pillar changes most significantly after impacting. Therefore, in order to measure every impact factor on the frame impacted, the axial force

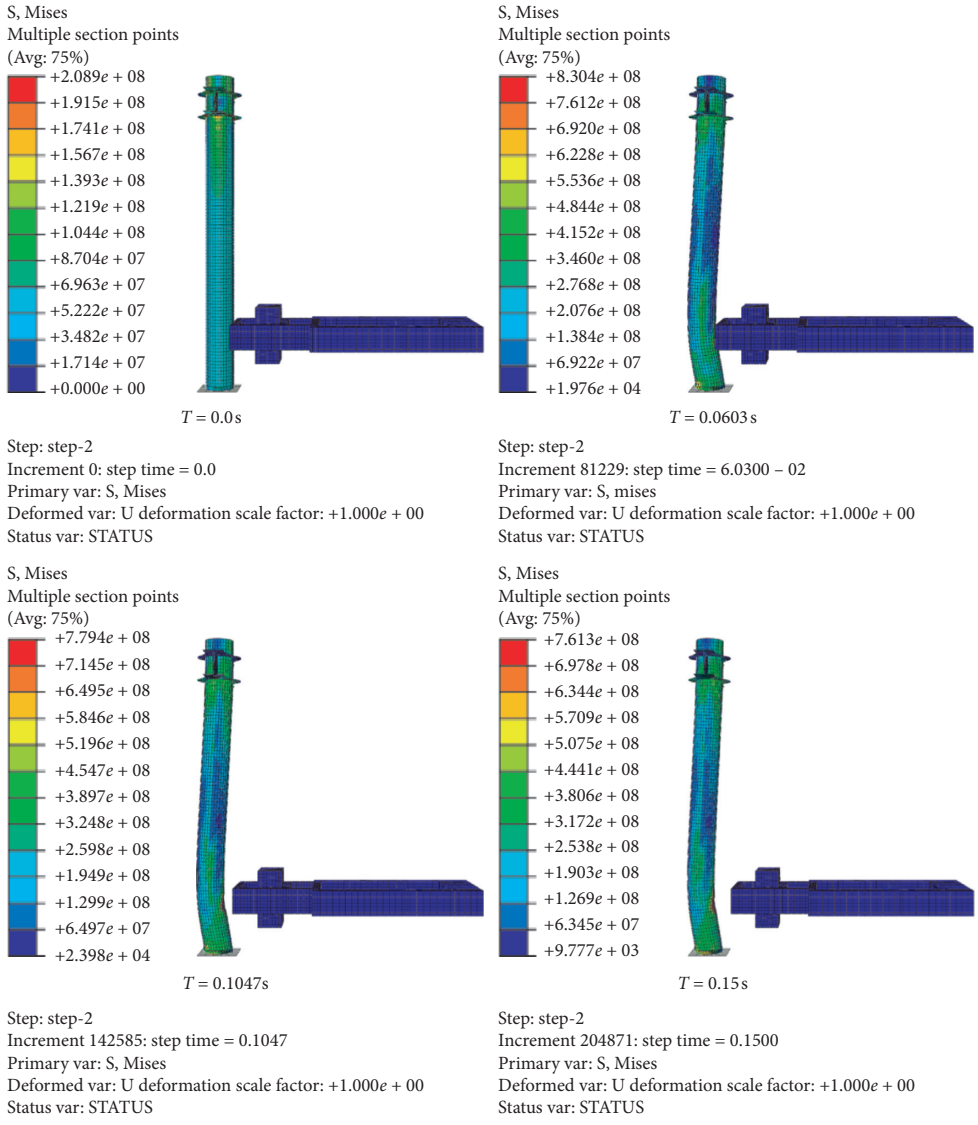

(a)

Figure 9: Continued.

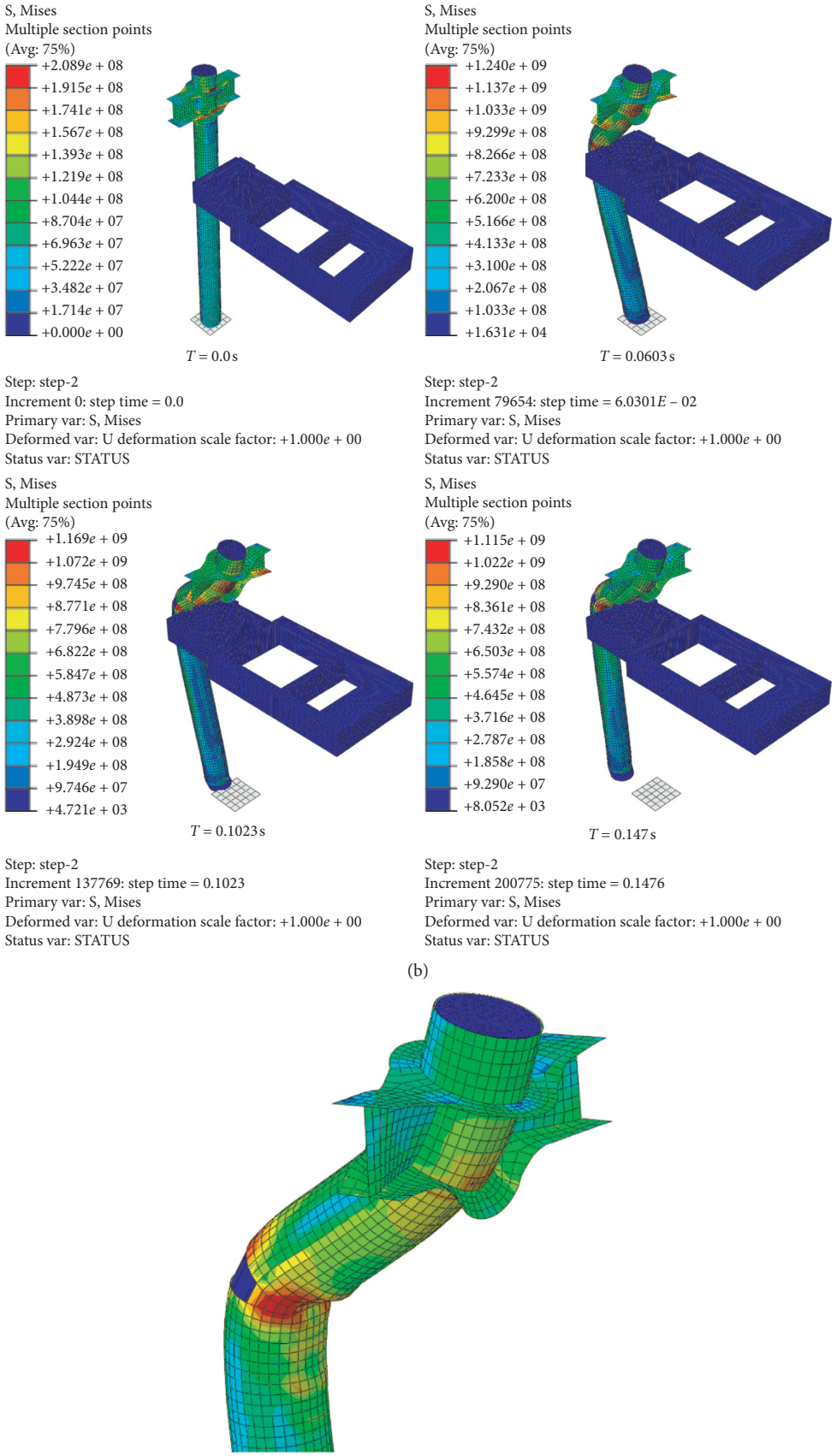

Figure 9: The collapse process by the DS method. (a) Local deformation of column failure. (b) Large deformation of column failure. (c) Failure deformation of the column and joint.

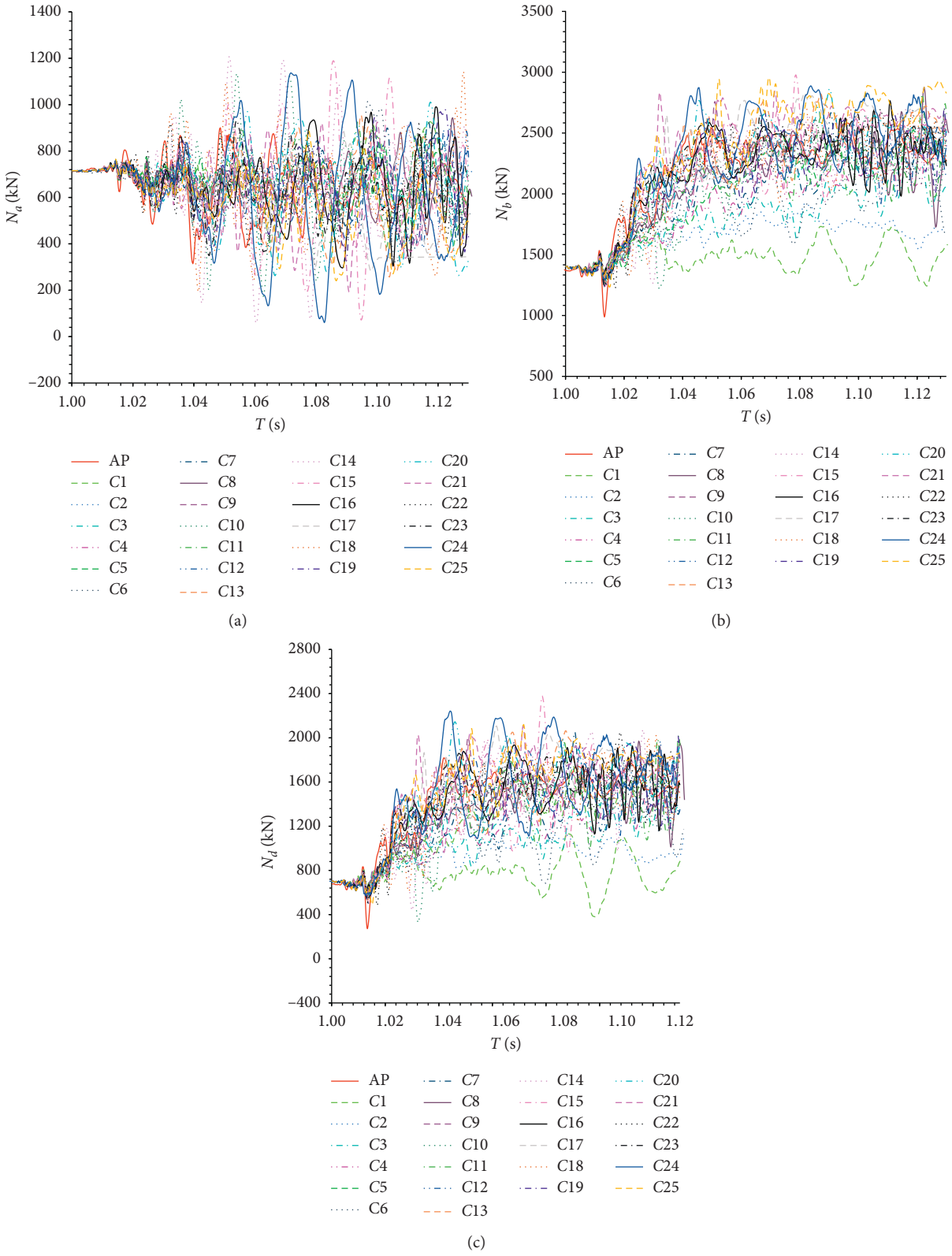

FIGURE 10: Internal force versus time (T) curves. (a) Axial force of the A bottom column. (b) Axial force of the B bottom column. (c) Axial force of the D bottom column.

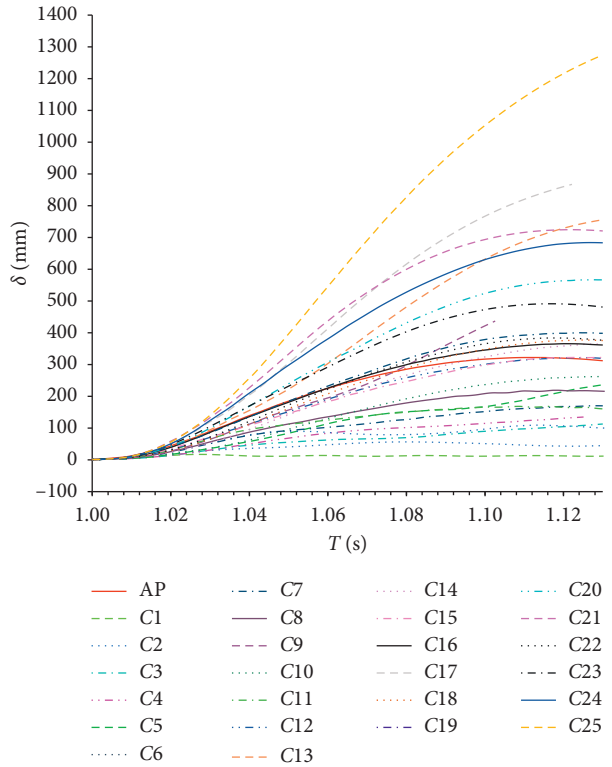

Figure 11: Vertical displacement of the failure column node versus time (T) curves.

Table 3: Summary of data analysis on transverse impact tests.

No.	Impact velocity (km/h)	Impact mass (t)	Impact position (m)	η
$c1$	40	1.5	0.7	**1.23**
$c2$	40	4.5	1.2	**1.37**
$c3$	40	7.5	1.5	**1.62**
$c4$	40	12	1.8	**1.73**
$c5$	40	20	2.5	**1.80**
$c6$	60	1.5	1.2	**1.74**
$c7$	60	4.5	1.5	**1.90**
$c8$	60	7.5	1.8	**2.05**
$c9$	60	12	2.5	**1.96**
$c10$	60	20	0.7	**1.92**
$c11$	80	1.5	1.5	**2.01**
$c12$	80	4.5	1.8	**1.89**
$c13$	80	7.5	2.5	**2.01**
$c14$	80	12	0.7	**1.93**
$c15$	80	20	1.2	**2.12**
$c16$	100	1.5	1.8	**1.97**
$c17$	100	4.5	2.5	**2.02**
$c18$	100	7.5	0.7	**1.94**
$c19$	100	12	1.2	**1.93**
$c20$	100	20	1.5	**2.04**
$c21$	120	1.5	2.5	**2.02**
$c22$	120	4.5	0.7	**1.92**
$c23$	120	7.5	1.2	**1.89**
$c24$	120	12	1.5	**2.06**
$c25$	120	20	1.8	**2.11**
k_1	**1.550**	**1.794**	**1.788**	—
k_2	**1.914**	**1.820**	**1.810**	—
k_3	**1.992**	**1.902**	**1.926**	—
k_4	**1.980**	**1.922**	**1.950**	—
k_5	**2.000**	**1.998**	**1.962**	—
R	**0.45**	**0.204**	**0.174**	

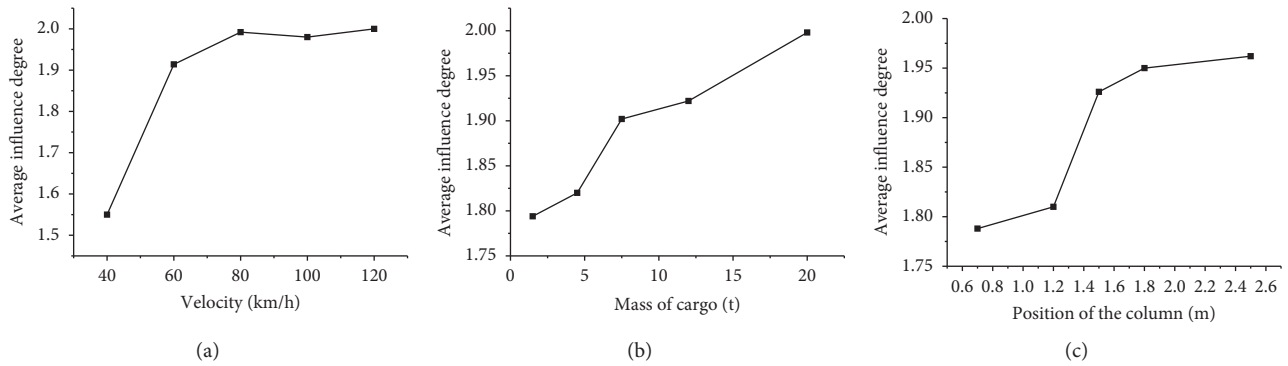

Figure 12: Single-factor analysis. (a) Velocity influence. (b) Massin fluence. (c) Position influence.

variation parameter η for the B pillar was introduced as the ratio of the postimpact axial force to that of preimpact in Table 3. By the principle of orthogonal design, the sum of the parameters η in the velocity (or mass and position) factor at the i level is given by K_i,

$$K_i = \sum_{j=1}^{n} \eta_{ji}, \tag{1}$$

where η_{ji}—the ratio value of velocity (or mass and position) factor for the jth test of frame at the ith level; n—the number of occurrences of each level in 25 tests, $n = 25/5 = 5$, $1 \le i \le 5$, $1 \le j \le 5$.

The average value of velocity (or mass and position) factor at each level is obtained by k_i, whose formula is shown in Table 3:

$$k_i = \frac{K_i}{n(i = 1, 2, 3, 4, 5)}. \tag{2}$$

For every factor (velocity, mass, or position), the parameter R value is the largest one of these five numbers minus the smallest one, which reflected the change with the level fluctuation of this factor. The R value is larger, and the influence factor is more important. According to the value of R, the order of the importance of the factors can be determined, and it can be seen that the most obvious factor is the velocity, as shown in Table 3.

$$R = \max(k_i) - \min\left(k_j\right)(i, j = 1, 2, 3, 4, 5). \tag{3}$$

The single-factor analysis is also shown in Figure 12, from which the following conclusions can be drawn: velocity in the range of 40–80 km/h, and the average influence degree increased significantly with the increase of velocity value, more than 80 km/h less affected in Figure 12(a). As shown in Figure 12(b), the effect of mass on the average influence degree is close to linear growth. It can be concluded from Figure 12(c) that the average influence degree increased with the increase of the distance of the impact point from the bottom of the column.

4. Conclusions

The application of two methods including the AP method and the DS method is discussed in this paper, which is studied on resisting the progressive collapse of the concrete-filled steel tubular (CFST) frame structure under low-velocity impact load. The conclusions and recommendations from this study can be summarized as follows:

(1) It is presented that the most obvious factor is the velocity for every factor (velocity, mass, or position) on impact effect.

(2) From the collapse criterion, no frame-progressive collapse occurred via the AP method; however, the vertical collapse nearly occurred by the DS method. Due to the failure of the C column in a moment by the AP method, the internal force of the remaining structure is redistributed. The loading which was once carried by the C column is transferred to the adjacent columns, and finally, a new equilibrium state of the structure is reached. It can be seen that the resisting collapse capacity of the CFST frame under impact loading cannot be accurately estimated by this method because the specific cause of component failure is not considered and the analysis is oversimplified.

(3) In the DS method, the C column failed in a very short time due to the rapid violent impact of the car. At the same time, some dynamic response and degree of damage are produced on the members adjacent to the C column immediately, resulting in a large vertical displacement, and the collapse may appear. The result by the DS method is closer to the actual condition, and the collapse process of the structure under impact load can be accurately described.

Data Availability

The data used to support the findings of this study are included within the article.

Conflicts of Interest

The authors declare no conflicts of interest.

Acknowledgments

This research was financially supported by the Natural Science Foundation of Chongqing (No. cstc2019jcyj-

msxmX0440), the Science and Technology Research Program of the Chongqing Municipal Education Commission (Grant No. KJQN201901339), and the science and technology project of Chongqing University of Arts and Sciences (Nos. 2017RJJ31 and P2018JG13).

References

[1] C. Pearson and N. Delatte, "Lessons from the progressive collapse of the ronan point apartment tower," *Third Forensic Engineering Congress*, pp. 190–200, 2003.

[2] J. D. Osteraas, "Murrah Building Bombing Revisited: a qualitative assessment of blast damage and collapse patterns," *Journal of Performance of Constructed Facilities*, vol. 20, no. 4, pp. 330–335, 2006.

[3] Z. P. Bažant, J. L. Le, F. R. Greening et al., "What did and did not cause collapse of world trade center twin towers in New York?" *Journal of Engineering Mechanics*, vol. 134, no. 10, pp. 892–906, 2008.

[4] GSA, *Progressive Collapse Analysis and Design Guidelines for New Federal Office Buildings and Major Modernization Projects*, US General Services, New York, NY, USA, 2013.

[5] Eurocode1-Actions on Structures, Part1-7: General Actions-Accidental Actions. EN1991-1-7. 2005.

[6] Japanese Society of Steel Construction Council on Tall Buildings, "Guidelines for collapse control design, I Design," *Journal of Womens Health*, 2005.

[7] Japanese Society of Steel Construction Council on Tall Buildings and Urban, "Guidelines for collapse control design, II Research," *Journal of Womens Health*, 2005.

[8] DoD, "Design of structures to resist progressive collapse," US Department of Defense (DoD), New York, NY, USA, 2009.

[9] Chinese standard CECS28, *Technical Specification for Concrete-Filled Steel Tubular Structures*, Chinese Standard, Beijing, China, 2012.

[10] M. M. Kou, Y. J. Lian, and Y. T. Wang, "Numerical investigations on crack propagation and crack branching in brittle solids under dynamic loading using bond-particle model," *Engineering Fracture Mechanics*, vol. 212, pp. 41–56, 2019.

[11] M. Kou, J. Bi, B. Yuan, and Y. Wang, "Peridynamic analysis of dynamic fracture behaviors in FGMs with different gradient directions," *Structural Engineering and Mechanics*, vol. 75, no. 3, pp. 339–356, 2020.

[12] S. Gerasimidis and J. Sideri, "A new partial-distributed damage method for progressive collapse analysis of steel frames," *Journal of Constructional Steel Research*, vol. 119, pp. 233–245, 2016.

[13] Y. Al-Salloum, T. Almusallam, T. Ngo et al., "Progressive collapse analysis of a medium-rise circular RC building against blast loads," *Asme International Conference on Ocean*, 2016.

[14] Y. Ding, X. Song, and H.-T. Zhu, "Probabilistic progressive collapse analysis of steel frame structures against blast loads," *Engineering Structures*, vol. 147, pp. 679–691, 2017.

[15] J. Jiang and G.-Q. Li, "Disproportionate collapse of 3D steel-framed structures exposed to various compartment fires," *Journal of Constructional Steel Research*, vol. 138, pp. 594–607, 2017.

[16] L. Shan, F. Petrone, and S. Kunnath, "Robustness of RC buildings to progressive collapse: influence of building height," *Engineering Structures*, vol. 183, pp. 690–701, 2019.

[17] J. Wang, B. Uy, D. Li et al., "Progressive collapse analysis of stainless steel composite frames with beam-to-column endplate connections," *Steel and Composite Structures*, vol. 36, no. 4, pp. 427–446, 2020.

[18] D.-Y. Kong, B. Yang, M. Elchalakani, K. Chen, and L.-M. Ren, "Progressive collapse resistance of 3D composite floor system subjected to internal column removal: experiment and numerical simulation," *Journal of Constructional Steel Research*, vol. 172, p. 106208, 2020.

[19] M. El-Desoqi, M. Ehab, and H. Salem, "Progressive collapse assessment of precast reinforced concrete beams using applied element method," *Case Studies in Construction Materials*, vol. 13, 2020.

[20] Y. Zhou, T. Chen, Y. Pei et al., "Static load test on progressive collapse resistance of fully assembled precast concrete frame structure," *Engineering Structures*, vol. 200, Article ID 109719, 2019.

[21] J. X. Zhang, G. Shi, Y. Q. Wang et al., "Research on progressive collapse of steel frames," *Steel Construction*, pp. 51–69, 2012.

[22] M. Yousuf, B. Uy, Z. Tao, A. Remennikov, and J. Y. R. Liew, "Impact behaviour of pre-compressed hollow and concrete filled mild and stainless steel columns," *Journal of Constructional Steel Research*, vol. 96, pp. 54–68, 2014.

[23] M. Zeinoddini, G. A. R. Parke, and J. E. Harding, "Axially pre-loaded steel tubes subjected to lateral impacts: an experimental study," *International Journal of Impact Engineering*, vol. 27, no. 6, pp. 669–690, 2002.

[24] L.-H. Han, C.-C. Hou, X.-L. Zhao, and K. J. R. Rasmussen, "Behaviour of high-strength concrete filled steel tubes under transverse impact loading," *Journal of Constructional Steel Research*, vol. 92, pp. 25–39, 2014.

[25] P. S. Symonds, "Survey of methods of analysis for plastic deformation of structures under dynamic loading," *Ciência E Tecnologia De Alimentos*, vol. 31, pp. 967–972, 1967.

[26] L. Chen, S. El-Tawil, and Y. Xiao, "Reduced models for simulating collisions between trucks and bridge piers," *Journal of Bridge Engineering*, vol. 21, no. 6, Article ID 04016020, 2016.

[27] S. El-Tawil, E. Severino, and P. Fonseca, "Vehicle collision with bridge piers," *Journal of Bridge Engineering*, vol. 10, no. 3, pp. 345–353, 2005.

[28] H. Dawson and D. Tennant, "Inelastic dynamic finite-element design of bollard systems to impact loading," *Structures Congress*, 2014.

[29] L. Chen, Y. Xiao, and S. El-Tawil, "Impact tests of model RC columns by an equivalent truck frame," *Journal of Structural Engineering*, vol. 142, no. 5, Article ID 04016002, 2016.

Hindawi
Advances in Materials Science and Engineering
Volume 2021, Article ID 5523989, 19 pages
https://doi.org/10.1155/2021/5523989

Research Article

Chloride Transport Performance of Basalt-Polypropylene Fiber Reinforced Concrete under Drying-Wetting Cycles

Li Su,[1] Ditao Niu ,[1,2] Daguan Huang,[1] and Qiang Fu[1,2]

[1]*School of Civil Engineering, Xi'an University of Architecture and Technology, Xi'an 710055, China*
[2]*State Key Laboratory of Green Building in Western China, Xi'an University of Architecture and Technology, Xi'an 710055, China*

Correspondence should be addressed to Ditao Niu; niuditao@163.com

Received 20 January 2021; Revised 26 February 2021; Accepted 22 March 2021; Published 5 April 2021

Academic Editor: Peng Zhang

This study investigated the chloride transport performance of basalt-polypropylene fiber reinforced concrete (BPFRC) subjected to drying-wetting cycles. The effects of the strength grade, basalt fiber (BF), polypropylene fiber (PF), and hybrid BF-PF on the pore solution pH, chloride concentration distribution, chloride peak concentration (C_{max}), and apparent chloride diffusion coefficient (D_a) of the BPFRC were analyzed, and a multifactor model of D_a was established. Moreover, the microstructures of BPFRC were studied to explore the effect of fibers on chloride transport performance of concrete in terms of theoretical pore volume, fiber-matrix interface, fiber bonding properties, and corrosion morphology. The results showed that the chloride concentration of the BPFRC increased and the pore solution pH of the BPFRC decreased with the increase in the exposure time. The chloride concentration and D_a of the BPFRC decreased with the increase in the strength grade. At a fiber volume content of 0.1%, the addition of BF and PF reduced the chloride concentration and D_a of the BPFRC; at a fiber volume content of 0.2%, the addition of hybrid BF-PF increased the chloride concentration and D_a of the concrete. The chloride peak concentration appeared at the depth of 2 mm inside the concrete, and the change of the chloride peak concentration with exposure time followed the power function model. The theoretical pore volume of the BPFRC specimens decreased initially and then increased with the increase in the exposure time. FE-SEM observed that the bonding property between BF and matrix was better than that of PF, which could effectively control the development of microcracks.

1. Introduction

Concrete is one of the most widely used building materials in the world [1]. However, its typical quasibrittle characteristics, low tensile strength, and low strain capacity have a significant effect on the application and development of concrete structures [2, 3]. The addition of short and disorderly distributed fibers can inhibit the generation and development of microcracks in concrete, control the stress at the crack tip, and play a bridging role, thereby significantly improving the toughness of the concrete [4–6] and increasing its application. At present, two types of fibers are mixed into concrete—rigid fibers and flexible fibers. Rigid fibers, such as steel fiber, carbon fiber, and basalt fiber (BF), have high elastic modulus and can improve the strength and bearing capacity of concrete, and steel fiber can increase the ductility of concrete [7, 8]. Flexible fibers, such as polyethylene fiber and polypropylene fiber (PF), have a low elastic modulus and good chemical stability and ductility and can significantly improve ductility and restrain cracking in concrete [9, 10].

To realize the benefits of various types of fibers and save costs, hybrid fibers of similar or different types and sizes have become an important area of research. Hybrid steel-polypropylene fibers are one of the most widely used hybrid fibers at present, and their synergistic effect can significantly improve the mechanical properties and toughness of concrete, while also improving its impermeability [11, 12]. However, hybrid steel-polypropylene fibers have an inherent fatal defect—the chemical composition of steel fiber is

similar to that of steel bars and is prone to rust in marine environments. Consequently, there is an urgent need to find other rigid fibers to replace steel fibers.

BF is a new type of environment-friendly fiber that has the advantages of excellent chemical stability, large elastic modulus, good wear resistance, and low cost [13]. It is a suitable replacement for steel fibers in hybrid fiber systems in marine environments. Due to differences in their physical and mechanical properties, the addition of BF and PF to concrete can reduce the brittleness of concrete, restrain the development of internal cracks, and improve impermeability [14]. The dispersion of the hybrid fibers in a hybrid fiber system is another important consideration. The addition of admixtures can increase the uniformity of the dispersion of hybrid fibers, improve the bond properties between the fibers and the concrete matrix [15], and improve the durability of concrete [16].

One of the main factors that threaten the durability of concrete structures in marine environments is chloride erosion. Based on the location of a building in a marine environment, the chloride erosion environment can be further divided into marine underwater zone (full immersion) and tidal zone (drying-wetting cycles). Owing to the action of the drying-wetting cycles, the deterioration rate of the structural performance of concrete structures in tidal zone is significantly higher than that in underwater zone, and the diffusion rate of chloride in concrete structures in tidal zone is higher than that in the underwater zone as well [17–19]. Consequently, the time required to reach the chloride concentration limit of steel bar corrosion in concrete is reduced [20], which is very easy to cause steel bar corrosion and shortens the service life of buildings.

At present, most researchers study the durability of basalt-polypropylene fiber reinforced concrete (BPFRC) through rapid chloride permeation and water absorption [16, 21–24]. However, very few studies exist on the chloride transport performance of BPFRC subjected to drying-wetting cycles. In this study, the long-term chloride transport performance of BPFRC subjected to drying-wetting cycles was investigated. The free chloride concentration and pore solution pH in the BPFRC were measured at various depths, and the effects of the strength grade, BF, PF, and hybrid BF-PF on pore solution pH, chloride concentration, chloride peak concentration (C_{max}), and apparent chloride diffusion coefficient (D_a) were analyzed. In addition, a multifactor model of D_a was established considering the effects of the exposure time, strength grade, and fibers content (BF and PF). Finally, the microstructures of BPFRC before and after erosion, such as theoretical total pore volume (P), the bonding performance between fiber and concrete matrix, and corrosion morphology, were evaluated by thermogravimetry (TG) and field emission scanning electron microscope (FE-SEM).

2. Materials and Experimental Methods

2.1. Raw Materials. The cementitious materials used to prepare the BPFRC specimens included P. O. 42.5 ordinary Portland cement (C), fly ash (FA), silica fume (SF), and granulated blast furnace slag (GGBS). The chemical composition and physical properties of the cementitious materials are listed in Tables 1–3. The appearance of the BF and PF are shown in Figure 1. The length, diameter, density, tensile strength, elastic modulus, elongation, and aspect ratio of the BF, prepared by Aerospace Tuoxin Basalt Industry Co., Ltd., Sichuan, China, were 18 mm, 15 μm, 2.56 g/cm^3, 4500 MPa, 75000 MPa, 3.15%, and 1200, respectively, and those of the PF, prepared by Subote New Material Co., Ltd., Jiangsu, China, were 19 mm, 30 μm, 0.91 g/cm^3, 270 MPa, 3000 MPa, 40%, and 633, respectively. The coarse aggregate (CA) was limestone gravel with a particle size of 5–20 mm and an apparent density of 2.7 g/cm^3. River sand with a fineness modulus and apparent density of 2.8 and 2.63 g/cm^3, respectively, was used as the fine aggregate (S). The mixed water (W) was laboratory tap water. A polycarboxylate superplasticizer (PBS) with a water-reducing rate of 30% was used.

2.2. Mix Proportions and Specimen Preparation. Seven groups of BPFRC specimens were fabricated. The detailed mix proportions of the BPFRC specimens are shown in Table 4. Groups 1–3 were used to compare the effects of different strength grades using the optimal mix proportions obtained from an orthogonal test. Groups 2 and 4–7 were used to compare the effect of single and hybrid fiber on the chloride transport performance of concrete and were fabricated based on the optimal mix proportion of the strength grade C40. HC, BC, PC, and BPC represent concrete without fiber, BF reinforced concrete, PF reinforced concrete, and hybrid BF-PF reinforced concrete, respectively. BF and PF are mixed such that equal volume content is obtained. The first group of numbers after the letters indicates the concrete strength grade and the second group of numbers indicates the fiber volume content. For example, BPC-30-0.1 denotes the fact that the fiber type is hybrid BF and PF, the concrete has a strength grade of C30, and the fiber volume content is 0.1%.

The mixing process of the BPFRC was as follows:

(i) The dried CA and S were poured into the mixer and mixed for 30 s;

(ii) Cementitious materials (C, FA, SF, and GGBS) were added and stirred for 2 min;

(iii) PF and BF were added to the mix and stirred for 2 min and 3 min, respectively;

(iv) W and PBS were poured into the mixture and stirred for 2 min.

The evenly mixed concrete mixtures were poured into 100 mm × 100 mm × 100 mm cube molds and vibrated on a shaking table for 15 s. After 24 h, the specimens were demolded and placed in a standard curing room maintained at a temperature of (20 ± 2)°C and a humidity of 95% for 28 d. Subsequently, the chloride diffusion test was conducted.

2.3. Experiment and Testing Methods

2.3.1. Chloride Drying-Wetting Cycle Test. High temperature and drying-wetting cycles were used to simulate the extreme

Table 1: Chemical composition of cementitious materials.

Composition (wt. %)	SiO_2	Al_2O_3	Fe_2O_3	CaO	MgO	SO_3	K_2O	Na_2O	MnO
C	21.18	5.02	3.14	63.42	3.12	2.3	0.65	0.42	0.05
FA	35.71	16.57	8.92	21.14	1.41	1.94	2.18	1.02	0.1
SF	85.04	0.97	1.04	1.63	0.32	—	0.81	0.19	0.32
GGBS	34.65	14.21	0.49	34.11	11.15	1.01	0.30	0.35	0.21

Table 2: Physical and mechanical properties of cement.

Density (g/cm^3)	Specific area surface (m^2/kg)	Fineness (%)	Ignition loss (%)	Setting time (h)		Compressive strength (MPa)		Flexural strength (MPa)	
				Initial	Final	3 d	28 d	3 d	28 d
3.10	334	3.8	2.79	2.3	3.4	28.8	48.6	6.4	8.6

Table 3: Physical properties of admixtures.

Type	FA	SF	GGBS
Water content (%)	0.2	0.06	0.7
Density (g/cm^3)	2.35	2.10	2.86
Ignition loss (%)	2.85	5.48	0.31
Specific area surface (m^2/kg)	340	23000	410
Fineness (%)	17	—	—
Average particle size (μm)	—	0.12	14.5

(a) (b)

Figure 1: Morphology of fibers. (a) Basalt fiber. (b) Polypropylene fiber.

Table 4: Mix proportions of BPFRC (kg/m^3).

	Mixture	C	SF	FA	GGBS	PBS	W	W/C	S	CA	BF	PF
1	BPC-30-0.1	234.2	22	73.2	36.6	3.66	161	0.44	683	1162.9	1.3	0.5
2	BC-40-0.1	241.6	15.8	79.2	59.4	3.96	150.5	0.38	683.4	1163.6	2.6	0
3	BC-50-0.05	333.1	29	48.3	72.4	4.83	140	0.29	774.1	1026.1	1.3	0
4	HC-40	241.6	15.8	79.2	59.4	3.96	150.5	0.38	683.4	1163.6	—	—
5	PC-40-0.1	241.6	15.8	79.2	59.4	3.96	150.5	0.38	683.4	1163.6	—	0.9
6	BPC-40-0.1	241.6	15.8	79.2	59.4	3.96	150.5	0.38	683.4	1163.6	1.3	0.5
7	BPC-40-0.2	241.6	15.8	79.2	59.4	3.96	150.5	0.38	683.4	1163.6	2.6	0.9

heat and humidity of ocean tidal zones. Before the experiment, an epoxy resin was used to seal each specimen, leaving only one surface free as the erosion surface, to study the chloride transport in one-dimensional space. The specimens were immersed in a closed box filled with NaCl solution (at a temperature of 28°C and a concentration of 3.5%) for 1 d and then dried at 50°C for 1 d, as shown in Figure 2. Five drying-wetting cycle durations were simulated, including 30 d (15 cycles), 60 d (30 cycles), 90 d (45 cycles), 120 d (60 cycles), and 180 d (90 cycles). As the immersion temperature was higher than the general environment, the NaCl solution was replaced every 5 d to ensure a constant concentration of solution. After the drying-wetting cycles test, the specimens were ground in layers using a grinder (1–10 mm, 1 layer/1 mm; 11–20 mm, 1 layer/2 mm) and passed through a 0.16 mm sieve. The powder was stored in a sealed bag for chloride concentration, pore solution pH, and TG testing.

2.3.2. Chloride Concentration and Pore Solution pH Testing. The free chloride concentration and pore solution pH in the BPFRC were measured using the solid-liquid extraction method [25] and the potentiometric method [26]. Solid-liquid extraction is the operation of separating substances from solids by liquid; that is, the eroded concrete powder is soaked in deionized water, the chloride ion is dissolved in deionized water after soaking for a corresponding time, and the filtrate is extracted by filtration. The test procedure is shown in Figure 3. The chloride ion concentration in the filtrate was measured using PXSJ−216F titrator with chloride ion electrode and saturated potassium sulfate reference electrode. The free chloride concentration in the BPFRC was calculated as follows:

$$W_{Cl^-} = \frac{M \times 10^{-pX} \times V}{G} \times 100\%, \tag{1}$$

where W_{Cl^-} is the concentration of free chloride in the BPFRC specimen, %; M is the molar mass of a chloride ion, 35.45 g/mol; pX is the negative logarithm of the free chloride concentration; V is the deionized water volume during immersion, 100 ml; and G is the mass of the soaked powder, 5.000 g.

2.3.3. Thermogravimetric Testing. The thermogravimetric differential scanning of the BPFRC samples subjected to various drying-wetting cycle durations was performed using a METTLER TOLEDO TGA/DSC 2. The mass of the test sample was 15 mg, the heating rate was 10 °C/min, the heating range was 30–900°C, and the protective gas used during the test was N_2 (99% purity).

2.3.4. Porosity Testing. Diamond [27] demonstrated that the theoretical total pore volume of concrete can be evaluated based on the mass loss of the sample measured by TG. Although the detailed pore size distribution is not obtained, this method serves as an evaluation method to characterize the pore structure of concrete [27, 28]. The theoretical pore volume calculation method established by Diamond is only suitable for mortar specimens; for concrete specimens, the influence of the coarse aggregate must be considered. Consequently, the equation to calculate the theoretical pore volume of concrete is as follows:

$$\begin{aligned} P(\%) &= \frac{V_p}{V_w + V_G} \times 100\% = \frac{M_w - (\mathrm{BW}/1.3)}{M_w + (M_G/\rho_G)} \times 100\%, \\ \frac{M_G}{\rho_G} &= \frac{M_c}{\rho_c} + \frac{M_{\mathrm{FA}}}{\rho_{\mathrm{FA}}} + \frac{M_{\mathrm{SF}}}{\rho_{\mathrm{SF}}} + \frac{M_{\mathrm{GGBS}}}{\rho_{\mathrm{GGBS}}} + \frac{M_{\mathrm{CA}}}{\rho_{\mathrm{CA}}} + \frac{M_S}{\rho_S}, \\ \mathrm{BW}(\%) &= \frac{M_{50} - M_{550}}{M_{550}} \times 100\%, \end{aligned} \tag{2}$$

where P is the theoretical pore volume, V_{P} is the volume of pores, V_{W} is the volume of the mixing water, V_{G} is the volume of the other components (including C, FA, SF, GGBS, CA, and S), M_{W} is the mass of the mixing water, M_{G} is the mass of all the other components except water (including C, FA, SF, GGBS, CA, and S), ρ_{G} represent the density values of the C, FA, SF, GGBS, CA, and S, respectively, BW is the content of the bound water and 1.3 is the average density of BW [29], M_{C}, M_{FA}, M_{SF}, M_{GGBS}, M_{CA}, and M_{S} are the masses of the C, FA, SF, GGBS, CA, and S, respectively, ρ_C, ρ_{FA}, ρ_{SF}, ρ_{GGBS}, ρ_{CA}, and ρ_S are the densities of C, FA, SF, GGBS, CA, and S, respectively, and M_{50} and M_{550} represent the mass values of sample measured by TG at 50°C and 550°C.

2.3.5. Microscopic Testing. After 0 d and 180 d of erosion, the BPFRC specimens were broken, and the mortar fragments with diameter of approximately 5 mm and smooth neat surface were selected as the test samples. During the test, the sample was first adhered to the bracket with double-sided conductive adhesive, and then the sample was sprayed with gold. Finally, the distribution of fibers in concrete and the microstructure of eroded concrete were observed using Zeiss GeminiSEM 500 FE-SEM.

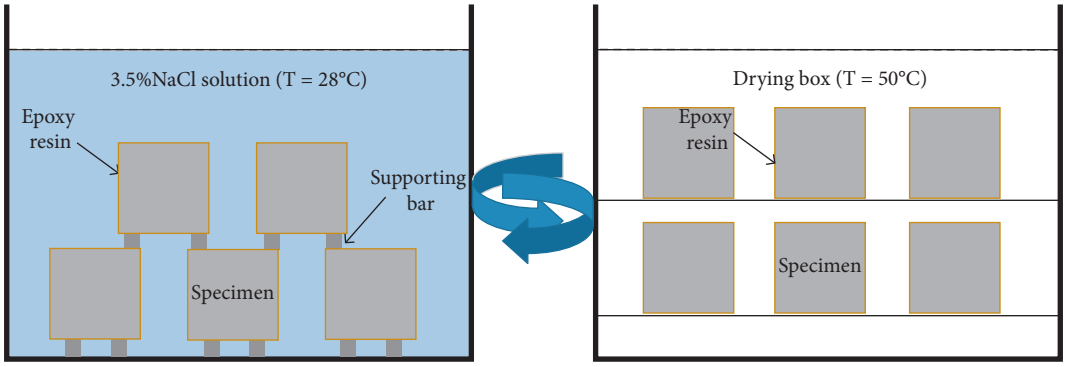

Figure 2: Schematic diagram of drying-wetting cycle test.

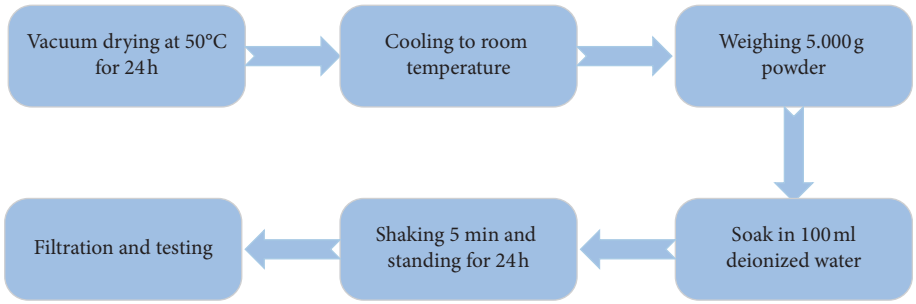

Figure 3: Testing process of pore solution pH and chloride concentration.

3. Results and Discussion

3.1. Pore Solution pH of BPFRC Subjected to Drying-Wetting Cycles

3.1.1. Effect of Strength Grade on Pore Solution pH. The pore solution pH of the BPFRC specimens with different strength grades is shown in Figure 4. As shown, the pH gradually decreases with an increase in the exposure time. This is because, in order to balance the anion charge during the erosion, OH^- ions dissolve out while chloride ions enter the concrete through capillary adsorption and diffusion, leading to a continuous decrease in the pore solution pH [30]. The higher strength grade for the BPFRC results in a higher pH value. The pH value at the 1 mm depth of C50 concrete is 2.43%–3.77% higher than that of the C30 concrete. During the drying-wetting cycle, the rate of reduction in the pH is slower, and the rising range of pH is small. After 180 d of exposure time, the pH value at a depth of 2 mm on concrete surface decreases from 11.92 of C50 concrete (BP-50-0.05) to 11.60 of C30 concrete (BPC-30-0.1). With the decrease in the strength grade, the porosity increased. During the drying process, the water in the pores evaporated more easily, and the concrete saturation decreased. During the subsequent wetting process, capillary adsorption was enhanced, and chloride ion exchange increased. Therefore, the pore solution pH of the low-strength grade BPFRC decreased rapidly.

3.1.2. Effect of Fibers on Pore Solution pH. The effect of BF, PF, and hybrid BF-PF on the pore solution pH of C40 concrete is shown in Figure 5. It can be seen from Figure 5 5(a) that the pH value of HC-40 concrete after 180 d of erosion is significantly lower than that after 120 d, especially at the depth of 3–10 mm. The main reason is that chloride enters into the concrete through capillary adsorption and diffusion in the process of continuous drying-wetting cycle, and the chloride concentration at different depths increases with the increase of erosion time. When chloride ions enter into the concrete, Ca^{2+} in the alkaline material will dissolve, which makes the hydration products decompose due to decalcification, resulting in the pH value of concrete to be greatly reduced in the later stage of erosion. With the addition of fiber, the pore size distribution of concrete is wider, which leads to the more prominent "ink bottle effect" in the process of drying-wetting cycle, and the more difficult evaporation and adsorption of water in concrete. Therefore, the decline of pH of fiber concrete is uniform in the process of erosion. At a depth of 2 mm below the surface of the specimen, the pH value of the specimen without fiber was the highest at 30 d of erosion time, which was 12.13, and the pH value of the specimen with 0.1% BF was the highest at 180 d of erosion time, which was 11.75. When the fiber volume content was 0.1%, the addition of BF, PF, and hybrid BF-PF increased the pH value at 180 d of exposure time, while a hybrid fiber content of 0.2% reduced the pH value of the concrete. The results demonstrate that an appropriate fiber content, whether BF or PF alone, or hybrid BF-PF, can inhibit the decrease in the pore solution pH during the later stages of erosion. This is because an appropriate amount of fiber can optimize the pore size distribution and reduce the

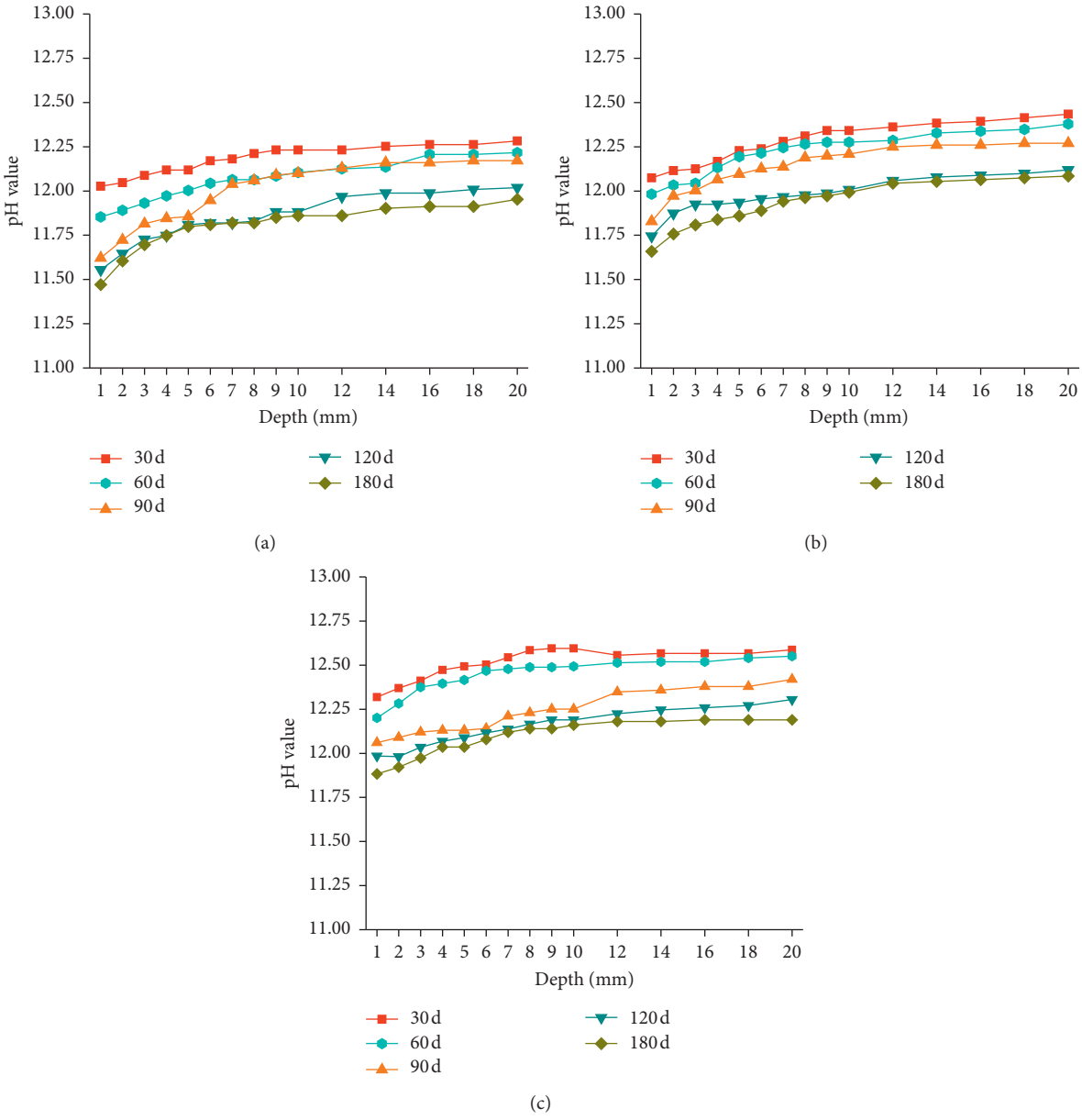

Figure 4: Pore solution pH of BPFRC with different strength grades. (a) BPC-30-0.1. (b) BC-40-0.1. (c) BC-50-0.05.

porosity and degree of anion exchange. With a high fiber content, the interface between the fiber and the matrix increases, a loose matrix and pores are formed around the fiber, the compactness of the concrete decreases, the capillary pore increases [31, 32], the chloride diffusion rate increases, the dissolution of alkaline substances increases, and the pore solution pH decreases rapidly during the process of erosion.

3.2. Chloride Concentration of BPFRC Subjected to Drying-Wetting Cycles

3.2.1. Effect of Strength Grade on Chloride Concentration. The chloride concentration distribution in the BPFRC specimens with different strength grades is shown in Figure 6. The chloride concentration increased from the concrete surface, and the C_{max} and convection zone appeared at a depth of 2 mm from the concrete surface; subsequently, it decreased and stabilized. The chloride concentration at each depth gradually increased the exposure time, but the increasing range gradually decreased. At a depth of 4 mm in BPC-30-0.1 specimen, the chloride concentration after 60 d of erosion was 15.72% higher than that after 30 d of erosion, while the chloride concentration after 180 d of erosion was 4.83% higher than that after 120 d of erosion. This is because the hydration of cementitious materials was still in progress during the drying-wetting cycles, decreasing the penetration rate of the chloride ions [33].

As the strength grade increased, the chloride concentration at a given depth in the concrete decreased, the chloride distribution curve was smoother, and the chloride diffusion range was smaller. After 30 d of erosion, the

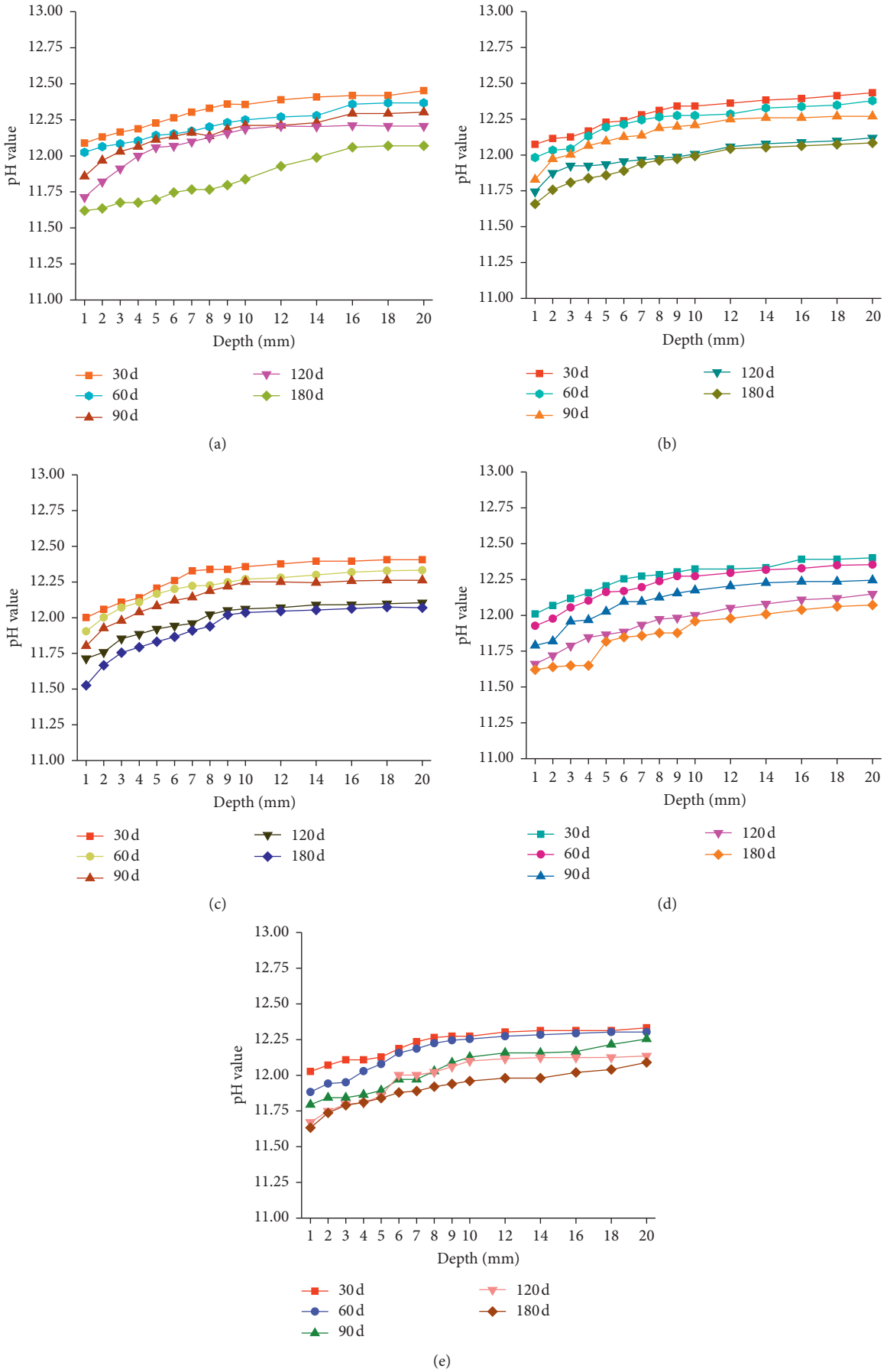

Figure 5: Pore solution pH of C40 concrete with different fiber type and content. (a) HC-40. (b) BC-40-0.1. (c) PC-40-0.1. (d) BPC-40-0.1. (e) BPC-40-0.2.

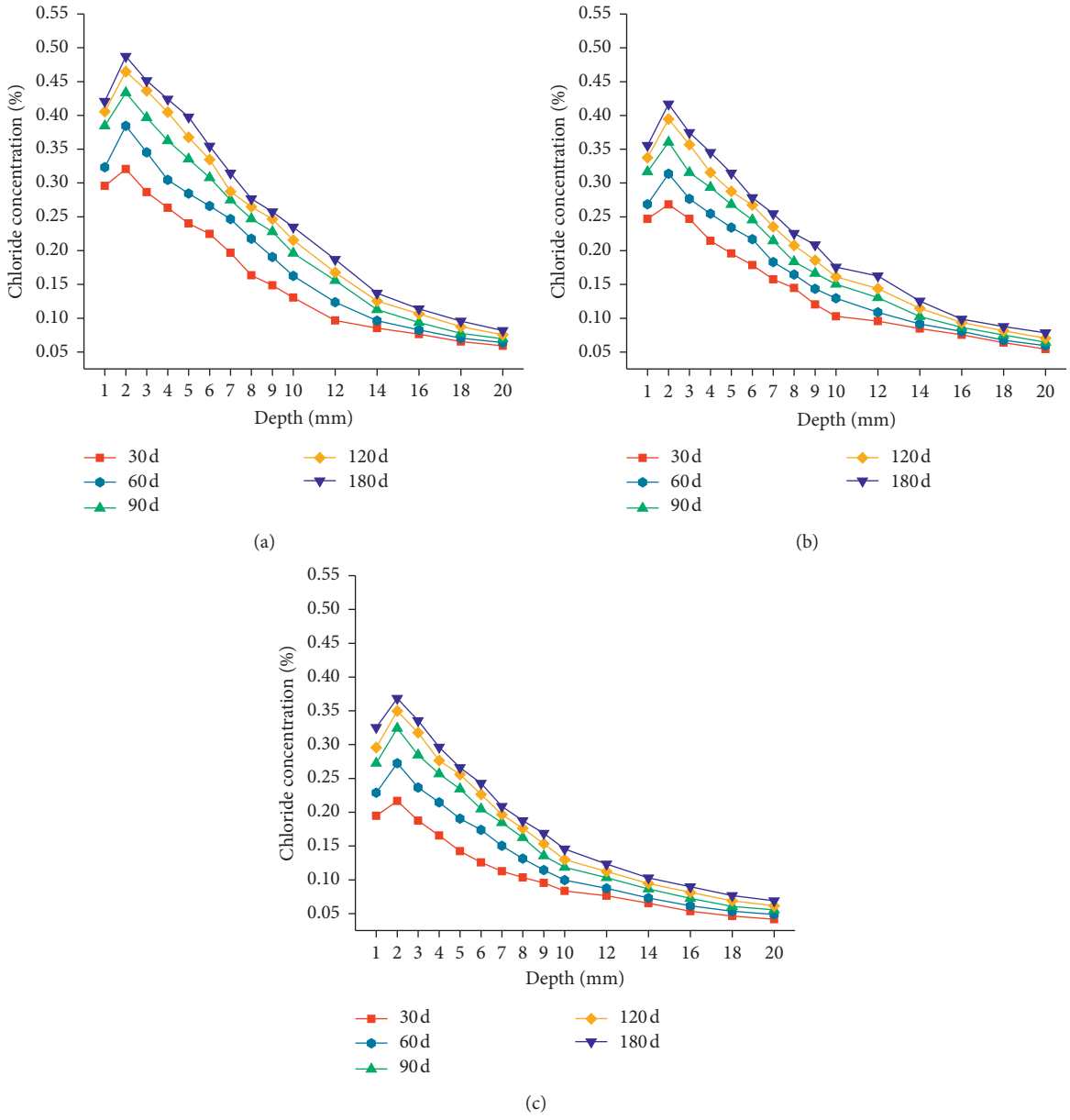

Figure 6: Chloride concentration distribution of BPFRC with different strength grades. (a) BPC-30-0.1. (b) BC-40-0.1. (c) BC-50-0.05.

chloride concentration at a depth of 2 mm decreased from 0.32% of C30 concrete (BPC-30-0.1) to 0.21% of C50 concrete (BC-50-0.05), a decrease of 34.4%. However, after 180 d of erosion, the chloride concentration decreased from 0.48% of C30 concrete (BPC-30-0.1) to 0.36% of C50 concrete (BC-50-0.05), a decrease of 25%. The porosity of BPFRC with low strength is higher, and the transport rate of chloride is faster in the wetting process. In the drying process, the water in the pores of low-strength concrete is easier to evaporate, the drying degree of surface concrete is greater, and the capillary negative pressure is higher. Therefore, in the next wetting process, the capillary adsorption is obvious, and more chloride ions enter into the concrete [34].

3.2.2. Effect of Fibers on Chloride Concentration. The effect of BF, PF, and hybrid BF-PF on the chloride concentration distribution in the BPFRC specimens is shown in Figure 7. At a fiber content of less than 0.1%, the addition of fiber hindered the entry of chloride ions into the concrete. However, when BF and PF were mixed, and the fiber content reached 0.2%, the chloride ion entry into the concrete accelerated. Considering the various erosion times, the order of the BPFRC chloride concentration from low to high was as follows: BC-40-0.1<BPC-40-0.1< PC-40-0.1< HC-40 <BPC-40-0.2. At the same volume content, the effect of the hybrid BF-PF on the chloride concentration at a given depth in the concrete was between those of the two fibers acting

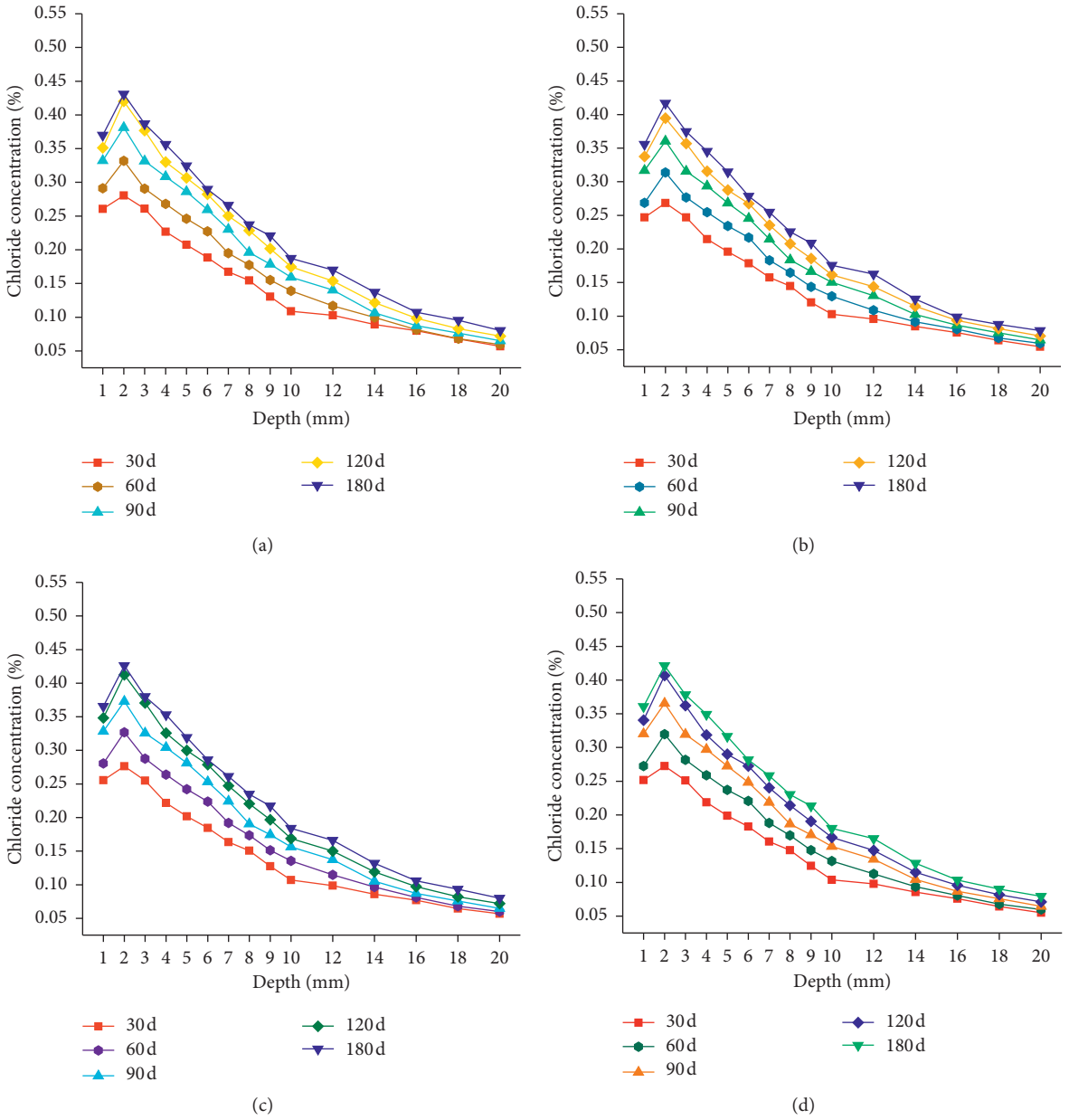

Figure 7: Continued.

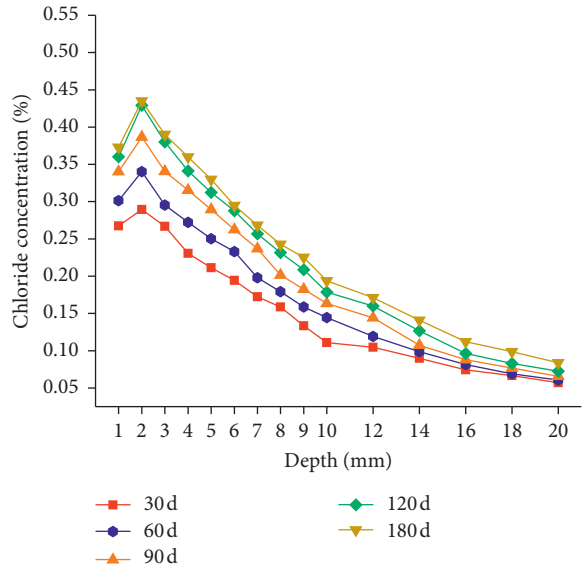

(e)

Figure 7: Chloride concentration distribution of C40 concrete different fiber type and content. (a) HC-40. (b) BC-40-0.1. (c) PC-40-0.1. (d) BPC-40-0.1. (e) BPC-40-0.2.

alone. After 30–180 d of erosion, the chloride concentration at a depth of 2 mm in BC-40-0.1, PC-40-0.1, BPC-40-0.1, and BPC-40-0.2 concrete was 6.07%–3.26%, 2.19%–1.11%, 4.07%–2.21%, and −3.2% to −0.91% lower than HC-40 concrete, respectively. This is because the hybrid fiber content was excessive, the fiber dispersion decreased, the BF introduced more pores, and the bond performance between PF and the concrete matrix decreased, resulting in an increase in the number of internal defects in the concrete [35]. Therefore, the capillary effect of concrete during the erosion increased, the chloride concentration in the convection zone was higher, and the diffusion driving force increased, leading to an increase in the chloride concentration at a given depth.

3.3. Chloride Peak Concentration of BPFRC. Concrete structures located in the ocean tidal zone are usually in an unsaturated state. Chloride ions accumulate on the surface due to the evaporation of pore liquids and the convection of chloride ions, forming a peak concentration in the convection zone. This acts as the driving force for chloride diffusion inside the concrete structure. The chloride concentration deep inside the concrete also increases accordingly. Figure 8 presents C_{max} of seven groups of BPFRC at different exposure times. It can be seen that although C_{max} exhibits fluctuations randomly with the strength grade, fiber type, and content varying, C_{max} of each group of concrete fluctuates within ±15% of the average value at different exposure times. With the increase of exposure time, C_{max} of BPFRC gradually increases, but the increasing range gradually decreases and finally tends to be stable. Therefore, the change of C_{max} of BPFRC is time-dependent. Some studies have shown that the variation of C_{max} with time can be described as linear, power, exponential, square root, and logarithmic functions [36–39].

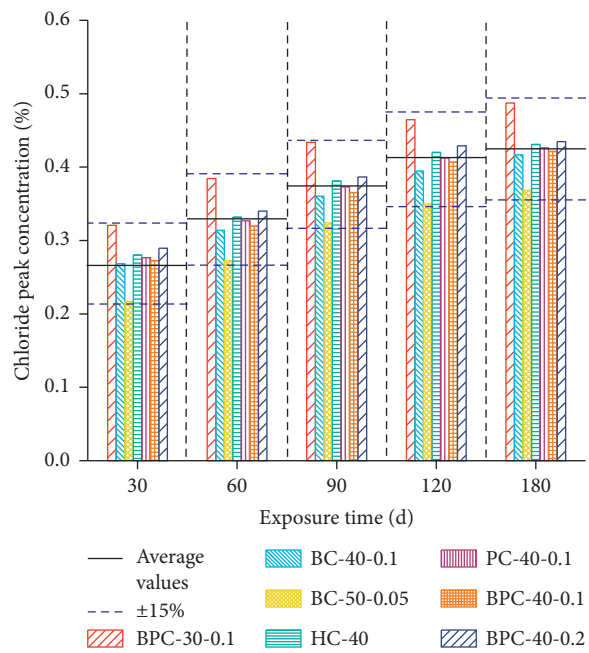

Figure 8: Chloride peak concentration of BPFRC at different exposure time.

The above five functions were used to fit the average value of C_{max} of BPFRC specimens with the exposure time, and the fitting results are shown in Figure 9. It can be seen that the fitting accuracy of linear function, exponential function, and square root function is relatively low. Although the fitting accuracy of logarithmic function is the highest, its initial value is negative, which is not consistent with the actual situation. Therefore, the power function model was finally selected to describe the change of peak

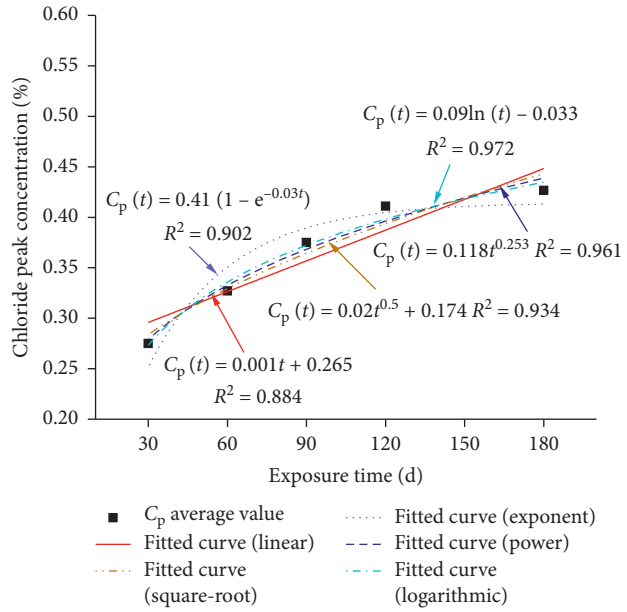

FIGURE 9: Fitted curves of time-dependent chloride peak concentration.

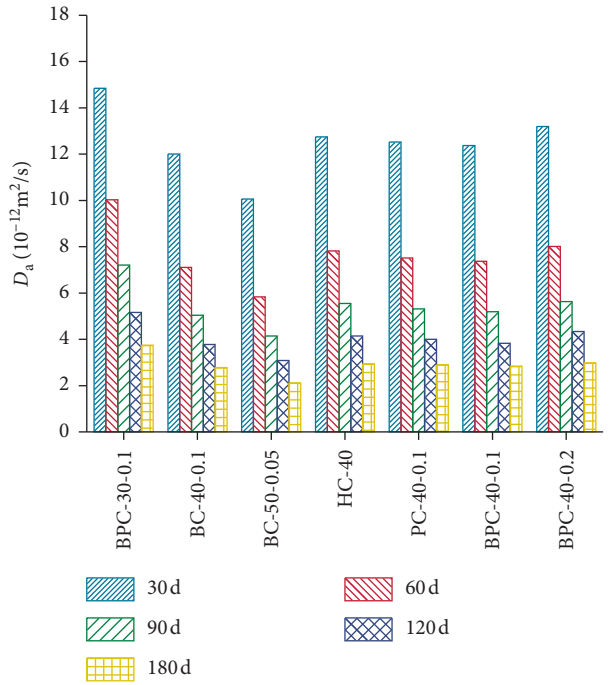

FIGURE 10: Apparent chloride diffusion coefficient of BPFRC.

chloride concentration of BPFRC with exposure time, as shown in the following equation:

$$C_{max}(t) = 0.118t^{0.253}, \quad (3)$$

where $C_{max}(t)$ is the chloride peak concentration at different exposure times (%) and t is the exposure time of the BPFRC (d).

3.4. Chloride Diffusion Coefficient of BPFRC

3.4.1. Analysis of Factors Influencing Chloride Diffusion Coefficient. In concrete subjected to drying-wetting cycles, the concrete is unsaturated, and the convection zone and C_{max} are formed in the surface layer after the chloride ion has entered the concrete. The value of D_a calculated using Fick's second law is unreliable. Andrade et al. [40] proposed a novel method to calculate D_a that first removes the chloride ion increase stage, then calibrates the depth position coordinates with C_{max} as the zero point, and finally fits the descending section. Chang et al. [41] verified the suitability of this method for calculating D_a in concrete subjected to drying-wetting cycle. The equation to calculate D_a is as follows:

$$C(x,t) = C_0 + \left(C_{s,\Delta x} - C_0\right) \times \left[1 - \text{erf}\frac{x - \Delta x}{2\sqrt{D_a(t)t}}\right], \quad (4)$$

where $C(x, t)$ is the chloride concentration in concrete subjected to a drying-wetting duration t and at a depth x, C_0 is the initial chloride concentration, $C_{s,\Delta x}$ is the chloride concentration at the depth of the convection zone, erf () is the error function, and $D_a(t)$ is the apparent chloride diffusion coefficient.

D_a of the BPFRC specimens under different exposure times was calculated using (4), as shown in Figure 10. D_a for all the BPFRC specimens decreased with increase in the exposure time. The strength grade had a significant effect on D_a; the apparent chloride diffusion coefficient of BPFRC decreased with an increase in the strength grade. D_a of BPC-30-0.1 after 30 d, 90 d, and 180 d of erosion was 47.67%, 73.99%, and 77.09% higher than that of BC-50-0.05, respectively. Concrete with a high strength grade has a lower porosity and denser matrix, which slows the diffusion rate of chloride ions. Compared to HC-40, after 30 d of erosion, D_a of BC-40-0.1, PC-40-0.1, BPC-40-0.1, and BPC-40-0.2 decreased by 5.79%, 1.75%, 2.91%, and −3.53%, respectively; after 180 d of erosion, D_a of BC-40-0.1, PC-40-0.1, BPC-40-0.1, and BPC-40-0.2 decreased by 5.38%, 1.54%, 3.45%, and −1.46%, respectively. This indicates that the effect of fibers on D_a of concrete decreased with increase in the erosion time.

3.4.2. Multifactor Model of Apparent Chloride Diffusion Coefficient. To investigate the effects of the exposure time, strength grade, and fiber content on D_a of BPFRC, an apparent chloride diffusion coefficient model was established based on the multifactor method, as shown in the following equation:

$$D_a(t,S,V) = D_{ref} \cdot f_1(t) \cdot f_2(S) \cdot f_3(V), \quad (5)$$

where $D_a(t, S, V)$ is the apparent chloride diffusion coefficient considering the exposure time, strength grade, and fiber content, respectively; D_{ref} is the reference chloride diffusion coefficient; and $f_1(t)$, $f_2(S)$, and $f_3(V)$ are the correction coefficients of the exposure time, strength grade, and fiber content, respectively.

(1) Time-Dependent Correction Factor $f_1(t)$. When only considering the time-dependent coefficient of D_a, D_a model can be expressed as follows:

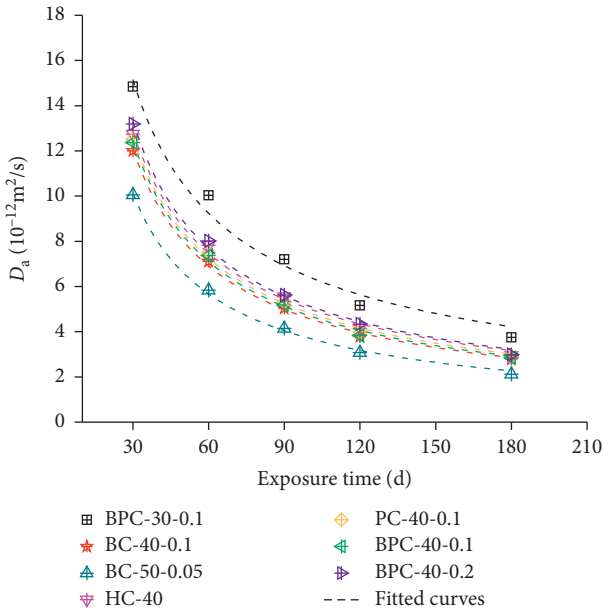

Figure 11: Relationship between apparent chloride diffusion coefficient and exposure time.

$$D_a(t) = D_{\text{ref}}\left(\frac{t_{\text{ref}}}{t}\right)^m, \tag{6}$$

where t_{ref} is the reference time, usually 28 d [42], and m is the time-dependent coefficient.

Time-dependent coefficient is an important parameter that affects the accuracy of concrete life prediction, which is usually related to strength grade, cementitious material, curing time, and exposure conditions [38]. The reference diffusion coefficient and time-dependent coefficient are calculated using (6), and the results are presented in Figure 11 and Table 5. It can be seen that the fitting accuracy values R^2 of all BPFRC specimens are greater than 0.95. The higher the strength grade, the greater the time-dependent coefficient m, indicating that the apparent chloride diffusion coefficient of concrete decreases rapidly with the increase of exposure time, which is consistent with the research results of Huang et al. [37]. Compared with the concrete without fiber, the influence of BF, PF, or hybrid BF-PF on time-dependent coefficient is less.

All BPFRC specimens were normalized according to C40 concrete (BC-40-0.1), i. e., reference chloride diffusion coefficient $D_{\text{ref}} = D_{\text{ref}}$ (BC-40-0.1) $= 12.76 \times 10^{-12}$ m^2/s. The influence factor $f_1(t)$, considering the effect of exposure time on the apparent chloride diffusion coefficient, can be defined as follows:

$$f_1(t) = \left(\frac{t_{\text{ref}}}{t}\right)^m. \tag{7}$$

The influence coefficient of strength grade and fibers (BF and PF) content on time-dependent coefficient m can be expressed as follows:

$$m(S,V) = 0.81 \cdot k_S \cdot k_V, \tag{8}$$

where k_S and k_V are the correction coefficients of strength grade and fiber content.

(2) Strength Grade Correction Factor f_2 (S). The correction factor f_2 (S), considering the effect of strength grade on the apparent chloride diffusion coefficient, can be defined as follows:

$$f_2(S) = \frac{D_{\text{ref}}(S)}{D_{\text{ref}}}, \tag{9}$$

where D_{ref} (S) is the reference chloride diffusion coefficient with different strength grade.

(3) Fiber Content Correction Factor f_3 (V). The correction factor f_3 (V), considering the effect of fiber contents (BF and PF) on the apparent chloride diffusion coefficient, is defined as follows:

$$f_3(V) = \frac{D_{\text{ref}}(V)}{D_{\text{ref}}}, \tag{10}$$

where D_{ref} (V) is the reference chloride diffusion coefficient with various fiber contents of BF and PF.

Based on the regression analysis of the test results, the multifactor model of apparent chloride diffusion coefficient for BPFRC considering exposure time, strength grade, and fiber content is established as follows:

$$\begin{cases} D_a(t,S,V) = D_{\text{ref}} \cdot f_1(t) \cdot f_2(S) \cdot f_3(V), \\ D_{\text{ref}} = \dfrac{12.76 \times 10^{-12} m^2}{s}, \\ f_1(t) = \left(\dfrac{t_{\text{ref}}}{t}\right)^{0.81\left(0.31S^{0.32}\right)\cdot\left(0.97+0.29V_B+0.19V_P\right)}, \\ f_2(S) = 2.24e^{-0.02S}, \\ f_3(V) = 1.08 - 0.81V_B - 0.37V_P, \end{cases} \tag{11}$$

where S is the strength grade and V_B and V_P are the BF and PF content.

The relationship between the predicted and experimental values of D_a of the BPFRC specimens at various exposure times is shown in Figure 12. The error between the predicted values of the model and the experimental values is less than 15%, which satisfies the error requirements. Therefore, the proposed model can be used to predict D_a of BPFRC subjected to drying-wetting cycles.

3.5. Theoretical Pore Volume of BPFRC. Figure 13 presents the theoretical pore volume of the BPFRC specimens at different erosion times. It can be seen that the theoretical pore volume of the BPFRC specimens initially decreased and then increased with the increase in the erosion time. The theoretical pore volume of the BPFRC specimens was the least after 30 d of erosion. During the initial stages of the

Table 5: Reference chloride diffusion coefficient and time-dependent coefficient of BPFRC.

Mixture	D_{ref} (10^{-12} m^2/s)	m	R^2
BPC-30-0.1	15.92	0.71	0.98
BC-40-0.1	12.76	0.81	0.99
BC-50-0.05	10.72	0.83	0.99
HC-40	13.58	0.78	0.99
PC-40-0.1	13.32	0.79	1.00
BPC-40-0.1	13.17	0.80	1.00
BPC-40-0.2	14.05	0.79	0.99

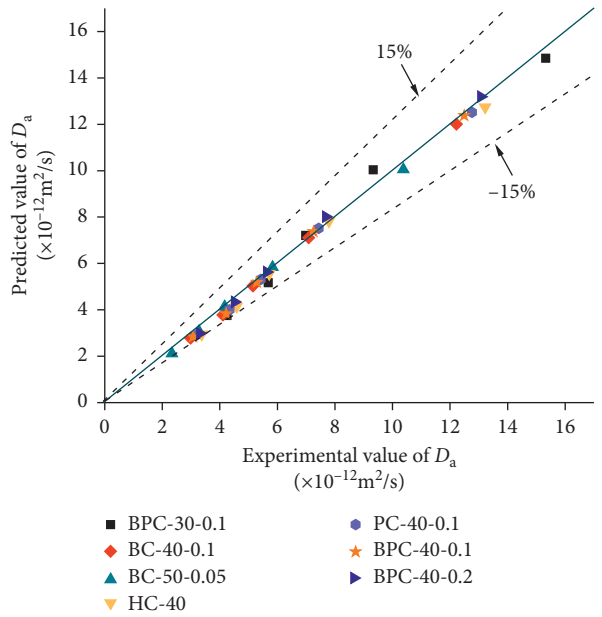

Figure 12: Comparison between predicted and experimental values of $(D)_a$ for the BPFRC.

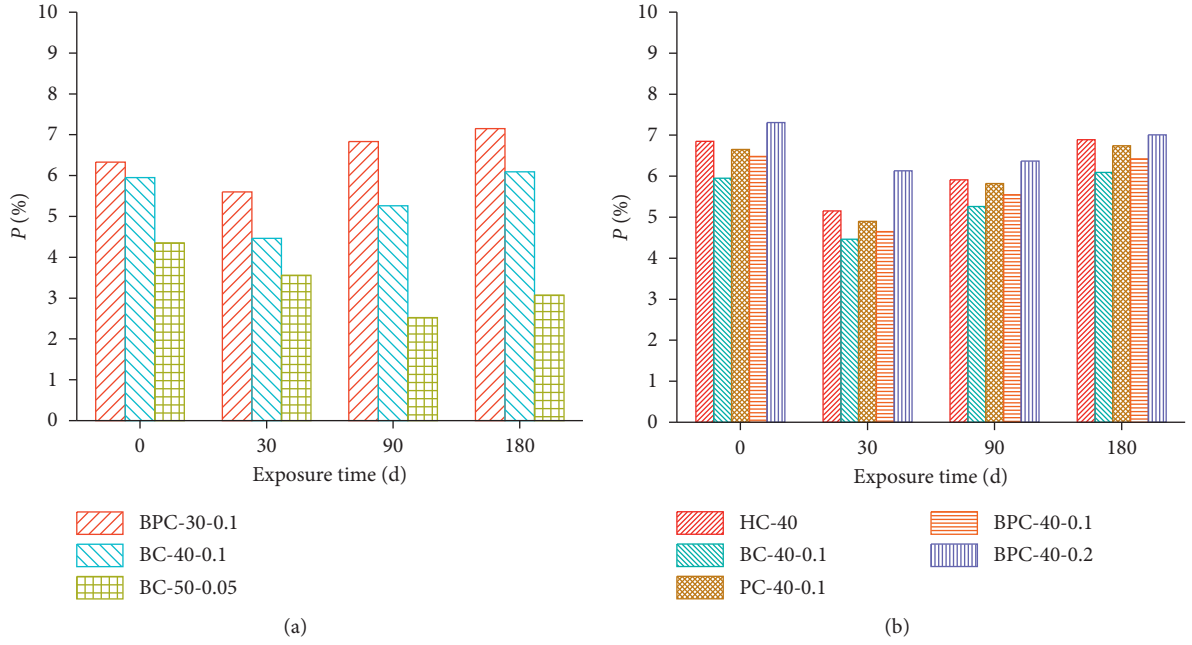

Figure 13: Theoretical pore volume of BPFRC. (a) Different strength grades. (b) Different fiber types and contents.

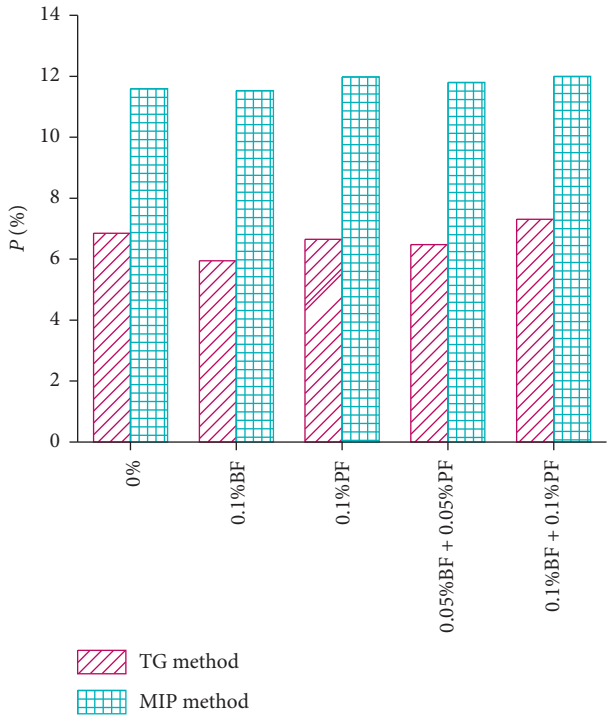

Figure 14: Comparison of pore volume of BPFRC [43].

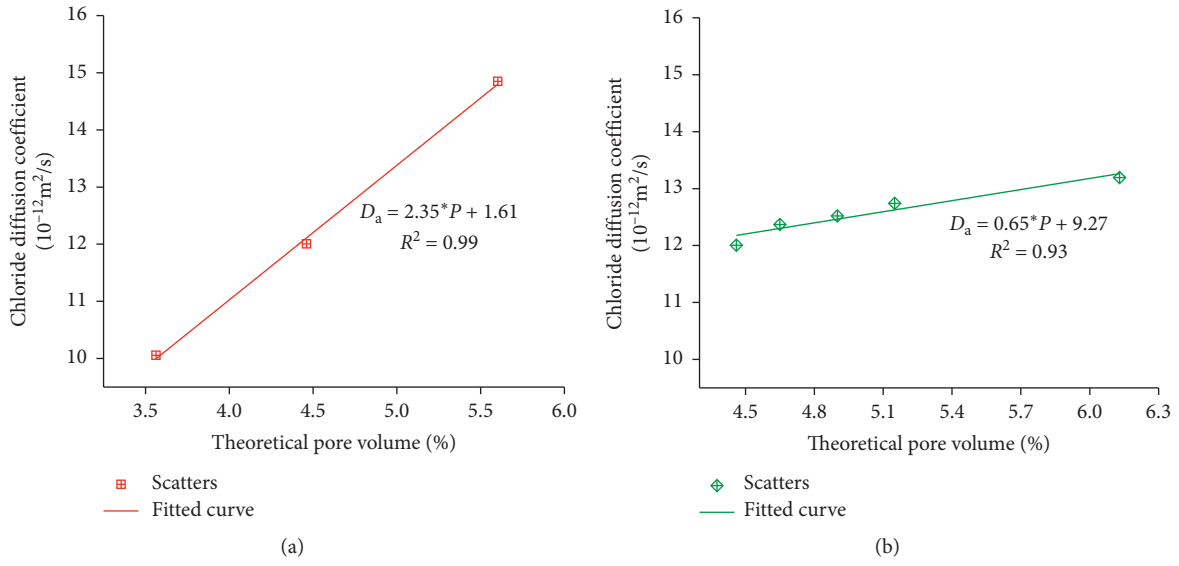

Figure 15: Relationship between theoretical pore volume and $(D)_a$ after 30 d of erosion. (a) Different strength grades. (b) Different fiber types and contents.

erosion, the continuous hydration of concrete and the formation of Friedel's salt by the chloride ions and the hydration products reduce the theoretical total pore volume of BPFRC. As the erosion time increases, alkali substances in the concrete such as $Ca(OH)_2$, NaOH, and KOH continuously dissolved, and the concrete matrix structure becomes loose. Consequently, the theoretical total pore volume increases. As shown in Figure 13(a), the theoretical total pore volume decreased with the increase in strength grade. After 180 d of erosion, the theoretical total pore volume of C30 concrete (BPC-30-0.1) was 1.17 times and 2.32 times that of C40 concrete (BC-40-0.1) and C50 concrete (BC-50-0.05), respectively.

The effects of BF and PF and hybrid BF-PF on the theoretical pore volume of concrete are shown in Figure 13(b). Before the erosion, the theoretical pore volume

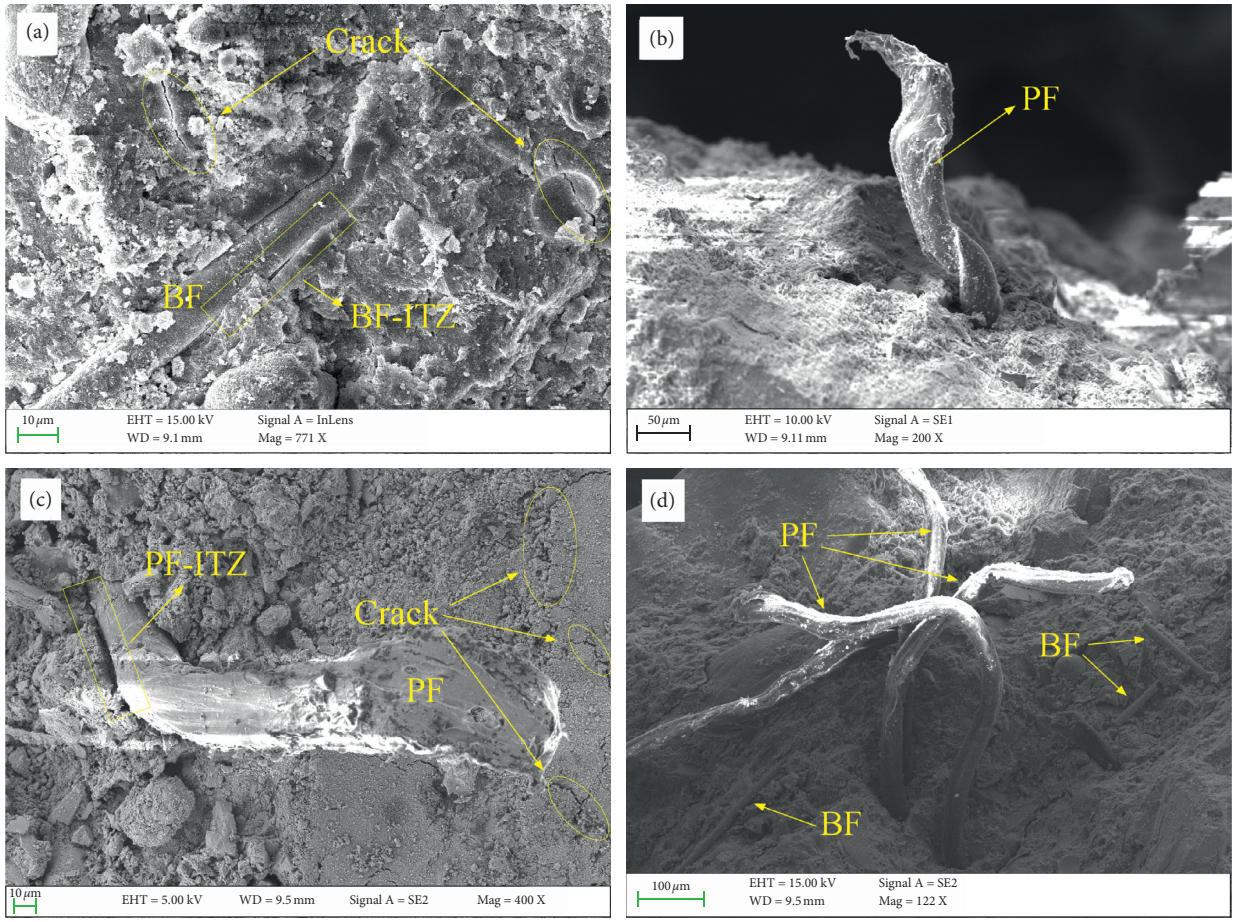

Figure 16: FE-SEM micrographs of BF and PF in BPFRC. (a) The interface between the BF and matrix. (b) Failure modes of PF. (c) The interface between the PF and matrix. (d) Distribution pattern of BF and PF with 0.2% hybrid fiber.

of the BC-40-0.1, PC-40-0.1, BPC-40-0.1, and BPC-40-0.2 specimens was 13.13%, 2.91%, 5.41%, and −6.71% lower than that of HC-40, respectively. After 180 d of erosion, the theoretical pore volumes of BC-40-0.1, PC-40-0.1, BPC-40-0.1, and BPC-40-0.2 were 11.61%, 2.17%, 6.82%, and −1.74% lower than that of HC-40. Compared to the concrete with single BF, the bonding performance between the PF and the concrete matrix is poor, which increases the theoretical pore volume of PC-40-0.1. When BF and PF are mixed and the fiber content is 0.1%, the two fibers have a certain degree of influence on the mixing process, and the dispersion and cohesiveness of the fiber are reduced. Consequently, the theoretical pore volume of BPC-40-0.1 is slightly larger than that of BC-40-0.1. However, when BF and PF are mixed with a fiber content of 0.2%, the interface between the fiber and concrete matrix increases due to the excessive amount of fiber. The uneven dispersion leads to a decrease in adhesion, increasing the theoretical pore volume of the concrete.

Niu et al. [43] measured the cumulative pore volume of basalt-polypropylene fiber concrete with different fiber content by Mercury intrusion porosimetry (MIP), and the cumulative pore volume is shown in Figure 14. It can be seen that the pore volume measured by Mercury porosimetry is 11.59%–14.59%, which is larger than that calculated by TG. This is because the pore size that can be measured using MIP technique is in the range of 0.005 μm–1000 μm, including gel pores, capillaries, and large pores, while the total pore volume calculated by TG is the pore volume formed by free water evaporation. Fallah and Nematzadeh [44] calculated the porosity of polymer and polypropylene fiber concrete according to capillary water absorption, and the porosity is 7.0%–9.39%, which is slightly higher than that of concrete of the same strength grade in this study. In addition to the different testing methods of pore volume, in this study, the addition of mineral admixtures can improve the degree of hydration of concrete and generate more bound water, thus reducing the content of free water, which is also the reason for the decrease of porosity of concrete.

The relationship between the theoretical pore volume of the BPFRC and D_a after 30 d of erosion is shown in Figure 15. As shown, a good correlation exists between the theoretical pore volume and D_a. D_a increases with the increase in the theoretical pore volume. The lower the theoretical pore volume, the better the compactness of concrete, and the smaller the chloride ion transport rate in concrete. Therefore, concrete presents excellent chloride resistance.

3.6. FE-SEM Analysis. To analyze the effect of BF and PF on chloride transport performance of BPFRC, the morphology

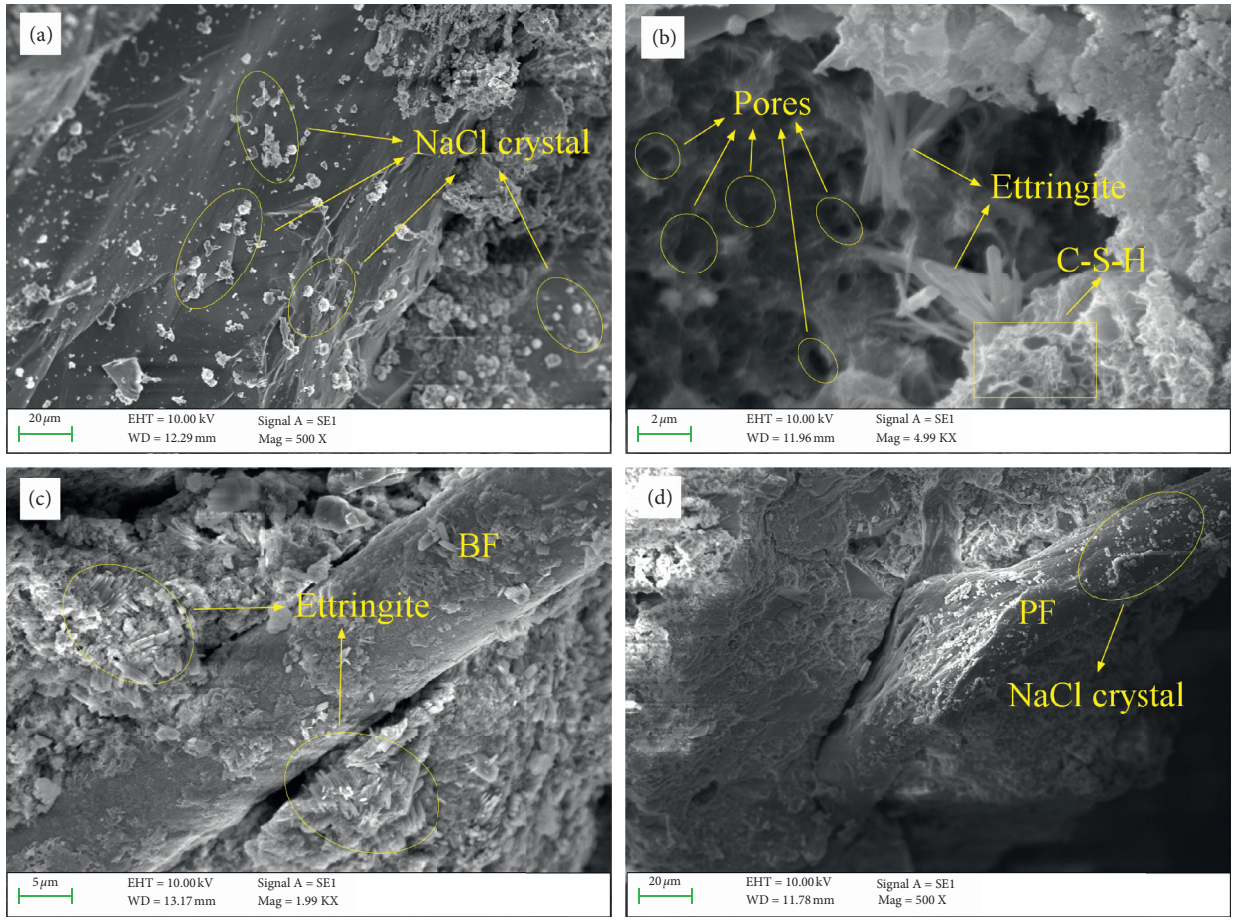

Figure 17: FE-SEM micrographs of BPC-40-0.1 concrete after 180 days of exposure time. (a) Sodium chloride crystals. (b) Corrosion products. (c) The interface between the BF and concrete matrix. (d) The interface between the PF and concrete matrix.

of BPFRC was observed by FE-SEM. Figure 16 shows the distribution of BF and PF in BPFRC without erosion. It can be seen from Figure 16(a) that a certain amount of hydration products are attached to the surface of BF, the interface structure of BF is dense, and the bond between BF and matrix is tight; there are microcracks distributed around BF, and there is no connection between microcracks, indicating that the addition of BF can effectively restrain the emergence and development of shrinkage cracks in concrete at the initial stage of hydration. The distribution of PF in concrete is shown in Figures 16(b) and 16(c). It can be seen that, compared with BF, PF has poor bonding performance with concrete matrix, and there is obvious gap between fiber and matrix. PF warps at the end after tension, and PF can consume a certain amount of fracture energy in the process of tension, which can restrain the development of cracks [45]. Figure 16(d) presents the fiber distribution of BPC-40-0.2 concrete. It can be seen that the fiber dispersion is uneven due to excessive fiber content. The bonding performance between the fibers and the concrete matrix decreases, which not only increases the weak interface between fiber and concrete matrix and reduces the compactness of concrete but also weakens the inhibition and control effect of fiber on cracks, thus providing more channels for the transport of chloride ions. Therefore, there are more chloride ions in BPC-40-0.2 concrete.

The morphology of BPC-40-0.1 concrete after 180 d of erosion is shown in Figure 17. As shown in Figures 17(a) and 17(b), a large number of sodium chloride crystals are distributed in BPFRC, and the hydration products exhibit loose and porous characteristics due to decalcification, forming many small pores. It can be seen from Figure 17(c) that salt crystallization and corrosion products are attached to the surface of BF and the fiber-matrix interface transition zone, but the bond strength between fiber and matrix decreases, which is due to the decrease of alkalinity of pore solution and serious loss of hydration products in concrete after erosion. Figure 17(d) shows the morphology of PF in concrete after erosion. Sodium chloride crystals exist on the fiber surface, but there are few hydration products attached around the fiber.

4. Conclusions

In this study, a tropical ocean tidal zone was simulated using a drying-wetting cycle test system in a high-temperature environment. The effects of the strength grade, fiber type, and fiber content on the chloride transport performance of

BPFRC were investigated. The main conclusions are as follows:

(1) The pore solution pH of the BPFRC specimens decreased with the increase in the exposure time, and the pore solution pH of the surface concrete decreased rapidly. In the process of erosion, the pH decrease rate of high strength concrete was slower, and the rising range of pH was smaller. The effects of BF, PF, and hybrid BF-PF on the pore solution pH of C40 concrete are as follows: BC-40-0.1>BPC-40-0.1>PC-40-0.1>HC-40>BPC-40-0.2.

(2) The chloride concentration at a given depth in the BPFRC specimens increased gradually with the increase in the exposure time; it increased rapidly initially and gradually during the later stages. The strength and fiber had little effect on the depth of convection zone, and the depth of convection zone of all specimens at each erosion time was 2 mm.The chloride concentration in the BPFRC specimens decreased with the increase in strength grade. At a fiber volume content of 0.1%, the single-doped BF had the largest effect on reducing the BPFRC chloride concentration in the C40 concrete. The effect of the hybrid BF-PF on the reduction of the chloride concentration was between those of the BF alone or PF alone. When the hybrid fiber content was 0.2%, the addition of fibers increased the chloride concentration at a given depth in the concrete.

(3) The chloride concentration of BPFRC presented a two-stage distribution, and the chloride peak concentration appeared at the depth of 2 mm. C_{max} in C30 concrete (BPC-30-0.1) was 16.78%–22.61% and 33.23%–48.84% higher than that of BC-40-0.1 and BC-50-0.05, respectively. C_{max} of C40 concrete with 0.1% BF was the lowest, which was 5.95%–3.24% lower than that of the specimen without fiber (HC-40). The addition of 0.2% hybrid fiber increased C_{max} of C40 concrete by 0.93%–3.21%.

(4) The chloride peak concentration increased with the exposure time. The power function was regarded as the best fitting formula to describe the chloride peak concentration model of BPFRC.

(5) D_a of the BPFRC specimens decreased with the increase of exposure time, exhibiting a power function attenuation law. D_a of C30 concrete (BPC-30-0.1) was 47.67%–77.09% higher than that of C50 concrete (BC-50-0.05). With the increase of erosion time, the decreasing effect of single fiber on D_a of concrete decreased, while that of hybrid fiber increased. A multifactor model was established considering the effects of exposure time, strength grade, and the content of BF and PF on D_a of BPFRC. The error between the calculated and experimental values of apparent chloride diffusion coefficient was within 15%.

(6) The theoretical pore volume of the BPFRC specimens initially decreased and then increased with the exposure time increasing. The higher the strength grade, the smaller the theoretical pore volume. BF, PF, and hybrid BF-PF had positive and negative effects on the theoretical pore volume of the C40 concrete. After 180 d of erosion, the addition of fiber reduced the porosity of C40 concrete by 11.61% to −1.74%.The theoretical pore volume demonstrated good correlation with D_a.

(7) FE-SEM results showed that the bond between BF and concrete matrix was better than that of PF before erosion, which could effectively control the development of microcracks. For the specimen containing 0.2% hybrid fiber, BF and PF presented agglomeration and uneven dispersion. After 180 d of erosion, a large number of salt crystals were distributed in BPFRC, and the bonding properties between fiber and matrix decreased.

Data Availability

The data used to support the findings of this study are included within the article.

Conflicts of Interest

The authors declare that they have no conflicts of interest.

Acknowledgments

This research was funded by the National Natural Science Foundation of China (Grant no. 51590914) and the Natural Science Foundation of Shaanxi Province (Grant no. 2019JQ-481).

References

[1] W. L. Jin and Y. X. Zhao, *Durability of Concrete Structures*, Science Press, Beijing, China, 2014.

[2] P. Rashiddadash, A. A. Ramezanianpour, and M. Mahdikhani, "Experimental investigation on flexural toughness of hybrid fiber reinforced concrete (HFRC) containing metakaolin and pumice," *Construction and Building Materials*, vol. 51, pp. 313–320, 2014.

[3] O. Kayali, M. N. Haque, and B. Zhu, "Some characteristics of high strength fiber reinforced lightweight aggregate concrete," *Cement and Concrete Composites*, vol. 25, no. 2, pp. 207–213, 2003.

[4] D.-Y. Yoo and N. Banthia, "Mechanical properties of ultra-high-performance fiber-reinforced concrete: a review," *Cement and Concrete Composites*, vol. 73, pp. 267–280, 2016.

[5] K. G. Kuder and S. P. Shah, "Processing of high-performance fiber-reinforced cement-based composites," *Construction and Building Materials*, vol. 24, no. 2, pp. 181–186, 2010.

[6] H. M. Vogel and D. "Svecova, "Evaluation of elastic modulus for high-strength concrete," *ACI Materials Journal*, vol. 109, no. 3, pp. 313–322, 2012.

[7] J. Thomas and A. Ramaswamy, "Mechanical properties of steel fiber-reinforced concrete," *Journal of Materials in Civil Engineering*, vol. 19, no. 5, pp. 385–392, 2007.

[8] B. H. Oh, D. G. Park, J. C. Kim, and Y. C. Choi, "Experimental and theoretical investigation on the postcracking inelastic

behavior of synthetic fiber reinforced concrete beams," *Cement and Concrete Research*, vol. 35, no. 2, pp. 384–392, 2005.

[9] C. Rooban, V. Srikanth, and P. Indubhushan, "Mechanical properties of high volume fly ash concrete reinforced with hybrid fibers," *Advances in Materials Science and Engineering*, vol. 2016, Article ID 1638419, 7 pages, 2016.

[10] M. Hsie, C. Tu, and P. S. Song, "Mechanical properties of polypropylene hybrid fiber-reinforced concrete," *Materials Science and Engineering: A*, vol. 494, no. 1-2, pp. 153–157, 2008.

[11] M. Pajak, "Investigation on flexural properties of hybrid fibre reinforced self-compacting concrete," *Procedia Engineering*, vol. 161, pp. 121–126, 2016.

[12] C. J. Yang, C. K. Huang, Y. Che, and B. X. Wang, "Mechanical properties and impermeability of hybrid fiber reinforced concrete," *Journal of Building Materials*, vol. 11, pp. 89–93, 2008.

[13] V. Fiore, T. Scalici, G. Di Bella, and A. Valenza, "A review on basalt fibre and its composites," *Composites Part B: Engineering*, vol. 74, pp. 74–94, 2015.

[14] D. C. Liu, *Study on the Properties of Basalt and Polypropylene Mixed Fiber Concrete*, M. S. Thesis, Chongqing Jiaotong University, Chongqing, China, 2018.

[15] M. Nili and V. Afroughsabet, "The long-term compressive strength and durability properties of silica fume fiber-reinforced concrete," *Materials Science and Engineering: A*, vol. 531, pp. 107–111, 2012.

[16] P. Zhang and Q.-f. Li, "Effect of polypropylene fiber on durability of concrete composite containing fly ash and silica fume," *Composites Part B: Engineering*, vol. 45, no. 1, pp. 1587–1594, 2013.

[17] J. Yuan, Y. Liu, Z. Tan, and B. Zhang, "Investigating the failure process of concrete under the coupled actions between sulfate attack and drying-wetting cycles by using X-ray CT," *Construction and Building Materials*, vol. 108, pp. 129–138, 2016.

[18] O. Helson, J. Eslami, A.-L. Beaucour, A. Noumowe, and P. Gotteland, "Durability of soil mix material subjected to wetting/drying cycles and external sulfate attacks," *Construction and Building Materials*, vol. 192, pp. 416–428, 2018.

[19] T. Simcic, S. Pejovnik, G. De Schutter, and V. B. Bosiljkov, "Chloride ion penetration into fly ash modified concrete during wetting-drying cycles," *Construction and Building Materials*, vol. 93, pp. 1216–1223, 2015.

[20] M. H. F. Medeiros, A. Gobbi, G. C. Réus, and P. Helene, "Reinforced concrete in marine environment: effect of wetting and drying cycles, height and positioning in relation to the sea shore," *Construction and Building Materials*, vol. 44, pp. 452–457, 2013.

[21] J. Liu, Y. Jia, and J. Wang, "Calculation of chloride ion diffusion in glass and polypropylene fiber-reinforced concrete," *Construction and Building Materials*, vol. 215, pp. 875–885, 2019.

[22] O. Karahan and C. D. Atiş, "The durability properties of polypropylene fiber reinforced fly ash concrete," *Materials & Design*, vol. 32, no. 2, pp. 1044–1049, 2011.

[23] M. Osama and A. H. Waddah, "Influence of fly ash and basalt fibers on strength and chloride penetration resistance of self-consolidating concrete," *Materials Science Forum*, vol. 866, 2016.

[24] Y. Guo, X. Hu, and J. Lv, "Experimental study on the resistance of basalt fibre-reinforced concrete to chloride penetration," *Construction and Building Materials*, vol. 223, pp. 142–155, 2019.

[25] China Architecture and Building Press, *Technical Specification for Test of Chloride Ion Content in Concrete*, China Architecture & Building Press, Beijing, China, 2013.

[26] J. B. Wang and D. T. Niu, "Investigation of chloride ion diffusion in shotcrete under bending loading," *China Civil Engineering Journal*, vol. 51, no. 120, pp. 95–102, 2018.

[27] S. Diamond, "Mercury porosimetry," *Cement and Concrete Research*, vol. 30, no. 10, pp. 1517–1525, 2000.

[28] C. Gallé, "Effect of drying on cement-based materials pore structure as identified by mercury intrusion porosimetry," *Cement and Concrete Research*, vol. 31, no. 10, pp. 1467–1477, 2001.

[29] M. Zajac, S. Hoock, C. Stabler, and M. Ben Haha, "Effect of hydration kinetics on properties of compositionally similar binders," *Cement and Concrete Research*, vol. 101, pp. 13–24, 2017.

[30] H. M. Hu and B. G. Ma, *Concrete Mineral Admixture*, China Electric Power Press, Beijing, China, 2016.

[31] B. Chen and J. Liu, "Contribution of hybrid fibers on the properties of the high-strength lightweight concrete having good workability," *Cement and Concrete Research*, vol. 35, no. 5, pp. 913–917, 2005.

[32] S. Arivalagan, "Study on the compressive and split tensile strength properties of basalt fibre concrete members," *Global Journal of Research in Engineering*, vol. 12, pp. 23–27, 2012.

[33] P. S. Mangat and B. T. Molloy, "Prediction of long term chloride concentration in concrete," *Materials and Structures*, vol. 27, no. 6, pp. 338–346, 1994.

[34] C. T. Sun and D. T. Niu, "Experimental study on chloride diffusion properties of concrete in freeze-thaw environment," *Bulletin of Chinese Ceramic Society*, vol. 33, no. 8, pp. 1863–1869, 2014.

[35] A. Ghazy, M. T. Bassuoni, E. Maguire, and M. O'Loan, "Properties of fiber-reinforced mortars incorporating nano-silica," *Fiber*, vol. 6, pp. 1–16, 2016.

[36] Y. X. Zhao, C. K. Wang, W. L. Jin, and C. Xu, "Experimental analysis on time-dependent law of surface chloride ion concentration of concrete," *Journal of Civil Architectural and Environmental Engineering*, vol. 32, no. 3, pp. 8–13, 2010.

[37] D. G. Huang, D. T. Niu, L. Su, and Q. Fu, "Chloride diffusion behavior of coral aggregate concrete under drying-wetting cycles," *Construction And Building Materials*, vol. 270, Article ID 121485, 2020.

[38] S.-W. Pack, M.-S. Jung, H.-W. Song, S.-H. Kim, and K. Y. Ann, "Prediction of time dependent chloride transport in concrete structures exposed to a marine environment," *Cement and Concrete Research*, vol. 40, no. 2, pp. 302–312, 2010.

[39] Y.-r. Zhang, Y. Zhang, J. Huang, H.-x. Zhuang, and J.-z. Zhang, "Time dependence and similarity analysis of peak value of chloride concentration of concrete under the simulated chloride environment," *Construction and Building Materials*, vol. 181, pp. 609–617, 2018.

[40] C. Andrade, M. A. Climent, and G. de Vera, "Procedure for calculating the chloride diffusion coefficient and surface concentration from a profile having a maximum beyond the concrete surface," *Materials and Structures*, vol. 48, no. 4, pp. 863–869, 2015.

[41] H. L. Chang, S. Mu, Y. J. Liu, and J. Z. Liu, "Chloride profile with a chloride concentration peak and calculating methods of its diffusion parameters," *Bulletin of Chinese Ceramic Society*, vol. 36, no. 1, pp. 14–19, 2017.

[42] M. D. A. Thomas and P. B. Bamforth, "Modelling chloride diffusion in concrete," *Cement and Concrete Research*, vol. 29, no. 4, pp. 487–495, 1999.

[43] D. Niu, D. Li, and Q. Fu, "A 3D-IFU model for characterising the pore structure of hybrid fibre-reinforced concrete," *Materials & Design*, vol. 188, Article ID 108473, 2020.

[44] S. Fallah and M. Nematzadeh, "Mechanical properties and durability of high-strength concrete containing macro-polymeric and polypropylene fibers with nano-silica and silica fume," *Construction and Building Materials*, vol. 132, pp. 170–187, 2017.

[45] C. Jiang, K. Fan, F. Wu, and D. Chen, "Experimental study on the mechanical properties and microstructure of chopped basalt fibre reinforced concrete," *Materials & Design*, vol. 58, no. 1, pp. 187–193, 2014.

Hindawi
Advances in Materials Science and Engineering
Volume 2021, Article ID 6643956, 8 pages
https://doi.org/10.1155/2021/6643956

Research Article

Influence of the ITZ Thickness on the Damage Performance of Recycled Concrete

Fuwei Xu,[1,2] **Bin Tian**,[1] **and Gang Xu**[1]

[1]*College of Hydraulic and Environmental Engineering, China Three Gorges University, Yichang, Hubei 443002, China*
[2]*College of Civil Engineering and Architecture, Hubei University of Arts and Science, Xiangyang, Hubei 441053, China*

Correspondence should be addressed to Fuwei Xu; 445757999@qq.com

Received 19 November 2020; Revised 2 February 2021; Accepted 14 March 2021; Published 25 March 2021

Academic Editor: Peng Zhang

The interfacial transition zone (ITZ) is a weak region of recycled concrete. To further study the influence of the ITZ on the damage performance of recycled concrete, a formula for calculating the ITZ thickness is derived, and the ITZ thickness is calculated for various recycled concrete mixtures with a recycled aggregate content of 30%. The concrete model test method and finite element analysis software were used to numerically simulate common concrete and recycled concrete with ITZ thicknesses of 0.05 mm, 1 mm, 2 mm, 3 mm, and 4 mm. The results show that the thickness of the ITZ has an obvious influence on the cracking strength of recycled concrete and that the cracking strength of recycled concrete decreases with increasing ITZ thickness. The cracks in recycled concrete initiate from the ITZ, and the damage degree increases with increasing ITZ thickness. Compared with that of common concrete, the cracking strength of recycled concrete with an ITZ thickness of no more than 2 mm (i.e., the replacement rate of the recycled aggregates is no more than 30%) is not significantly reduced.

1. Introduction

Similar to ordinary concrete, recycled concrete is a kind of heterogeneous composite material, containing solid, liquid, and three-phase gas materials, made of recycled aggregates mixed with a certain proportion of natural aggregates, cement, water, and a certain proportion of additives for curing and hardening. However, unlike natural aggregates, recycled aggregates, which contain a large number of microcracks from mechanically damaged concrete, have old mortar attached to their surfaces. This is one of the main factors leading to the high porosity, strong water absorption, and relatively low density of recycled aggregates. At the microlevel, recycled concrete components include natural aggregates, an interfacial transition zone (ITZ) between the old mortar and natural aggregates, an ITZ between the new mortar and old mortar on the surface of the native aggregates and at the cross section between the transition layer (hereinafter referred to as the old interface layer) and old mortar, an ITZ between the new mortar and natural aggregates (hereinafter referred to as the new ITZ), and the new mortar matrix. In this paper, the old interface layer, the old mortar, and the new ITZ (i.e., the transition between the surface of the natural coarse aggregates and the new mortar matrix), collectively known as the regeneration region, is the primary ITZ between the coarse aggregates. The new mortar is called the common ITZ, as shown in Figure 1.

The ordinary concrete ITZ refers to the transition area between the aggregate and mortar matrix. Xie [1] studied the ITZ of concrete in 1983, and he divided the ITZ from the aggregates to the mortar into the following four microstructural models: the permeation and diffusion layer, contact layer, enrichment layer, and weak effect layer. According to Berger's sidewall effect [2], the water-cement ratio of the water film layer near the aggregate surface is higher than that of the cement slurry, and ettringite and other crystalline compounds with large crystals easily form around the aggregates, resulting in a loose structure and high porosity of the ITZ. The loose structure and high porosity reduce the bonding strength and permeability resistance of the interfacial zone, so the ITZ is referred to as the weak link in concrete. Professor Wu [3] studied the microstructure of

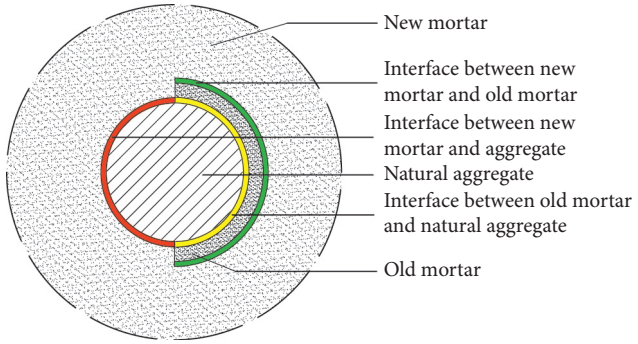

Figure 1: Microstructure and scanning electron microscope (SEM) image of recycled concrete [1].

the ITZ of concrete and found that the contents of calcium hydroxide and ettringite are obvious and that larger crystals, growth orientation, a high water-cement ratio, and a large porosity are observed. In addition, the weak region in concrete is the fundamental problem associated with composite materials; therefore, the macromechanical properties of the composite material were studied.

The recycled concrete ITZ contains the regeneration region of the ITZ and the common ITZ. The regeneration region of the ITZ combines the old interface layer and two mortar layers, such that the two old interface layers and the mortar layer produce a complex ITZ structure with a loose degree, and the porosity is much higher than that of the common ITZ, as shown in Figure 2. Etxeberria et al. [4] studied the ITZ structure of recycled concrete and found that the bond strength of the common ITZ was higher than that of the new interface layer and that the old interface layer was the weakest interface among the three. Dhir et al. [5] found that there was a large number of CH crystals in the new interface transition layer of the recycled concrete ITZ and that the crystal arrangement was obvious, which was also the weakest point in the recycled concrete. Tam et al. [6] carried out a model test containing 9 cylindrical recycled aggregate samples, and the model test methods were similar to those of Buyukozturk et al. [7] and Liu et al. [8]. The porosity of the old interface layer was higher than that of the old mortar and that of the new mortar was higher than that of the old mortar. Cracks appeared and developed mainly along the new surface layer of the recycled concrete with a large water-cement ratio (0.67), while cracks appeared and developed mainly along the old ITZ of the recycled concrete with a small water-cement ratio (0.40).

The ITZ (especially the recycled ITZ) is the area where cracks occur and develop and is the weakest region in recycled concrete. Many studies of the structure and cracking mechanism of the ITZ of recycled concrete have been carried out at home and abroad, but there are few reports on the quantitative analysis of the ITZ and the influence of its thickness on the performance of recycled concrete, so further research is needed. In this paper, the thickness and volume of the ITZ of recycled concrete are quantitatively analysed, and the variation in the thickness of the ITZ is numerically analysed for recycled concrete, which provides a reference for research on recycled concrete.

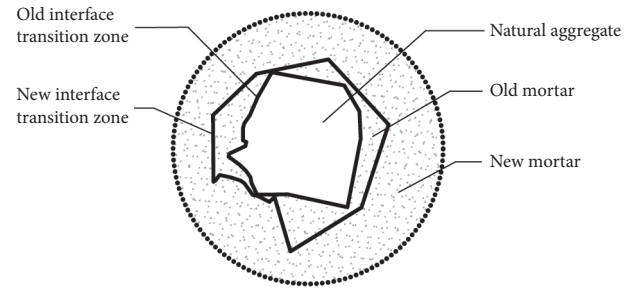

Figure 2: Schematic diagram of the interface transition zone of the recycled aggregates.

2. Quantitative Analysis of the ITZ of Recycled Concrete

The ITZ of recycled concrete includes the recycled ITZ and common ITZ. The common ITZ is the same as the ITZ in common concrete, which can be determined by referring to the research results for the common concrete ITZ [9]. Therefore, it is necessary to quantitatively analyse the recycled ITZ.

2.1. Quantitative Analysis of the ITZ Thickness. The regeneration ITZ from the natural aggregate surface inside the recycled aggregates to the edge of the new mortar includes the old interface layer, the old mortar, and the surface layer of the new materials. Recycled aggregates are mechanically obtained from waste concrete, and a large amount of old mortar is attached to the surface of the recycled aggregates produced from waste concrete. The old mortar layer is externally attached to the recycled aggregates and consists of the old interface layer and the old mortar layer. To quantitatively analyse the thickness of the recycled ITZ, the thickness of the old mortar externally attached to the recycled aggregates should be calculated first. The thickness of the recycled ITZ can be calculated based on the thickness of the old mortar and the surface layer of the new materials. The old mortar directly affects the water absorption rate of the recycled aggregates. Therefore, the old mortar adhesion rate is simplified in the literature [10] to be a single factor function of the water absorption rate, as shown in the following equation:

$$w_{\text{water}} = F\left(w_{\text{oldcem}}\right), \tag{1}$$

where w_{water} is the water absorption of the recycled aggregates and w_{oldcem} is the adhesion rate of the old mortar of the recycled aggregates.

Considering that the mechanical damage of the recycled aggregates results in a relatively high measured water absorption rate, the correction coefficient λ (generally 1.2~1.3) is introduced, and equation (1) is amended as

$$w_{\text{water}} = \frac{F\left(w_{\text{oldcem}}\right)}{\lambda}. \tag{2}$$

The experimental results in the literature [11] show that there is a good linear correlation between the adhesion rate

of the recycled aggregate mortar and the water absorption rate, apparent density, and crushing index as well as the randomness and uncertainty of the value λ in equation (2). The expression of equation (2) can be directly used to obtain the linear expression in

$$w_{\text{water}} = a \cdot w_{\text{oldcem}} + b. \tag{3}$$

According to relevant studies, when the maximum particle size of the recycled aggregates is 16 mm, $a = 0.177$ and $b = 0.36$ [12]; when the maximum particle size of the recycled aggregates is 32 mm, $a = 0.0825$ and $b = 1.2828$ [13].

According to equation (3), the mortar adhesion rate can be expressed by

$$w_{\text{oldcem}} = \frac{w_{\text{water}} - b}{a}. \tag{4}$$

The difference in the linear expansion coefficient of different materials at different temperatures can also be used to conduct calcination tests to separate the old mortar from the surface of the aggregates and determine the content of old mortar. Bruno et al. [14] studied the linear expansion rate of cement mortar, limestone, pebbles, and green schist at different temperatures, and the linear expansion rate of different materials varied with temperature. When the temperature was low (≤120°C), the difference in the linear expansion rate between different components was small, and the maximum expansion rate was only 0.04%; however, when the temperature rose to 800°C, the linear expansion rate of green schist reached more than twice that of cement mortar in C40, and the linear expansion rate of commonly used pebbles was also nearly twice that of cement mortar in C40, with obvious differences. After high-temperature calcination, the aggregates were put into a high-speed ball mill for ball grinding. The mutual collision of the ball grinding beads could effectively separate the mortar and aggregates, and an accurate mortar content could be obtained. The mortar content is given by

$$w_{\text{oldcem}} = \frac{\Delta G}{G_{\text{Rag}}} \times 100\% = \frac{G_{\text{Rag}} - G_{\text{ag}}}{G_{\text{Rag}}} \times 100\%, \tag{5}$$

where G_{Rag} is the weight of the recycled aggregate sample after drying, G_{ag} is the weight of the recycled aggregate sample after high-temperature calcination, and $\Delta G = G_{\text{Rag}} - G_{\text{ag}}$ is the mortar content in the reclaimed aggregates.

In addition, the volume of recycled aggregate mortar content can be expressed by

$$V_{\text{oldcem}} = \frac{\Delta G}{\rho_{\text{cement}}} = \frac{G_{\text{Rag}} w_{\text{oldcem}}}{\rho_{\text{cement}}} \times 100\%. \tag{6}$$

According to equations (4) and (6), the relationship between the mortar content volume and water absorption can be expressed by

$$V_{\text{oldcem}} = \frac{G_{\text{Rag}} (w_{\text{water}} - b)}{\rho_{\text{cement}} \cdot a} \times 100\%. \tag{7}$$

The volume of recycled aggregates after residue is removed from the process of sieving is as follows: $V_{\text{ag}} = V_{\text{Rag}} - V_s$. Relevant studies [15, 16] show that the volume percentage of the aggregates in concrete is basically the same as the area percentage of the aggregates in a certain section. Therefore, the area ratio between the old mortar and primary aggregates at a certain interface of the reclaimed aggregates can be calculated to obtain the thickness of the mortar attached to the reclaimed aggregates. Therefore, the area ratio f_A between the old mortar and the natural aggregates in the recycled aggregates can be expressed by

$$f_A = \frac{V_{\text{cement}}}{V_{\text{ag}}} = \frac{\rho_{\text{ag}} w_{\text{oldcem}}}{\rho_{\text{cement}} (1 - w_{\text{oldcem}})}. \tag{8}$$

The thickness $\delta_{\text{ITZ}}^{\text{old}}$ of the old mortar attached to the outside of the recycled aggregates with particle size d is obtained in

$$\delta_{\text{ITZ}}^{\text{old}} = \frac{D - D \cdot \sqrt{1/(1 + f_A)}}{2}. \tag{9}$$

The thickness of the mortar attached to the outside of the recycled aggregates as well as the thickness of the old interface layer and the old mortar is obtained. Therefore, the thickness $\delta_{\text{ITZ}}^{\text{RC}}$ of the regenerated ITZ is equal to the sum of the thickness $\delta_{\text{ITZ}}^{\text{old}}$ of the attached old mortar (including the old mortar and the old interface layer) and the thickness $\delta_{\text{ITZ}}^{\text{new}}$ of the surface layer of the new materials (which is also equal to that of the ordinary ITZ). $\delta_{\text{ITZ}}^{\text{RC}}$ can be expressed by

$$\delta_{\text{ITZ}}^{\text{RC}} = \delta_{\text{ITZ}}^{\text{old}} + \delta_{\text{ITZ}}^{\text{new}}. \tag{10}$$

2.2. Analysis of the Thickness of the ITZ. According to [16], the mortar contents of reclaimed concrete prepared with recycled coarse aggregates (labelled C20~C50) are shown in Table 1.

According to the first-order mixture of the recycled coarse aggregate particles with sizes of 5~25 mm, the thickness of the ITZ corresponding to different particle sizes of recycled coarse aggregates is shown in Table 2 and Figure 3.

Table 2 and Figure 3 show that the strength of abandoned concrete has a significant influence on the mortar adhesion thickness on the surface of recycled aggregates, and the average mortar adhesion thickness on the surface increases with the increase in the particle size of the recycled aggregates.

In the literature [3], academician Wu pointed out that the thickness of the ITZ of ordinary concrete is generally 30~40 μm, and Prokopski and Halbiniak [9] found that the final thickness of the ITZ is not more than 100 μm based on the quantitative calculation of the thickness of the ITZ of ordinary concrete. When the approximate thickness of the common ITZ is taken as 70 μm, the thickness of the regenerated ITZ corresponding to different aggregate particle sizes is shown in Table 3.

Table 1: Mortar contents of reclaimed concrete with coarse aggregates.

Strength grade of abandoned concrete	Mortar content (%)
C20	44.8
C30	40.4
C40	33.4
C50	26.4

Table 2: Average thickness of the adhesive mortar of the recycled coarse aggregates with different particle sizes and abandoned concrete strength (mm).

Strength grade of abandoned concrete	Particle size (mm)				
	5	7.5	12	17.5	20
C20	0.42	0.63	1.01	1.47	1.68
C30	0.39	0.58	0.93	1.36	1.56
C40	0.33	0.5	0.81	1.17	1.34
C50	0.27	0.41	0.676	0.96	1.10

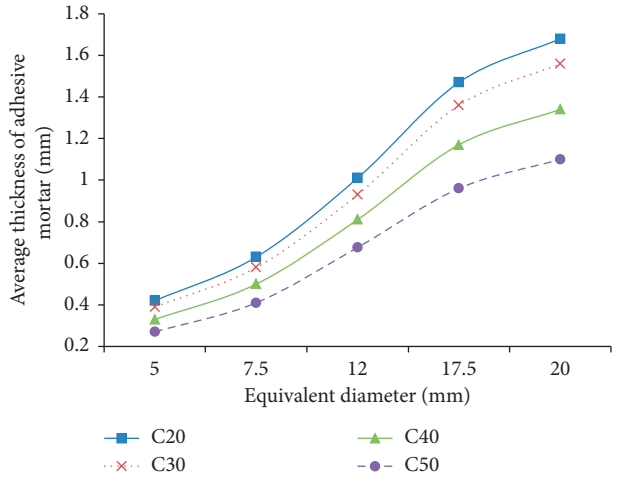

Figure 3: Average thickness of the mortar attached to the surface of the reclaimed aggregates with different particle sizes.

Table 3: Interfacial transition zone thickness corresponding to different particle sizes and abandoned concrete strengths in recycled concrete (mm).

Strength grade of abandoned concrete		Particle size (mm)				
		5	7.5	12	17.5	20
Recycled ITZ	C20	0.49	0.70	1.08	1.54	1.75
	C30	0.46	0.65	1.00	1.43	1.63
	C40	0.40	0.57	0.88	1.24	1.41
	C50	0.34	0.48	0.75	1.03	1.17
Normal ITZ		0.07	0.07	0.07	0.07	0.07

3. Influence of the ITZ Thickness on the Damage Performance of Recycled Concrete

Model tests or numerical analyses based on model tests are commonly used to simplify the analysis of the mechanical properties of concrete. In 1966, Shah and Winter [17] proposed the concrete model test method for the first time and carried out a uniaxial compression test on a model containing 1 aggregate. The ITZ was the first area to experience damage. In 1971, Buyukozturk et al. [7] conducted uniaxial compression tests on a model containing 9 aggregates, and in 1972, Liu et al. [8] conducted uniaxial and biaxial compression tests on a model containing 9 aggregates and found that concrete cracks first appeared in the ITZ. In 2001, Lawler et al. [18] used digital image processing technology (DIC) to study concrete models containing 1, 5, and 13 aggregates. From the perspective of compression failure characteristics, the damage is also initiated in the ITZ. In 2020, Harish et al. [19] researched the tensile constitutive relation of recycled concrete aggregate performance and the influence of nine recycled concrete aggregates in uniaxial tensile modelling. The results showed that the damage in the recycled concrete began in the ITZ, that the tensile peak stress increased with the increase in recycled aggregates outside the thickness of the attached old mortar, and that the damage decreased in the elastic model. The above model tests show that the ITZ is the first to be damaged in either ordinary concrete or recycled concrete. However, the influence of the thickness of the ITZ on the mechanical properties of recycled concrete has not been completely clarified. In this paper, 9 recycled aggregates were used to carry out numerical simulation model tests of recycled concrete to study the influence of the ITZ on the mechanical properties of recycled concrete with different thicknesses.

3.1. Model Design and Material Property Determination. The numerical model of the recycled concrete has dimensions of 150 mm × 150 mm × 30 mm, and the diameter of the recycled aggregates is 38 mm with a spacing of 9 mm. The thicknesses of the ITZ (including the old ITZ, old mortar, and new ITZ) are 0.05 mm, 1 mm, 2 mm, 3 mm, and 4 mm, corresponding to models of ordinary concrete (NCA) and four kinds of recycled concrete (RC10, RC20, RC30, and RC40), as shown in Figure 4(a). The strength of the natural aggregates in the reclaimed aggregates is much larger than the strength of the ITZ and mortar. According to [20], the natural aggregates in the reclaimed aggregates are taken as the elastic material in the numerical simulation. The density is set to 2600 kg/m^3, the elastic modulus is 70 GPa, and μ is set to 0.16. The density of the new mortar is set to 2200 kg/m^3, the elastic modulus is 23 GPa, and μ is set to 0.2. In the selection of the material properties of the ITZ, Lutz et al. [21] considered that the elastic modulus of the ITZ at 28 days was 30–50% of the mortar, so the elastic modulus of the ITZ was set to 12 GPa, and μ was 0.2.

ABAQUS finite element analysis software is used for numerical analysis of the model. The numerical model is established by sweeping segmentation. The model mesh element is C3D8R, an 8-node linear hexahedral reduction integral element (Figure 4(b)). The new mortar and the ITZ adopt the plastic damage model of concrete without cracks, and the damage state of the model is judged by the compression damage. The new mortar in the model adopts the constitutive relation of the mortar stress-strain curve as in [22] (as shown in Figure 5). As presented in [21], the stress in

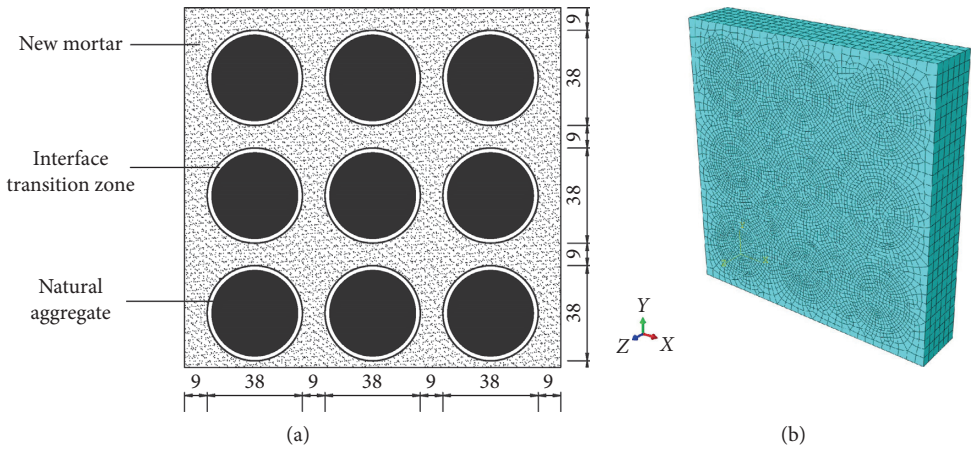

Figure 4: Schematic diagram of the (a) recycled concrete model and (b) finite element mesh.

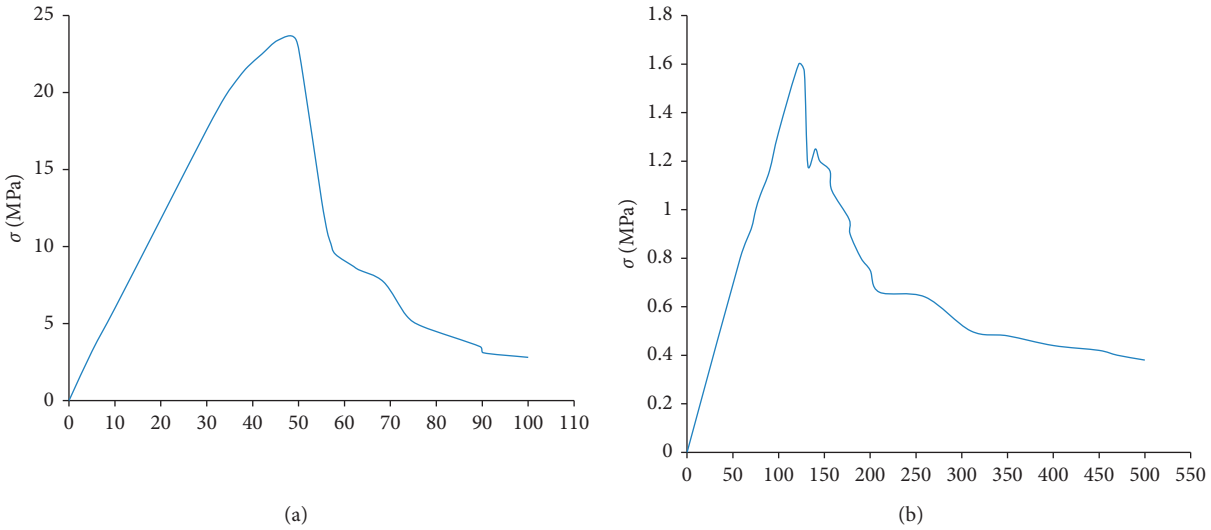

Figure 5: Stress-strain curve of new mortar. (a) Uniaxial compression stress-strain curve. (b) Uniaxial tensile stress-strain curve.

the ITZ is selected according to 50% of the new mortar, and the strain is taken as 100% of the strain in the new mortar. Stress control loading is adopted for the recycled concrete model, and surface loads are simultaneously applied at both ends. The initial load is 5 MPa, the maximum load is 40 MPa, the loading time is 10 s, the maximum incremental steps are set to 5,000 steps, and the calculation stops if the increment exceeds 10 s or 5,000 steps.

3.2. Numerical Simulation Results of the Recycled Concrete Model. The results of the 5 models are analysed, and the thickness of the ITZ has an obvious influence on the damage of the concrete model during loading. With the increase in the thickness of the ITZ, the first damage location of the concrete model in the loading process is in the ITZ, and the damage area increases with the increase in the load. RC30 is the regenerated concrete model; for example, when the load reaches 4.022 s, the ITZ of the X-direction stress reaches 1.65 MPa, and cracks initiate in the ITZ; after 10 s of loading, the model of the ITZ and the tensile stress area of the new mortar expand continuously, the damage area expands continuously, and the mortar surrounding the ITZ exhibits a large area of damage, as shown in Figures 6 and 7. The concrete model with an ITZ thickness ranging from 0.05 mm to 4 mm shows that cracking begins to appear in the ITZ when loading becomes more severe with increasing thickness, as shown in Figure 8.

By comparing the damage evolution process of 5 different concrete models, the concrete models with different ITZ thicknesses start to crack at different times. The normal concrete model begins to crack at 7.128 s, and the recycled concrete model of RC10~RC40 begins to crack from 6.525 s to 5.375 s. In general, cracking initiates sooner in recycled concrete than ordinary concrete; the damage evolution in the ITZs with thicknesses of 1 mm and 2 mm is close to that in the ITZs with thicknesses of 3 mm and 4 mm; and in the ITZs with thicknesses of 3 mm and 4 mm, damage occurs

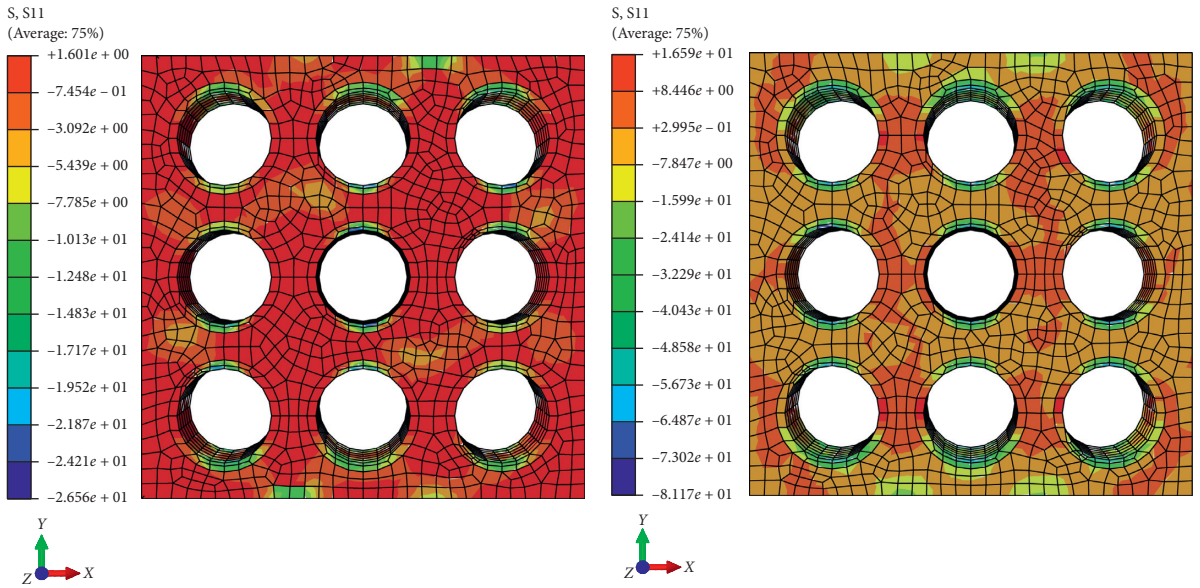

Figure 6: Stress in the X-direction of RC30 (unit: MPa). (a) 4 s. (b) 10 s.

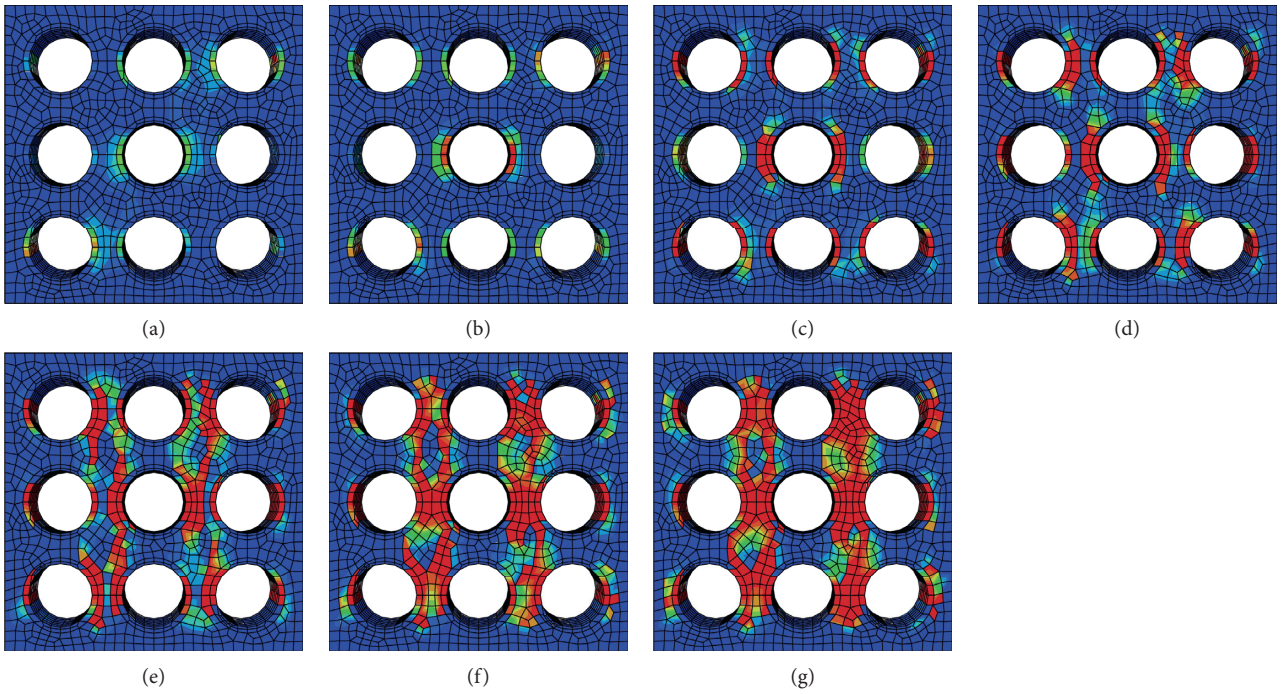

Figure 7: Damage evolution in the RC30 concrete model. (a) 4 s. (b) 5 s. (c) 6 s. (d) 7 s. (e) 8 s. (f) 9 s. (g) 10 s.

earlier in recycled concrete than ordinary concrete, as shown in Figure 8.

When the thicknesses of the ITZs are 1 mm, 2 mm, 3 mm and 4 mm, the replacement rates of the recycled aggregates in the recycled concrete based on the volume ratio are approximately 20%, 30%, 50%, and 80%, respectively. When the model concrete cracks, the loads are 33 MPa, 31.6 MPa, 30.9 MPa, 27.75 MPa, and 26.6 MPa. Compared with the test results in [23–25], the results and the variation trend in the current study are consistent, as shown in Figures 9 and 10. Figures 9 and 10 show that compared with that of normal concrete, the cracking load of the recycled concrete decreases with increasing ITZ thickness, especially when the thickness of the ITZ is more than 2 mm. The concrete cracking load of the model with a recycled aggregate replacement rate greater than 30% is

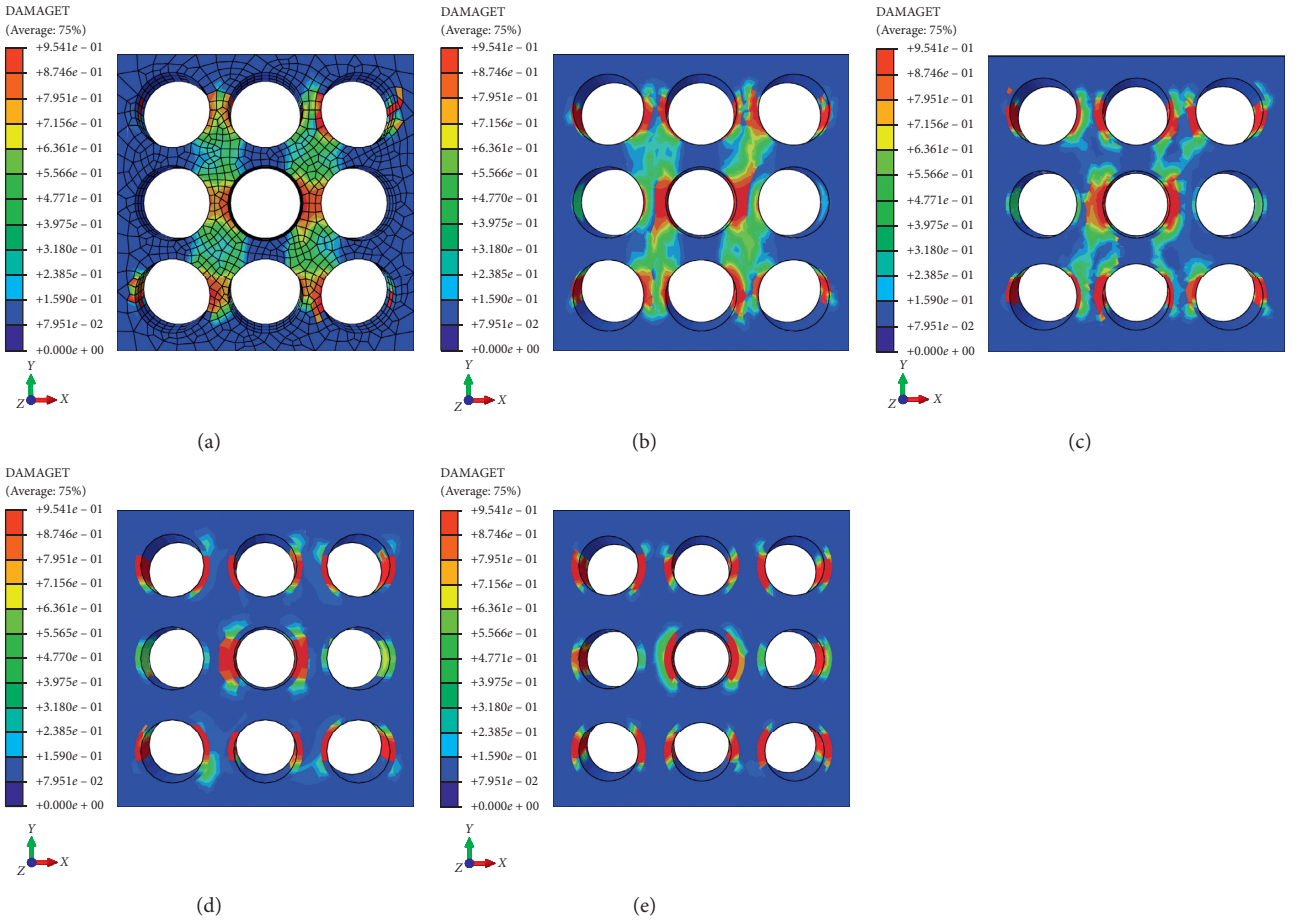

Figure 8: Initial damage diagram in the ITZ for 5 types of recycled concrete models. (a) NCA. (b) RC10. (c) RC20. (d) RC30. (e) RC40.

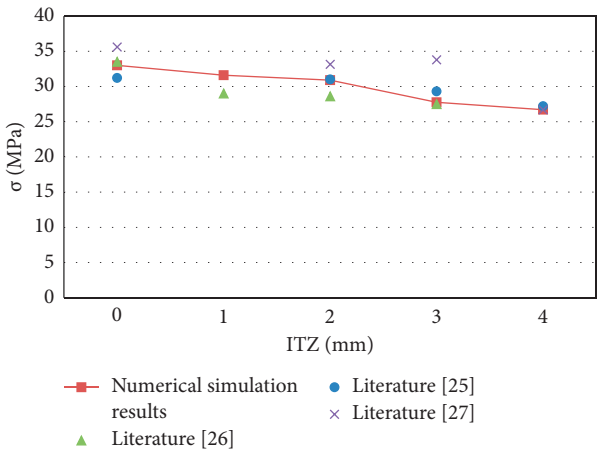

Figure 9: Cracking load in different concrete models.

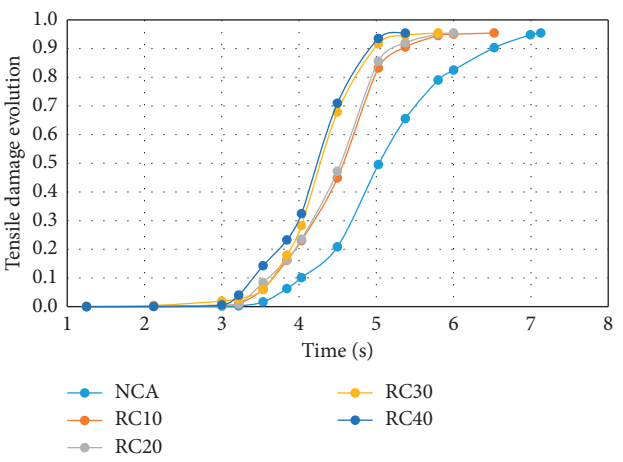

Figure 10: Damage evolution of concrete models with different ITZ thicknesses.

significantly reduced, and the decrease in the concrete strength is not very obvious. When the thickness of the ITZ is more than 2 mm, the thickness of the ITZ has a significant influence on the damage performance of recycled concrete, and the cracking strength of concrete is also significantly reduced.

4. Conclusion

The following conclusions can be drawn based on the quantitative analysis of the ITZ thickness of recycled concrete and the numerical simulation of the cracking evolution of the concrete model: (1) the thickness of the old mortar

attached to the recycled aggregates and the recycled ITZ thickness increase with the increase in the aggregate particle size and decrease with the increase in the strength of the abandoned concrete; (2) with the increase in the thickness of the ITZ, the cracking strength of the recycled concrete model decreases continuously, which is consistent with the variation law of the test results in the relevant literature; (3) the numerical simulation results of different concrete models show that the cracking of recycled concrete starts from the ITZ and that the damage degree increases with the increase in the thickness of the ITZ; and (4) when the thickness of the ITZ is no more than 2 mm (i.e., the replacement rate of recycled aggregates is not more than 30%), the cracking strength of recycled concrete is not significantly reduced compared with that of ordinary concrete.

Data Availability

The data used to support the findings of this study are available from the corresponding authors upon request.

Conflicts of Interest

The authors declare that they have no conflicts of interest.

Acknowledgments

The authors are grateful to the Natural Science Foundation of China for supporting this paper via the Surface Performance Evolution of Concrete Face Rockfill Dam under the Action of Multi-Factor Coupling project (No. 51879145). The authors would also like to thank Professor Tian Bin, Professor Xu Gang, Dr. Chen Bofu, and Dr. Chen Lei for several useful discussions during the course of this research.

References

[1] S. Xie, "Study on interfacial bonding in cement-based composites," *Journal of the Chinese Ceramic Society*, vol. 11, no. 4, pp. 489–497, 1983.

[2] R. L. Berger, D. S. Cahn, and J. D. Mcgregor, "Calcium hydroxide as a binder in portland cement paste," *Journal of the American Ceramic Society*, vol. 53, no. 1, pp. 57-58, 2010.

[3] Z. Wu, "Interface problems of cement-based composites," *Journal of Wuhan University of Technology*, vol. 2, pp. 143–149, 1982.

[4] M. Etxeberria, E. Vázquez, and A. Marí, "Microstructure analysis of hardened recycled aggregate concrete," *Magazine of Concrete Research*, vol. 58, no. 10, pp. 683–690, 2006.

[5] R. K. Dhir, M. C. Limbachiya, and T. Leelawat, "Suitability of recycled concrete aggregate for use in BS 5328 designated mixes," *Proceedings of the Institution of Civil Engineers—Structures and Buildings*, vol. 134, no. 3, pp. 257–274, 1999.

[6] V. W. Y. Tam, X. F. Gao, and C. M. Tam, "Microstructural analysis of recycled aggregate concrete produced from two-stage mixing approach," *Cement and Concrete Research*, vol. 35, no. 6, pp. 1195–1203, 2005.

[7] O. Buyukozturk, A. H. Nilson, and F. O. Slate, "Stress-strain response and fracture of a concrete model in biaxial loading," *ACI Materials Journal*, vol. 68, no. 8, pp. 590–599, 1971.

[8] T. Y. Liu, A. H. Nilson, and F. O. Slate, "Stress-strain response and fracture of a concrete in uniaxial and biaxial compression," *ACI Journal Proceedings*, vol. 69, no. 31, pp. 291–295, 1972.

[9] G. Prokopski and J. Halbiniak, "Interfacial transition zone in cementitious materials," *Cement and Concrete Research*, vol. 30, no. 4, pp. 579–583, 2000.

[10] Y. Wang, *Strength and Constitutive Relationship of Recycled Aggregate Concrete under Multiaxial Stress States*, Guangxi University Press, Nanning, China, 2017.

[11] S. Feng, H. Xiao, and H. Li, "Study on Comparative studies of the effect of ultrahigh-performance concrete and normal concrete as repair materials on interfacial bond properties and microstructure," *Engineering Structures*, vol. 222, Article ID 111222, 2020.

[12] M. Sánchez de Juan and P. Alaejos Gutiérrez, "Study on the influence of attached mortar content on the properties of recycled concrete aggregate," *Construction and Building Materials*, vol. 23, no. 2, pp. 872–877, 2008.

[13] J. Xiao, B. Yuan, and B. Lei, "Effect of recycled concrete coarse aggregates on service-load deflections of reinforced concrete columns," *Coal Ash China*, vol. 1, pp. 14–16, 2007.

[14] R. Bruno, T. Yamamoto, and Y. Yamashiki, "A study on the reduction in hydration heat and thermal strain of concrete with addition of sugarcane bagasse fiber," *Materials*, vol. 13, no. 13, p. 3005, 2020.

[15] P. Stroeven, "Stereological estimation of fractal number of fracture planes in concrete," *Disordered Materials and Interfaces*, pp. 343–348, Materials Research Society, Pittsburgh, PA, USA, 1995.

[16] P. Yi-jiang and Y. Li-ping, *Meso-Analysis Method for Recycled Concrete*, Science Press, Beijing, China, 2018.

[17] S. P. Shah and G. Winter, "Inelastic behavior and fracture of concrete," *ACI Materials Journal*, vol. 63, no. 9, pp. 5–28, 1966.

[18] J. S. Lawler, D. T. Keane, and S. P. Shah, "Measuring three dimensional damage in concrete under compression," *ACI Materials Journal*, vol. 98, no. 6, pp. 465–475, 2001.

[19] B. A. Harish, N. Venkata Ramana, and K. Gnaneswar, *Experimental and Analytical Studies on Recycled Coarse Aggregate Concrete*, Elsevier, Amsterdam, Netherlands, 2020.

[20] J.-z. Xiao, J.-t. Du, and Q. Liu, "Numerical simulation on stress-strain curve of recycled concrete under uniaxial compression with lattice model," *Journal of Building Materials*, vol. 12, no. 5, pp. 511–518, 2009.

[21] M. P. Lutz, P. J. M. Monteiro, and R. W. Zimmerman, "Inhomogeneous interfacial transition zone model for the bulk modulus of mortar," *Cement and Concrete Research*, vol. 27, no. 7, pp. 1113–1122, 1997.

[22] X.-l. Du, Y. Wang, and D.-c. Lu, "Experimental study of biaxial compression test of cement mortar material," in *Proceedings of the 2nd National Engineering Safety and Protection Academic Conference*, vol. 2, pp. 236–241, Beijing, China, 2010.

[23] Z. Deng, B. Liu, B. Ye et al., "Mechanical behavior and constitutive relationship of the three types of recycled coarse aggregate concrete based on standard classification," vol. 22, no. 2, pp. 30–45, 2020.

[24] S. B. Huda and M. S. Alam, "Mechanical behavior of three generations of 100% repeated recycled coarse aggregate concrete," *Construction and Building Materials*, vol. 65, pp. 574–582, 2014.

[25] J. Zhou, H. He, X. Meng, and Y. Yang, "Basic mechanical properties of recycled concrete experimental study," *Journal of Shenyang Jianzhu University (Natural Science)*, vol. 26, no. 3, pp. 464–468, 2010.

Hindawi
Advances in Materials Science and Engineering
Volume 2021, Article ID 6620577, 13 pages
https://doi.org/10.1155/2021/6620577

Research Article

Experimental Study on CFRP-Confined Circularized Concrete-Filled Square Steel Tube Short Columns

Yuchuan Wen, Zhongjun Hu, Anningjing Li, Quanheng Li, Xuepeng Li, and Yan Xu

College of Construction Engineering, Jilin University, Changchun 130026, China

Correspondence should be addressed to Zhongjun Hu; huzj@jlu.edu.cn

Received 17 November 2020; Revised 17 December 2020; Accepted 4 March 2021; Published 17 March 2021

Academic Editor: Peng Zhang

This study investigates the suitability of the circularization technique for strengthening square concrete-filled square steel tube (CFSST) short columns. A total of 16 specimens were tested under axial compression. The main parameters under investigation were concrete strength, the thickness of arc cement mortar layer components (CAM), and the layers of carbon fiber-reinforced polymer (CFRP) sheets. Test results indicated that the failure mode of CFRP-confined circularized CFSST (C-C-CFSST) columns was similar to that of CFRP-confined concrete columns. The CFRP-confined circularized strengthening method can increase confinement efficacy and reduce the stress concentration at the corners of CFSST columns. Three existing CFRP-confined concrete stress-strain models were evaluated using the test results. The predictions of the Lam and Teng stress-strain model agree well with the test data.

1. Introduction

Concrete-filled steel tube (CFST) has the advantages of high bearing capacity and ductility and is widely used in civil structures [1, 2]. However, the exposed CFST structures are easily failed by corrosion in engineering practice, especially in the moisture environment [3–5]. When the corrosion occurs on steel tube, the durability and bearing capacity of CFST will degrade [6]. Consequently, finding a method to enhance the corrosion resistance of CFST columns is necessary [7].

Fiber-reinforced polymer (FRP) composites have been widely used in retrofitting existing columns [8, 9]. FRP-confined concrete has been proven to be feasible in theoretical research and engineering practice [10]. Strengthening CFST columns with FRP material has the dual advantages of improving bearing capacity and durability [11–13].

In recent years, concrete-filled square steel tube (CFSST) has been increasingly applied in various building structures because of its advantages of easy joint connection and construction [14–16].

Tao, Han, and Wang studied the section shape influence on the axial compression performance of CFRP-confined CFST short columns. The results indicated that the CFRP confinement efficacy of a CFSST column is lower than a circular CFST column because of the stress concentration at the corners of the square steel tube and the reduction of the effective area of the confined section [17, 18].

To improve the confinement efficiency of CFSST columns by CFRP jackets and to reduce stress concentration, the circularizing technique has been proven to be an effective method before FRP wrapping by some scholars. The experimental study of Priestley and Seible first indicated that shape modification by bonding concrete segments can improve the confinement efficiency of CFRP jackets [19]. Hadi et al. carried out relevant research on the CFRP-confined arc-treated concrete rectangular columns; the results show that using precast concrete arc-treated components as transitions between CFRP and rectangular columns could significantly reduce stress concentration and enhance the effective constraint area of the cross section [20, 21]. The above studies showed that circularizing concrete columns by bonding precast segments can increase the axial load capacity and change the stress-strain curve from softening to hardening the branch of reinforced concrete (RC) columns [20].

Yang et al. performed an experimental study on the axial compressive performance of rectangular concrete-filled FRP-steel composite tube columns for various corner radiuses and proposed that FRP-confined CFSST concrete stress-strain curve can be divided into four phases (i.e., initial linear phase, transition to yield phase, hardening phase, and residual phase). Different corner radii significantly affect the confinement effectiveness and the third phase of the FRP-confined CFSST stress-strain curve [22]. Most of the existing CFSST columns have sharp corners, which cause stress concentration, and the CFSST columns cannot round the corners similar to RC columns in practical engineering. Therefore, shape modification before FRP wrapping may effectively reduce stress concentration. To solve this problem further, an experimental study was undertaken to investigate the suitability of the circularization technique for strengthening CFSST short columns. This study utilizes the bonding CAM components between FRP and the CFSST column as a circularizing method. Sixteen specimens were tested under axial compression to study the influence of different CAM thicknesses (the middle height of CAM component), layers of CFRP, and concrete strength on bearing capacity, deformation performance, and stress-strain relationship.

2. Experimental Program

2.1. Test Specimens. All of the specimens were 100 mm × 100 mm in cross section and 300 mm in height. Twelve specimens were C-C-CFSST columns, two specimens were CFRP-confined CFSST columns, and two specimens were CFSST columns. Sixteen specimens were divided into two groups according to the concrete strength. The specimens of group 1 were C20, and those of group 2 were C30. Each group had six C-C-CFSST specimens with 5, 10, and 15 mm CAM thickness. The corresponding radius of rounded corners was 20, 30, and 40 mm. T700 CFRP sheets with 1.72% elongation were used in this test. The performances of steel tubes, epoxy adhesive, and CFRP sheets were tested in a structural laboratory, as shown in Table 1. The test specimens are listed in Table 2. The cross section and FRP bonding position of specimens are shown in Figure 1.

The concrete specimens were prepared with Portland cement. The diameter of the coarse aggregate was 5–10 mm, which was used for fine aggregate in continuous grading and medium sand. The axial compressive strength measured values of two groups' specimens were 20.7 and 27.1 MPa.

The main processes of specimen preparation are as follows: (1) Prefabricated CAM was configured with a high mark cement mortar, and the CAM mold was made with a PVC tube and a plate. The specimen and the CAM should have similar strength values to satisfy the equal-strength principle. The test using CAM strength was slightly higher than the specimen. (2) The epoxy resin was smeared on the surface of the steel tube, and the CAM was bonded on corresponding positions. (3) The CAM components were fixed to dry using adjustable circular steel rings for 48 h. (4) The specimens were wrapped with CFRP sheets after circularizing. The overlap length of the CFRP was 100 mm. The making process of specimen is shown in Figure 2.

2.2. Test Setup and Instrumentation. All specimens were tested under axial compression using a pressure testing machine with 2000 kN capacity. Four axial strain gauges and four hoop strain gauges were pasted on the mid-height of the specimen. Four linear variable differential transducers (LVDTs) were used to monitor the axial deformation of specimens. The LVDTs were installed at the corner of the specimen and covered the mid-height of the specimen. The layout of the test setup and measuring point are shown in Figure 3. The loading program was based on standard for test method of concrete structures (GB/T 50152–2012) [23]. To avoid the premature failure of specimens, the top and bottom ends of specimens were wrapped with additional two layers of CFRP with 50 mm width.

3. Test Results and Discussion

3.1. Main Test Results. The key test results of axial compression specimens are shown in Table 3. f_{c0} is the compressive strength of unconfined concrete columns, f_{co}' is the compressive strength calculated value of CFSST, and N is the ultimate bearing capacity of specimens.

3.2. Test Failure Modes. The typical failure mode of specimens is shown in Figure 4. The tested CFRP-confined CFSST columns failed by CFRP jacket rupture near the corners. These ruptures occurred in the mid-height region of all the specimens. The failure mode of C-C-CFSST columns was similar to CFRP-confined concrete columns.

The specific breakpoint locations of test specimens after loading are shown in Figure 5. L is the horizontal distance from the breakpoint to the corner. The CFRP-confined CFSST column failed by CFRP rupture at the corner of the steel tube because of stress concentration. The CFRP breakpoints of C-C-CFSST columns occurred away from the corner when CAM thickness increases from 5 mm to 15 mm. The changing position of CFRP breakpoints showed that the stress concentration of the steel tube corner gradually reduced with the increasing CAM thickness.

3.3. Load-Strain Response. Figure 6 shows the load-strain curves of C-C-CFSST specimens (group 2). The axial and hoop strains were obtained by the average of four axial strain gauges and four hoop strain gauges, respectively. For specimens C30-5-1-11, C30-10-1-13, and C30-15-1-15, the ultimate load is 738.3, 843.9, and 893.4 kN, respectively. For specimens C30-5-2-12, C30-10-2-4, and C30-15-2-16, the ultimate load is 867.1, 950.3, and 1069.8 kN, respectively. Similar to those FRP-confined concrete load-strain curves, all specimens' curves showed the same trend with a bilinear shape and a monotonically ascending characteristic. When the load was less than 80% of the ultimate load, the axial and hoop strain developed slowly. When the load was more than 80% of the ultimate load, the curves came into the plastic stage, and the deformation grew rapidly. The hoop rupture failure of CFRP occurred when reaching the ultimate loads of specimens, and the ultimate hoop strain slightly increased with the increasing CAM thickness.

Table 1: Material properties.

Materials	Thickness (mm)	Yield strength (MPa)	Tensile strength (MPa)	Tensile elastic modulus (MPa)
Steel tube	2	313.9	392.6	2.07×10^5
CFRP	0.167	—	3094	2.44×10^5
Epoxy resin	—	—	58	2.584×10^3

Table 2: Test parameters of specimens.

Specimen	CAM thickness	Confinement condition
C20-0-0-1	—	—
C20-0-1-2	—	1-layer CFRP confinement
C20-5-1-3	5 mm	1-layer CFRP confinement
C20-5-2-4	5 mm	2-layer CFRP confinement
C20-10-1-5	10 mm	1-layer CFRP confinement
C20-10-2-6	10 mm	2-layer CFRP confinement
C20-15-1-7	15 mm	1-layer CFRP confinement
C20-15-2-8	15 mm	2-layer CFRP confinement
C30-0-0-9	—	—
C30-0-1-10	—	1-layer CFRP confinement
C30-5-1-11	5 mm	1-layer CFRP confinement
C30-5-2-12	5 mm	2-layer CFRP confinement
C30-10-1-13	10 mm	1-layer CFRP confinement
C30-10-2-14	10 mm	2-layer CFRP confinement
C30-15-1-15	15 mm	1-layer CFRP confinement
C30-15-2-16	15 mm	2-layer CFRP confinement

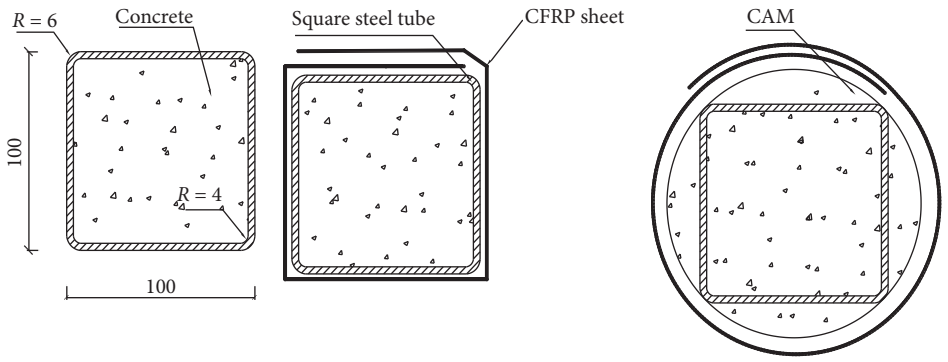

Figure 1: Cross sections of specimens. (a) CFSST column. (b) CFRP-confined CFSST column. (c) C-C-CFSST column.

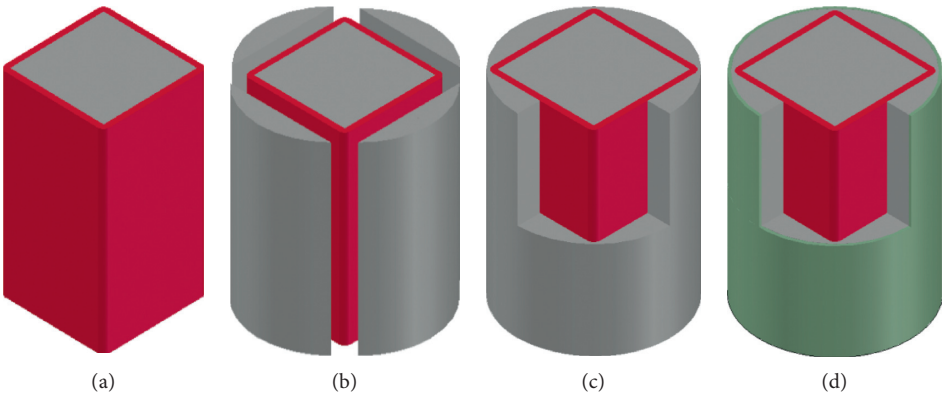

Figure 2: Production process of specimens. (a) CFSST column. (b) CAM bonding. (c) CAM fixing. (d) CFRP wrapping.

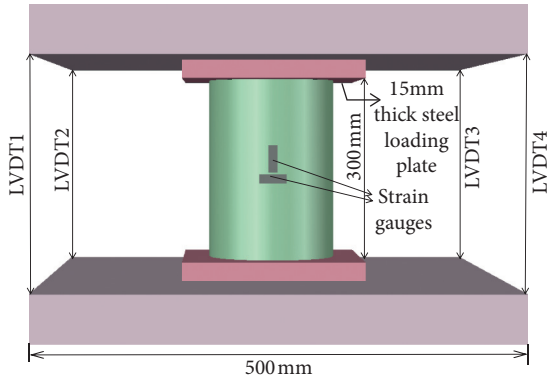

Figure 3: Loading apparatus and LVDTs.

Table 3: Experimental results of specimens.

Specimen	f_{c0} (MPa)	f_{co}' (MPa)	N (kN)
C20-0-0-1	20.7	45.82	488.0
C20-0-1-2	20.7	45.82	542.7
C20-5-1-3	20.7	45.82	650.5
C20-5-2-4	20.7	45.82	765.0
C20-10-1-5	20.7	45.82	760.0
C20-10-2-6	20.7	45.82	875.6
C20-15-1-7	20.7	45.82	800.4
C20-15-2-8	20.7	45.82	1019.3
C30-0-0-9	27.1	53.39	539.9
C30-0-1-10	27.1	53.39	631.6
C30-5-1-11	27.1	53.39	738.3
C30-5-2-12	27.1	53.39	867.1
C30-10-1-13	27.1	53.39	843.9
C30-10-2-14	27.1	53.39	950.3
C30-15-1-15	27.1	53.39	893.4
C30-15-2-16	27.1	53.39	1069.8

3.4. CAM Influence on Bearing Capacity and Vertical Displacement. Figures 7 and 8 show vertical displacement and bearing capacity of test specimens with different CAM thickness. When the CAM thickness increases from 5 mm to 15 mm, the bearing capacity and vertical displacement increase gradually. Compared with C20-0-1-2, the bearing capacity of C20-5-1-3, C20-10-1-5, and C20-15-1-7 increased by 19.9%, 40.2%, and 47.5%, respectively. Compared with C30-0-1-10, the bearing capacity of C30-5-1-11, C30-10-1-13, and C30-15-1-15 increased by 16.9%, 33.6%, and 41.4%, respectively. The increasing bearing capacity and vertical displacement showed the great effectiveness of CAM between CFRP sheets and CFSST columns. The increase of the CAM thickness generally leads to an increase in the bearing capacity and vertical displacement, which indicated that the circularization technique for strengthening CFSST short columns is a suitable and alternative strengthening method in engineering.

4. Stress-Strain Models of CFSST Columns

4.1. Axial Stress-Strain Curves. The axial stress-axial strain curves of all the test specimens are shown in Figure 9. All the curves had an obvious bilinear shape with two segments. The first-segment slope of the curve was much bigger than the second-segment slope. The CAM thickness affected mainly the second segment of the stress-strain curve. The second-segment slopes of C-C-CFSST specimens became slightly larger with the increase of CAM thickness. The ultimate axial stress f_{cc}' was affected by the CAM thickness and the layers of CFRP. As for specimens with no CAM, f_{cc}' and the second-segment slope were the smallest. The stress-strain curve of C20-5-1-3 and C30-5-1-11 was close to the stress-strain curve of C20-0-1-2 and C30-0-1-11, respectively, showing that CFRP wrapping was less effective for specimens with a CAM thickness of 5 mm. The specimens with a CAM thickness of 10 or 15 mm increased the effectiveness of CFRP confinement. To ensure the strengthening effectiveness in practical engineering, the CAM thickness should be large. The layers of CFRP affected f_{cc}' and ductility. The ultimate axial strain $\varepsilon_{cc}'$and ultimate axial stress f_{cc}' of specimens with two layers of CFRP were significantly larger than those of specimens with one layer of CFRP.

4.2. Existing Stress-Strain Models. The existing FRP-confined concrete stress-strain models are mainly separated into two types. The first type uses a single function to express the stress-strain relationship and includes the Mander model, Samaan model, Yu model, and Yang and Feng model [24–27]. The second type uses piecewise function to express the stress-strain relationship and includes the Lam and Teng model, Lai model, Miyauchi model, and Wei and Wu model [28–34]. Among all existing models, the Lam and Teng model, Lai model, and Yang model are appropriate to predict the stress-strain relationship of CFRP-confined circularized concrete columns according to the published literature [8, 27].

4.2.1. Lam and Teng Model. The first segment of the Lam and Teng model is a parabolic type, and the second segment is a linear type. This model has a high degree of accuracy in predicting FRP-confined concrete strength. The model is described by the following equation:

$$\begin{cases} \sigma_c = E_c\varepsilon_c - \dfrac{(E_c - E_2)}{4f_0}\varepsilon_c^2 \left(0 \le \varepsilon_c \le \varepsilon)_t, \right. \\ \sigma_c = f_{co}' + E_2\varepsilon_c \left(\varepsilon_t \le \varepsilon_c \le \varepsilon_{cu}\right), \end{cases} \tag{1}$$

where σ_c and ε_c are the axial stress and axial strain, respectively. The ultimate axial stress and the ultimate strain are calculated as follows:

$$\begin{aligned} \frac{f_{cc}'}{f_{co}'} &= 1 + 3.3k_1\frac{f_l}{f_{co}'}, \\ \frac{\varepsilon_{cu}}{\varepsilon_{co}} &= 1.75 + 12k_s\frac{f_l}{f_{co}}\left(\frac{\varepsilon_{ru}}{\varepsilon_{co}}\right)^{0.45}, \end{aligned} \tag{2}$$

where ε_{ru} is the confinement effectiveness coefficient k_1 and transition strain ε_t is given as follows:

Figure 4: Failure mode of some specimens.

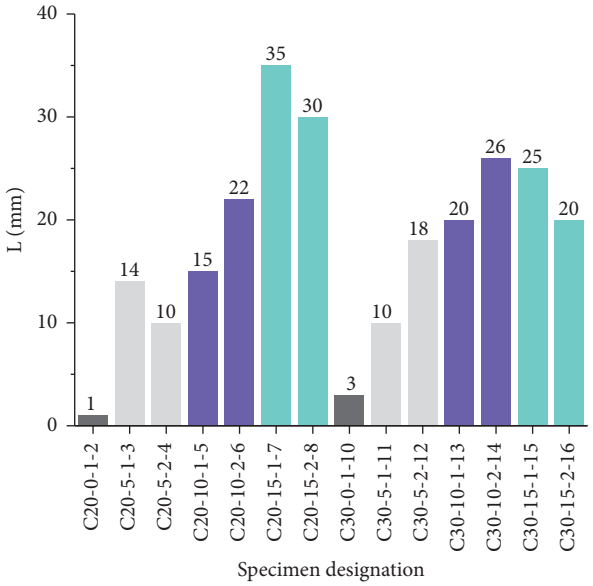

Figure 5: Influence of CAM thickness on CFRP breakpoint location.

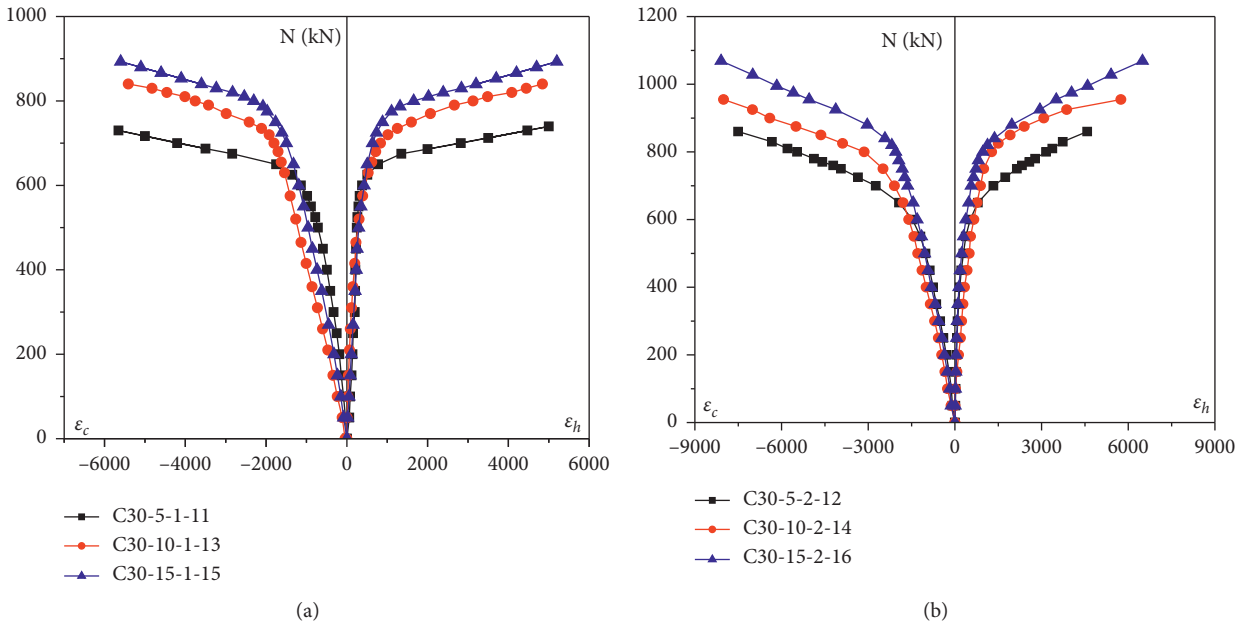

Figure 6: Test load-strain curves. (a) Specimens warped with one-layer CFRP. (b) Specimens warped with two-layer CFRP.

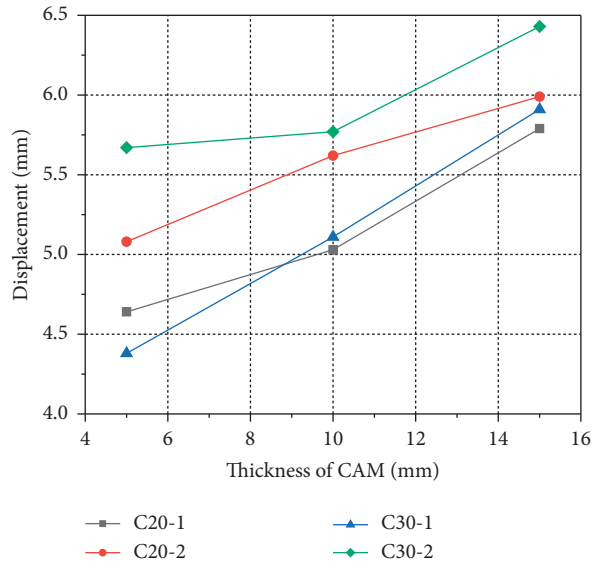

Figure 7: The effects of CAM thickness on vertical displacement.

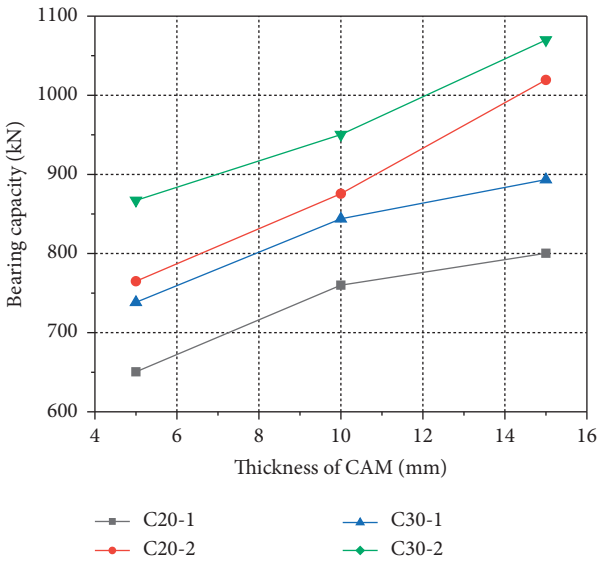

Figure 8: The effects of CAM thickness on bearing capacity.

$$k_s = 1 - \frac{(b-2r)^2 + (h-2r)^2}{3A_{\text{cor}}},$$
$$\varepsilon_t = \frac{2f_0}{E_c - E_2}, \tag{3}$$

where $E_c = 4730\sqrt{f'_{co}}$ is the elastic modulus of the unconfined concrete, $E_2 = (f'_{cc} - f_0)/\varepsilon_{cu}$ is the slope of the linear second portion, $\varepsilon_{co} = 0.002$ is the axial strain with ultimate load, and k_s is the constraint coefficient.

4.2.2. Lai Model. The Lai model has a high accuracy to predict the CFRP-confined rectangular concrete column with corner radii, which is described by the following equation:

$$\begin{cases} \sigma_z = \dfrac{\varepsilon_z}{A + B\varepsilon_z + C\varepsilon_z^2}, & 0 \le \varepsilon_z \le \varepsilon_{zb}, \\ \sigma_z = \sigma_{zb} + E_2(\varepsilon_z - \varepsilon_{zb}), & \varepsilon_{zb} \le \varepsilon_z \le \varepsilon_{zc}. \end{cases} \tag{4}$$

A, B, and C are given as follows:

$$\begin{cases} A = \dfrac{1}{E_0}, \\ B = \left(\dfrac{1}{E_p} - \dfrac{2}{E_0} + \dfrac{1}{E_p}\dfrac{E_2}{E_p}\right), \\ C = \left(\dfrac{1}{E_0} - \dfrac{1}{E_p}\dfrac{E_2}{E_p}\right)\dfrac{1}{\varepsilon_t^2}, \end{cases} \tag{5}$$

where $E_p = \sigma_{zb}/\varepsilon_{zb}$.

FRP-confined concrete E_2/E_c in different sections is given as follows:

$$\frac{E_2}{E_c} = \begin{cases} 0.0331\ \ln(\beta_j) - 0.0564, & \beta_j \ge 5.6, \\ 0.1217\ \ln(\beta_j) - 0.2091, & \beta_j < 5.6. \end{cases} \tag{6}$$

Constraint stiffness β_j is given as follows:

$$\beta_j = \frac{E_f t_f}{f_c R}, \tag{7}$$

where R represents the radii of equivalent circle $= 2(b+h)/2\pi$.

Transition stress and strain are given as follows:

$$\frac{\sigma_{zb}}{f_{c,m}} = 0.0568\beta_j^{0.46} + 1,$$
$$\frac{\varepsilon_t}{\varepsilon_{cu}} = 0.011\beta_j + 1. \tag{8}$$

4.2.3. Yang and Feng Model. The Yang and Feng model is different from the two above models, which have no obvious transition segment. This model has high accuracy to predict the CFRP-confined concrete column, which is given as follows:

$$\sigma_c = \frac{(\varepsilon_c/\varepsilon^*_{cc})f^*_{cc}r}{r - 1 + (\varepsilon_c/\varepsilon^*_{cc})r},$$
$$r = \frac{E_c}{E_c - (f^*_{cc}/\varepsilon_{cc})},$$
$$\frac{f^*_{cc}}{\varepsilon_{cc}} = 1 + 3.33\left(\frac{\sigma_l}{f'_{co}}\right)^{0.9}, \tag{9}$$
$$\frac{\varepsilon^*_{cc}}{\varepsilon_{cc}} = 1 + 17.4\left(\frac{\sigma_l}{f'_{co}}\right)^{1.07}.$$

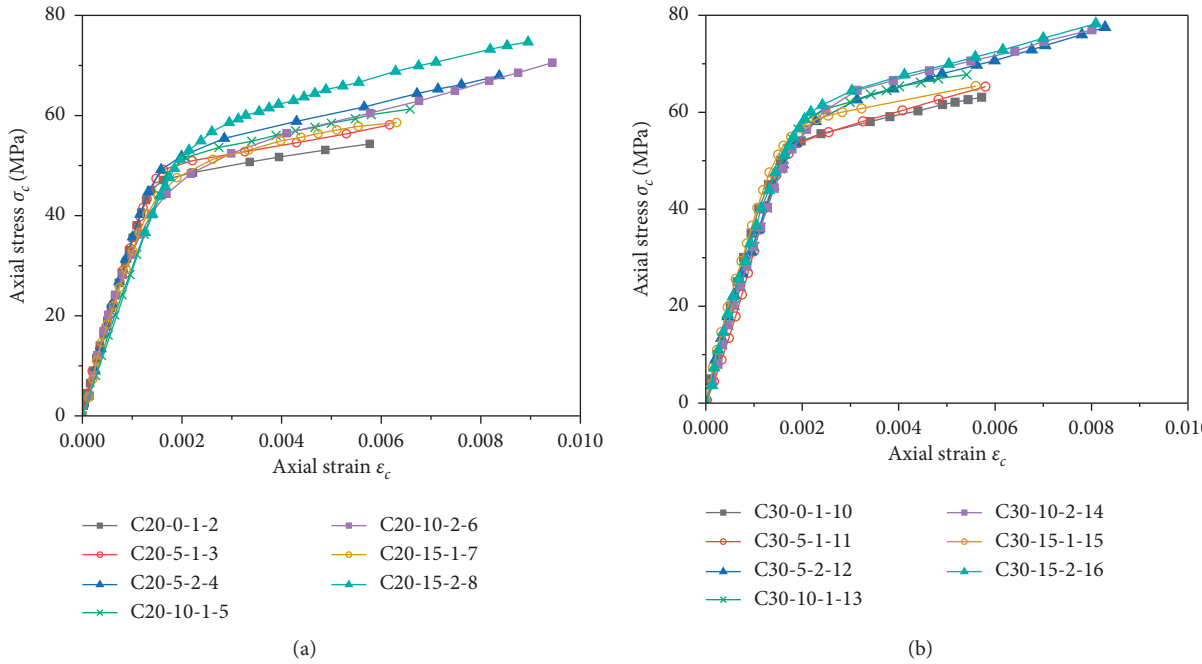

Figure 9: Test stress-strain curves. (a) Specimens of group C20. (b) Specimens of group C30.

where f_{cc}^{*} and ε_{cc}^{*} are the peak axial stress and corresponding axial strain of concrete under a specific level of lateral confining stress.

4.3. CFSST Column Strength f'_{co}. CFSST column strength f'_{co} is given in *technical code for concrete filled steel tubular structures* (GB50936-2014) [35]. It is calculated as follows:

$$f'_{co} = \left(1.212 + B\theta_{sc} + C\theta_{sc}^{2}\right) f_{co},$$

$$B = \frac{0.131 f_y}{235} + 0.723,$$

$$C = -\left(\frac{0.07 f_{ck}}{14.4}\right) + 0.026, \tag{10}$$

$$\theta_{sc} = \alpha_{sc} \frac{f}{f_c},$$

$$\alpha_{sc} = \frac{A_s}{A_c},$$

where A_s and A_c are the steel tube area and core concrete area, respectively; f_y and f are the tensile strength standard value and design value, respectively; α_{sc} and θ_{sc} are the steel ratio and confinement coefficient of the specimen, respectively; B and C are the influence coefficients.

4.4. Effective CFRP Confinement Coefficient k_e. The theoretical fracture strain ε_{fu} can be calculated as fiber strength divided by the elastic modulus. However, the actual fracture strain ε_{ru} is much smaller than the theoretical fracture strain. Lam and Teng suggested that ε_{ru} can be calculated from ε_{fu} as follows:

$$\varepsilon_{ru} = k_e \varepsilon_{fu}, \tag{11}$$

where the effective CFRP confinement coefficient k of the circular column is approximately 0.586 [15] and was taken as 0.5, 0.53, and 0.56 corresponding with CAM thickness of 5, 10, and 15 mm, respectively, according to the test results.

4.5. Intercept of the Stress Axis by the Linear Second Portion f_0. Lam and Teng showed $f_0/f'_{co} = 1.09$ from the test and suggested that $f_0 = f'_{co}$ approximately [15]. However, this method ignores the influence of FRP confinement. The intercept f_0 was affected by the confinement effectiveness, which can be calculated by confinement stiffness ratio β_j and confining factor ξ. Yu [26] suggested that f_0 can be calculated as follows:

$$f_0 = (1 + 1.1\xi) f'_c. \tag{12}$$

However, for FRP-confined CFSST columns, confining factor ξ should value FRP and steel tube confining factor, and f_0 is given as follows:

$$\frac{f_0}{f'_{co}} = 1 + k\xi, \tag{13}$$

where k is modified based on the test results. The linear fitting between f_0/f'_{co} and ξ is shown in Figure 10, and $k = 0.04854$.

4.6. Stress-Strain Model Verification. The experimental stress-strain curves of 12 C-C-CFSST columns were compared with the calculation curves of the Lam and Teng

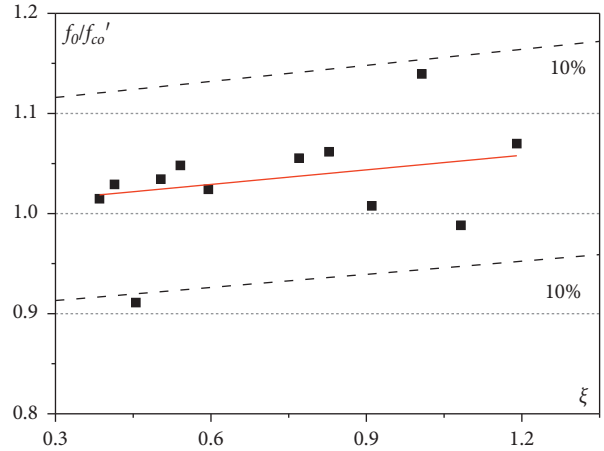

Figure 10: Relationship between f_0/f_{co}' and ξ.

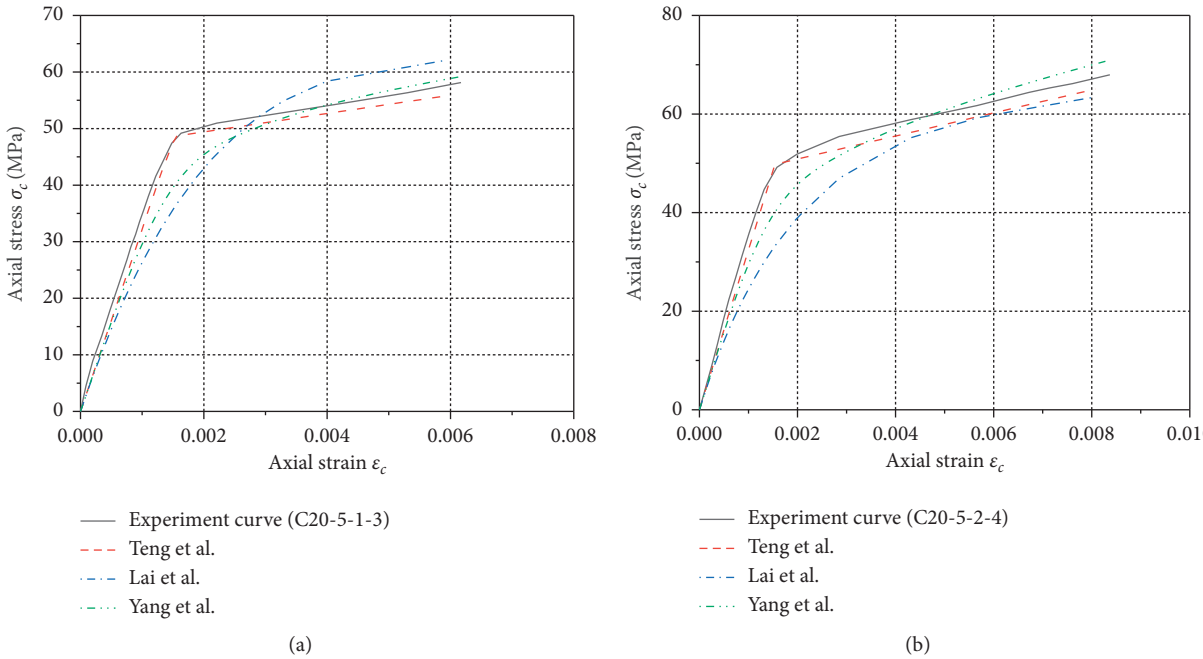

Figure 11: Continued.

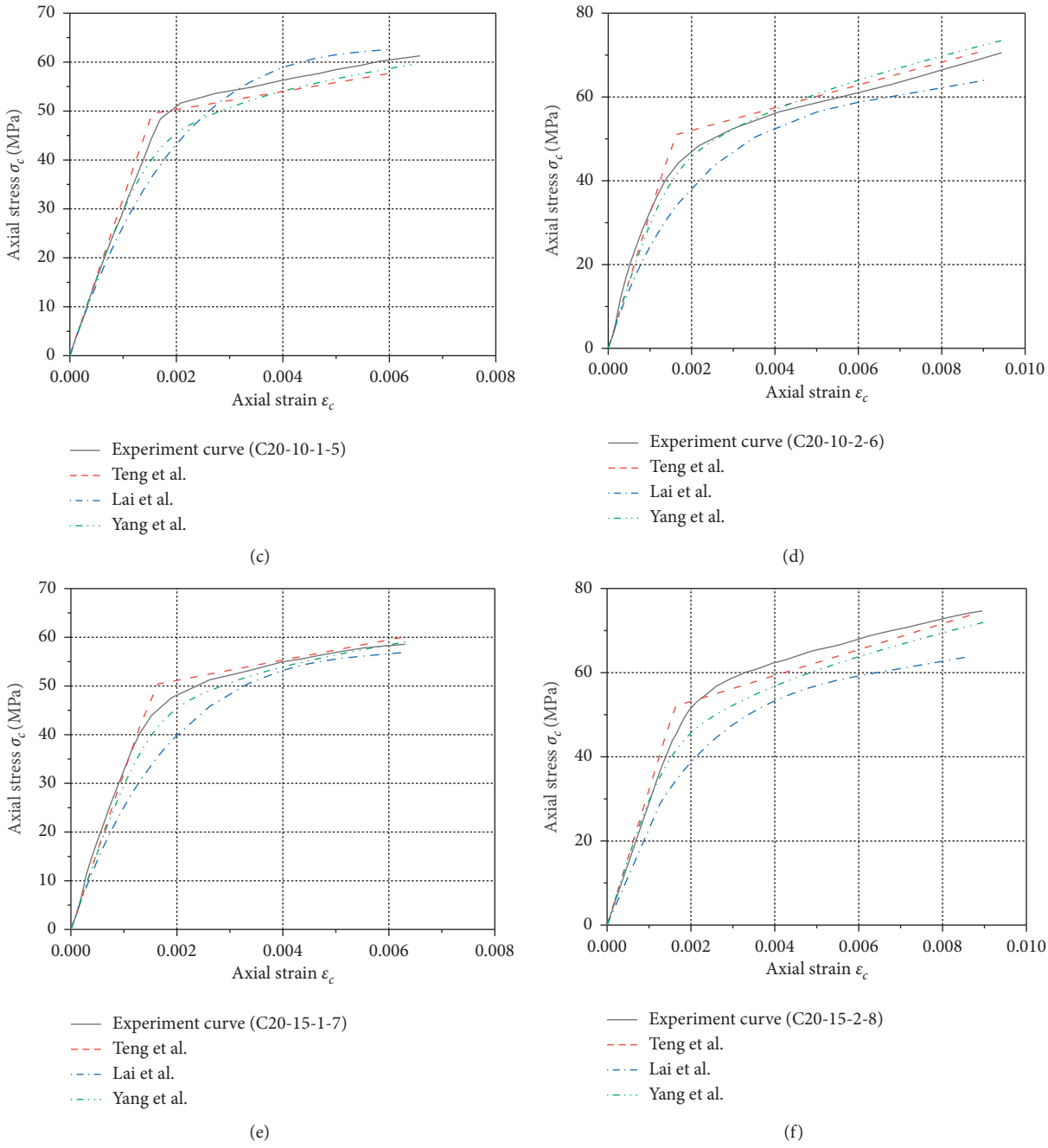

Figure 11: Comparison of calculated stress-strain curves with the experiment curve of group C20. (a) C20-5-1-3. (b) C20-5-2-4. (c) C20-10-1-5. (d) C20-10-2-6. (e) C20-15-1-7. (f) C20-15-2-8.

model, Lai model, and Yang and Feng model. The comparison of calculated stress-strain curves with experiment curve is shown in Figures 11 and 12.

The Lam and Teng model had the highest fitting grade on C-C-CFSST column stress-strain curves among three models. The Yang and Feng model fitted well in some situations, such as C20-10-2-6, C20-15-1-7, C30-5-1-11, and C30-15-2-16. The Lai model had a big deviation compared with other models. The stress-strain curves of the C-C-CFSST column can be separated into three segments, as shown in Figure 13.

In segment I, the Lam and Teng model shows a great prediction on the stress-strain relationship of the C-C-CFSST column. The Lai model and the Yang and Feng model generally underestimated the axial stress of specimens in segment I. The Lam and Teng model has an unobvious segment II slightly overestimating the axial stress. The Yang and Feng model has a similar trend to the experiential curves of segment II. Although similar to segment I, this model underestimates the axial stress of specimens. The Lai model also greatly underestimates the axial stress because of the inaccuracy of the calculated transition strain. In segment III, the ultimate axial stress $f_{cc}^{'}$ calculated

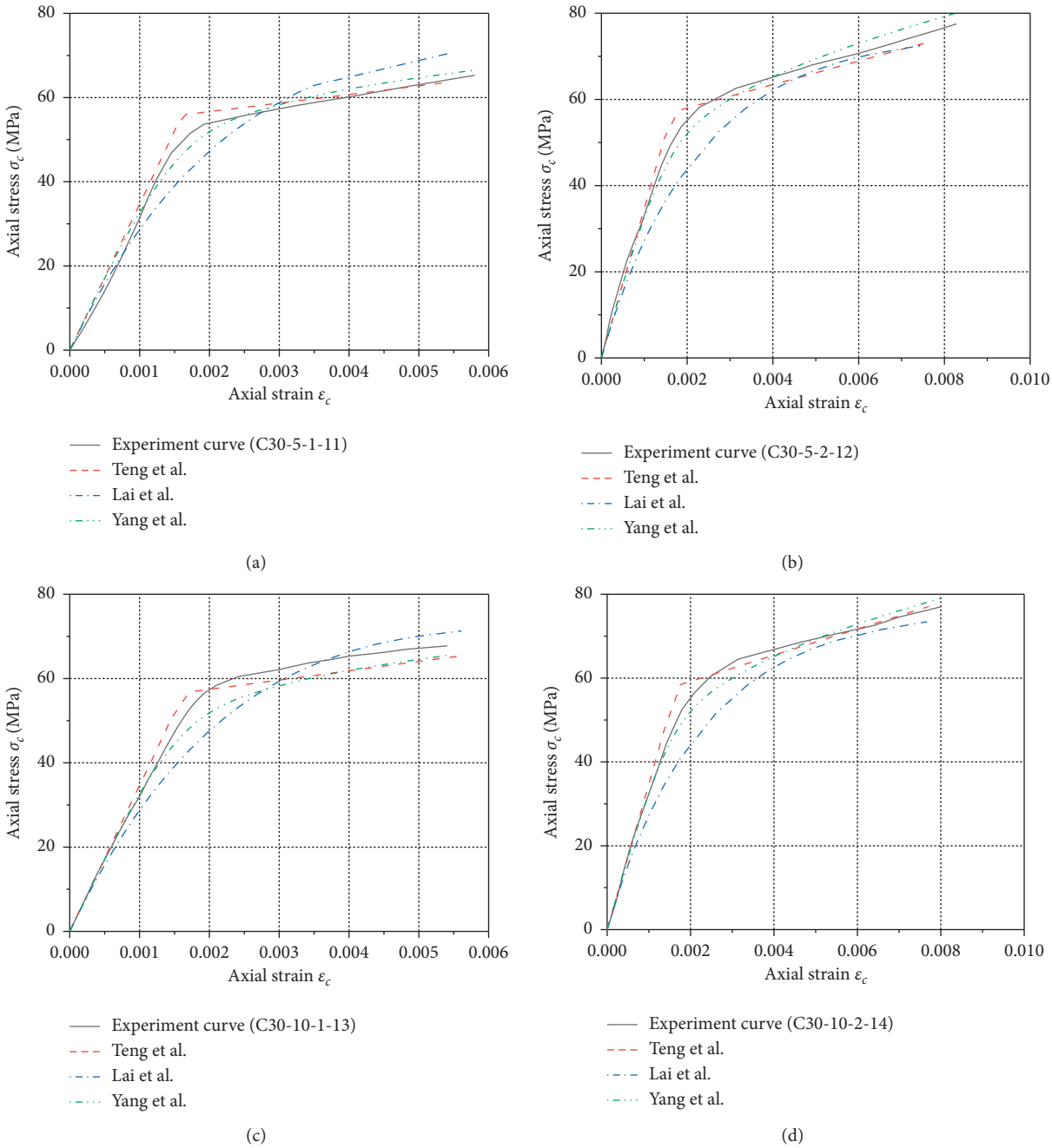

Figure 12: Continued.

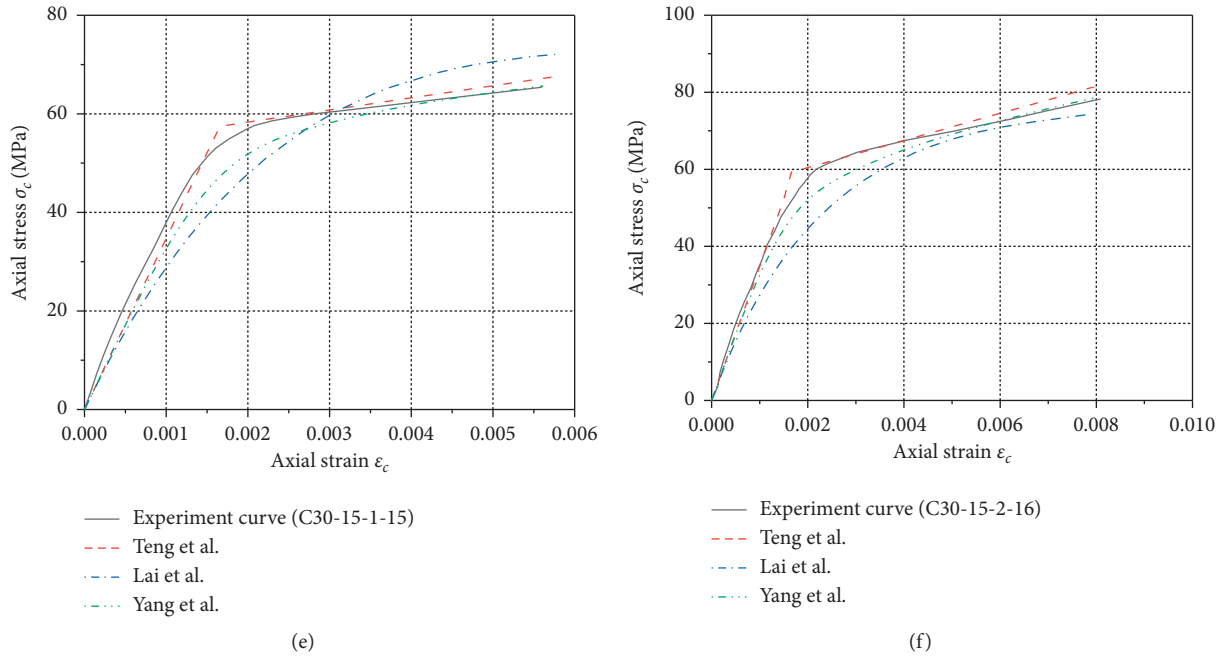

Figure 12: Comparison of calculated stress-strain curves with the experiment curve of group C30. (a) C30-5-1-11. (b) C30-5-2-12. (c) C30-10-1-13. (d) C30-10-2-14. (e) C30-15-1-15. (f) C30-15-2–16.

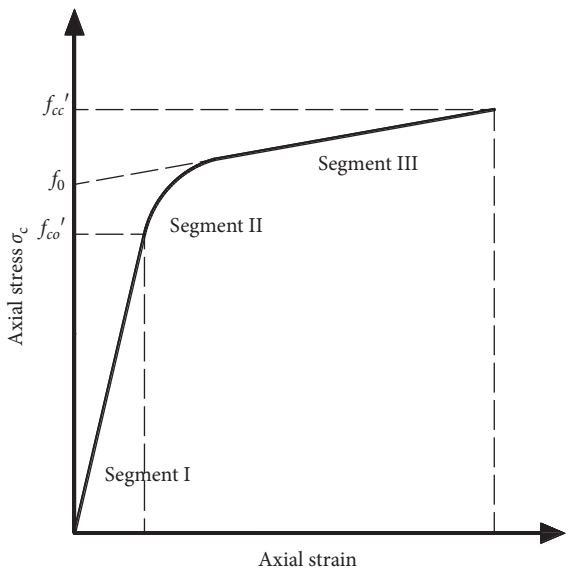

Figure 13: Proposed stress-strain model for C-C-CFSST.

from the Lam and Teng model and the Yang and Feng model is well estimated to the test value. The stress-strain curves calculated from the Lam and Teng model are dramatically close to the test curves. In conclusion, the Lam and Teng model has the greatest prediction for the stress-strain relationship of the C-C-CFSST column among the three models. The Yang model has a more accurate prediction, while CAM thickness is increasing. The transition strain of the Lai model is always larger than the test transition strain, which leads to the inaccuracy of the calculated curves. A more accurate stress-strain model for C-C-CFSST columns should be developed in experimental and theoretical research.

5. Conclusions

This study presents the results from an experimental investigation on the compressive behavior of 16 C-C-CFSST short columns. Based on test data, the effect of CAM thickness on the failure model and the axial stress-strain relationship is discussed. The following conclusions can be made:

(1) CFRP confinement using the CAM could effectively enhance the ductility and axial load carrying capacity of CFSST short columns. For the increasing CAM thickness, the bearing capacity of C20-5-1-3, C20-10-1-5, and C20-15-1-7 is improved by 19.9%, 40.2%, and 47.5%, respectively.

(2) The increasing CAM thickness leads to the CFRP breakpoint gradually moving far from the specimen corner, which led to the decrease of stress concentration of CFRP hoop stress in the corner of the square steel tube. The increasing CAM thickness also made the lateral stress well distributed. The effective fracture strain and constraint efficiency of CFRP increased well.

(3) The stress-strain curve characteristic of the C-C-CFSST column is similar to the CFRP-confined circular concrete column. The applicability of the existing model for FRP-confined concrete was evaluated and compared with the test data. The predictions of the Lam and Teng model agree well with the test data.

Data Availability

The data used to support the findings of this study are listed in this paper.

Conflicts of Interest

The authors declare no conflicts of interest regarding the publication of this paper.

Acknowledgments

This research work was financially supported by the National Natural Science Foundation of China (Grant no. 42072296).

References

[1] X. Zhou, D. Gan, J. Liu, and S. Zhang, "Experiment and analysis on square tubed reinforced concrete stub columns under axial compression," *Journal of Building Structures*, vol. 32, no. 1, pp. 68–74, 2011.

[2] J. Wang, Q. Shen, F. Wang, and W. Wang, "Experimental and analytical studies on CFRP strengthened circular thin-walled CFST stub columns under eccentric compression," *Thin-Walled Structures*, vol. 127, pp. 102–119, 2018.

[3] Y.-X. Hua, L.-H. Han, Q.-L. Wang, and C. Hou, "Behaviour of square CFST beam-columns under combined sustained load and corrosion: experiments," *Thin-Walled Structures*, vol. 136, pp. 353–366, 2019.

[4] C. Hou, L.-H. Han, and X.-L. Zhao, "Full-range analysis on square CFST stub columns and beams under loading and chloride corrosion," *Thin-Walled Structures*, vol. 68, pp. 50–64, 2013.

[5] F. Zhang, J. Xia, G. Li et al., "Degradation of axial ultimate load-bearing capacity of circular thin-walled concrete-filled steel tubular stub columns after corrosion," *Materials*, vol. 13, no. 3, 2020.

[6] H. Huang, Y. Xu, L. Guo et al., "Axial compressive behavior of CFRP-reinforced circular concrete-filled steel tubular stub columns with local corrosion," *Journal of Building Structures*, vol. 41, pp. 109–116, 2020.

[7] S. Zhong, "Application and development in China of concrete filled steel tubular structure," *Architecture Technology*, vol. 02, pp. 80–82, 2001.

[8] J. Zhu, G. Lin, J. Teng et al., "FRP-confined square concrete columns with section curvilinearization under axial compression," *Journal of Composites for Construction*, vol. 24, no. 2, 2020.

[9] Y. Wang, G. Chen, B. Wan et al., "Behavior of circular ice-filled self-luminous FRP tubular stub columns under axial compression," *Construction and Building Materials*, vol. 232, 2020.

[10] Y. Guo and Y. Zhang, "Comparative study of CFRP-confined CFST stub columns under axial compression," *Advances in Civil Engineering*, vol. 18, Article ID 7109061, 8 pages, 2018.

[11] H. Elsanadedy, T. Almusallam, Y. Al-Salloum, and R. Iqbal, "Effect of high temperature on structural response of reinforced concrete circular columns strengthened with fiber reinforced polymer composites," *Journal of Composite Materials*, vol. 51, no. 3, pp. 333–355, 2017.

[12] J. Liang, W. Zou, Z. Wang, and D. Liu, "Compressive behavior of CFRP-confined partially encased concrete columns under axial loading," *Composite Structures*, vol. 229, 2019.

[13] X. Song, X. Gu, Y. Li, T. Chen, and W. Zhang, "Mechanical behavior of FRP-strengthened concrete columns subjected to concentric and eccentric compression loading," *Journal of Composites for Construction*, vol. 17, no. 3, pp. 336–346, 2013.

[14] T. Zhong, "State of the art of concrete filled square steel columns," *Building Structure*, vol. 7, pp. 20–23, 2003.

[15] Z. Tao and L.-H. Han, "Behaviour of fire-exposed concrete-filled steel tubular beam columns repaired with CFRP wraps," *Thin-Walled Structures*, vol. 45, no. 1, pp. 63–76, 2007.

[16] J. Dong, Q. Wang, and Z. Guan, "Structural behaviour of recycled aggregate concrete filled steel tube columns strengthened by CFRP," *Engineering Structures*, vol. 48, pp. 532–542, 2013.

[17] Z. Tao, L.-H. Han, and J.-P. Zhuang, "Axial loading behavior of CFRP strengthened concrete-filled steel tubular stub columns," *Advances in Structural Engineering*, vol. 10, no. 1, pp. 37–46, 2007.

[18] Q. Wang, Y. Xue, Y. Shao, and X. Yan, "Study of static performance of axially compressed concrete filled square steel tubular stub columns confined by CFRP," *China Civil Engineering Journal*, vol. 41, pp. 32–39, 2011.

[19] F. Seible and M. J. N. Priestley, "Strengthening of rectangular bridge columns for increased ductility," in *Proceeding of the Symposium on Practical Solutions for Bridge Strengthening & Rehabilitation*, pp. 239–248, Des Moines, IA, USA, April 1993.

[20] M. N. S. Hadi, T. M. Pham, and X. Lei, "New method of strengthening reinforced concrete square columns by circularizing and wrapping with fiber-reinforced polymer or steel straps," *Journal of Composites for Construction*, vol. 17, no. 2, pp. 229–238, 2013.

[21] M. T. Jameel, M. N. Sheikh, and M. N. S. Hadi, "Behaviour of circularized and FRP wrapped hollow concrete specimens under axial compressive load," *Composite Structures*, vol. 171, pp. 538–548, 2017.

[22] W. Yang, Y. Zhang, J. Chai, G. Wu, and Z. Dong, "Experimental investigation of rectangular concrete-filled fiber reinforced polymer (FRP)-steel composite tube columns for various corner radii," *Composite Structures*, vol. 244, 2020.

[23] National Standard of the People's Republic of China, *Standard For test Method of Concrete Structures. GB/T 50152-2012*, China Architecture & Building Press, Beijing, China, 2012.

[24] J. B. Mander, M. J. N. Priestley, and R. Park, "Theoretical stress-strain model for confined concrete," *Journal of Structural Engineering*, vol. 114, no. 8, pp. 1804–1826, 1988.

[25] M. Samaan, A. Mirmiran, and M. Shahawy, "Model of concrete confined by fiber composites," *Journal of Structural Engineering*, vol. 124, no. 9, pp. 1025–1031, 1998.

[26] Q. Yu, "Stress-strain relationship of FRP-confined concrete subjected to axial compression," *Industrial Construction*, vol. 4, pp. 5–8, 2001.

[27] L. Lam and J. Teng, "Design-oriented stress–strain model for FRP-confined concrete," *Construction & Building Materials*, vol. 17, no. 6-7, pp. 471–489, 2003.

[28] J. G. Teng, T. Jiang, L. Lam, and Y. Z. Luo, "Refinement of a design-oriented stress-strain model for FRP-confined concrete," *Journal of Composites for Construction*, vol. 13, no. 4, pp. 269–278, 2009.

[29] J. Yang and P. Feng, "Analysis-oriented models for FRP-confined concrete: 3D interpretation and general methodology," *Engineering Structures*, vol. 219, 2020.

[30] W. Lai, J. Pan, and X. Jin, "Compressive stress-strain behavior of concrete confined by fiber reinforced polymer," *Industrial Construction*, vol. 10, pp. 81–84, 2004.

[31] X. Jin, J. Pan, G. Liu, and W. Lai, "Research of stress-strain curve of concrete confined by fiber reinforced plastics under

axial compression," *Journal of Building Structures*, vol. 04, pp. 47–53, 2003.

[32] J. Pan, Y. Wang, and W. Lai, "Effect of sectional shape of concrete column on the bearing capacity of short columns wrapped with FRP," *Industrial Construction*, vol. 06, pp. 17–19, 2001.

[33] K. Miyauchi, S. Inoue, T. Kuroda et al., "Strengthening effects of concrete column with carbon fiber sheet," *Transactions of the Japan Concrete Institute*, vol. 21, pp. 143–150, 1999.

[34] Y.-Y. Wei and Y.-F. Wu, "Unified stress-strain model of concrete for FRP-confined columns," *Construction and Building Materials*, vol. 26, no. 1, pp. 381–392, 2012.

[35] National Standard of the People's Republic of China, *Technical Code for Concrete Filled Steel Tubular Structures. GB 50936-2014*, China Architecture & Building Press, Beijing, China, 2014.

Hindawi
Advances in Materials Science and Engineering
Volume 2020, Article ID 6683429, 12 pages
https://doi.org/10.1155/2020/6683429

Research Article

Axial Compression Behaviors of the Steel Tube Confined Reinforced Concrete Columns with Binding Bars

Hao Hu,[1,2] **Zhengliang Li**,[3] **Xi Tu**,[3] **and Junfeng Tang**[3]

[1]*School of Civil Engineering, Chongqing University of Arts and Sciences, Chongqing 402160, China*
[2]*Institute of Civil Engineering Disaster Prevention and Reduction, Chongqing University of Arts and Sciences, Chongqing 402160, China*
[3]*School of Civil Engineering, Chongqing University, Chongqing 400045, China*

Correspondence should be addressed to Hao Hu; hhxkfy@126.com

Received 12 November 2020; Revised 30 November 2020; Accepted 16 December 2020; Published 28 December 2020

Academic Editor: Peng Zhang

An experimental study on the steel tube confined reinforced concrete (STCRC) column with binding bars under axial compression is conducted. The bearing capacity and failure modes are obtained. It can be known that the axial deformation of concrete occurred under compression. The core concrete is wrapped and constrained by the steel tube wall, and the steel tube wall is constrained by binding bars locally, so the local buckling shape of the wall between the binding bars is like wave shape. The 3D finite element model is also developed to analyze the behavior of this type of column under axial compression. Good agreement is shown between the test and predicted results in terms of the load-deformation curves and ultimate strength. The parametric studies indicate that the spacing of binding bars, diameter of longitudinal bars, concrete strength, thickness of the steel tube wall, and section dimension of the column generate different influence on the mechanical properties and bearing capacity. The diameter of longitudinal bars, concrete strength, and section dimension of the column have a great effect on the ultimate bearing capacity. The numerical results also show that the spacing of binding bars has little effect on the ultimate bearing capacity. The larger thickness of the steel tube wall leads to adverse effect on the specimen performance. Finally, the theoretical calculation is carried out, and the result is good.

1. Introduction

Due to the shortcomings of concrete-filled steel tubular (CFST) columns which have poor binding effect on core concrete leading to low bearing capacity and poor ductility, some improved methods on CFST columns have been investigated by scholars.

Ge and Usami [1] reported the experimental results of square CFST columns with and without longitudinal stiffeners under concentric compressive load studied on the strength and deformation of specimens. Huang et al. [2, 3] presented the axial load behavior of CFST columns of square section stiffened with steel reinforcing ties forming an octagonal shape; however, the construction is difficult, and the quality is not easy to guarantee for the columns. Ding et al. [4, 5] discussed the mechanical performances of round-ended CFST columns which may be used as bridge piers under axial loading by experimental study and finite element analysis. The influences of width-thickness ratio, concrete strength, steel yield strength, and wall thickness of the steel tube on the ultimate bearing capacity of the CFST columns were studied. Xia et al. [6] investigated the improving mechanism of reinforcement on load transformer performance of CFST columns with high-strength concrete and thin-walled steel tube (where the thickness is 1.2 mm) subjected to axial compression and concluded that reinforcement was more effective to improve the performance than enlarging the wall thickness of steel tubes.

In order to further improve the confined effect of the steel tube on concrete, CFST with binding bars and steel tube confined reinforced concrete (STCRC) columns have been put forward by some scholars.

Cai and He [7, 8] proposed a constitutive relationship for square CFST columns with binding bars, and a calculation of complete load-stress relationship curves was conducted for some certain experimental specimens using this constitutive relationship. Experimental investigation and theoretical research on specially shaped (L-, T-, and cross-shaped) CFST columns with binding bars were shown by Long et al. [9–12]. Finite element analyses of rectangular CFST columns with binding bars were carried out using five material models including von Mises, Mohr–Coulomb, Drucker–Prager, smeared cracking, and damaged plasticity by Chen and Zhou [13]. Ren et al. [14] reported that the axial compression mechanism of round-ended CFST short columns with binding bars was carried out with different diameters of the binding bar, concrete strength, distance between binding bars, steel content of section, height-width ratio, etc.

STCRC is a kind of composite member that is similar to CFST by wrapping the thin-walled steel tube on the outside of concrete and confining it. However, steel tube wall does not directly bear external load, which is disconnected at the joint for the connection conveniently between the reinforced concrete column and beam. Zhang et al. [15] discussed axial compression test and analysis of circular section STCRC columns with high-strength concrete. Zhou et al. [16, 17] investigated the mechanical performances of square STCRC short columns by test and then reported the axial load behavior of circular section STCRC columns with different length-to-diameter ratios. Gao et al. [18] completed properties of 12 STCRC columns with different steel tube diameter-thickness ratios, slender ratio, and loading eccentricity ratio by test, and effective experience was obtained.

Based on the above research, it is easy to know that steel tubes and binding bars all provide constraint effects on concrete. However, studies on the collective effect from them on concrete are rare. Considering the advantages of STCRC and binding bars, a new type of component named STCRC column with binding bars is proposed in this paper. When the STCRC column with binding bars is loaded under axial compression, the core concrete is pressed first because both ends of the outer steel tube are shorter than those of the core concrete. The steel tube and binding bars are not directly loaded, which mainly confine the concrete. So, the test study, the finite element analysis, and theoretical calculation on this kind of component are carried out under axial compression in order to provide the reference for the engineering design.

2. Experimental Program

2.1. Specimen and Material. In order to investigate the mechanical properties of the square-tubed reinforced concrete column with binding bars, an axial compression specimen is made. The average concrete properties are all from material quality testing: f_{cu}, f_c, ε_o, and ε_c are cube compressive strength, uniaxial compressive strength, yield strain, and ultimate strain, respectively, where $f_{cu} = 43.7$ MPa, $f_c = 33.2$ MPa, $\varepsilon_o = 0.002$, and $\varepsilon_c = 0.0033$. The steel reinforcement bars are of 400 MPa grade with the diameters of longitudinal and binding bars 14 mm and 6 mm, respectively, where HRB400, **C**14, and **C**6. The grade Q235 thin-walled steel tube has a thickness of 2 mm. The mechanical properties of steel from material quality testing are shown in Table 1, where E is the elastic modulus, f_y is the yield strength, and f_u is the ultimate strength.

The specimen is adopted in the test as shown in Figure 1. Before assembling the member, circular holes on the steel walls were made by punching where the binding bars are arranged. Each binding bar joins together with the steel tube through two circular stiffening steel plates on its two ends by welding, which is detailed in Figure 1(b).

2.2. Experimental Setup and Instrumentation. The specimen is tested by an electric-hydraulic serving compression machine with a capacity of 20,000 kN. The compressive load is applied from the top of the specimen through a force loading mode. The load pattern is uniaxial monotonic loading. After the load-displacement curve becomes nonlinear, load is increased slowly and continuously until final failure and data are recorded continuously.

The axial deformation of the concrete column and strains of longitudinal bars, binding bars, and steel tube are measured in this test. The axial deformation is obtained by the electric-hydraulic serving compression machine. Strain gauges are placed on the tube wall to measure vertical strain and hoop strain of the steel tube wall. Strain gauges are placed on longitudinal bars and some binding bars to measure the tension strains of the bars. Experimental setup and instrumentation are shown in Figure 2.

3. Test Results and Analysis

3.1. Failure Mode. The failure modes of the specimen on each tube face are shown in Figure 3. The axial deformation of concrete occurred under compression, by which transverse expansion deformation of concrete is caused. The core concrete is wrapped and constrained by the steel tube wall, and the steel tube wall is constrained by binding bars locally, so local buckling of the wall between the binding bars is like wave shape.

3.2. Load-Strain and Load-Displacement Responses. As shown in Figure 4, the variation on strain of longitudinal reinforcements with the axial load P can be seen, where the negative sign represents compressive strain. From Figures 4(a)~4(c), the strains of the angular reinforcements ZA and ZB are greater than the ones of ZC and ZD. From Figures 4(d)~4(f), the strains of the reinforcements ZE, ZF, ZG, and ZH are greater than the ones of ZI, ZJ, ZK, and ZL. This is because that it is difficult to ensure the uniform symmetry of concrete and steel bars in the concrete casting procedure, by which the specimen under the axial pressure lightly becomes the one under eccentric compression. Stress on both faces A and B of the specimen is greater than that on both faces C and D by which the compression deformation of the angular reinforcement ZB and concrete near it is induced bigger, as shown in Figure 5. It can also be seen that the microstrains at the measuring points are close to 2000 $\mu\varepsilon$,

Table 1: Mechanical properties of steel from material quality testing.

Steel reinforcement and tube	E (MPa)	f_y (MPa)	f_u (MPa)
C6	217897.33	482.00	644.33
C14	206675.67	482.00	580.33
Q235	161702.67	158.00	265.67

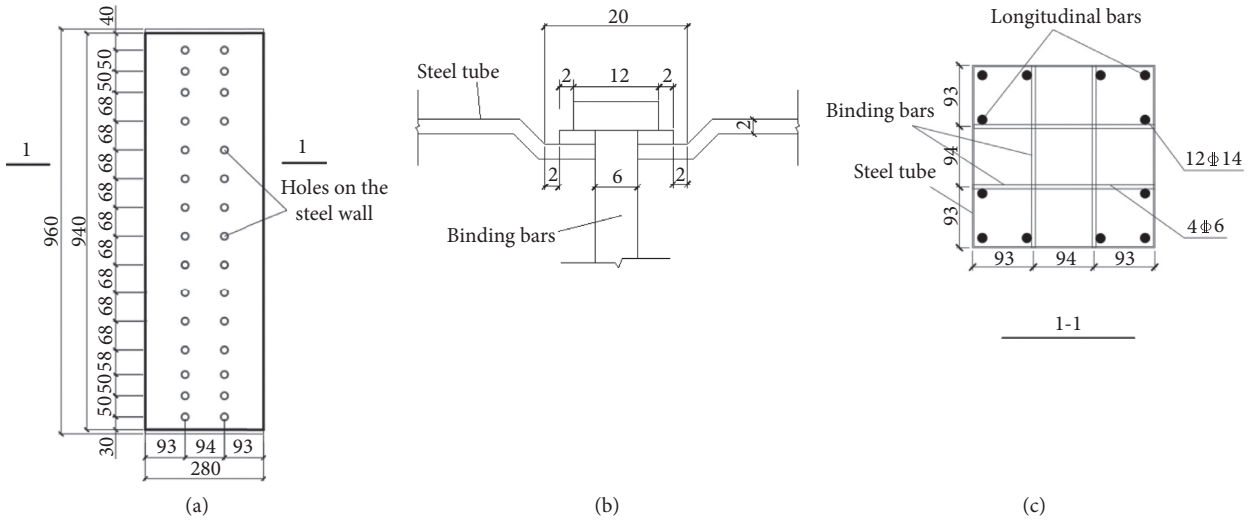

Figure 1: Dimension and detailing of specimens (unit: mm): (a) elevation drawing, (b) detail of binding bar construction, and (c) section of reinforcing bars.

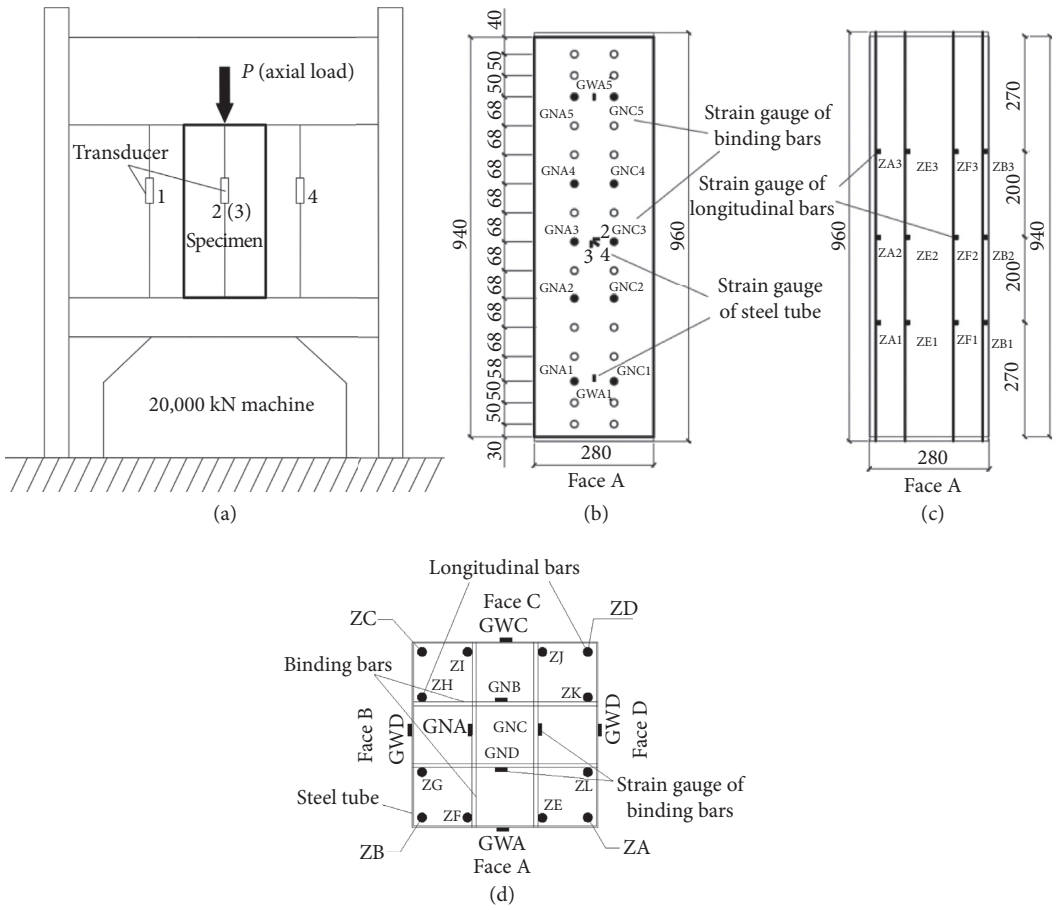

Figure 2: Sketch of test setup and location of strain gauges: (a) test setup, (b) binding bars and steel tube, (c) longitudinal bars, and (d) plane arrangement chart.

(a) (b) (c) (d)

Figure 3: Failure modes.

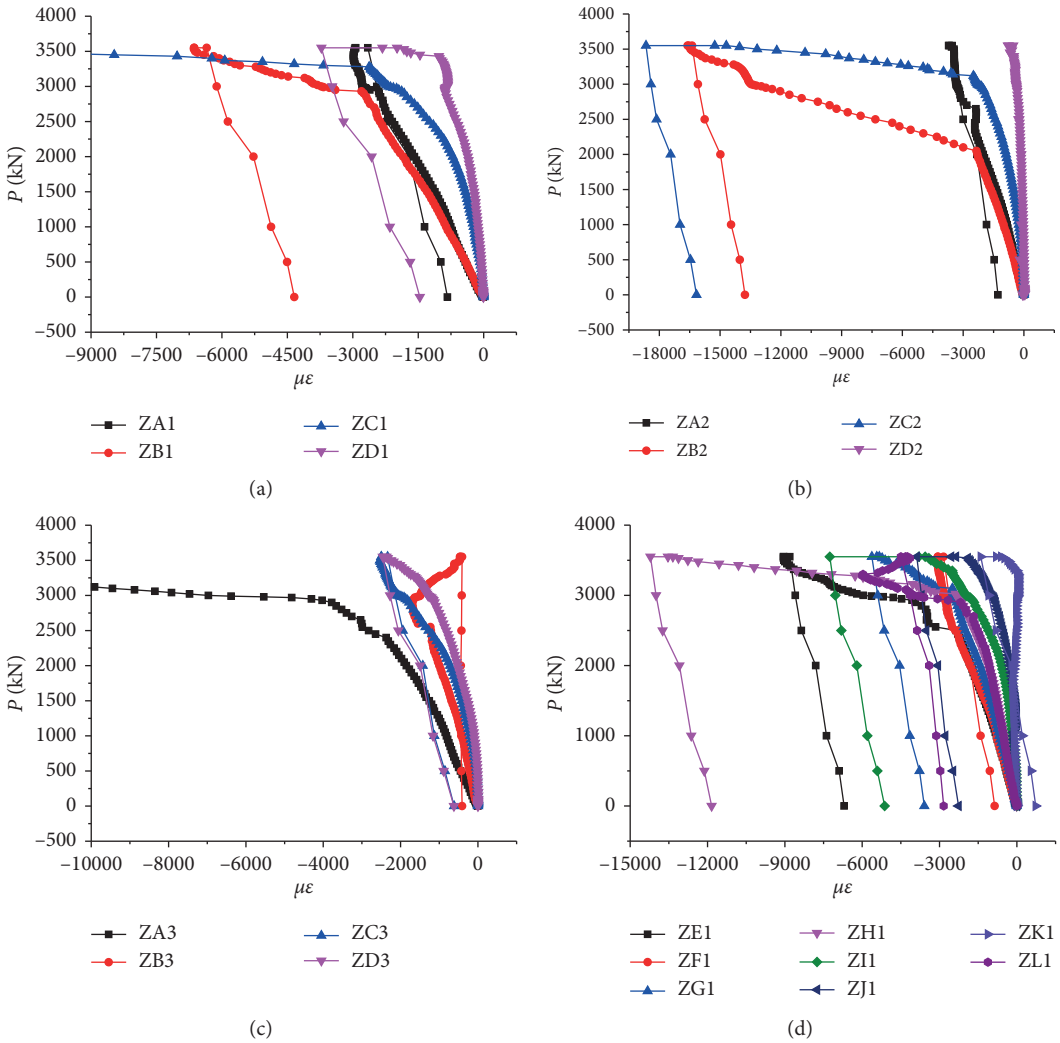

(a) (b) (c) (d)

Figure 4: Continued.

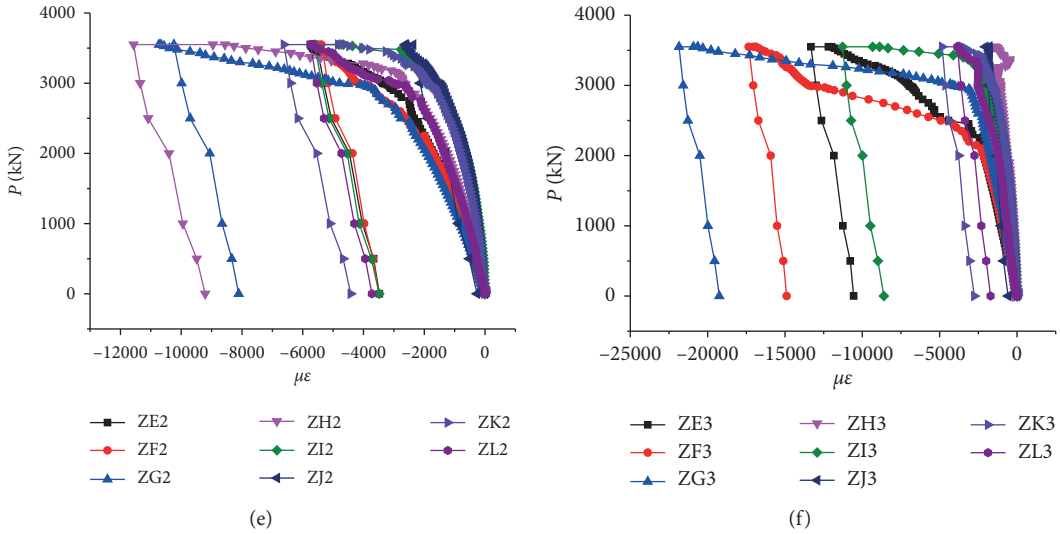

Figure 4: Load-strain curves of longitudinal bars.

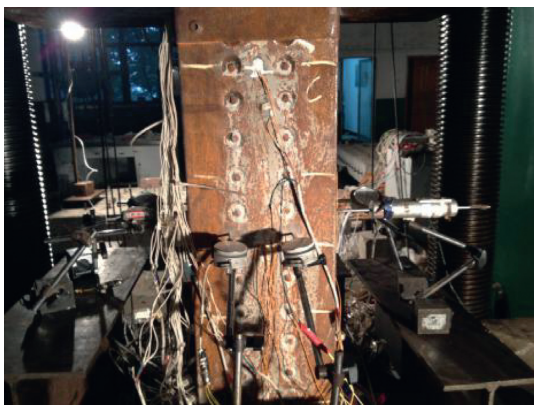

Figure 5: The specimen is inclined to the B face.

and the steel bars basically begin to yield when the load is applied near 2200 kN.

As shown in Figure 6, the variation curves of tensile strain with axial pressure of binding bars at different height sections of the column are given. The tension strains at the measuring points GNB and GND are larger than those at the points GNA and GNC from Figures 6(a) and 6(b). The tensile strains of the binding bars are close to each other in Figures 6(c) and 6(d), and it can be known that the bending deformation of the column body in this section is very small. Figure 6(e) shows that the tensile strains at all measuring points are larger than those of Figures 6(a)~6(d), which indicates that the upper deformation of the column is more obvious. It can also be seen from Figure 6 that the upper binding bars of the column begin to yield when the axial pressure is applied to near 1600 kN; while the load is applied to 3000 kN, the tension bars yield completely.

As shown in Figure 7, the variation curves of the strain with the axial pressure of the steel tube at different positions are given. The strains on face A of the steel tube wall are very large. The strains on face A at both ends of the column are much larger than those of the other three faces especially, and the strains on the other three faces at both ends are very close to each other. In Figure 7(b), the strains at the measuring points of the wall are basically in the elastic range and are very small mainly due to the transverse strains measured here. However, the axial strains of the steel wall basically reach the yield value.

The curve between axial load P and average axial displacement Δ is shown in Figure 8. It can be seen that the load is applied to the maximum value $P_{max} = 3490$ kN corresponding to the displacement $\Delta_{max} = 5.9$ mm.

4. Finite Element Analysis

4.1. Model Description. In order to study the axial compression members of STCRC with binding bars and to verify the effectiveness of the finite element model at the same time, numerical simulation analysis for the test specimen is conducted by using finite element software ANSYS.

The stress-strain curve of the steel tube is simulated by the bilinear isotropic hardening (BISO) model in ANSYS program, meeting von Mises yield criterion, and the plastic modulus of the hardening section is 0.01 times of the initial elastic modulus. The W-W failure criterion is defined by the order "TB, concr, matnum" for the concrete material model. The stress-strain relationship of concrete before cracking and crushing is linear. After cracking and crushing, the multilinear kinematic hardening (KINH) model is adopted for the constitutive relation of concrete.

The concrete is simulated by using SOLID65 element. The steel tube, end plates, and stiffening plates are simulated by using SOLID187 element. Initial defects of the component and the mutual slippage between concrete and steel tube were ignored. The longitudinal reinforcements and binding bars are simulated by using LINK180 element. In order to facilitate mesh generation, the circular holes on the steel walls are replaced by square ones. The lower surface of

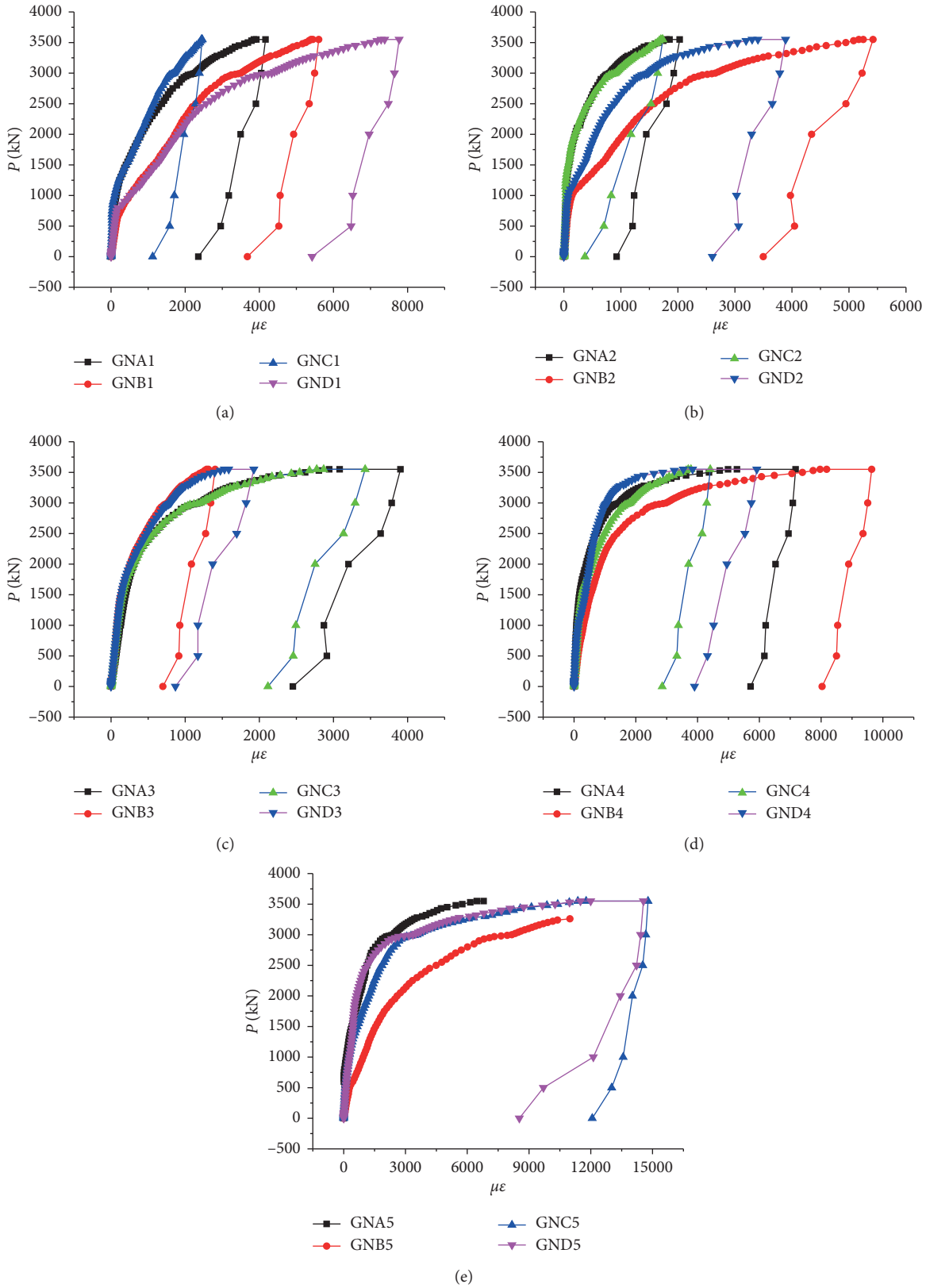

Figure 6: Load-strain curves of binding bars.

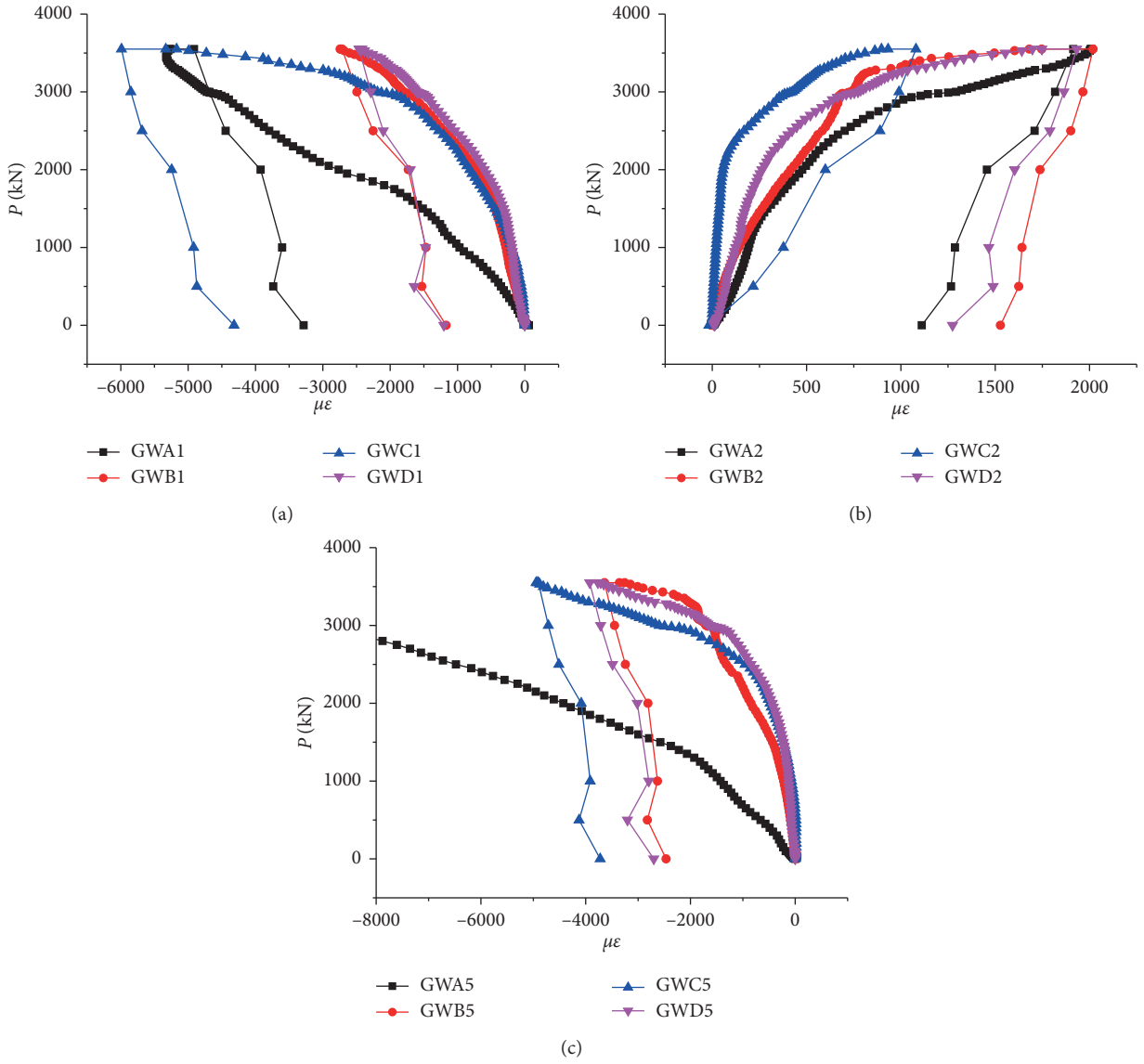

Figure 7: Load-strain curves of the steel tube.

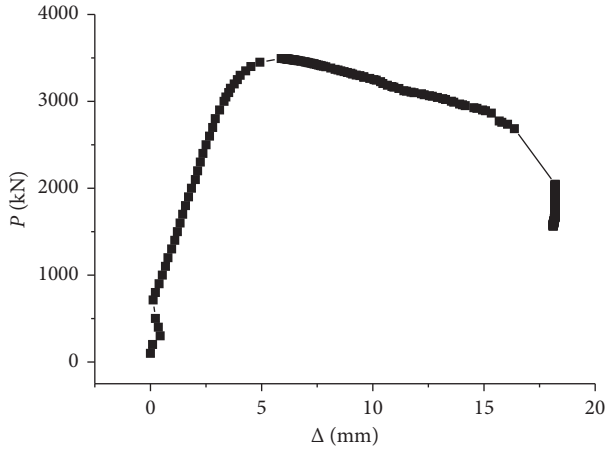

Figure 8: The load-displacement curve.

the steel tube and concrete is fixed against all degrees of freedom, and the upper end is free while encountered by axial load. The nonlinear equations are solved by the incremental iterative method. Material characteristics, boundary conditions, and loading method of the finite element model are all the same as those of the test. The model is meshed freely as shown in Figure 9.

4.2. Model Verification. The comparison of experimental and modeling ultimate load-displacement curves is shown in Figure 10. A good agreement is found in general, and the discrepancies between experimental and predicted ultimate load bearing capacity are close to each other except that the ultimate displacement of the finite element model is smaller than the experimental one. In addition, the predicated cloud

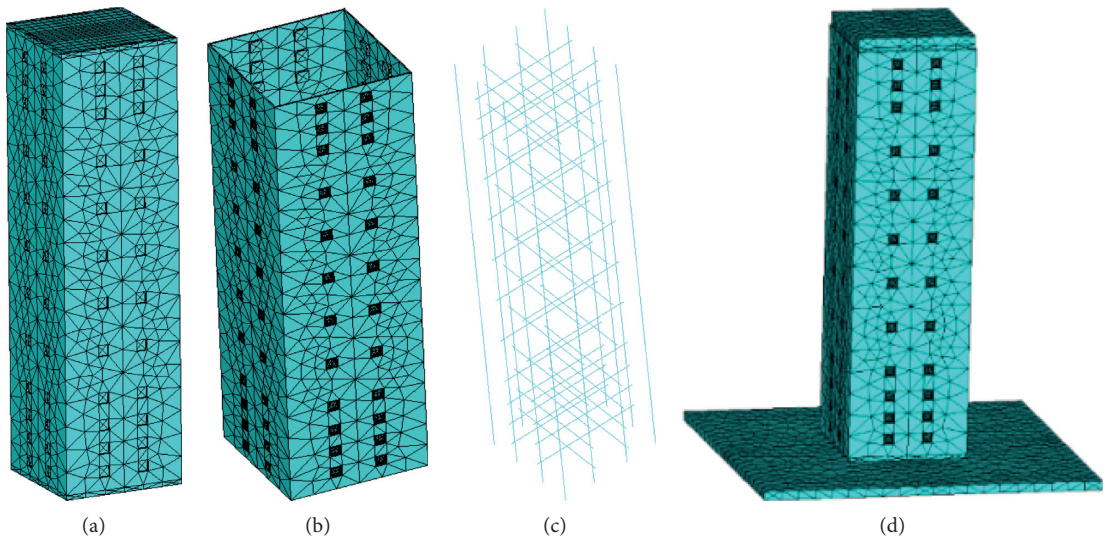

Figure 9: Models of the finite element: (a) concrete element, (b) steel tube element, (c) reinforcement element, and (d) integrated model.

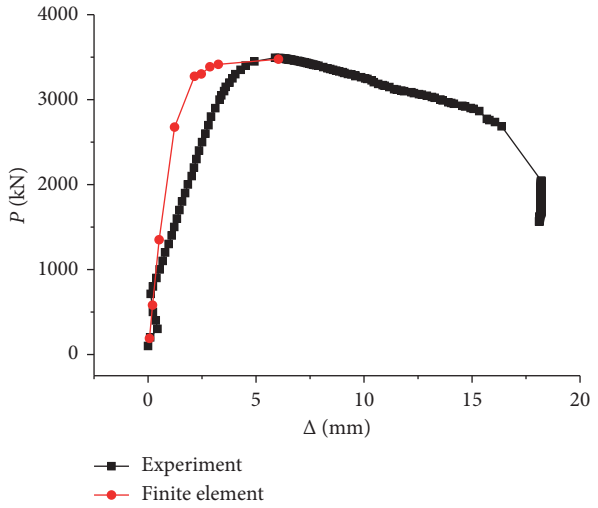

Figure 10: Comparison of load-displacement curves.

pictures of holistic displacement at the moment of component failure are shown in Figure 11. It can be seen that lateral bending of the column and uneven distribution of displacement at the same cross section occurred. As can be seen from these figures, local buckling of the steel tube appeared at the upper end of the steel wall which is consistent with the experimental failure modes. In all, although there is some gap between experimental and modeling results, it is feasible for parameter analysis.

5. Parametric Studies

The following parameters of the specimen are analyzed and discussed in order to further investigate the mechanical properties of concrete-filled square thin-walled steel tubular columns with binding bars, including spacing of binding bars, diameter of longitudinal bars, concrete strength, thickness of the steel tube wall, and section dimension of the column. During the parameter analysis, only the individual parameter is changed, and the other parameters remain unchanged as test value every time.

5.1. Effect of Spacing of Binding Bars. Comparison of load-displacement curves with different spacings of binding bars is shown in Figure 12. The axial bearing capacity (P_u) and displacement (Δ_u) of members can be seen in Table 2. It can be known there is little effect on the load-displacement curve for different spacings of binding bars. The ultimate bearing capacity and displacement are slightly changed with the increase of the spacing.

5.2. Effect of Diameter of Longitudinal Bars. Comparison of load-displacement curves with different diameters of longitudinal bars is shown in Figure 13. The axial bearing capacity (P_u) and displacement (Δ_u) of members are shown in Table 3. It can be seen that there is a little effect on the

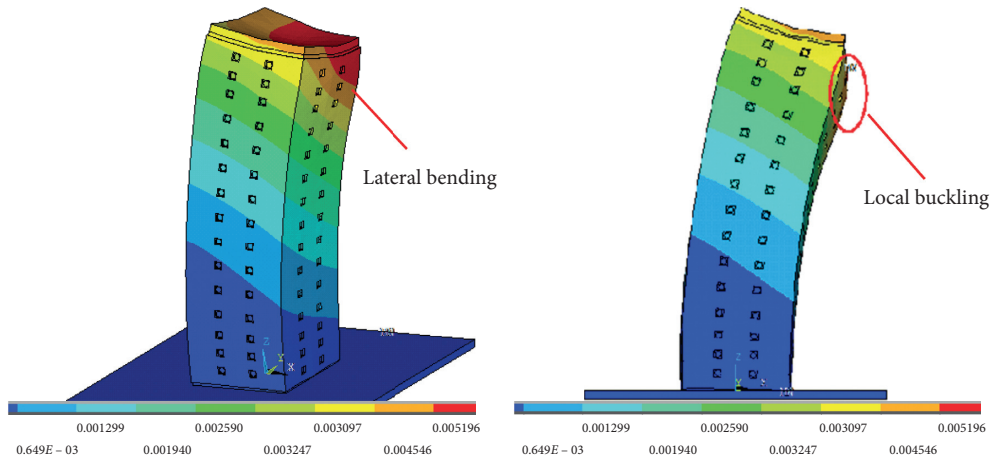

Figure 11: Cloud pictures of holistic displacement.

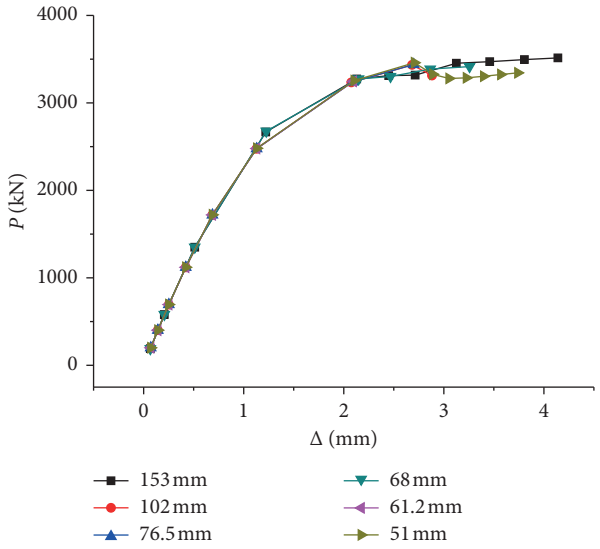

Figure 12: Influence of binding bar spacing on specimen performance.

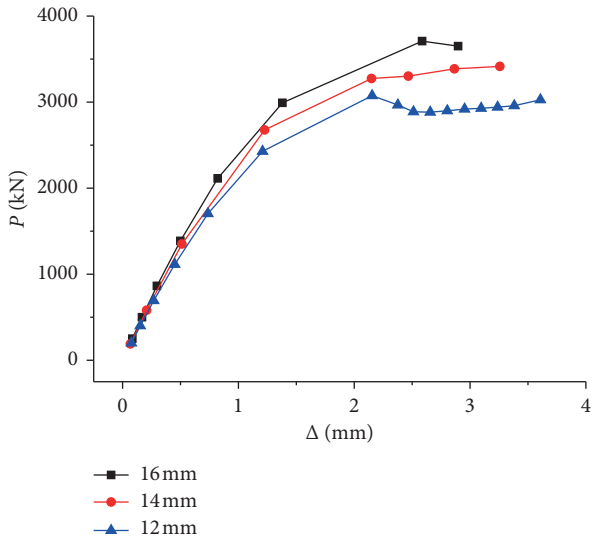

Figure 13: Influence of longitudinal bar diameter on specimen performance.

Table 2: Influence of binding bar spacing on ultimate axial bearing capacity and displacement of the specimen.

Spacing of binding bars (mm)	P_u (kN)	Δ_u (mm)
153	3514.26	4.1403
102	3434.64	2.8828
76.5	3439.43	2.6999
68	3415.27	3.2574
61.2	3246.27	2.0963
51	3343.11	3.7391

elastic stiffness of the specimen. With the increase of diameter, the bearing capacity of the members increases, while the peak displacement and the ductility decrease slightly.

5.3. Effect of Concrete Strength. Comparison of load-displacement curves with different concrete strengths is shown in Figure 14. The axial bearing capacity (P_u) and displacement (Δ_u) of members are shown in Table 4, where f_{cu} is the cube compressive strength and f_c is the corresponding uniaxial compressive strength. It can be seen that the stiffness and bearing capacity increase with the increase of concrete strength.

5.4. Effect of Thickness of the Steel Tube Wall. Comparison of load-displacement curves with different thicknesses of the steel tube wall is shown in Figure 15. The axial bearing capacity (P_u) and displacement (Δ_u) of members are shown in Table 5. It can be seen that there is little change for the elastic stiffness and bearing capacity with the increase of the wall thickness. However, the peak displacement decreases gradually. Therefore, with the increase of thickness, there is some increase about bearing capacity and stiffness. It leads to adverse effect on the specimen performance when the wall thickness reaches a certain value.

Table 3: Influence of diameter of longitudinal bars on ultimate axial bearing capacity and displacement of the specimen.

Diameter of longitudinal bars (mm)	P_u (kN)	Δ_u (mm)
16	3709.18	2.8967
14	3415.27	3.2574
12	3027.26	3.6075

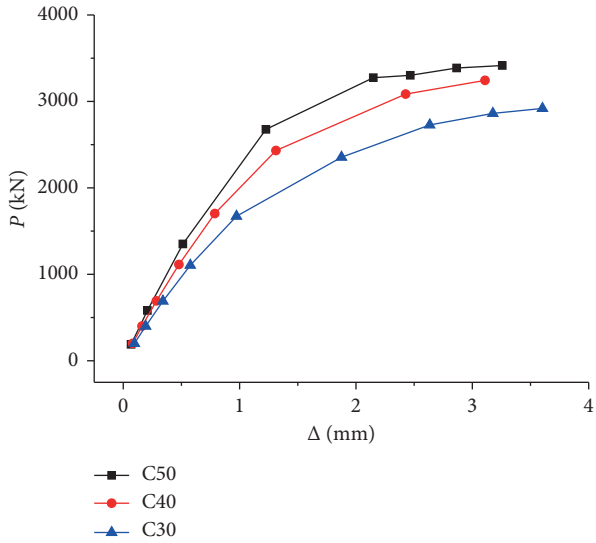

Figure 14: Influence of concrete strength on specimen performance.

Table 4: Influence of concrete strength on ultimate axial bearing capacity and displacement of the specimen.

Concrete strength grade	f_{cu} (MPa)	f_c (MPa)	P_u (kN)	Δ_u (mm)
C50	50	23.1	3415.27	3.2573
C40	40	19.1	3243.68	3.1095
C30	30	14.3	2918.77	3.6033

5.5. Effect of Section Dimension. Comparison of load-displacement curves with different section dimensions of the column is shown in Figure 16. The axial bearing capacity (P_u) and displacement (Δ_u) of members are shown in Table 6. It can be seen that the increase of cross-section size can improve the bearing capacity and stiffness. The peak displacement, bearing capacity, and ductility of the specimen with 320 mm × 320 mm increase significantly.

6. Theoretical Analysis

The model of the square steel pipe constrained on the core concrete is assumed in Figure 17. The shaded part is an effectively confined area, and nonshadowed areas are ineffectively confined ones whose boundary lines are parabolas, where θ is a tangent slope of the boundary, b is the section length, and a_s and b_s are the horizontal and vertical spacing of binding bars, respectively. The confinement effectiveness coefficient k_e is given by

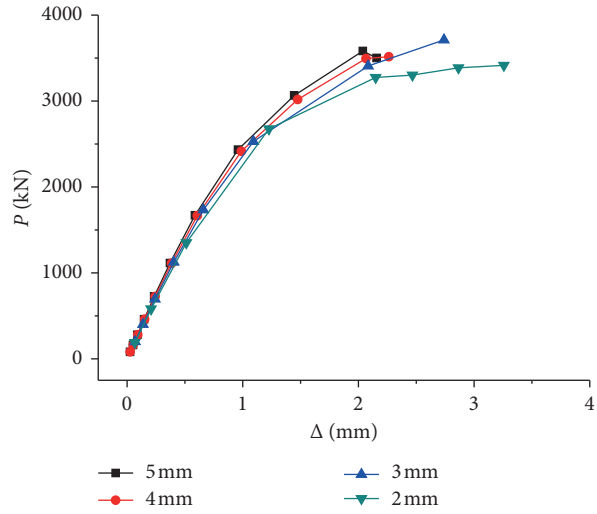

Figure 15: Influence of steel wall thickness on specimen performance.

Table 5: Influence of steel wall thickness on ultimate axial bearing capacity and displacement of the specimen.

Thickness of the steel tube wall (mm)	P_u (kN)	Δ_u (mm)
5	3582.14	2.1573
4	3515.63	2.2630
3	3710.65	2.8248
2	3415.27	3.2573

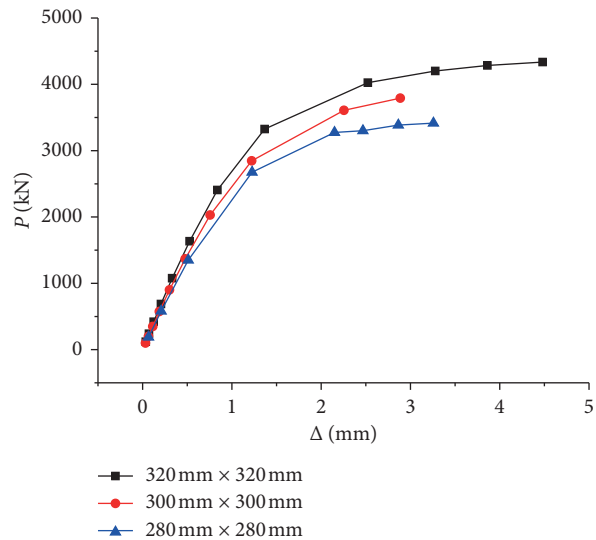

Figure 16: Influence of section dimension on specimen performance.

$$k_e = \left[1 - \sum_{i=1}^{n} \frac{(a_s/b)^2 \tan\theta}{6}\right]\left[1 - \frac{b_s \tan\theta}{2(b-2t)}\right]^2. \quad (1)$$

As shown in [8], the effective lateral confining pressure is

Table 6: Influence of section dimension on ultimate axial bearing capacity and displacement of the specimen.

Section dimension of the column (mm × mm)	P_u (kN)	Δ_u (mm)
320 × 320	4335.85	4.4799
300 × 300	3792.56	2.8860
280 × 280	3415.27	3.2573

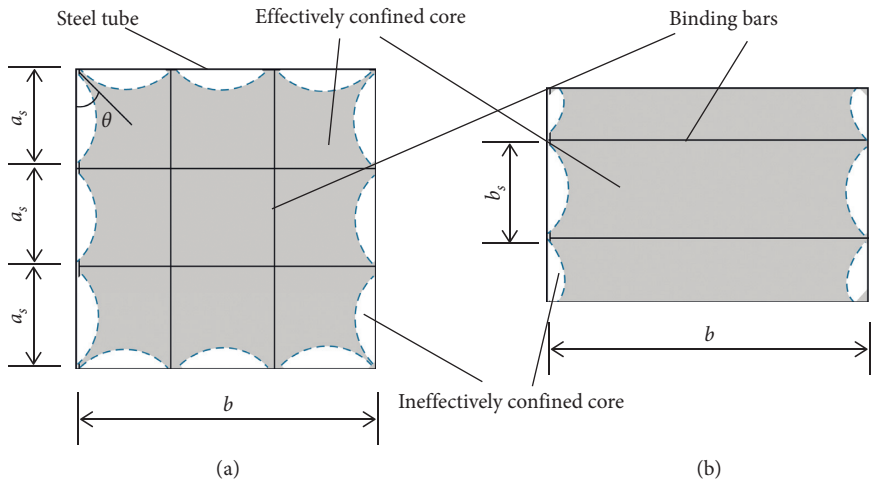

Figure 17: Effectively confined area of core concrete: (a) lateral section and (b) longitudinal section.

$$f_l = k_e f_l',$$
$$f_l' = \frac{2f_{sr} + E_s\varepsilon_s\left(A_s(b-a_s)/a_s b_s t\right)}{(b/t)-2}, \quad (2)$$

where f_l' is the lateral pressure from the transverse reinforcement, assumed to be uniformly distributed over the surface of the concrete core.

When the confined concrete core is placed in triaxial compression with equal effective lateral confining stresses f_l from spirals or circular hoops, it can be shown that the confined compressive strength is given by Mander and Priestley in [19]:

$$f_{cc} = f_{co}\left(-1.254 + 2.254\sqrt{1 + \frac{7.94f_l}{f_{co}}} - 2\frac{f_l}{f_{co}}\right). \quad (3)$$

The meaning of each parameter in the aforementioned formulas can be seen in [8].

The bearing capacity of the STCRC column with binding bars is

$$N_u = f_{cc}A_c + f_y A_b, \quad (4)$$

where A_c and A_b are the areas of concrete and longitudinal bars and f_y is the yield strength of longitudinal bars, respectively.

The above theoretical equation (4) denotes the common bearing capacity of concrete and longitudinal bars, and f_{cc} is the compressive strength of concrete considering the confined effect from binding bars and steel tube. Axial bearing capacity of STCRC columns can be obtained with various strengths and square sections of concrete, bars, and steel tube via the equation.

Table 7: Axial bearing capacity of the specimen.

N_e (kN)	N_{u1}/N_e	N_{u2}/N_e	N_{u3}/N_e	N_{u4}/N_e	N_{u5}/N_e
3490	1.003	1.037	0.682	0.824	0.926

The bearing capacity of the member is reached, and the binding bars and steel tube nearly yield according to the test. The stress of concrete, binding bars, and steel tube is taken as design strength as in [20]. The boundary line is assumed as approximating a quarter circle with the tangent slope $\theta = 45^\circ$ as seen in [16].

The axial bearing capacity ratio of the specimen between test, finite element, and equation (4) is shown in Table 7, where N_e, N_{u1}, and N_{u2} are the axial load strength from test, finite element, and equation (4), respectively. For comparison, the results of the specimens assumed as reinforced concrete (RC), CFST, and STCRC columns all without binding bars are also given here, listing out as N_{u3}, N_{u4}, and N_{u5}, respectively. The formula of N_{u5} can be seen in [16]. It is easily known that the strength of the STCRC column with binding bars is the highest than that of RC, CFST, and STCRC. Although there is a little difference between the previous three results which is acceptable, the restraint effect from binding bars and steel tube on core concrete is obvious.

7. Conclusions

Through the experimental study, finite element parameter, and theoretical analysis on the steel tube confined reinforced

concrete (STCRC) columns with binding bars, the following conclusions are obtained:

(1) For this type of axial compression reinforced concrete column, the core concrete is wrapped and constrained by the steel tube wall, and the steel tube wall is constrained by binding bars locally. The effect controlled and restrained by layer upon layer makes the concrete not easily to be crushed under pressure and improves bearing capacity of the column.

(2) The results of finite element and theoretical analysis agree well with those of the test. It is feasible for qualitative parameter analysis and equation (4) though they are slightly larger. The restraint effect from binding bars and steel tube on core concrete is obvious by comparing the axial bearing capacity theoretically.

(3) The parameters, including spacing of binding bars, diameter of longitudinal bars, concrete strength, thickness of the steel tube wall, and section dimension of the column, generate different influence on the mechanical properties and bearing capacity of the specimens.

Data Availability

The data used to support the findings of this study are included within the article.

Conflicts of Interest

The authors declare that they have no conflicts of interest.

Acknowledgments

This research was financially supported by the Natural Science Foundation of Chongqing (no. cstc2019jcyj-msxmX0440), the Science and Technology Research Program of Chongqing Municipal Education Commission (Grant no. KJQN201901339), the Science and Technology Project of Chongqing University of Arts and Sciences (no. 2017RJJ31), and the Major Breeding Project of Chongqing University of Arts and Sciences (no. P2018JG13).

References

[1] H. Ge and T. Usami, "Strength of concrete-filled thin-walled steel box columns: experiment," *Journal of Structural Engineering*, vol. 118, no. 11, pp. 3036–3054, 1992.

[2] C. S. Huang, Y.-K. Yeh, G.-Y. Liu et al., "Axial load behavior of stiffened concrete-filled steel columns," *Journal of Structural Engineering*, vol. 128, no. 9, pp. 1222–1230, 2002.

[3] H.-T. Hu, C.-S. Huang, M.-H. Wu, and Y.-M. Wu, "Nonlinear analysis of axially loaded concrete-filled tube columns with confinement effect," *Journal of Structural Engineering*, vol. 129, no. 10, pp. 1322–1329, 2003.

[4] F. X. Ding, L. Fu, Z. Yu et al., "Mechanical performances of concrete-filled steel tubular stub columns with round ends under axial loading," *Thin-Walled Structures*, vol. 97, pp. 22–34, 2015.

[5] M. F. Hassanein and V. I. Patel, "Round-ended rectangular concrete-filled steel tubular short columns: FE investigation under axial compression," *Journal of Constructional Steel Research*, vol. 140, pp. 222–236, 2018.

[6] M. X. Xia, L. Ai, and X. R. Liu, "Experimental study on the axial compressive performance of reinforced high-strength concrete filled thin-walled steel tubular column," *Progressing Steel Building Structures*, vol. 22, no. 1, pp. 85–91, 2020.

[7] J. Cai and Z.-Q. He, "Axial load behavior of square CFT stub column with binding bars," *Journal of Constructional Steel Research*, vol. 62, no. 5, pp. 472–483, 2006.

[8] J. Cai and Z. Q. He, "Constitutive relationship of square CFT with binding bars," *Engineering Mechanics*, vol. 23, no. 10, pp. 145–150, 2006.

[9] Y. L. Long and J. Cai, "Experimental investigation into axial compressive behavior of L-shaped concrete-filled steel tubular stub columns with binding bars," *Journal of South China University of Technology*, vol. 34, no. 11, pp. 87–92, 2006.

[10] J. Cai and G. Sun, "Constitutive relationship of L-section CFT with binding bars," *Engineering Mechanics*, vol. 25, no. 10, pp. 173–179, 2008.

[11] X. Shanbin, M. Fanqiang, Z. Peng, B. Jiuwen, W. Junjie, and Z. Kaiyue, "Influence of water re-curing on microstructure of heat-damaged cement mortar characterized by low-field NMR and MIP," *Construction and Building Materials*, vol. 262, Article ID 120532, 2020.

[12] Z. G. Zuo and J. Cai, "Equivalent uniaxial constitutive relationship for the encased concrete of cross-shaped steel tubular with binding bars," *Engineering Mechanics*, vol. 29, no. 2, pp. 177–184, 2012.

[13] X. Chen and D. Y. Zhou, "Comparison among axial behaviors of rectangular CFT stub column by adopting five material models of concrete," *Journal of Building Structures*, vol. 30, no. 3, pp. 120–125, 2009.

[14] Z. G. Ren, C. Liu, D. D. Wang et al., "Axial compression mechanism of round-ended concrete-filled steel tubular stub short columns with binding bars," *Journal of Architecture and Civil Engineering*, vol. 36, no. 5, pp. 39–51, 2019.

[15] S. M. Zhang, J. P. Liu, L. Ma et al., "Axial compression test and analysis of circular tube confined HSC stub columns," *China Civil Engineering Journal*, vol. 40, no. 3, pp. 24–31, 2007.

[16] X. H. Zhou, D. Gan, J. P. Liu et al., "Experiment and analysis on square tubed reinforced concrete stub columns under axial compression," *Journal of Building Structures*, vol. 32, no. 2, pp. 68–74, 2011.

[17] X. H. Zhou, B. Yan, and J. P. Liu, "Axial load behavior of circular tubed reinforced concrete columns with different length-to-diameter ratios," *Journal of Building Structures*, vol. 39, no. 12, pp. 11–21, 2018.

[18] C. Y. Gao, M. Y. Liu, Y. X. Duan et al., "Experimental study on mechanical properties of the tube confined reinforced concrete compression members," *Journal of Xi'an University of Architectural Science and Technology (Natural Science Edition)*, vol. 51, no. 6, pp. 833–838, 2019.

[19] J. B. Mander and M. J. N. Priestley, "Theoretical stress-strain model for confined concrete," *Journal of Structural Engineering, ASCE*, vol. 114, no. 8, pp. 1807–1826, 1988.

[20] GB 50010-2010, *Code for Design Concrete Structures*, China Architecture & Building Press, Beijing, China, 2015.